A Transportable Strontium Optical Lattice Clock Towards Space

by

Lyndsie Laura Smith

A thesis submitted to
The University of Birmingham
towards the degree of
Doctor of Philosophy

Midlands Ultracold Atoms Group
School of Physics and Astronomy
College of Engineering and Physical Sciences
The University of Birmingham

August 2016

For Andreas.

Acknowledgements

There are a huge number of people who have been a great support to me personally and professionally over the duration of my doctoral studies. Professionally, I would first and foremost like to thank the all of the past and present members of the Quantum Matter (QM) group at the University of Birmingham (UoB) where it all began. With my supervisor, Professor Kai Bongs as the Head of Group, I believe the group will continue to achieve great results along with the new Quantum Hub. I am very proud to have known you all and worked alongside such fun and brilliantly minded people.

Working in at UoB has been a journey I'll never forget, working in the office was very distracting at times (I'm looking at you, Mark and Harry. And in my first year, Dan and Mat) but so much fun. I must thank everyone that has helped me, discussed with me, laughed with me and in the case of Andrew Hinton, the unfortunate pleasure of living with me. Wherever life takes you all, I wish you the best of luck and I hope we keep in touch! Within the clock group, I must give particular thanks to Dariusz S̀weirad for his invaluable help in the transportation stages of the project and for numerous discussions and support. To Wei He for his support and unwavering positive attitude. To all of the master's project students for being a constant source of entertainment and questionable music choices and finally to the post docs Dr. Ole Kock, Dr. Joshua Hughes and Dr. Yeshpal Singh for discussions and advice. I must also acknowledge the exceptional work performed by the mechanical workshop at UoB managed by Steve Brookes along with all of their help and advice with anything related to mechanical engineering.

Within the Space Optical Clocks 2 (SOC2) collaboration there are many individuals among the 16 collaborative partners who I am exceptionally grateful to have worked with. I hope and believe that the transportable, space-prototype clock that I have realised will continue to serve the collaboration well under the guidance of the project coordinator Professor Stephan Schiller and through the commitment of everyone in the collaboration. I would like to acknowledge the work and/or help of the following collaborative partners:

- The team at Heinrich-Heine Universität Düsseldorf (HHUD) for the use of their Frequency Stabilisation System (FSS) made by Soroosh Alighanbari, leadership from Prof. Schiller and in particular the immense help of the brilliant Ph.D student Stefano Origlia who came to UoB and Physikalisch-Technische Bundesanstalt (PTB) with me over the last year of my Ph.D and took over responsibility for the clock and achieving further results after my departure.

- The use of the SOC2 laser breadboards made by Dr. Stefan Vogt at PTB and corresponding electronics by their workshop staff, and later the use of their facilities and very valuable expertise. In particular I acknowledge the help from Dr. Christian Lisdat, Dr Uwe Sterr and the rest of the Time and Frequency Division at PTB for their hospitality and advice. Getting to know all of you and working alongside such expertise and knowledge was a genuine pleasure.

- The group at Università degli Studi di Firenze (UNIFI) for teaching me about how to operate all of lasers for some of the first months of my PhD and for the use of their lattice and repumper breadboard designs. I thank Dr. Nicola Poli and Dr. Denis Sutryn for guiding and teaching me and the kind hospitality of the clock group at UNIFI with the head of group Professor Guglielmo Tino. The time I spent in Florence was unforgettable and I loved every moment.

- The use of the permanent magnet Zeeman slower as realised and tested by colleagues at the National Physical Laboratory (NPL).
- And finally the use of all of the TOPTICA lasers and electronics and for very helpful, thorough and kind support from the technical staff whenever I had any questions about the systems.

Personally, my family and friends have been an invaluable support during my doctoral studies and I am grateful for everything that each and every one of them has done to help me. And in particular, at last but certainly in no ways least, I must finally thank my parents, Germaine Smith and Mark Bodley, my best friend Amy Edwards and her family and my boyfriend Andreas Pajuvirta and his family. All of you have always there for me if I needed you, no matter how far away I was.

Abstract

This work presents the realisation and characterisation of the world's smallest transportable optical lattice clock as part of the Space Optical Clocks 2 EU project built at the University of Birmingham. Housed in a transportable rack of dimensions 170 x 100 x 60 cm, such a device aims to measure the frequency of the doubly-forbidden $^1S_0 -^3 P_0$ clock transition in ^{88}Sr in an unprecedented compact apparatus as a major technological milestone towards an optical clock upon the International Space Station. A master optical clock in space would serve with unrivalled accuracy and stability to disseminate a precise and accurate reference for terrestrial clocks and the coordination of international time. Such a clock has the potential to redefine the second, revolutionise timekeeping and precision measurements, and perform fundamental science experiments in space.

Using a combination of novel design, innovative cooling techniques, and robust, compact commercially available products, the clock portability, robustness and operational simplicity have been improved. The apparatus simply and effectively cools and traps up to 10^5 ^{88}Sr atoms at a temperature of $1.3\pm 0.2\,\mu$K in an optical lattice with a lifetime of 0.52 ± 0.01 s within 400 ms. The most recent preliminary clock spectroscopy measurement was 3.6 ± 0.2 Hz. The instability of the clock has been measured at 8×10^{-17} after averaging for 300 s with the goal instability being 5.8×10^{-17} within the same averaging time. These results show the experiment will lead transportable optical clock research and continue with the goal of being a master clock in space.

Table of contents

List of figures

List of tables

Chapter 1

Introduction

Since the realisation of the first atomic clock in 1955, caesium frequency standards have been adopted as the basis for the fundamental definition of the SI unit of time; the second [1] having proven to surpass existing frequency standards in terms of the two factors by which clocks are characterised. These measurements are the accuracy and stability of the clock.

The stability is a measure of how much the frequency of the clock varies over time. Variations in the measured frequency of a clock come from drifts and noise affecting the frequency measurement. A stability measurement is typically the fraction by which it is expected that the clock will drift given a certain time frame. For example, a clock with a stability measurement (instability) of 1×10^{-6} will lose 1 ms every second. Quoting the instability of a clock after just 1 s makes the assumption that the drift is constant and that 10 ms will be lost in 10 s and so on. However, the stability of a clock can be improved (the instability reduced) by averaging the frequency measurement for a long time period. For this reason, often clock stability is quoted over a longer time frame or alternatively as the $1/\sqrt{\tau}$ stability. The latter gives an indication of how the fractional stability changes for increasing averaging times τ by fitting the instability as a function of time to a trendline of $1/\sqrt{\tau}$.

The accuracy of the clock is a measure of how much the frequency measurement of the clock differs from the true frequency reference. It can be attributed to the sum of all possible frequency shifts (in the case of optical atomic clocks: Doppler, Stark, Zeeman and collisional shifts etc) which cause the measured frequency to differ from the true frequency. Shifts in the measurement are not detrimental to the performance of a clock if they can be characterised and then compensated. However, if these shifts are not well understood and characterised, this leads to an uncertainty in the accuracy of the clock. The uncertainty is again a fractional measurement. It is the ratio of the error on the frequency shifts to the clock frequency. It is this uncertainty which is the underlying measurement which determines the quality of a clock. The measurement noise (stability) ultimately limits the uncertainty of a clock, so these two factors are linked strongly.

Modern development in caesium atomic clocks has been in the area of reducing the uncertainty and size. The uncertainty of the best caesium fountain, NIST-F2 at The American National Institute of Standards and Technology (NIST) is 1.6×10^{-16} [2] but occupies an entire laboratory. Whereas the most compact atomic clock, a CSAC (Chip Scale Atomic Clock), has a total volume of only 17 cubic centimetres with an uncertainty of 5×10^{-11} at shipment [3]. The aim of these clocks is research/time dissemination and commercial technologies respectively.

The uncertainty and instability of atomic clocks can be reduced in two ways: to increase the interaction time of the fourier limited caesium clock transition by placing a microwave clock in space or to increase the frequency of the clock transition to the optical instead of microwave domain. The former option is being investigated by the ACES mission (Atomic Clock Ensemble in Space) [4], however, due to the use of caesium, the clock would still suffer from a relatively poor stability from inherent high frequency noise of the interrogation oscillator and would require calibration with hydrogen masers - reducing the payload for the caesium clock and increasing the complexity of the system. The latter option offers a range of benefits including that of fundamental uncertainty (most of the absolute frequency shifts in an optical clock do not depend on the frequency of the transition. For example, collisional shifts and second order Zeeman shifts) and instability (an increase from microwave to optical frequencies leads an increase in precision of 10^5 leading to a quantum limit of $\approx 10^{-18}\tau^{-1/2}$). This new field of optical clocks has been investigated by many research groups around the world such as NIST/JILA [5], SYRTE [6], NPL [7], PTB [8] and Tokyo [9] to name only a handful of contributions.

Terrestrial optical clocks are influenced by the Earth's local gravitational potential. This contributes an unavoidable uncertainty of the order of 10^{-17} meaning that the limit of optical clocks cannot be reached on Earth. Therefore the field is slowly moving towards transportable clocks as the first step towards an optical clock in space. A master clock in space would disseminate an ultra stable and precise time signal to terrestrial atomic clocks improving accuracy and enables research to be performed into several fundamental science streams, improving and enhancing the precision of established technologies and the eventual redefinition of the second. An improvement in stability and uncertainty of atomic clocks will also revolutionise GNSS in the future. Currently the limiting factor of Global Navigation Satellite Systems (GNSS) is environmental (density fluctuations and unpredictable weather patterns). An optical clock in space would also improve navigation of deep space probes allowing a lower failure rate from navigational errors.

There are many possible candidates for use in an optical lattice clock and strontium and ytterbium are the most commonly used. Strontium has been used in this work. The most naturally abundant bosonic isotope, ^{88}Sr, does not possess nuclear spin meaning it is not strongly influenced by magnetic fields. The electronic structure of strontium is sufficiently complex that it contains suitable transitions both for cooling and clock in the optical domain.

Optical frequencies are easily and cheaply utilised by compact, cheap, commercial laser diodes.

This thesis contains the design and realisation of the first fully transportable optical clock as a prototype for a clock to be used on board the international space station (ISS) and is a vital and well defined step towards an optical clock in space. The clock has novel, compact and robust design features and cooling methods. The novel solutions that I have developed and utilised with the aim to produce a simple, efficient, compact and transportable piece of apparatus pave the way for an optical clock in space. The short-term aims of the project are equal parts technology development in the field of atomic clock miniaturisation and novel techniques which can be employed in neutral atom atomic clocks.

Atomics package: I have designed, built and tested the atomics package which is the heart of the experiment and the smallest known optical clock chamber globally to date whilst maintaining more than sufficient optical access for all of the necessary components for the operation of a strontium optical lattice clock. The miniaturisation of the atomics package also led naturally to reducing local Blackbody radiation and the removing the requirement noisy external cooling of the system.

Mini mobile clock housing: I have designed and realised a robust and versatile clock housing for all modular clock components. This rack is constructed from commercial components and is also easy to use, efficient, lightweight and mobile. The rack has been demonstrated to safely and securely house the optical clock after transportation across Europe without causing any damage to the equipment and with minimal realignment required.

Low power atomic oven: I designed and built a low power, efficient and versatile atomic oven which can be used on any vacuum system using CF16 or CF35 tubing.

Novel atomic cooling techniques: To cool an ensemble of strontium atoms sufficiently for use in an optical clock requires the utilisation of two optical transitions. The second cooling stage uses a narrow linewidth transition. The capture rate when using this transition is conventionally broadened to cover the Doppler broadened velocity profile of atoms cooled in the first stage by applying modulation upon the laser via an accousto-optic modulator. In this work, the idea of power broadening the transition is introduced which has not been reported previously in literature when applied to this cooling transition. The power broadening technique boasts a higher capture rate than conventional methods, simplifies the second stage cooling laser breadboard, reduces electrical power use and optical power waste.

Preliminary spectroscopy measurements of the clock transition of ^{88}Sr : The most recent preliminary clock spectroscopy measurement was found to be only 3.6 Hz (natural linewidth $\approx$ 1 Hz). A low linewidth measurement is indicative of a system with low noise and of high stability as each measurement on the spectroscopic curve is taken approximately 1 s apart.

Preliminary stability measurement: The most recent measurement of the stability of the clock was 8×10^{-17} after an averaging time of 300 s. After the 300 s mark, long term drifts and noise sources began to dominate and the rapid improvement in stability of the clock laser frequency gained from averaging down the measurement was compromised. Long term drifts and source of noise can be reduced by gaining a better control upon the environment of the clock - which is planned to take place before the most stable measurements can be made. The best recorded stability of previous iteration of the Space Optical Clocks project using the same lasers was 2×10^{-15} at 1 s [10]. To provide comparison with this project, the preliminary stability measurement of this clock at 1 s is 1.4×10^{-15}.

This thesis is further divided into the following sections.

Chapter 2 is an introduction to and the historical background of atomic clocks and explains potential future applications.

Chapter 3 presents the basic theoretical principles and motivations of cooling and trapping neutral atoms which serves to cover the foundation of operating optical atomic clocks.

Chapter 4 builds on the theory of the cooling and trapping principles of the previous chapter and applies it to the specific physical principles involved when cooling and trapping strontium for use as an atomic clock.

Chapter 5 gives an overview of the design, construction and realisation of the components required for a transportable strontium optical lattice clock with the focus on energy efficiency, compactness and robustness.

Chapter 6 shows the experimental results obtained using this clock apparatus including each cooling and trapping stage and investigations into improving the efficiency of the atomic loading.

Chapter 7 concludes the experimental results, compares them to the guidelines set out by the project specifications and gives an outlook for the potential use of the apparatus in the future.

Appendix A gives an overview of the Space Optical Clocks 2 (SOC2) project participants and the responsibilities of each participant with regards to the workpackages outlined in the SOC2 proposal [11].

Appendix B gives details about the different detection and control systems used on the SOC2 clock apparatus. This includes the detection methods used with the detection systems and the function of the FPGA computer control and temperature stabilisation systems.

Chapter 2

Introduction to the Measurement of Time

Living in a world which is becoming increasingly more concerned with enabling activities in life to be more fast-paced means that research and development has always been ongoing into ensuring that each task that mankind must undertake is as efficient as possible. This means always trying to reduce the time over which actions are performed. To enable this, one must possess a keen, precise and accurate grasp of time. As a result, mankind has striven to increase the precision and accuracy of timekeeping, to synchronise timekeeping on a wider scale as well as improving the stability. The most modern form of this endeavour is the use of the weighted average of the frequency signal kept by over 400 atomic clocks found in over 50 laboratories globally [12]. These time signals constitute international atomic time (TAI) which is a high-precision atomic coordinate time standard based on the rotation of the Earth [13]. TAI is the basis of Universal Coordinated Time (UTC) used in civil timekeeping over the surface of the Earth.

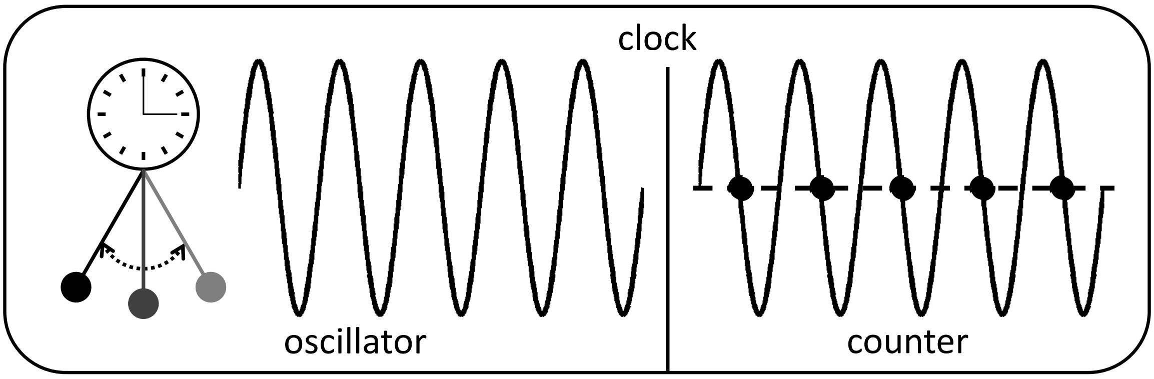

Fig. 2.1 A clock can be visualised as the combination of an oscillator and a counter.

This chapter will serve as an introduction into the background of timekeeping up until the present, to motivate the need for the development of atomic clocks and furthermore, establish the potential applications of a transportable optical clock.

2.1 Clocks Throughout Time

Fundamentally, a clock can be visualised as an oscillator as shown in figure 2.1. If your clock oscillates (ticks) once per second, you have an oscillator with a frequency of 1 Hz. If your clock oscillates 100 times per second, you have an oscillator with a frequency of 100 Hz - and each oscillation has a period of $1/100$ s (0.01 s). Thus, one can see that increasing the number of ticks per second decreases the time period of each oscillation. The more oscillations per second, the more precisely the second can be determined. In other words, the duration of the second stays the same but the number of parts to which can be determined is larger. This can be visualised spatially instead of temporally by considering that one wishes to measure the precise distance between two points that are exactly 0.873 m apart. If the tool to hand is a metre rule with no subdivisions, one can only accurately say that the distance between the two points is less than 1 m. If then the metre rule is marked with 10 equally spaced divisions, the distance between the two points can be determined to be within 0.8 m

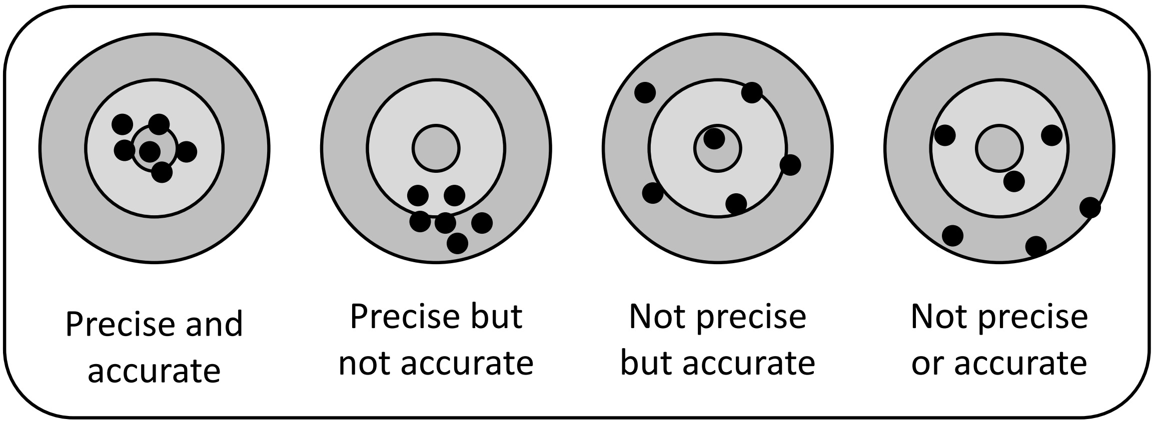

Fig. 2.2 A schematic demonstrating the difference between precision and accuracy

and 0.9 m. If these are then divided again into 10 equally spaced divisions, the distance can be determined to be between 0.87 m and 0.88 m. And further dividing again to millimetres means that the distance can be determined to a precision of 0.001 m.

One may have a clock which ticks many times per second but one needs to know that the duration of each tick is the same. If the duration varies then the accuracy of your clock is compromised - that is, it may be precise, but how do you establish that your clock is accurate? Is the value that you count as one second is in fact one second? The difference between precision and accuracy is illustrated in figure 2.2 via the anagolous use of a bullseye. To establish this, one requires a reference to the oscillator which serves to fix the duration of each period to be exactly $1/f$ of the frequency that you require of the oscillator. Using the spatial example employed above, this problem can be visualised in two ways. Firstly, if the full length of the metre rule was not actually 1 m (it is possible that the ruler could change in length due to temperature fluctuations) then all of the further subdivisions would not be correct. And secondly, how accurately one can determine that each division measures exactly the same. The accuracy of this ruler can then be improved if it could be compared to another piece of equipment which you know to be influenced to a smaller degree than the ruler. The same reasoning applies temporally. The limitation to the number of parts to which the second can be divided is largely technological. It is limited by being able find a reference which is unchanged for a long period of time and the ability to source such a high frequency oscillator which is itself precise enough.

2.1.1 Uncertainty and Instability Measurements of a Clock

Clocks are characterised by two factors; accuracy and stability. The stability of a clock is the absolute measurement of the noise upon the measurement whereas the accuracy of the clock is determined by the sum of all possible shifts causing the measurement to differ from the true value. The measurement noise (stability) ultimately limits the accuracy, so these two factors are linked strongly.

The instantaneous frequency (beat note) of a clock signal can be described as

$$\omega(t) = \frac{d}{dt}\left(\omega_0 t + \phi(t)\right) = \omega_0 + \frac{d\phi}{dt} \tag{2.1}$$

where $\omega(t)$ is the time dependent frequency of the oscillator, ω_0 is the absolute frequency of the reference and ϕ is the oscillation phase. Therefore, the stability of this frequency can be described as the magnitude of relative frequency fluctuations where the frequency fluctuations are given by,

$$y(t) = \frac{\omega(t)}{\omega_0} \tag{2.2}$$

and is characterised with the Allan variance which gives a measure of typical frequency fluctuations averaged over τ. Put in other words, it is defined as half the time average of the square of the difference between successive measurements of the frequency deviation when sampled over a certain averaging time, τ,

$$\sigma_y^2(\tau) = \frac{1}{2}\langle (y_{k+1}(\tau) - y_k(\tau))^2 \rangle \tag{2.3}$$

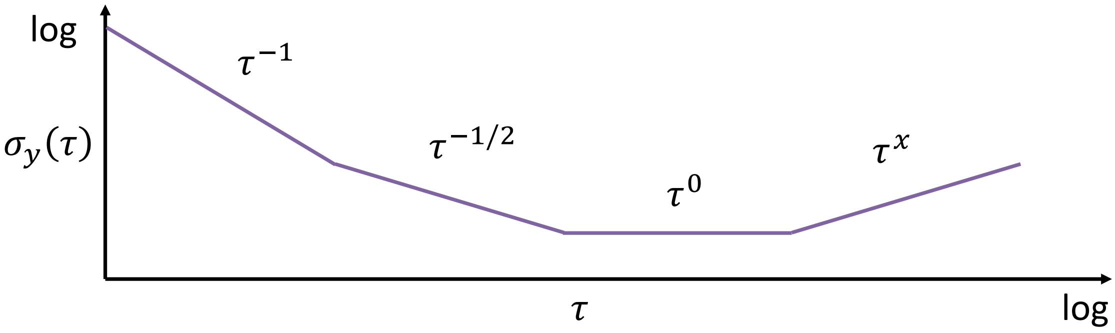

Fig. 2.3 An illustration of the Allan deviation measurement of stability in clocks where τ represents the averaging time. Clock stability measurements are fitted with a slope of $\tau^{-1/2}$.

it is a function of τ and is therefore shown graphically as a result. A lower Allan variance indicates a more stable clock. $y_k(\tau)$ can be described as,

$$y_k(\tau) = \frac{1}{\tau} \int_{t_k}^{t_{k+1}} y(t)dt \tag{2.4}$$

where $t_k + \tau = t_{k+1}$. The Allan deviation $\sigma_y(\tau)$ is the square root of the Allan variance $\sigma_y^2(\tau)$. As Some types of noise can be removed by averaging, this means that the stability (Allan deviation) of a clock improves as the averaging period gets longer and converges to a noise floor. This is where more averaging no longer improves the stability and the remaining noise consists of non-stationary processes such as ageing or random walk frequency noise. Figure 2.3 shows a typical Allan deviation curve with the τ trendlines indicated.

Typically clock stability measurements are fitted to the $\tau^{-1/2}$ region which is dominant over the longest time period in this case. A slope of -1 is indicative of white noise and flicker phase noise, $-1/2$ indicates white frequency noise, a slope of 0 indicates flicker frequency noise and where the noise floor is reached and finally $1/2$ measures random walk frequency noise.

Frequency accuracy is defined as the average value at which the measured frequency of an oscillator differs from the reference frequency. With reference to equation 2.1, the time averaged frequency of the instantaneous frequency is

$$\langle \omega(t) \rangle = \omega_0 = \omega_t + \delta \tag{2.5}$$

where δ is $\frac{d\phi}{dt}$ from equation 2.1 and physically is the sum of all the possible frequency shifts evaluated from measurements of the frequency, i.e. the accuracy of the measurement. Therefore the definition of uncertainty is how well we can measure δ. This means that uncertainty and stability are strongly linked; the total fractional uncertainty cannot be measured to be lower than the fractional instability of the clock.

2.1.2 Clock Development

The development of clocks throughout time has followed this search for both a stable, unchanging reference and an oscillator with a defined period. A summary of some of the most major developments can be seen in table 2.1. This table gives a brief overview of the important factors in timekeeping technologies as they have developed over time. The inaccuracy recorded for each of the timekeeping devices in table 2.1 before the pendulum clock are all calculated with reference to the calendar. An overview of clock performance can be seen graphically in figure 2.4 from the invention of the pendulum clock in 1750 to the present day. The first optical clock was a iodine stabilised helium neon laser in the 1980s.

Modern optical lattice clocks are known to be accurate to a few parts in 10^{18} [18, 19, 20, 21, 22, 23]. The technological challenge comes down to the question: how does one keep an oscillator and reference accurate on that level of precision?

Clock	First Use	Reference	Oscillator	Counter	Inaccuracy / precision
Calendar year	3000 BC	Seasons and stars	Earth orbit	Eyes	4.8×10^{-3} / 1 wk / 4 y
Month	3000 BC	Moon phases	Moon orbit	Eyes	6.8×10^{-4} / 1 d / m
Day	3000 BC	Astronomical	Earth rotation	Eyes	5.7×10^{-5} / 2 h
Sundial	3000 BC	Astronomical	Earth rotation	Stick with clockface	4.6×10^{-6} / 10 min
Water clock	1600 BC	Water flow	Water wheel	Cogs	4.6×10^{-6} / 10 min
Pendulum clock	1656	Pendulum properties	Pendulum	Verge escapement mechanism	3.2×10^{-8} [14]
Marine chronometer	1737	Spring properties	Spring	Balance spring mechanism	2.4×10^{-7} [15]
Quartz clock	1927	Quartz crystal	Electronic circuit	Cog mechanism	1×10^{-7} [16]
Atomic clock	1955	Microwave atomic transition	Laser	Electronics and BIPM	1.5×10^{-16}* [17]
Optical atomic clock	2002	Optical atomic transition	Laser	Frequency comb, electronics and BIPM	1.6×10^{-18}* [18, 19]

Table 2.1 Table showing the developments and characteristics of many historical clocks. All Precision / accuracy values are states at the time of invention with the exception of * denoting the best result to date

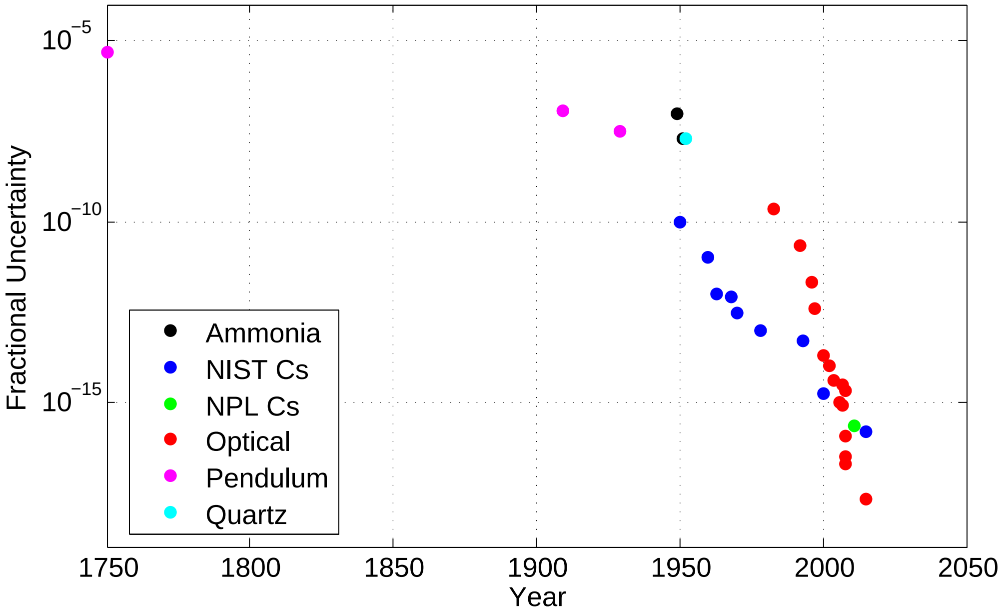

Fig. 2.4 A graph showing the historical improvements of clocks from the invention of the pendulum clock in 1750 to the present day. Data points recorded are the best performance of each clock. A variety of pendulum clocks are shown in pink, ammonia clocks are shown in black, quartz clocks shown in light blue, caesium clocks are shown in blue and green and optical clocks are shown in red.

In the specific case of modern optical lattice clocks, this question can be answered by first having a very precise, stable reference such as an atomic transition and secondly, a laser probe for such a reference. However, it is insufficient to have only one stable reference and probe as the laser probing the atomic transition may drift slightly in time or the frequency of the atomic reference might be influenced by some external noise sources. To assess the accuracy of the clock, it must be compared to another of comparable or better precision.

The reasoning for this can be understood following the previous analogy of the metre ruler. If one also had access to a ruler which measured to a precision of 0.0001 m, then this would enable the ability to assess the accuracy of each mm on the meter ruler. The original ruler could then be adjusted accordingly and the accuracy would be improved. If the second ruler also had a precision of 0.001 m then the same procedure could still take place but it would be unknown whether the discrepancy between the two measurements was due to the original or second ruler. The accuracy could be improved if the measurement of the distance was performed periodically over a long time period and the results averaged. This would increase the accuracy of the measurement by averaging out any errors introduced by the fluctuations in length of the ruler. The same procedure is followed by atomic clocks. Clocks around the world are compared to each other to assess the accuracy of each one and to recalibrate equipment if necessary. The measurements that are compared are the averaged measurements of the frequency of the atomic transition. In this way, the most accurate time signal can be produced.

2.2 Modern Technology

The modern research field of metrology has been improved vastly by scientific developments in last 100 years which have enabled stable references such as atomic transitions to be probed. The use of an atomic transition as a reference was theorised as early as 1879 in a text by Lord Kelvin and Tait and the idea was attributed to Maxwell [24]. The architecture of an atomic clock can be seen in figure 2.5. Provided that the atom is sufficiently shielded from external noise sources, the benefit to using an atomic transition is that electronic frequencies remain unchanged regardless of where the atom is found, and they will remain constant [25]. Because of this, it was decided in 1967 that the definition of the second should be based upon the frequency difference between the two hyperfine levels of the ground state in caesium [1].

2.2.1 Microwave Atomic Clocks

The first microwave atomic clocks were first realised due to the advancements made in the first half of the 20th century in the field of microwave electronics. These microwave clocks

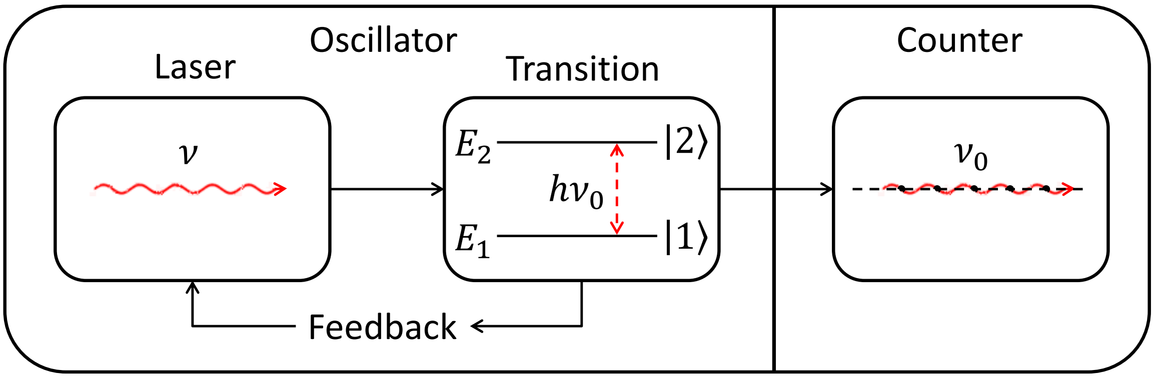

Fig. 2.5 A schematic diagram visualising the architecture of an atomic clock

were more accurate and stable than any previous frequency standards as seen in figure 2.4. In the 1950's, research had begun in several laboratories into utilising the properties of caesium in an atomic clock.

Shortly after this research had begun, the first caesium atomic clock was realised at the National Physical Laboratory (NPL) in London with an inaccuracy of 1×10^{-9} [26]. The modern caesium fountain clocks around the world that contribute to the dissemination of time have an inaccuracy at the level of 10^{-16} [17] after the subsequent 60 years of development [25]. As can be seen in figure 2.4, this level of precision and accuracy has been unsurpassed until the recent development and improvements to optical clocks.

The present benefit to microwave clocks when compared to optical clocks is that microwave clocks can be made to be very compact at the expense of inaccuracy. An example of such miniature clock is the CSAC or rubidium frequency standards. Such very mobile frequency standards are used in research laboratories and for industrial use the world over and can be mass produced. However, given the advancements in optical clock miniaturisation as presented in this work, it is foreseeable that in the future, optical clocks could replace their microwave counterparts in this domain.

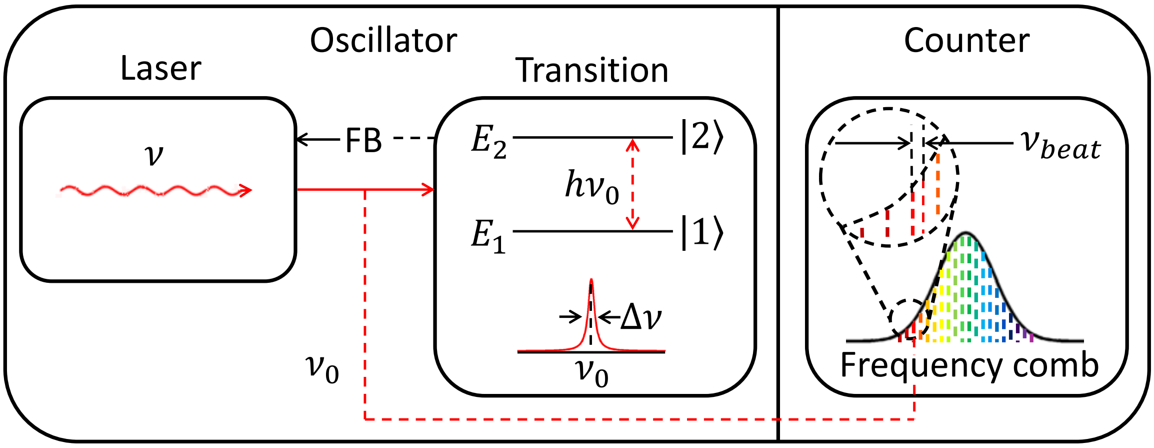

Fig. 2.6 A schematic diagram visualising the architecture of an optical atomic clock

It is not the case however that research has halted into microwave clocks, the modern era of microwave clocks aims to place them in space. An example of such is the Atomic Clock Ensemble in Space (ACES) / PHARAO mission. This is a European Space Agency (ESA) ultra-stable clock experiment to be flown on the International Space Station (ISS). The mission is scheduled for launch sometime in 2016 with a duration of 18 to 36 months. The benefit to a microwave clock in space is that the interrogation time of the atoms is increased in micro-gravity conditions, this should enable unprecedented precision for a microwave clock [27].

2.2.2 Optical Atomic Clocks

The scientific advancements which have allowed the development of optical clocks are improvements in laser technology, electronics, and the invention of the frequency comb. Lasers with a frequency in the optical domain have become smaller, more stable and more coherent since their first invention in 1960 by Theodore H. Maiman at Hughes Research laboratories based upon theoretical work done by Townes and Shawlow [28]. In 1983 a method born from gravitational wave research allowed lasers to be locked using new electronics to form a feedback loop. The technique is named after it's founders as the Pound-

Drever-Hall technique for laser stabilisation [29]. The aim of this technique is to negate the effects of external noise upon a laser spectrum and to further increase the coherency of the light produced by the laser. Using these improvements, the optical atomic clock was born in 2000. A large and unavoidable difficulty in the idea of using an optical transition as a frequency reference was how to solve the problem that the optical frequency needed to be measured. There exists no electronic equipment which is fast enough to count terahertz frequencies and the optical frequencies needed to be divided down to a frequency which could be counted or which could be compared to the microwave frequency of the microwave atomic clocks to assess the performance. This was initially solved via the use of complex frequency conversion chains using the second harmonic generation (SHG) properties of non-linear crystals, where the phenomenon of SHG was only first demonstrated by Hill, Peters, Franken and Weinreich in 1961 [30]. This conversion process was made simpler since the invention of the frequency comb in the year 2000 which earned Hall and Hänsch the Nobel prize for physics in 2005 [31] and enabled the realisation of the optical atomic clock in 2000 [32]. In brief, a frequency comb is a frequency spectrum of equally spaced laser frequencies most often generated by a mode-locked laser. The heirachy of how an optical clock functions can be seen in figure 2.6.

The first optical clock was based on a single mercury ion and realised in NIST in 2006 and with a prototype being operational as early as the year 2000 [32]. With the first neutral-atom optical clock being realised in 2002 using calcium at PTB. However, the first optical lattice clock was realised at the University of Tokyo by Hidetoshi Katori in 2005 [33] showing a linewidth one order of magnitude narrower than that observed for neutral-atom optical clocks, and a stability better than single-ion clocks [33] which paved the way for further research into this new era of optical clocks. Currently, the clock with the best precision in the world is the strontium optical lattice clock at NIST [18, 19] with a total fractional uncertainty of 1.6×10^{-18}, the results of which were published in Science in 2013 and again in Nature

Communications in 2015. This result has been closely followed by the single-ion ytterbium clock at PTB which reports in a publication to Physical Review Letters in February 2016 a total systematic relative uncertainty of just 3.2×10^{-18} [23]. These results show that the most promising candidate for further research is currently the strontium optical lattice clock as is pursued in this thesis.

Due to the size and complex nature of such experiments, much research has been undertaken by the best frequency standard laboratories around the world into miniaturising optical clocks [33, 34, 35, 36]. This development came about after the realisation that terrestrial optical lattice clocks were reaching their fundamental limit of precision on earth as the gravitational effects upon the clock transition cause an annual frequency shift on the 10^{-15} level [37]. Because of this, it would be beneficial to place an optical clock in space. Much like the microwave clock, there are numerous benefits to operating an optical clock in space. The first benefit would be the removal of the gravitational effects upon the clock transition, other benefits include fundamental science research (e.g. a test of the Einstein Equivalence Principle [38], Einstein's theory of relativity, geophysics, and astronomy [39]) and the possibility of using an optical clock in space as a reference for all terrestrial clocks and those on satellites which currently are used for GPS and GNSS systems [40].

2.3 Applications of Optical Atomic Clocks

It is not the case that the only benefit that optical clocks should be to improve the precision, accuracy and stability of timekeeping (and in turn, GNSS), although that is the main driving force for the research. Precise clocks have the ability to be used as extremely sensitive detectors for other attributes other than just time. For example, instead of viewing the external noise sources which alter the frequency of the clock transition as a problem to be reduced, the fact that the clock is altered by such factors could be useful to measure them. These factors include the measurement of gravity, magnetic and electric fields, motion, force and temperature. An example of a clock as a sensor is precision geodesy which is the mapping of gravitational fields near to the surface of the earth. A change in height of 10 cm corresponds to a change in the clock frequency of around 10^{-17}. If it were possible to construct an optical clock with an uncertainty lower than 10^{-17} which could be transportable, then precise gravity measurements could be made. Such measurements could be useful in the fields of geology or hydrology [41]. An interesting new paper published by Jun Ye et. al. in June 2016 proposes the use of space based optical lattice clocks as a tool for measuring gravitational waves [42]. This proposal is particularly current since the first publication of the measurement of gravitational waves made headline news the world over in February 2016 [43] from data taken in September 2015. This proposal shows the broad range of science which is capable for an optical clock in space.

Optical clocks have also been used to provide measurements of possible changes in the fundamental constants of nature which has large implications in cosmological research and to perform tests of Einstein's theories of relativity and are likely to contribute to the redefinition of the SI second [44]. Optical lattice clocks offer unprecedented levels of both precision and stability, if optical clocks were used to redefine the second, this could lead to a revolution in the way that time is disseminated around the world [41].

2.4 Transportable Clocks

As an intermediate stage between stationary and space clocks, the transportability of terrestrial optical clocks could open a whole new range of scientific possibilities. Not only could optical clocks be able to be used as sensors as described in section 2.3 but also they could be used as a device to travel between metrology institutes to give a comparison between clocks around the world. Currently, if one wishes to compare two optical clocks in two different geographical locations, it is required that this be performed via GPS or fibre link. Comparison via GPS is limited by the accuracy of the GPS signal i.e. the caesium clock, therefore, for a more precise comparison between two optical clocks, a fibre link can be used. Three such links have been installed in Europe [45, 46, 47] one in Italy, one from London to Paris and one from Paris to northern Germany. These links can be costly, and require collaborative planning. Should a transportable optical lattice clock be constructed, which could be easily taken from one laboratory to another, then this extra complication could be avoided. Then one would simply need to transport the clock and make comparisons on site of the stationary clock.

A problem arises here in that according to special relativity, in the frame of reference of a moving clock, it tick slower than at rest by a factor of $\gamma = \frac{1}{\sqrt{1-v^2/c^2}}$. Therefore, a transported clock would have a discrepancy when compared with the stationary clock which had never been transported. This effect is referred to as kinematic time dilation. An additional effect is predicted by general relativity, which states that the clock ticks faster at a higher altitude due to the increase in gravitational potential. This effect is referred to as gravitational time dilation.

In an attempt to test general and special relativity with respect to time dilation, Joseph C. Hafele and Richard E. Keating took four caesium-beam atomic clocks on two trips around the earth in 1971; first flying eastwards and then westwards. After each trip they measured the clocks against the stationary terrestrial clocks where it was found in each case that the clocks disagreed with each other but the differences were consistent with predictions of special and general relativity. In the case of kinematic time dilation, the difference can be explained by considering the clock onboard the plane to be the rest reference frame. The clock moving eastwards in the same direction as the Earth's rotation is moving faster than the clock on the surface of the Earth, whereas the clock moving westwards against the Earth's rotation was moving slower than the clock on the surface of the Earth. In the case of gravitational time dilation, as the planes both flew at roughly the same hight, the effect was the same in both directions but caused a measurable difference when compared with the terrestrial clocks. The results of the experiment were published in Science in 1972 [48, 49].

Even though the clock will not be transported as far as a complete turn around the globe in one sitting, this is a factor which cannot be ignored when considering the possibility of utilising a transportable clock. The transported clocks in Hafele and Keatings experiment gained $-29\pm\ 10\,\mathrm{ns}$ eastward and $+273\pm\ 7\,\mathrm{ns}$ westward. The expected measured time difference to a first approximation from just kinematic time dilation was given and motivated in the theory paper that Hafele and Keating published [48] and shown in 2.6 as the fractional difference measured.

$$\frac{\tau-\tau_0}{\tau_0} = -\left(2R\Omega v + v^2\right)/2c^2 \tag{2.6}$$

assuming the stationary clock and travel to be on the equator. Where R is the radius of the Earth, and Ω it's angular speed, v is the velocity of the moving clock compared to the stationary clock, c is the speed of light and $\tau-\tau_0$ is the measured time difference of the clocks with the subscript 0 denoting the stationary clock.

As an example of the possible time discrepancies which could occur, if one considers travelling from the uk around 1000 km to northern Germany at an average speed of around $70\,\mathrm{kmh^{-1}}$, eastwards along the surface of the Earth (as was done in this experiment) the estimated frequency shift would be 2.5×10^{-10} which is a significant shift on the scale of the uncertainty goals for this experiment on the order of 10^{-17}.

As mentioned above in section 2.2.1, in 2016 the ACES mission [50, 27] aims to operate a cold-atom microwave clock on the ISS. Within the framework of the ELIPS (ESA's ISS utilisation program), an improved clock was proposed in 2005 as a follow-on mission. The aim for this follow-on mission being that the performance of the clock and time/frequency links will be improved by at least a factor of 10 compared to that of the ACES mission . A promising candidate for an improved clock for this mission is an optical lattice clock [35, 34, 36]. To allow the use of microwave link technology for time and frequency transfer between Earth and the ISS, the payload will contain a frequency comb to convert the ultra-stable optical frequency to a microwave frequency.

2.4.1 Space Optical Clocks Project

The Space Optical Clock (SOC) consortium have been developing technologies towards the realisation of a robust and compact strontium optical lattice clock since 2007 [51]. There are a number of important requirements to allow the operation of an optical clock in space, these can be summarised as: an improved performance compared to microwave clocks (with an inaccuracy lower than 10^{-16}), compact size and moderate mass in compliance with the ISS payload, radiation hardness and low downtime. The clock must have the ability to be operated automatically, to be remotely switched from operational to non-operational mode, and to withstand shocks and vibrations during launch when in non-operational mode. After consideration of these requirements, some advancement was made towards miniaturising an optical clock with the first-generation breadboard using ^{88}Sr [10]. To further advance along the path of realising a space optical clock, the development of an advanced breadboard system with much improved specifications was initiated; which is the subject of this thesis. Preliminary developments using the first generation breadboard are reported in Refs. [34, 36, 39]

The second stage of the Space Optical Clocks project was started in 2011 as a collaboration between 16 universities and institutions shown in table A.1 and the workpackages are outlined in Appendix A and coordinated at Heinrich-Heine-Universität Düsseldorf (HHUD) by Professor Stephan Schiller.

The main goals of the SOC2 project are an instability below $1 \times 10^{-15}\tau^{-1/2}$ and an innaccuracy below 5×10^{-17} in a volume of less than 1000 litres (excluding electronics). Such improvements will enable new applications such as those described above in section 2.3 to become possible. An optical clock in space will allow the best terrestrial clocks to be compared to a higher accuracy within a shorter averaging time than is possible for the ACES mission. The primary objective of the SOC2 project was to develop and characterise two transportable high performance optical clock demonstrators. The second objective was to heighten compactness, robustness and longevity through the development and testing of components and sub-systems. Both objectives relate directly to the implementation of a space clock [11].

Chapter 3

Cooling and Trapping of Neutral Atoms

The capability of utilising atomic properties for use in a frequency standard relies on the ability to access the natural spectral features of the atomic species under investigation. This involves precisely manipulating an ensemble of atoms to reduce frequency shifts and spectral broadening upon the electronic transitions. In the ideal case, one would perform an experiment in the absence of any external causes of perturbations such as electric and magnetic fields, background gas, radiation and gravity and for the atomic sample to be approaching 0 K. In practise however, one can only act to reduce these noise sources as much as possible.

The largest contribution to frequency shifts and spectral broadening is the average temperature and velocity distribution of the probed atoms. An efficient way to cool atoms is via laser cooling. Laser cooling was first introduced as a method for cooling atoms in 1978 by Wineland, Drullinger [52], and Walls after being theorised in 1975 by two groups simultaneously. The first being Wineland and Dehmelt [53] and the second being Hänsch and Schawlow [54] and it is now the standard method employed in cold atom physics to prepare an atomic sample to observe and utilise the spectral features. Laser cooling involves using a coherent source of radiation which is slightly off resonance with an atomic transition.

This frequency detuning is equal to the frequency shift induced by the thermal properties of the atoms. The net effect is that the average atomic temperature is reduced significantly and the velocity distribution of the atomic sample after cooling is limited by the linewidth of the transition which was probed. The scattering force is not sufficient to trap the atoms spatially. Thus, a spatially varying magnetic field which further shifts the energy levels of the atoms causing scattering force can be introduced to act upon the atoms with a larger velocity away from the trap centre. This method is called Magneto-Optical Trapping and was first demonstrated in 1987 by Chu and Prichard using sodium [55] and is the most frequently used technique to trap and simultaneously cool an atomic sample.

The specific details of these processes are important to understand in the field of frequency standards and metrology and I will outline the physical processes in general in this chapter and applying these generalised processes to a more specific case of a strontium optical lattice clock in Chapter 4

3.1 Light-Atom Interactions

Ideally, one would be able to probe an ensemble of atoms at rest in the laboratory reference frame. This would mean that the unperturbed atom would be free from any energy level shifts. The aim is to prepare the atomic sample as close to this ideal case as possible. At the heart of this process is laser cooling.

Laser cooling relies on the force resulting from radiation pressure. Radiation pressure is caused by momentum transfer from scattering events between laser photons and atoms. This force is defined as,

$$F_{scat} \equiv \frac{\Delta p_{total}}{\Delta t} \tag{3.1}$$

where Δt is the decay rate of the transition and Δp_{total} is the total momentum transfer from N_{scat} scattering events, each with a momentum transfer of,

$$\Delta p = \hbar k_L \tag{3.2}$$

where k_L is the wavevector of the scattered photon. With reference to equation 3.1, the scattering force is therefore equal to

$$F_{scat} = \frac{N_{scat} \hbar k_L}{\Delta t} \equiv \Gamma_{scat} \hbar k_L \tag{3.3}$$

where Γ_{scat} is defined as the scattering rate of the transition and is given by,

$$\Gamma_{scat} \equiv \frac{N_{scat}}{\Delta t} \tag{3.4}$$

Which is thus crucial to the understanding of laser cooling.

A scattering event is defined as a photon being absorbed by an atom causing an electron to be excited to a higher energy level. The electron will then either decay naturally to the ground state after some time given by the decay rate of the transition, Δt by spontaneous emission or, in the presence of other resonant photons, the electron can be stimulated to the ground state by stimulated emission. These processes can be seen for the case of a simple two level atom in figure 3.1.

Both of these decay mechanisms result in an emitted photon of exactly the same frequency as the atomic transition with a frequency spread given by the linewidth, $\Gamma = 1/\Delta t$, of the transition. However, stimulated emission results in a momentum transfer in the opposite direction of the incoming photons, whereas spontaneous emission results in momentum transfer in a purely random direction, θ, as can be seen in figure 3.1. Therefore, the total

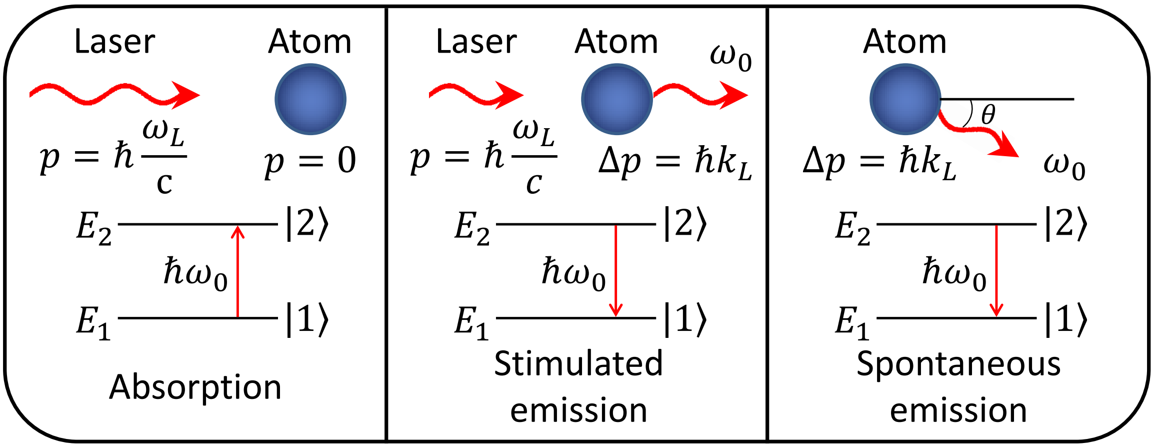

Fig. 3.1 Light-atom interactions: momentum transfer from an incident photon upon an atom in the cases of left: absorption, middle: stimulated emission and right: spontaneous emission.

momentum transfer to the atom over N_{scat} scattered photon events due to spontaneous emission averages to zero and the only contributing factor to the direction of momentum transfer comes from stimulated emission

The number of scattering events, N_{scat}, also gives the population of atoms which are in the excited state $\langle P_2 \rangle$. This can be measured by recording the absorption/scattering response, S_m, of an ensemble of atoms to the frequency, ω_L, of incoming laser photons with intensity of I, driving a transition with a saturation intensity of I_{sat} (the intensity at which the transition must be driven in order to cause the gain in spontaneous emission to become half of the maximum gain), and a transition frequency of ω_0,

$$S_m = N_{scat} \equiv \langle P_2 \rangle = \frac{1}{2} \frac{s}{1 + s + 4\left(\delta_L/\Gamma\right)^2} \tag{3.5}$$

where $\delta_L = \omega_L - \omega_0$ is defined as the detuning of the laser frequency and $s = I/I_{sat}$ is defined as the saturation parameter which is a dimensionless quantity scaling the laser intensity to the saturation intensity of the transition. With reference to equations 3.4 and 3.5 , the scattering

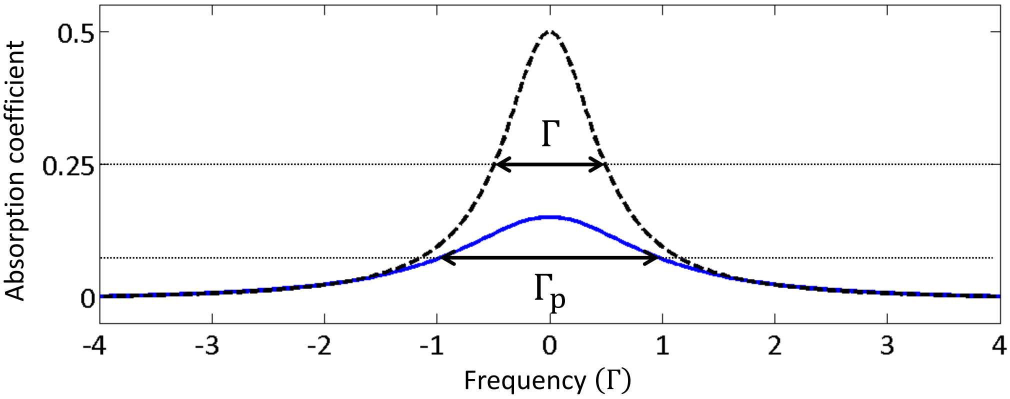

Fig. 3.2 A plot of the absorption coefficient as a function of the frequency used to probe the transition to show the effects of power broadening upon a spectral line. Black shows the spectral response using a laser intensity lower than saturation. Blue is the spectral response using a laser intensity larger than the saturation intensity. Γ is the natural linewidth of the transition and Γ_p is the power broadened linewidth.

rate can therefore be written as,

$$\Gamma_{scat} = \frac{\Gamma}{2}\frac{s}{1+s+4\left(\delta_L/\Gamma\right)^2} \tag{3.6}$$

This has a Lorenzian shape and the full width at half maximum (FWHM) gives the linewidth of the transition

$$\Delta\omega_{FWHM} = \Gamma\sqrt{1+s} \tag{3.7}$$

Therefore the measured linewidth increases with increasing laser intensity. This phenomenon which causes the spectral width of an atomic absorption line to broaden with increasing laser probe intensity is called power broadening.

Power broadening can be understood by considering the population of atoms in the excited state $\langle P_2 \rangle$ as shown in equation 3.5. The atomic populations are generally determined by an equilibrium between excitation and relaxation processes such as collisional relaxation or spontaneous emission.

Power broadening occurs once the transition is saturated. Atoms spend a greater fraction of time in the excited state as the excitation field becomes more intense - saturation essentially reduces the absorption near to resonance whilst far from resonance the absorption changes little (see figure 3.2). However, the proportion of atoms in the excited state will never be greater than half [58]. An overview of power broadening can be found in refs. [59, 58, 57].

Consider now that the atoms have some velocity. If one considers a cloud of thermal atoms at a certain finite temperature, T, these atoms will have a velocity distribution given by the Maxwell Boltzmann distribution,

$$f(\mathrm{v})d\mathrm{v} = \frac{1}{\mathrm{v}_0\sqrt{\pi}} \exp\left[-\left(\frac{\mathrm{v}}{\mathrm{v}_0}\right)^2\right] d\mathrm{v} \tag{3.8}$$

where $f(\mathrm{v})d\mathrm{v}$ gives the number of atoms with a velocity between v and $\mathrm{v}+d\mathrm{v}$ and the most probable velocity, v_0 is given by equating the average kinetic energy of an atom with the ideal gas law which can be rearranged to give v_0 as the argument,

$$\mathrm{v}_0 = \sqrt{\frac{3k_BT}{M}} \tag{3.9}$$

where M is the mass of each atom and k_B is the Boltzmann constant.

In the reference frame of an atom, its velocity, v, causes an observed Doppler shift on the frequency of any incoming radiation. Incident radiation with wavevector k_L can be used to measure the natural (angular) frequency ($\omega_0 = 2\pi\nu_0$) of an electronic transition between two energy levels. The frequency shift from the true frequency of the radiation can be related to the velocity of the atoms with respect to the observer by the well known Doppler equation,

$$\omega_0{}' = \omega_0 + k_L \cdot \mathrm{v} \tag{3.10}$$

And thus, each velocity class (dv) of the atomic cloud will exhibit a different Doppler shifted frequency response to the interrogation light which is characterised by a Gaussian function.

Therefore, the inhomogeneous linewidth is characterised by the convolution of the Lorentzian distribution arising from the spectral line and a Gaussian distribution from the Doppler shift. This lineshape is called a Voigt function which is given (in terms of previously defined parameters) by,

$$V = \int_{-\infty}^{+\infty} G(\nu_L) \cdot L(\nu_L) = I_0 \int_{-\infty}^{+\infty} d\nu \sqrt{\frac{4ln2}{\pi}} \cdot \frac{1}{\Delta\nu_D} e^{4ln2\left(\frac{\nu_0 - \nu_D}{\Delta\nu_D}\right)^2} \cdot \frac{1}{2} \frac{s}{1+s+4\left(\delta_L/\Gamma\right)^2} \tag{3.11}$$

where $\omega_L = 2\pi\nu_L$, $\Delta\nu_D$ is the linewidth of the Gaussian contribution and $\Delta\nu_L$ is the linewidth of the Lorentzian contribution. There is no closed-form solution of this integral so numerical methods for different contributions of $\Delta\nu_D$ and $\Delta\nu_L$ are applied in order to find the correct fit to the data.

In the case that the intensity of the laser probing the transition is roughly that of the saturation intensity of the transition, i.e. $s \approx 1$, the full width at half maximum (FWHM) of the Lorenzian contribution to the Voigt profile is simply the natural linewidth (Γ) of the transition. The FWHM of the Gaussian contribution to the Voigt profile is defined as the Doppler broadened linewidth ($\Delta\nu_D$) of the sample,

$$\frac{\Delta\nu_D}{\nu_0} = 2\sqrt{\ln 2} \cdot \frac{\mathrm{v}_0}{c} \tag{3.12}$$

In the special case that the Doppler shifts are much larger than the natural linewidth of the transition then the Doppler broadened linewidth can be characterised by a Gaussian distribution.

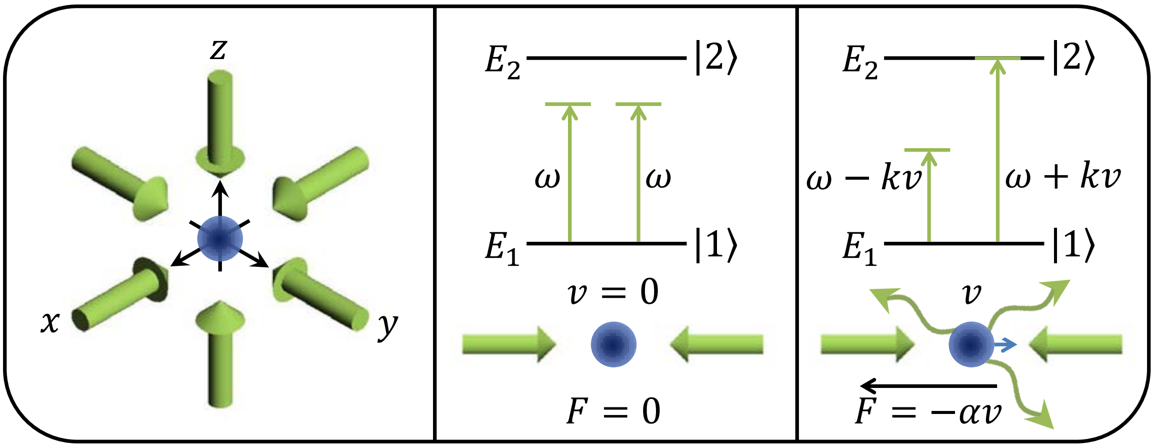

Fig. 3.3 Optical molasses: velocity dependent force acting upon an ensemble of atoms with an average velocity by 3 pairs of opposing laser beams on resonance with an electronic transition

3.1.1 Optical Molasses

In order to cool a thermal gas of two-level atoms with an average velocity, v_0 utilising light-atom momentum transfer, it is required to have a force component in both positive and negative directions in three orthogonal directions. This is commonly performed using six laser beams of identical intensity. If an atom is stationary in the centre of these six beams - the radiation force is balanced in all directions. A moving atom experiences a Doppler shift which leads to an imbalance of forces. This phenomenon is referred to as Optical Molasses and the dynamics of such can be seen in figure 3.3.

In the reference frame of a moving atom, the Doppler effect leads to an increase in the frequency of the laser beam propagating opposite to the direction of travel of the atom. If the laser beam is detuned below resonance, this Doppler shift causes the light to be closer to resonance with the atom and the rate of absorption for this beam is increased.

In the one dimensional, low velocity ($k\mathrm{v} \ll \Gamma$) case the force exerted upon the atom can be expressed as:

$$\begin{aligned} F_{molasses} &= F_{scat}\left(\omega-\omega_0-k_L\mathrm{v}\right)-F_{scat}\left(\omega-\omega_0+k_L\mathrm{v}\right) \\ &\simeq F_{scat}\left(\omega-\omega_0\right)-k_L\mathrm{v}\frac{\partial F}{\partial\omega}-\left[F_{scat}\left(\omega-\omega_0\right)+k_L\mathrm{v}\frac{\partial F_{scat}}{\partial\omega}\right] \\ &\simeq -2\frac{\partial F_{scat}}{\partial\omega}k_L\mathrm{v} \end{aligned} \tag{3.13}$$

The imbalance in forces arising from the Doppler shift can be written as

$$F_{molasses} = -\alpha\mathrm{v} \tag{3.14}$$

And thus the light exerts a frictional force upon the atoms. The damping coefficient α is given as

$$\alpha = 2k_L\frac{\partial F_{scat}}{\partial\omega} = 4\hbar k_L^2 s\frac{-2\delta/\Gamma}{\left[1+(2\delta/\Gamma)^2\right]^2} \tag{3.15}$$

With the $s \ll 1$ term neglected in the denominator. Damping requires a positive value for α and therefore $\delta = \omega-\omega_0 < 1$ which is red detuning.

In order to assess the cooling limits of optical molasses in the general 3D case, it is important to know the theoretical minimum temperature achievable. It is easy to see that the limitations of laser cooling arise from spontaneous emission which is uncontrolled. These spontaneously emitted photons scatter in random directions and thus each atom performs a random walk in velocity space. A random walk of N steps gives a mean displacement proportional to $\sqrt{N}$. During a time t an atom scatters a average number of photons given by,

$$N = \Gamma_{scat}t \tag{3.16}$$

Where Γ_{scat} is given by equation 3.6. Spontaneous emission causes the mean square velocity to increase as $\bar{\mathrm{v}}^2 = \Gamma_{scat} \cdot \mathrm{v}\,(r)^2$ where $\mathrm{v}_r = \hbar k_L/M$ is the recoil velocity of the atom or in the z-direction

$$\left(\bar{\mathrm{v}}_z^2\right)_{sp} = \frac{1}{3}\mathrm{v}_r^2 \Gamma_{scat} t \tag{3.17}$$

The factor of $1/3$ accounts for the fact that photons are emitted in all directions in 3D.

The heating arising from absorption and spontaneous emission can be found by considering the forces imparted upon the atom in the presence of each pair of laser beams and considering the conservation of energy and momentum in the scattering of photons. In the general case of a six beam configuration, the mean square velocity spread is found to be

$$\bar{\mathrm{v}}_z^2 = 2E_r \frac{2\Gamma_{scat}}{\alpha} \tag{3.18}$$

where $E_r = \frac{1}{2}M\mathrm{v}_r^2$ is the recoil energy and $z = x = y$ refers to each of the pairs of laser beams. From this it can be seen that the recoil temperature is determined as the recoil energy divided by the Boltzmann constant,

$$T_r = \frac{\hbar^2 k^2}{2Mk_B} \tag{3.19}$$

According to the equipartition theorem, the kinetic energy of the atomic motion is related to the temperature by $\frac{1}{2}Mv_z^2 = \frac{1}{2}k_B T$. Substituting for α and Γ_{scat} gives

$$k_B T = \frac{\hbar\Gamma}{4} \frac{1 + (2\delta L/\Gamma)^2}{-2\delta_L/\Gamma} \tag{3.20}$$

And the minimum of this function occurs when the value of $-2\delta_L/\Gamma$ has a value of $\delta_L = \omega - \omega_0 = -\Gamma/2$ to give the Doppler cooling limit

$$k_B T_D = \frac{\hbar\Gamma}{2} \tag{3.21}$$

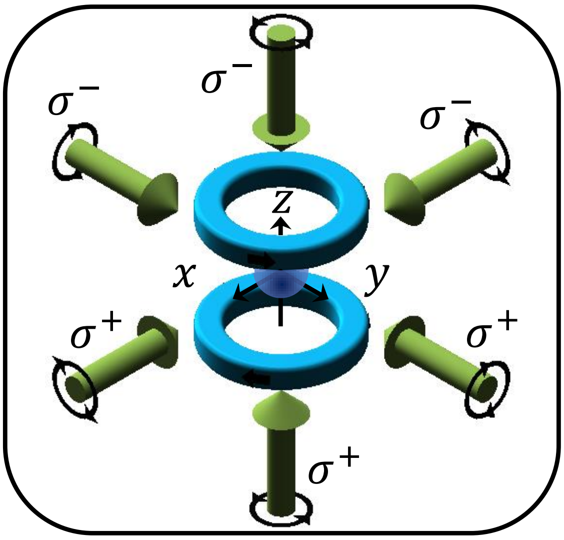

Fig. 3.4 Schematic diagram of the configuration of a magneto-optical trap showing the coils which generate the magnetic field in blue, and the laser beams in green with the atom cloud illustrated in the centre. The polarisation of the laser beams is shown.

3.1.2 Magneto Optical Trap (MOT)

The optical molasses technique lacks a restoring force to confine the atoms to a particular volume in space. The introduction of a linear, spatially varying magnetic field over the atomic position would create the spatially dependent force required to trap atoms the configuration of which can be seen in figure 3.4 and is referred to as a magneto-optical trap (MOT).

A pair of anti-Helmholtz coils can be used to create a quadrupole magnetic field. At the centre point in the quadrupole field the magnetic field is equal to zero and in the volume occupied by the overlapping laser beams, the magnetic field gradient is roughly linear. The Zeeman effect causes the energy of the $M_J = 0, \pm 1$ levels of the $J = 1$ level to vary linearly with the position of the atomic trap position. This causes an imbalance in the scattering forces of the laser beams where the atoms become strongly confined by the radiation force provided that the beams are detuned to a frequency below the resonance frequency. The principle of the MOT is shown in figure 3.5 for a simple $J = 0$ to $J = 1$ transition.

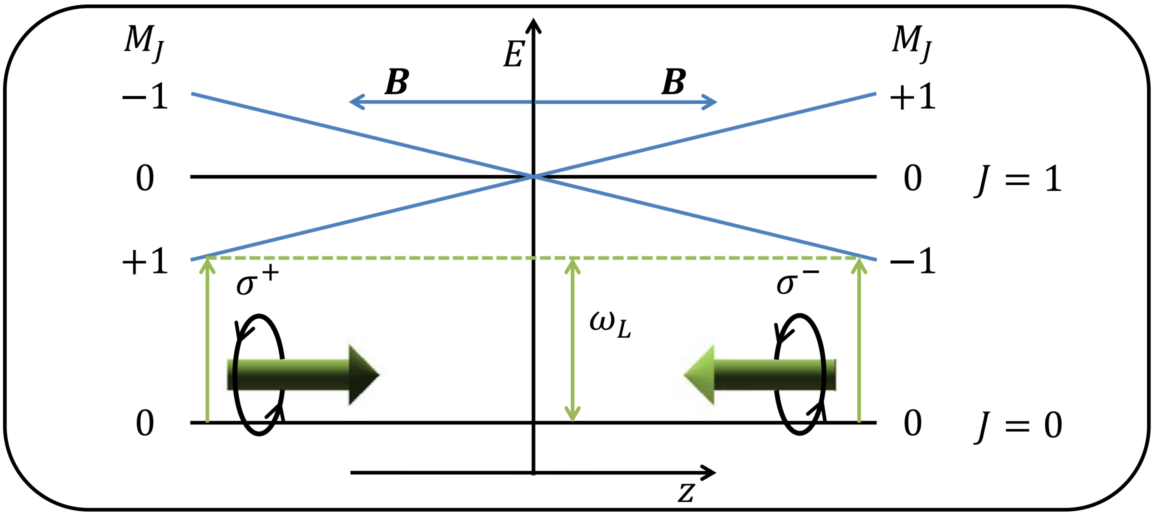

Fig. 3.5 A schematic showing the forces which act upon an atom when in a magneto-optical trap in 1D. The pair of opposing laser beams with their respective polarisations is shown in green. The atomic energy levels are shown in black and the M_J splitting of the $J = 1$ energy level is shown in blue.

The success of this approach is dependent upon correct choice of beam polarisations along with the presence of a magnetic field gradient [56]. The laser beams must be circularly polarised and each opposing pair must contain a beam of both σ^+ and σ^- to break the degeneracy of the magnetic sublevels.

The $\Delta m_J = -1$ transition is Doppler shifted closer to resonance in the reference frame of an atom in the ground state $J = 0$ at a position $z > 0$, and the atom will absorb photons more strongly from the σ^- beam as predicted by quantum mechanical selection rules for momentum transfer. The resulting force pushes the atom towards the centre of the trap at $z = 0$ as shown in figure 3.5. In a magnetic field described by,

$$B(z) = Az\,(A > 0) \tag{3.22}$$

the Zeeman shift of the magnetic m_J sub-levels is

$$\begin{aligned} \Delta E(z) &= \mu m_J B(z) \\ \omega_0(z) &= \omega_0 + m_J \beta z \end{aligned} \tag{3.23}$$

where $\beta = \mu A/\hbar$. It can be seen that the force experienced by an atom in a MOT in the limit of small Zeeman shift $\beta z \ll \Gamma$ and small atom velocity $k_L\mathrm{v} \ll \Gamma$ can be mathematically described as

$$\begin{aligned} F_{MOT} &= F_{scat}^{\sigma^+}(\omega_L - k_L\mathrm{v} - (\omega_0 + \beta z)) - F_{scat}^{\sigma^-}(\omega_L - k_L v - (\omega_0 - \beta z)) \\ &\simeq -\alpha\mathrm{v} - kz = -\alpha(k_L\mathrm{v} + \beta z) \end{aligned} \tag{3.24}$$

where $k = \alpha\beta/k_L$ and α is the damping coefficient given by equation 3.15. This shows that the force experienced by an atom in a MOT can be roughly approximated as the addition of the velocity of the atom ($k_L\mathrm{v}$) with the Zeeman shift (βz) scaled by the damping coefficient which depends on the linewidth of the transition and the intensity and detuning of the trapping lasers. Indicating that the addition of the magnetic field acts as a positionally dependent force, whereas the optical molasses acts as a velocity dependent force.

The capture velocity of a MOT can be estimated by taking the radius r of the MOT laser beams as the stopping distance of a captured atom and using standard kinematic equations to find the following condition,

$$\left(\mathrm{v}_c^{MOT}\right)^2 = 2ra_{eff} \tag{3.25}$$

where a_{eff} is the effective deceleration as experienced by the atom. This is generally expressed as half the acceleration at $I = I_{sat}$ to take into account the fluctuation of the force arising from the random nature of the scattered photons,

$$a_{eff} = \frac{1}{2}a(I = I_{sat}) = \frac{a_{max}}{4} \tag{3.26}$$

where a_{max} is given by equation 3.28. The stopping distance of the MOT is considered to be the radius of the beams r as this is the average distance travelled by an atom until it is outside of the spherical MOT region in 3D. This is the volume over which all of the laser beams overlap, outside of which trapping does not occur. The MOT capture velocity is expressed using equations 3.25, 3.26 and 3.28

$$\mathrm{v}_c^{MOT} = \sqrt{\frac{\hbar k_L}{M}\frac{\Gamma}{4}r} \tag{3.27}$$

The temperature of the atoms trapped in a magneto-optical trap is higher than that of atoms cooled only by the optical molasses technique. The sub-Doppler cooling mechanism offered by the optical molasses technique is suppressed because the strong magnetic field breaks the energy degeneracy of the magnetic sublevels. An extra heating element is introduced in the case of a high atomic density in the trap volume by some atoms in the MOT re-absorbing some of the spontaneously emitted photons.

As the average velocity of atoms emitted directly from an atomic oven is around $200\,\mathrm{ms}^{-1}$ and the capture velocity of a typical MOT is around $50\,\mathrm{ms}^{-1}$, only a small percentage of atoms would be trapped directly from a hot atomic beam into a MOT. It would be beneficial if a pre-cooling mechanism could be employed to reduce the average velocity of the atoms to below that of the MOT capture velocity to ensure as many atoms as possible cam be collected by the MOT for further experimentation.

3.1.3 Zeeman Slowing

In the reference frame of a thermal atom, the frequency of a correctly chosen red-detuned laser beam is Doppler shifted to be on resonance. This technique could be employed to pre-cool the atoms before the MOT stage by a laser beam in the direction opposing the atomic motion. Thermal atoms would absorb detuned photons and the momentum transfer would

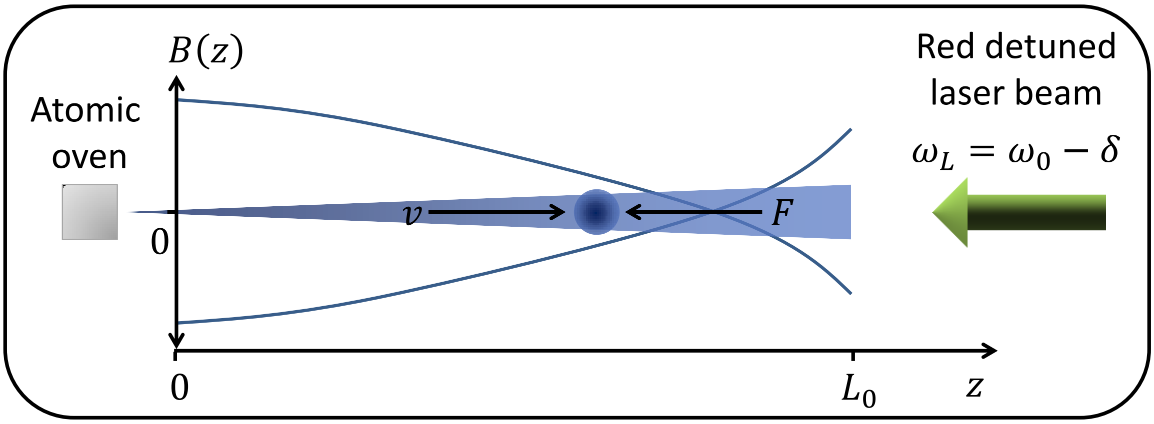

Fig. 3.6 Basic principle of Zeeman slowing atoms with a single detuned laser beam opposing atomic motion in a shaped magnetic field. Superimposed upon a graph of the Zeeman magnetic field is the laser beam is shown in green and is linearly polarised. The atomic beam is shown in blue with the atomic beam divergence exaggerated. L_0 denotes the length of the Zeeman slower, v is the atom velocity and F is the scattering force from the Zeeman slowing beam upon the atoms.

cause the average atomic velocity to decrease. However, a change in average atomic velocity results in the detuned photons no longer being on resonance with the atomic transition. The application of an external varying magnetic field to compensate for the change in average velocity would cause the photons to remain on resonance (see figure 3.6).

Using equation 3.3, it can be seen that maximal slowing and cooling of the scattering force F_{max} occurs when $\delta_L = \Gamma/2$ and therefore the optimal deceleration can be expressed as,

$$a_{max} = \frac{F_{max}}{M} = \frac{\hbar k_L}{M}\frac{\Gamma}{2} \tag{3.28}$$

where M is the mass of the atom. In order to compensate for the velocity of the atoms exiting from the atomic oven, the spatially varying magnetic field $B(z)$ must be designed so that the Zeeman shift upon the atomic energy levels, $\mu B(z)/\hbar$ compensates for the varying Doppler shift caused by the slowing of the atoms $k_L \mathrm{v}(z)$. Mathematically, the Zeeman shift must equal to the Doppler shift plus the detuning of the laser beams δ_L :

$$\frac{\mu B(z)}{\hbar} = k_L \mathrm{v}(z) + \delta_L \tag{3.29}$$

Assuming a constant deceleration a from an initial velocity v_i at position $z = 0$, the average velocity of the atoms can be calculated using standard kinematic equations to be

$$\mathrm{v}(z)^2 = \mathrm{v}_i^2 - 2az \rightarrow \mathrm{v}(z) = \mathrm{v}_i \sqrt{1 - \frac{z}{L_0}} \tag{3.30}$$

where L_0 can be defined as the stopping distance and is given by

$$L_0 = \frac{\mathrm{v}_i^2}{2a} \tag{3.31}$$

Knowing the stopping distance required means that a Zeeman slower can be designed to be as compact as possible. The substitution of equation 3.30 into equation 3.29 describes the magnetic field required for the Zeeman slower.

3.2 Narrowline Laser Cooling

In the event that the cooling supplied by the first stage cooling is insufficient, it would be beneficial if a narrower transition could be found upon which second stage cooling could be performed as the lowest achievable MOT temperature is proportional to the linewidth of the transition as described by equation 3.21. The first stage cooling is required as the capture velocity of a MOT (equation 3.26) is also proportional to the linewidth of the transition, so to trap a large number of atoms, it is necessary to utilise first stage cooling with a large linewidth.

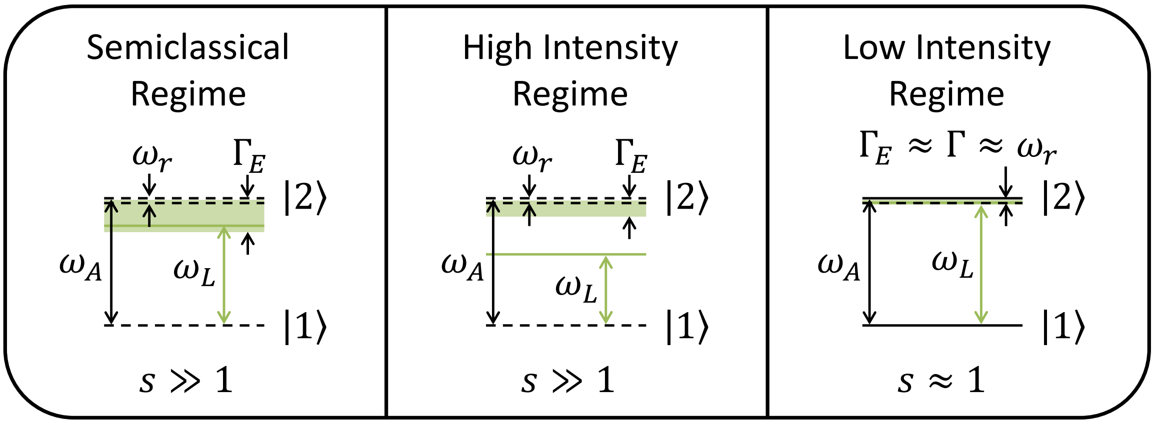

Fig. 3.7 Narrow-line trap parameters for each regime. Left: Semiclassical regime. The effective linewidth of the transition is much larger than the recoil frequency and comparable to the MOT laser detuning. Middle: High intensity regime. The effective linewidth of the transition is larger than the recoil frequency and smaller than the laser detuning. Right: Low intensity regime. The effective linewidth of the transition is equal to the recoil frequency and the laser detuning.

Provided that the linewidth of the second stage cooling transition is narrow (on the order of kHz), temperatures down to 1 µK become easily achievable. However, cooling would only occur upon a small velocity spread of the entire velocity distribution of the pre-cooled atomic sample. In the example of strontium, the method pioneered by Katori [60] in 1999 was to apply a specific modulation to the narrowline lasers used for the second stage cooling. The result of which causes a spread of frequencies which covers the range of Doppler shifted frequencies caused by the velocity distribution of the pre-cooled atoms. Then the laser was unmodulated and a much larger proportion of atoms collected in the first stage cooling could be cooled to the limit imposed by the narrow line. Cooling on a narrow line operates on very similar principles to cooling on a broad line but there are subtle differences which must be understood to fully appreciate narrow laser line cooling.

Typically, broad lines can be defined by $\Gamma/\omega_r \gg 1$. Such an example is the ${}^1S_0 - {}^1P_1$ transition in ${}^{88}Sr$ at 461 nm which has $\Gamma/\omega_r \approx 3 \times 10^3$. Thus it can be seen that in this case, Γ determines the natural energy scale, or in general, the power broadened linewidth Γ_E which depends on the saturation parameter $s = I/I_{sat}$. In this case, the effective power broadened linewidth becomes the natural energy scale rather than that determined by the recoil frequency as the effective linewidth is much larger than the recoil frequency. Therefore photon recoil driven trap dynamics are dominated by the heating effects which depend upon the transition linewidth. Even though semiclassical physics describes the cooling processes and the effects of photon recoil when cooling on broad lines, photon recoil is not the dominant cooling process; if the saturation parameter is increased, then the value of Γ_E and therefore Γ_E/ω_r is not significantly affected. The effect of gravity upon the trapping force is also negligible when operating upon broad lines; the ratio of the maximum radiative force to the gravitational force ($R = \hbar k\Gamma/2mg$) can typically be on the order of 10^5.

Narrow cooling lines however, can be typically defined by $\Gamma/\omega_r \approx 1$ or less. The ${}^1S_0 - {}^3P_1$ transition in ${}^{88}Sr$ at 689 nm, has $\Gamma/\omega_r = 1.6$ where $\Gamma/2\pi$ $\left(\omega_r/2\pi = \hbar k^2/4\pi m\right)$ is 7.5 kHz (4.7 kHz). In this case, the relevant energy scale and cooling mechanics depend strongly on s. Power broadening increases s, the effective linewidth Γ_E and therefore Γ_E/ω_r

The nature of the cooling process under different parameters can be understood by considering the laser detuning. The cooling dynamics for the red MOT can be split into three distinct regimes in the condition that $\delta < 0$ in which the cooling dynamics are dominated by qualitatively different processes. The treatment of each requires a different approach. As referred to in refs. [60, 61, 62, 63, 64] each regime will be defined by the relative sizes of $|\Delta|$, Γ, ω_r and Γ_E and the cooling dynamics of each regime can be seen schematically in figures 3.8, 3.9 and 3.10 and the trap parameters for each regime with respect to the transition frequency can be seen in figure 3.7.

3.2.1 Semiclassical Regime

In the semiclassical regime the trap parameters are defined as follows $|\Delta| \leq \Gamma_E \gg \omega_r$ and $s \gg 1$; detuning is less than the effective linewidth of the transition, which is much larger than the single photon recoil frequency and the intensity of the trapping beams is much larger than the saturation intensity.

If the intensity of the trapping beams is increased such that $s \gg 1$, then the system evolves such that $\Gamma_E \gg \omega_r$ and the natural energy scale becomes dependent upon Γ_E and Δ. This situation can be described semiclassically as shown in figure 3.8 as the radiative $\Delta < \Gamma_E$ force controls the trapping dynamics to exert a damped harmonic motion upon the atoms. The trap thermodynamics are therefore determined entirely by the velocity dependence of the radiative force as in classical Doppler cooling. The minimum achievable temperature in this regime is determined by the Doppler cooling limit when $\Delta = \Gamma_E/2$ (equation 3.21).

3.2.2 High Intensity Regime

In the high intensity regime, the trap parameters are defined as follows $|\Delta| > \Gamma_E \gg \omega_r$ and $s \gg 1$. This means that the laser beam detuning is larger than the effective linewidth of the transition and the effective linewidth of the transition is much greater than the single photon recoil frequency. This requires that the intensity of the narrowline MOT trapping beams is much larger than the saturation intensity for the transition. This causes power broadening to occur on the spectral line.

In the high intensity regime, the semiclassical approach is still valid but with the exception that the force only acts upon a small, spatially well-defined shell upon the outer trap boundary defined by the detuning of the laser as seen in figure 3.9. The position where the magnetic

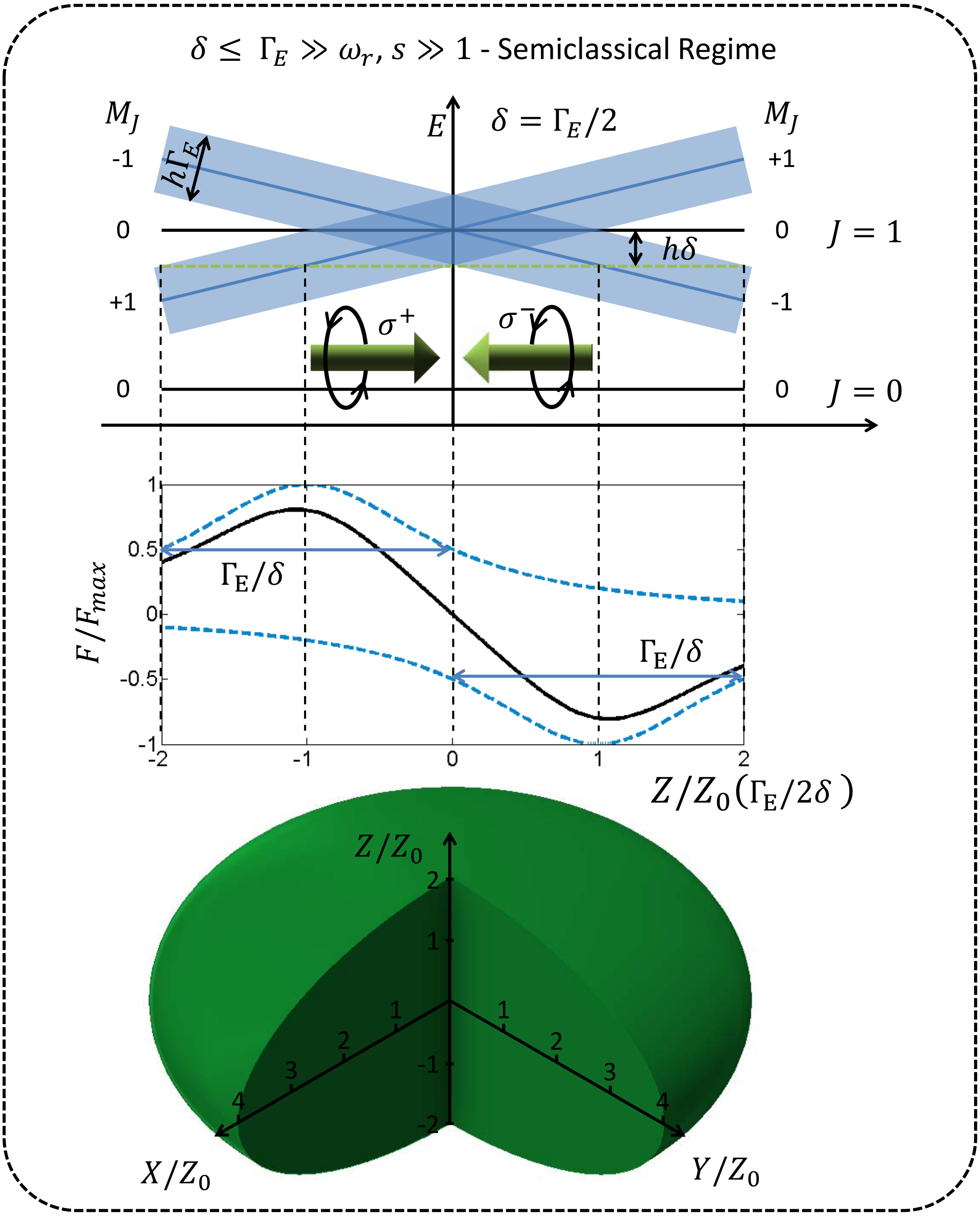

Fig. 3.8 Dynamics of laser cooling using a narrow-line magneto-optical trap in the semiclassical regime. Top: Schematic diagram showing the forces which act upon an atom when in a semiclassical magneto-optical trap in 1D. Middle: The force experienced by an atom as a function of the distance away from the centre of the magneto optical trap in 1D. Bottom: the volume over which the MOT acts as a function over the distance from the centre of the trap in 3D. The subscript 0 represents the centre of the trap in each dimension.

field gradient compensates the laser detuning is denoted by z_{eq} and is not necessarily at the trap centre along the vertical z axis.

In this regime, gravity cannot generally not be neglected as in the example of the strontium second stage MOT, the as the trapping force is only around 16 times larger than the gravitational force. As a result of this the shape of the trapped atom cloud becomes deformed and the atoms fall to positions where the Zeeman shift balances the laser beam detuning, δ_L and the resultant radiative force balances the effect of gravity.

This is the result of a box potential which is formed from this specific set of trapping parameters, with the addition of a gravitationally induced tilt in the gravitational axis (z axis). In the x - y plane, the atoms scatter within the boundaries of the box potential, whereas in the z axis, the atoms sink to the lower boundary of the trap and interact only with the vertical beam components. The equilibrium position z_{eq} can be found with the condition that the force attributed to the upward components of the trapping beams in the z axis, F^+ is equal to the force provided by gravity,

$$F^+\left(v_z = 0, z = z_{eq}\right) - Mg = 0 \qquad \left(F^+ \geq Mg\right), \tag{3.32}$$

where F^+ can be found by isolating the scattering force components acting vertically against gravity,

$$F^+ = \hbar k_L \frac{\Gamma}{2} \frac{s}{1 + s + 4\left[-\delta_L\left(1 + z/z_{eq}\right) - k_L \mathrm{v}_z\right]^2/\Gamma^2} \tag{3.33}$$

where the contribution to the force from the laser detuning δ_L is replaced with $\delta_L\left(1 + z/z_{eq}\right) - k_L \mathrm{v}_z$ to describe the force component acting vertically against gravity. Where $k_L \mathrm{v}_z$ is the frequency shift caused by the vertical atomic velocity v_z and $(\delta_L \cdot z_{eq} - \delta_L \cdot z)/z_{eq}$ is a scaling factor on the frequency detuning as a function of the distance in the z from the equilibrium atomic position z_{eq}. This causes a spatial dependence to the force.

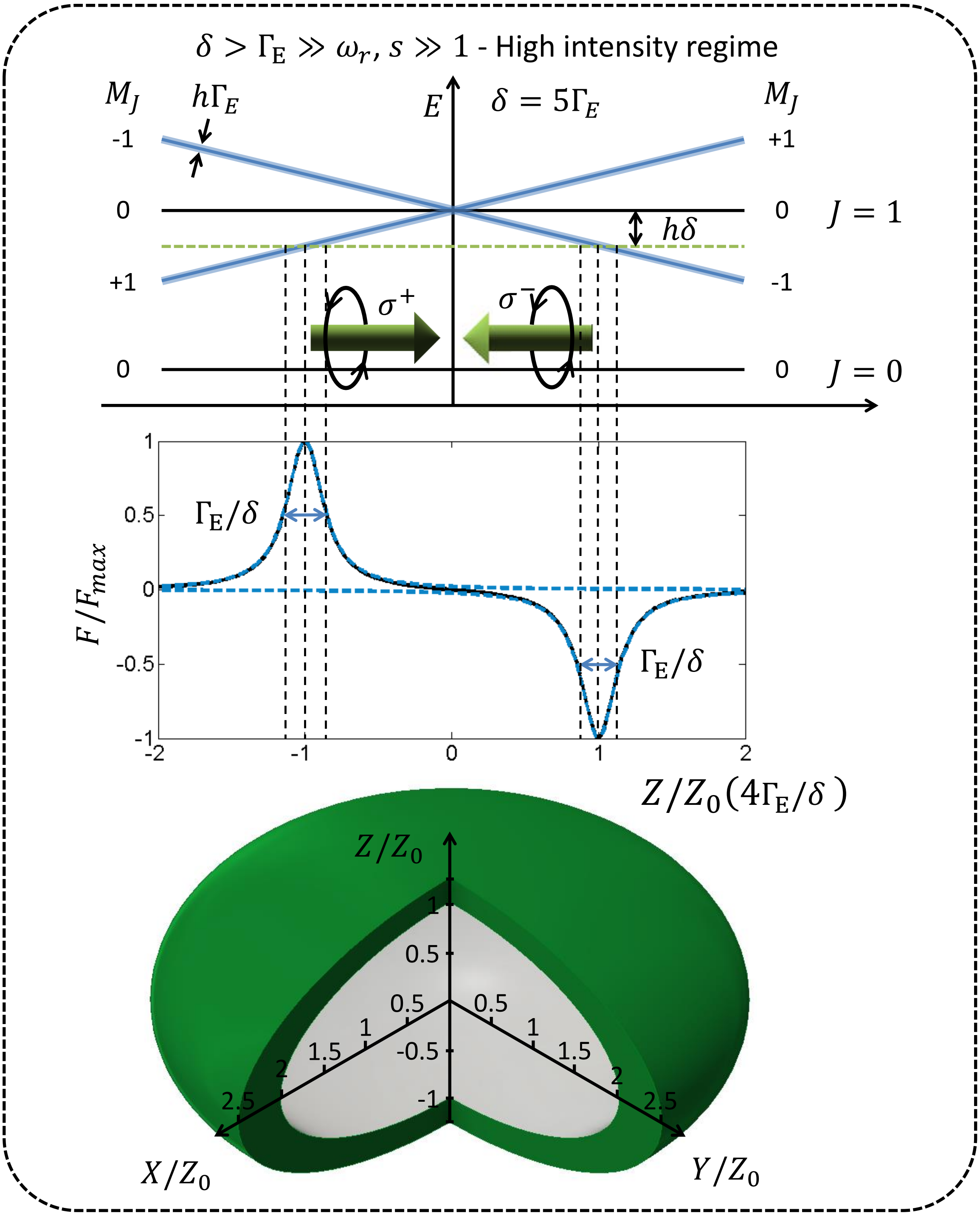

Fig. 3.9 Dynamics of laser cooling using a narrow-line magneto-optical trap in the high-intensity regime. Top: Schematic diagram showing the forces which act upon an atom when in a high-intensity narrow-line magneto-optical trap in 1D. Middle: The force experienced by an atom as a function of the distance away from the centre of the magneto optical trap in 1D. Bottom: the volume over which the MOT acts as a function over the distance from the centre of the trap in 3D shown in green. The subscript 0 represents the centre of the trap in each dimension.

The thermodynamics of the MOT are dependant upon the atomic velocity and spatial dependence of the radiative force. This means that single beam photon scattering is the heating which dominates and the thermodynamics of the MOT can be determined by the damping coefficient α at $z = z_{eq}$ as done previously with equation 3.15.

$$\alpha = -\left(\frac{\partial F^{+}}{\partial \mathrm{v}_z}\right)_{\mathrm{v}_z=0, z=z_{eq}} \tag{3.34}$$

In the equilibrium conditions and with reference to equation 3.18 along with the substitutions that $\mathrm{v}_r = \hbar k_L/M$ and $E_r = \frac{1}{2}M\mathrm{v}_r^2$ this leads to,

$$-\alpha\bar{\mathrm{v}}_z^2 + \frac{\Gamma_{scat}\left(\hbar k_L\right)^2}{2M} = 0 \tag{3.35}$$

with the first term describing due to optical molasses and the second term describing the heating coefficient due to scattering of photons (equation 3.6) from one laser beam component.

The scattering rate is slightly altered in these conditions and using equation 3.32 is given by,

$$\Gamma_{scat} \cong \frac{F^{+}\left(\mathrm{v}_z = 0, z = z_{eq}\right)}{\hbar k_L} = \frac{Mg}{\hbar k_L} \tag{3.36}$$

Therefore, the equilibrium temperature can be estimated as a function of the saturation parameter in these conditions by

$$T\left(s\right) \cong \frac{\hbar\Gamma}{2k_B}\sqrt{1+s} \tag{3.37}$$

This states that the final temperature of the second stage MOT is not predicted by standard Doppler theory and is dependent only on the saturation parameter s rather than the frequency detuning δ_L provided that the condition of $F^{+} \geq Mg$ is maintained.

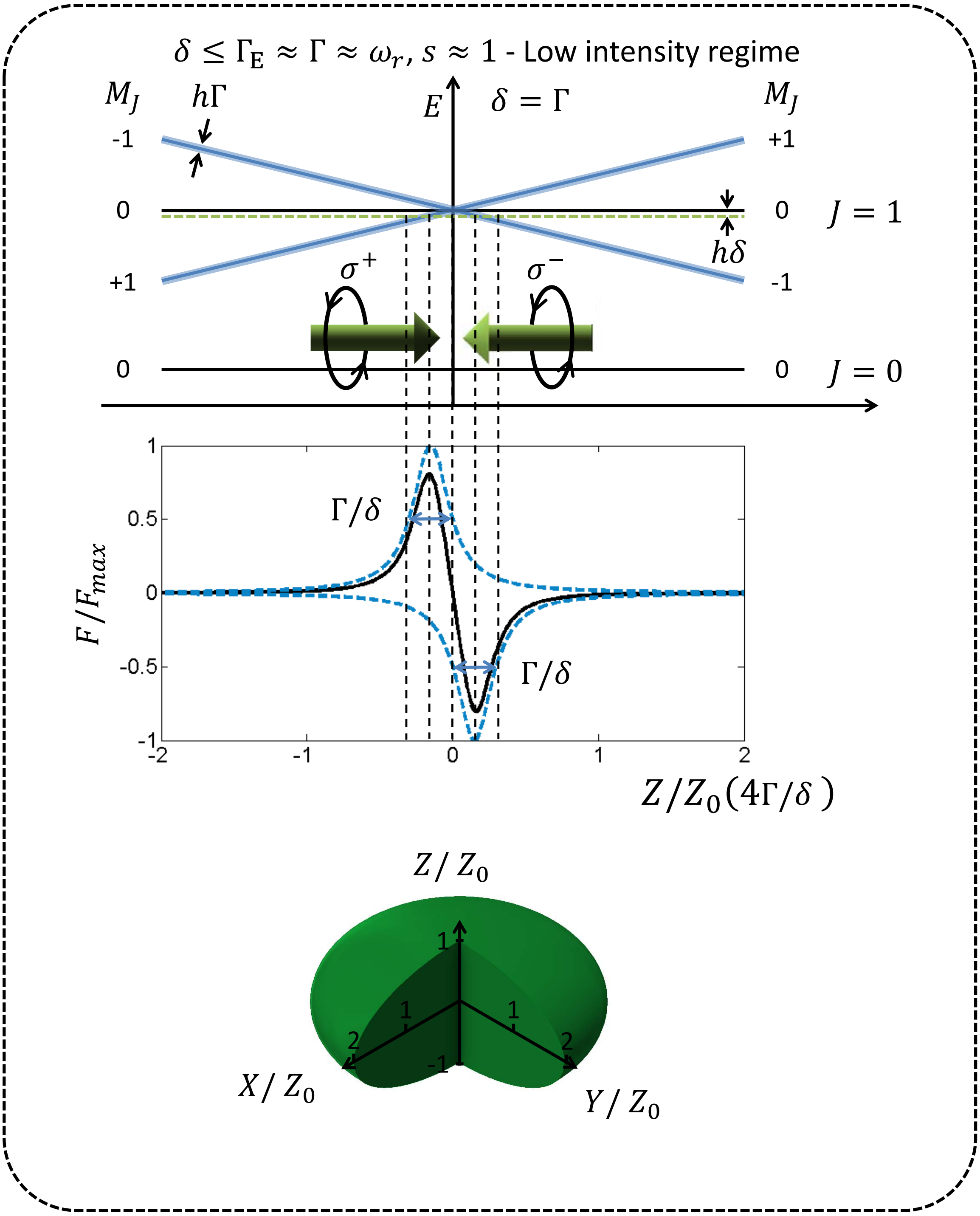

Fig. 3.10 Dynamics of laser cooling using a narrow-line magneto-optical trap in the low-intensity regime. Top: Schematic diagram showing the forces which act upon an atom when in a low-intensity narrow line magneto-optical trap in 1D. Middle: The force experienced by an atom as a function of the distance away from the centre of the magneto optical trap in 1D. Bottom: the volume over which the MOT acts as a function over the distance from the centre of the trap in 3D. The subscript 0 represents the centre of the trap in each dimension.

3.2.3 Low Intensity Regime

In the low intensity regime, the trap parameters are defined as follows $\Gamma_E \cong \Gamma \approx \omega_r$ and $s \approx 1$. This means that the trapping beam intensity is of the same order as the saturation intensity which is $I_{sat} = 3\,\mathrm{mW\,cm^{-2}}$ for the second stage transition in ^{88}Sr. Under this condition, the effective linewidth is approximately that of the natural linewidth of the transition and no power broadening occurs, and in the case of ^{88}Sr this happens to be of the same order of magnitude as the single photon recoil limit as found using equation 3.19 and the dynamics can be seen in figure 3.10.

The natural energy scale therefore becomes the single photon recoil frequency ω_r. In this regime, single photon recoils dominate trap dynamics and thus must be described in a fully quantum mechanical nature. The theoretical minimum temperature achievable can be estimated as roughly half the photon recoil limit [62] given by equation 3.19 (which in this example of ^{88}Sr is around 460 nK) even though incoherent excitation is provided by the trapping beams.

Thus, when the atoms have been cooled to the temperature limit of the second stage trap, one requires a method to trap the atoms which does not perturb the energy levels of the clock transition such as any electric field present in the trapped atom region which would cause an unequal Stark shift upon the ground and excited states of the clock transition. This would be possible if a trapping mechanism could be employed which caused an equal shift upon the ground and clock excited state.

3.3 Dipole Force

The use of the dipole force to trap atoms in the field of atomic physics is well established. An in depth review of the progression made in the field can be seen in [65] as well as the

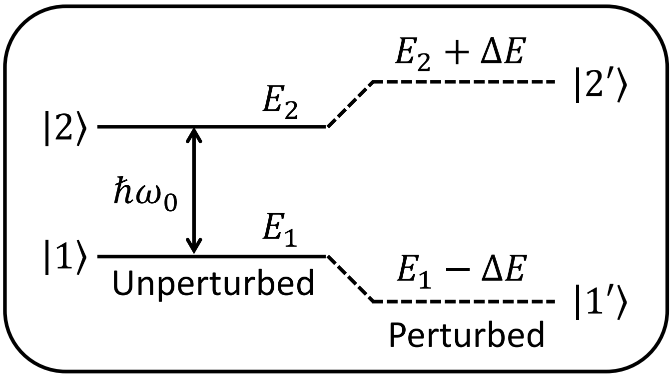

Fig. 3.11 The effect of the AC Stark shift upon electronic energy levels

applicability of the method to other experiments. A mathematical overview and explanation can be seen in refs. [65, 57].

The important results for optical clocks is the consideration of the shifts that this electric field causes upon the energy levels of the atomic sample. This effect is called the AC Stark shift and at a large frequency detuning $|\omega_L - \omega_0| \gg \Gamma$ where ω_L is the laser beam frequency, ω_0 is the transition frequency and Γ is the linewidth of the transition, the effect of upon atomic energy levels can be seen in figure 3.11. At a large frequency detuning, absorption of the radiation by the atoms can be considered as negligible. In the case that the frequency detuning is much larger than the Rabi frequency, $\Omega = \Gamma / \sqrt{I/2I_{sat}}$ the AC Stark shift can be shown to be [57].

$$\Delta E \simeq \frac{\hbar\Omega^2}{2\left(\omega_L - \omega_0\right)} \tag{3.38}$$

The figure of merit of this equation is that it shows that the effect of the AC Stark shift acts as a potential well U_{dipole} for an atom found in the ground state. Thus the atom will experience this potential as

$$U_{dipole} \simeq \Delta E \equiv \frac{\hbar\Gamma}{4} \frac{\Gamma}{\omega_L - \omega_0} \frac{I\left(\vec{r}\right)}{I_{sat}} \tag{3.39}$$

and the force experienced by an atom found in such a potential is thus given by

$$\mathbf{F}_{dipole} = -\vec{\nabla} U_{dipole} \tag{3.40}$$

This force arises from the interaction between the intensity gradient of the light field with the induced atomic dipole moment of the atom caused by the strong electric field of the incident laser beam. Should there be a non-uniform intensity, $I(\vec{r})$, of the far detuned laser beam, equation 3.39 shows that there exists a potential in which the atoms can be trapped at the minima. This means that one can design the trap geometry simply by altering the intensity profile of the laser.

When considering the kind of geometry that one would wish to create in the case of a dipole trap for an optical clock, there are a number of points to take into consideration.

> **Depth of potential:** Firstly, one should ensure that the depth of the potential is large enough that it is greater than the thermal energy of the atomic sample $U_{depth} \gg k_B T$. If this was not the case, the atoms with a larger velocity would escape the trap and evaporative cooling would occur. Whilst this is advantageous in some atomic physics experiments, in this case it is more important to trap as many atoms as possible to improve the signal to noise ratio of the spectroscopy of the clock transition.
>
> **Heating mechanisms:** Secondly one would aim to avoid any heating mechanisms arising from this trapping technique. One obvious form of heating comes from scattering of photons from the atomic sample. The ratio of the potential energy to the heating caused by photon absorption is approximately equal to the detuning of the trapping laser beam to the linewidth of the transition, $U_{dipole}/\hbar\Gamma_{scatt} \simeq \delta_L/\Gamma$. A larger detuning would therefore minimise the heating effect, provided that the trap depth is constant which can be compensated by the intensity of the laser beam.

Detuning: Thirdly one should consider whether the trap should be operated with negative or positive detuning - that is, red or blue detuned from the transition. For red (blue) detuning, the laser frequency is less (greater) than that of the transition frequency and thus the potential minima are located at the positions in the intensity profile that are maximal (minimal).

A high intensity laser beam is required to have a large trap depth, a large frequency detuning minimises any heating effect from the trap, and for a Gaussian beam profile, red detuning is required.

3.3.1 Focussed Dipole Trap

Instead of increasing the power of a laser beam, the intensity can be increased by a factor of $1/w(z)^2$ where $w(z)$ is the radius of the laser beam. Additional trapping is also provided in the radial direction by the beam focus. The reduction of the beam waist for increased laser beam intensity increases the depth of the trap at the expense of the volume of the trap.

The spatial intensity distribution of a focussed Gaussian beam with a maximum intensity of I_0 propagating along the z axis can be described by

$$I_z(r,z) = I_0 \left(\frac{w_0}{w(z)}\right)^2 \frac{2P}{\pi w^2(z)} \exp -2\frac{r^2}{w^2(z)} \tag{3.41}$$

where r is the radial coordinate and $w(z)$ gives the size of the beam as a function of the propagation direction z,

$$w(z) = w_0\sqrt{1+\left(\frac{z}{z_R}\right)^2} \tag{3.42}$$

where $z_R = \pi w_0^2/\lambda_L$ is the Rayleigh range which gives the distance by which the radius of the beam is $\sqrt{2}$ larger than at $w(z) = w_0$ and can be seen in figure 3.12.

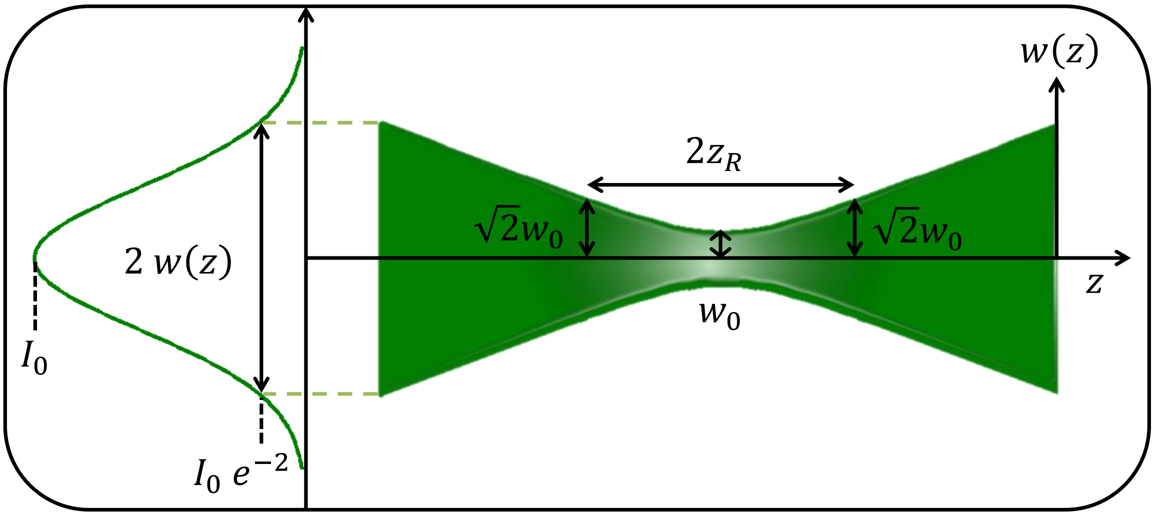

Fig. 3.12 Schematic of Gaussian laser beam parameters.

When using a focussed dipole trap with the assumption that the thermal energy k_BT of the atomic sample is much smaller than the trap depth U_{depth}, the atoms can be assumed to be trapped at or close to the trap minimum (see figure 3.13). An approximation of the potential experienced by the atoms is given by the Taylor expansion of equation 3.41,

$$U_{dipole}\left(r,z\to 0,0\right)\simeq U_{depth}\left[-1+2\left(\frac{r}{w_0}\right)^2+\left(\frac{z}{z_R}\right)^2\right] \tag{3.43}$$

where the depth of the dipole trap U_{depth} is given by equation 3.39. This describes a harmonic potential which is cylindrically symmetric. The potential has two different trap frequencies along the radial $\left(\omega_\phi\right)$ and axial $\left(\omega_z\right)$ directions given by [61]

$$\omega_\phi=\sqrt{\frac{4U_{depth}}{Mw_0^2}} \tag{3.44}$$

$$\omega_z=\sqrt{\frac{4U_{depth}}{Mz_R^2}} \tag{3.45}$$

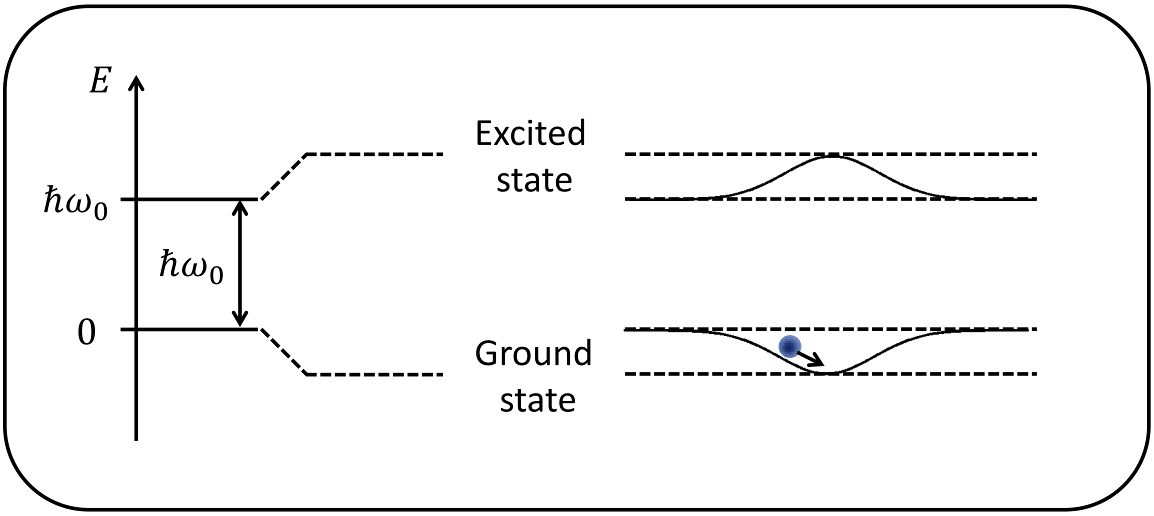

Fig. 3.13 An illustration of the use of a dipole potential to trap atoms

The ratio shows the potential in the radial direction has a larger gradient than the potential in the axial direction: $\omega_\phi/\omega_z = \pi\sqrt{2}w_0/\lambda_L$ where the waist size w_0 is much larger than the wavelength of the trapping laser λ_L. Therefore, a focussed beam trap is typically horizontal with respect to gravity to minimise any gravitational perturbations.

3.3.2 Optical Lattice

Reflecting the trapping beam back to produce a so-called optical lattice increases the potential depth of the trap and ensure that the effects of gravity can be neglected. The method involves retroreflecting a Gaussian laser beam whilst also conserving the radius of curvature of the wavefronts and polarisation. Considering the case where two counter-propagating beams interfere in the near field approximation as two plane waves, the electric field can be described as

$$\begin{aligned} E &= E_0cos(\omega_Lt - k_Lz) + E_0cos(\omega_Lt + k_Lz) \\ &= 2E_0cos(k_Lz)cos(\omega_Lt) \end{aligned} \tag{3.46}$$

and when taking the square of this electric field value will give the intensity of the field

$$I(z) = 4I_0 cos^2(k_L z) \tag{3.47}$$

And therefore it can be seen that the intensity of the beam is altered by a factor of $4cos^2(k_L z)$ which can be substituted into equations 3.39 and 3.43 to give

$$\begin{aligned} U_{lattice}(r, z \rightarrow 0, 0) &= 4cos^2(k_L z) \\ U_{dipole} &= U_{lattice} cos^2(k_L z) \left[-1 + 2\left(\frac{r}{w_0}\right)^2 + \left(\frac{z}{z_R}\right)^2 \right] \end{aligned} \tag{3.48}$$

with $U_{lattice} = 4U_{depth}$ meaning that the potential depth is four times larger than for a single focussed beam shown in equations 3.46 and 3.47. The shape of the potential is modulated by the cos^2 term in the axial direction with a period of $\lambda_L/2$ and thus a restoring force of $\approx U_{depth} k_L$ is found around the potential minima. The confinement can be approximated as a harmonic potential with a trapping frequency of

$$\omega_z = k_L \sqrt{\frac{2U_{depth}}{M}} \tag{3.49}$$

In the radial direction, the confinement is the same as that of the single focussed beam which can be approximated as the ratio of the potential depth to the waist size.

If one is using a red detuned laser frequency, the atoms will be trapped to the intensity maxima of the standing wave pattern, and to the minima for a blue detuned frequency (see figure 3.14). The depth of the lattice potential in terms of temperature can be expressed as simply the potential depth divided by the Boltzmann constant. Measuring the depth of the lattice in terms of temperature allows simple determination of the maximum atomic temperature which can be trapped.

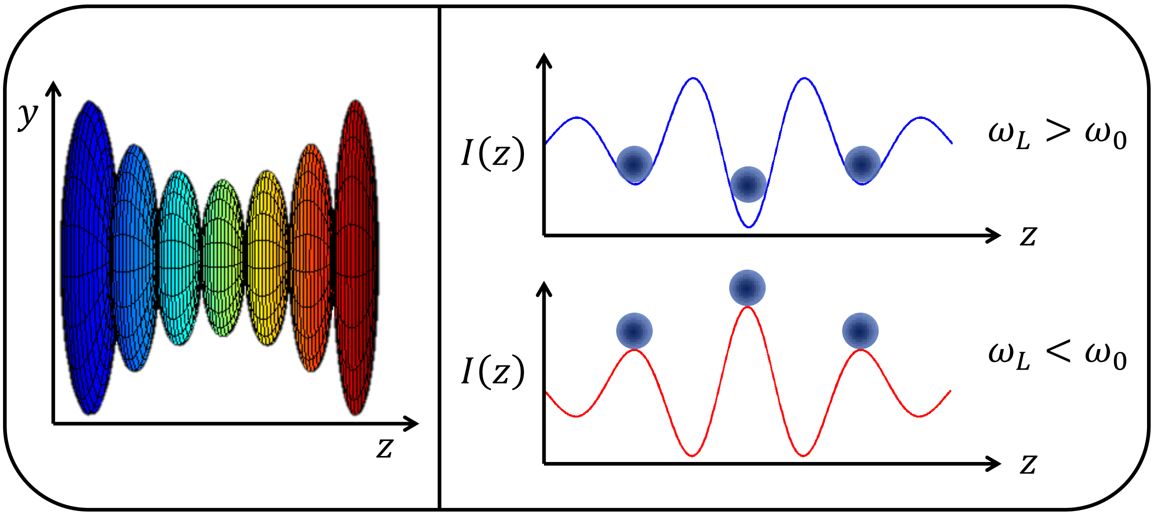

Fig. 3.14 An illustration of the various lattice sites which are found in a 1D optical lattice. Left: A 3D render of the optical lattice standing wave. Right: Lattice sites for red and blue detuned optical lattice traps.

Chapter 4

Strontium Optical Lattice Clocks

Strontium optical lattice clocks are currently at the forefront of optical clock performance worldwide [19]. In this chapter, the basic principles of successful operation of a strontium optical clock are presented. The atomic trapping background theory given in chapter 3 will be used as a foundation for the specific cooling and trapping dynamics of ^{88}Sr in this chapter.

4.1 Strontium

The strontium atom has been shown in laboratories worldwide to be a suitable candidate for a frequency reference. Other candidates include ytterbium and single-ion clocks using mercury and aluminium. Strontium is an alkaline earth metal with characteristics as shown in table 4.1 with data from the NIST database of spectroscopic data [67]. It is reactive with oxygen and water and thus it is important to note that handling must be performed in a low pressure environment or within an inert gas such as argon or hydrogen. The electronic energy levels in strontium (figure 4.1) are particularly of interest to the field of frequency metrology as there exists an optical transition from the ground $^1S_0$ state to the $^3P_0$ state which has a very narrow linewidth of $\approx 1\,\text{Hz}$ which is accessible with commercial, stabilised diode lasers. This holds promising features for use as a clock transition and will be discussed later in this

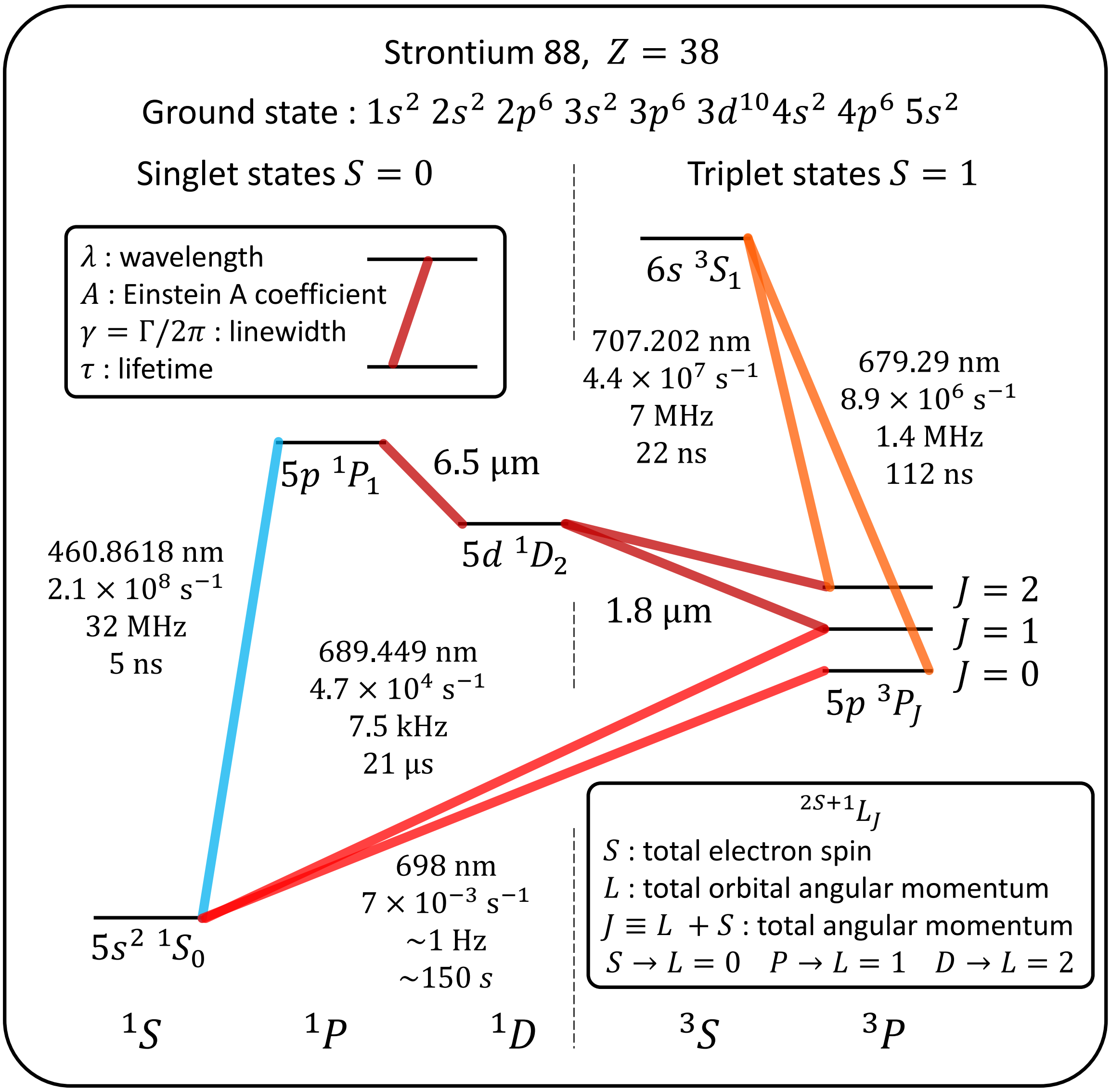

Fig. 4.1 Strontium energy levels using data from [66]

Isotope	Atomic mass	Natural abundance	Nuclear spin
^{88}Sr	87.905 6143(24)	82.58(1)%	0
^{86}Sr	85.909 2624(24)	9.86(1)%	0
^{87}Sr	86.908 8793(24)	7.00(1)%	9/2
^{84}Sr	83.913 425(4)	0.56(1)%	0

Table 4.1 Properties of the naturally occurring isotopes of strontium (NIST data [67])

chapter in section 6.8. In order to probe this transition the atomic sample must be as isolated as possible from external influences which may perturb the difference in the electronic energy levels of the atom.

Laser cooling is used as a technique to control the temperature of the atoms. This technique holds a great advantage as it can be performed in vacuum and the frequency, linewidth, power, stability, size and direction of the lasers and laser beams can be accurately and precisely controlled.

4.2 Atomic Slowing Methods

As previously mentioned in chapter 3, one can utilise more than one resonance transition that exists within an atomic species to precisely manipulate and control an atomic sample. Strontium has two transitions which are good candidates to use for laser cooling in the first and second stages. This first one being the ground $^1S_0$ to the excited $^1P_1$ state. This state has a linewidth of 32 MHz and can cooled the atomic sample to a theoretical minimum temperature of 768 μK. Even if this temperature was practically achievable, it would introduce appreciable shifts upon the clock transition of around 100 kHz and thus the atomic sample must be cooled further. Another optical frequency exists which could be utilised for this second stage cooling. This is the $^1S_0$ to $^3P_1$ state. Utilising this transition allows cooling to a theoretical minimum temperature of 460 nK.

4.2.1 Pre-cooling the Atoms - Permanent Magnet Zeeman Slower

As introduced in 3.1.3, to increase the yield of trapped atoms, one can use a Zeeman slower. Such a device takes advantage of the shifting of energy levels by an external magnetic field. The idea is oppose the atomic beam with a $\approx 10\Gamma$ red detuned laser beam from the $^1S_0$ to $^1P_1$ transition. Then, to introduce a large magnetic field close to the atomic oven which is generally tapered and shaped such that the Zeeman shifts compensate for the Doppler shift experienced by the atoms which are initially at a very high temperature ($\approx 400\,°\mathrm{C}$) and are subsequently cooled.

A spatially varying magnetic field has been produced historically [10, 18, 61, 68, 69, 70] by tapered coils and is called a Zeeman slower due to the exploitation of the Zeeman shift on the atomic energy levels. This method is cheap and sufficient at slowing the atomic beam however, to generate the magnetic field required, the tapered coils are rather large (around 50 cm in diameter), produce a significant amount of heat and must be water cooled [61] and thus consume a large amount of power.

One could also use permanent magnets to produce the required external magnetic field. These magnets could vary in strength along the path of the atomic beam and the magnetic field could be finely tuned by varying the distance of these magnets from the axis of the atomic beam path. Such a Zeeman slower has been produced by the National Physical Laboratory (NPL) [71] and an image of the Zeeman Slower can be seen in figure 4.2. This Zeeman slower was produced specifically for the SOC2 project after some years of research and development at NPL. The slower was designed to be used with an atomic beam temperature of around 600 K and with a slowing beam with power of approximately 70 mW and diameter around 16 mm. As can be seen in [71], the performance of the slower has been evaluated for different atomic beam temperatures, different detuning of the laser beam, different power

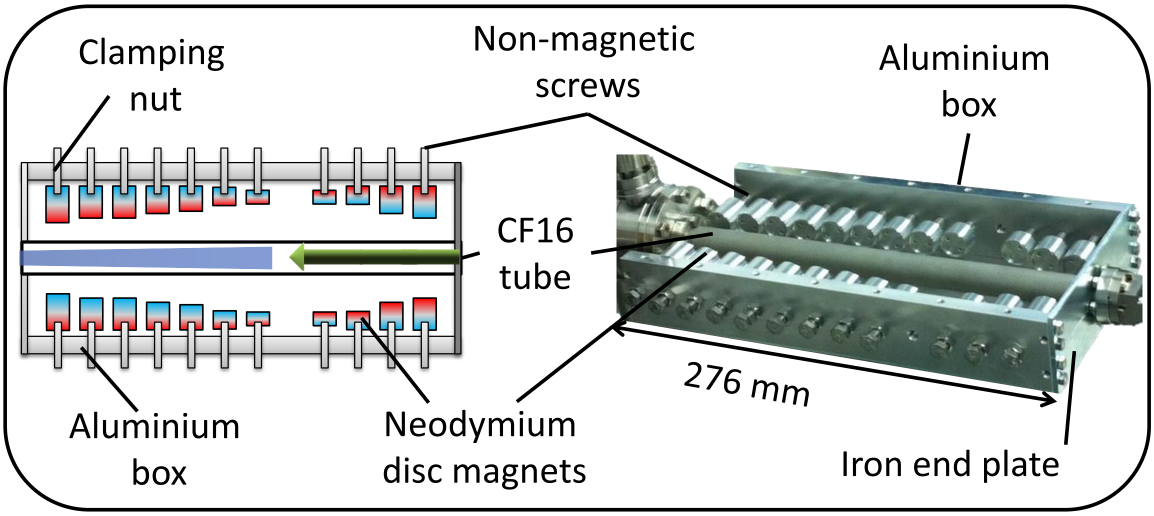

Fig. 4.2 A novel permanent magnet Zeeman slower produced at NPL for the Space Optical Clocks project. Left: a schematic of the Zeeman slower. Atomic beam is shown in blue and laser beam in green. The polarity of the magnets is shown as blue - red. Right: A photograph of the realised Zeeman slower.

in the laser beam and the shape of the magnetic field has been very carefully chosen and motivated by mathematical simulations.

4.2.2 First Stage Cooling - Broad Line MOT Using the $^1S_0 \rightarrow {}^1P_1$ Transition

The a broad, quasi-closed optical electronic transition at 461 nm from the $^1S_0$ to $^1P_1$ state is well suited for efficient cooling a thermal sample to around 1 mK in a magneto-optical trap (MOT). This transition can be accessed using coherent, frequency doubled light emitted from a commercial extended cavity laser diode.

Once electrons are excited to the $^1P_1$ state, they decay spontaneously back to the ground $^1S_0$ state or to the $^1D_2$ state. In the latter case, these atoms decay further to two of the three triplet states, $^3P_2$ or $^3P_1$. The atoms which decay to the $^3P_1$ state will spontaneously decay only to the ground state, however, the $^3P_2$ state is a dark state with a lifetime on the order of

150 s. This decay path can be closed with the use of two repumper lasers as seen in figure 4.1.

4.2.3 Second Stage Cooling - Narrow Line MOT Using the $^1S_0 \rightarrow {}^3P_1$ Transition

A narrow, closed optical electronic transition at 689 nm from the $^1S_0$ to the $^3P_1$ state which can be used for narrow line cooling. Strontium is cooled and trapped via the narrow intercombination line globally by ultracold strontium experiments and early work towards this goal can be seen in refs.[60, 62, 63, 72]. This transition has a natural linewidth of only 7.5 kHz and thus has a lifetime of approximately 21 µs.

The idea of using the closed $^1S_0 -^3 P_1$ 7.5 kHz transition which exists in strontium to operate a second stage MOT was pioneered in 1999 by the Tokyo group led by Hidetoshi Katori [60] and has been used in low temperature strontium experiments since. The benefit to using a narrow transition is obvious; narrow linewidth translates to a much lower Doppler temperature (see equation 3.21). The red MOT has a very low capture velocity of 79 cms^{-1} and a yield of around 5 % of the number of atoms in the blue MOT is possible by transferring directly from the blue with the atoms at an average velocity of 30 ms^{-1} to the red MOT. The method used by Katori as an intermediate stage between these two cooling stages was to utilise the 689 nm transition and to artificially broaden the linewidth of the MOT via modulation of the frequency, this stage I will refer to as the broadband red MOT. In the frequency domain, this creates a spread of frequency components of the laser radiation centred around a set frequency with a separation set by the modulation frequency. If the modulation bandwidth is chosen such that the spread of frequencies is large enough that it covers the Doppler shift for entire velocity distribution of the atoms in the blue MOT (approximately 1.6 MHz at 1 mK), then a larger number of atoms can be captured and further cooled by the red MOT to a theoretical minimum temperature of 460 nK. Practically, temperatures of 1 μK are achievable. This stage I will refer to as the single frequency red MOT.

The aim for using the narrow line for cooling in strontium optical clock experiments is to cool as many atoms as possible, as quickly as possible to around 1 - 2 μK to then be transferred into a 1D optical lattice where clock measurements can take place. A large number of atoms maximises the signal to noise ratio of the final clock measurements. A short loading time ensures that the measurement is not limited by the shot to shot drift of the external cavity to which the clock laser is normally stabilised.

Broadband Red MOT

As previously explained fully in section 3.2, broad transition lines are defined by $\Gamma_E/\omega_r \gg 1$ where Γ_E is the effective linewidth of the transition and ω_r is the photon recoil frequency (equation 3.19). Therefore, as the effective linewidth of the $^1S_0$ to $^3P_1$ transition does not meet these requirements, the line is characterised as a narrow line. Thus cooling with this line will not be in the semiclassical regime but in the high or low intensity regimes as described in section 3.2. This subtle difference and finding an effective solution is what has driven much of the following research into efficient loading and cooling for the red MOT stage in this work.

A consequence of cooling on a narrow line is that effective temperature of the red MOT operating in the high intensity regime is not dependent upon the detuning of the laser beams but only the saturation parameter and the linewidth of the transition. As a result, cooling occurs only upon a thin spatial shell within the volume of the atoms. The boundaries of this shell are determined by the detuning of the laser beams with the thickness determined by the effective linewidth of the transition. If the detuning is chosen to be too small, then cooling only occurs for the atoms which are spatially very near the central MOT position. These are

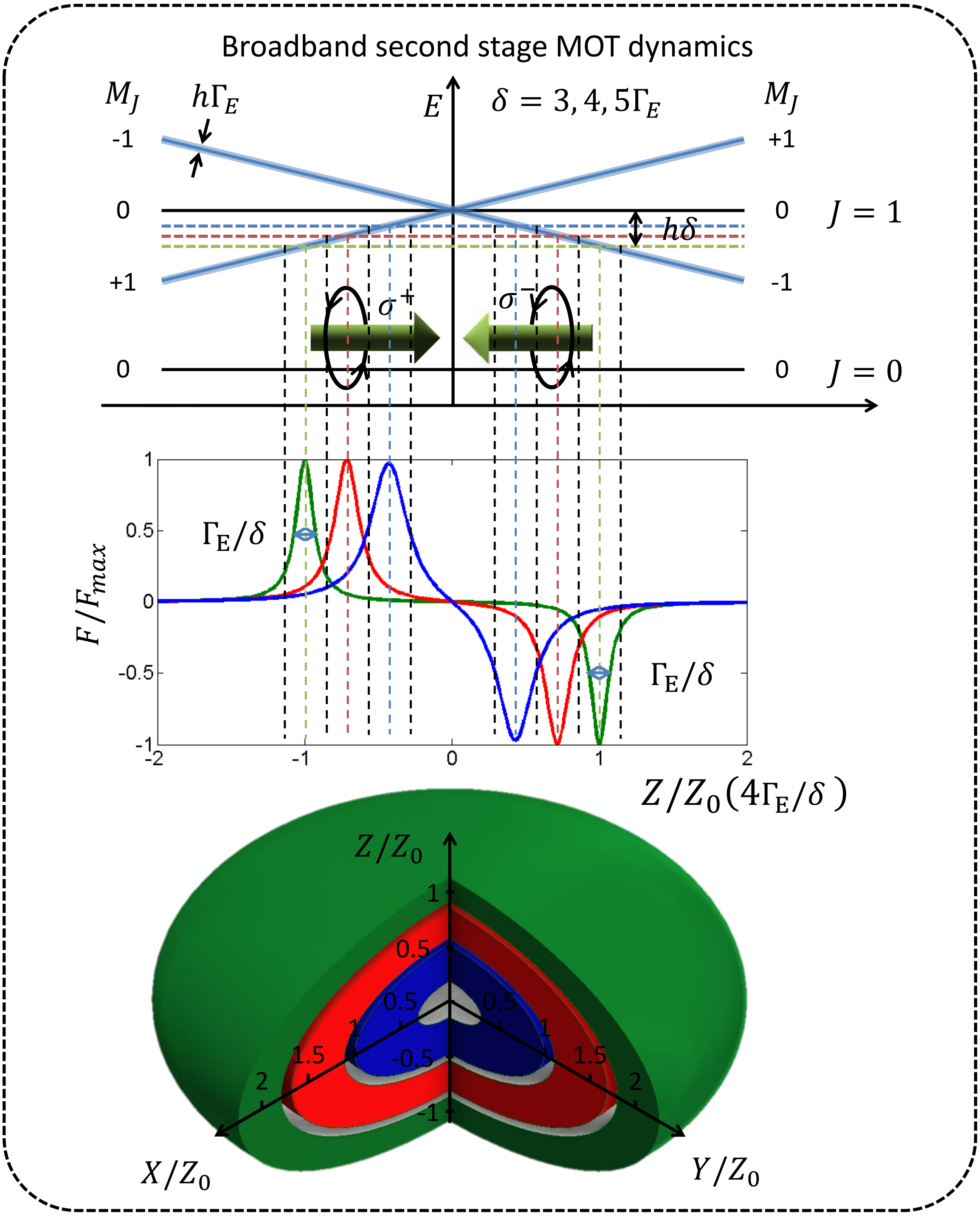

Fig. 4.3 Dynamics of laser cooling using a narrow-line laser modulated magneto-optical trap in the low intensity regime. Top: Schematic diagram showing the forces which act upon an atom when in a narrow-line laser modulated magneto-optical trap in 1D. Middle: The force experienced by an atom as a function of the distance away from the centre of the narrow-line laser modulated magneto optical trap in 1D. Bottom: the volume over which the MOT acts as a function over the distance from the centre of the trap in 3D shown in green, red and blue as an illustration for the laser frequencies present. The subscript 0 represents the centre of the trap in each dimension.

the atoms which are the coolest and thus, the detuning must be chosen such that as many of the atoms in the cloud as possible are cooled and captured. This introduces a problem that the atoms inside this shell are not being cooled will collide and their temperature will reach an equilibrium which is larger than the shell of atoms which are being cooled. Therefore, a solution must be invented which ensures that this effect is minimised.

This is where the idea of modulating the red MOT beams arose [60]. The dynamics of performing such a modulation can be seen in figure 4.3. In order to ensure that this method is used effectively, one must carefully choose the modulation frequency (frequency difference between subsequent detuning lines), the modulation amplitude (the range of frequencies used) and the intensity of each line.

This has been used to great effect in all other strontium clock experiments applying frequency modulation upon an AOM (for example: [8, 35, 61, 70, 73, 74] among many others). However, the use of such an AOM introduces optical power loss, an increase in electrical power (as each AOM typically requires 1 W of amplified input signal) and extra complexities in the laser breadboards. A method which I have investigated is to modulate the laser lock point and to use the phenomenon of power broadening to achieve the same improvement in the number of atoms trapped and cooled, but without the power consumption and added complexity of the inclusion of an AOM to the laser breadboard.

Lock Modulation Method for Broadband Red MOT

The lock modulation method can be readily used if the 689 nm laser is sideband locked to a stable reference cavity as in this apparatus. Instead of applying modulation to an AOM to produce a range of frequencies around the central AOM frequency, one can achieve the same effect by applying a modulation upon the frequency sent to the EOM used in PDH locking the laser to a reference cavity.

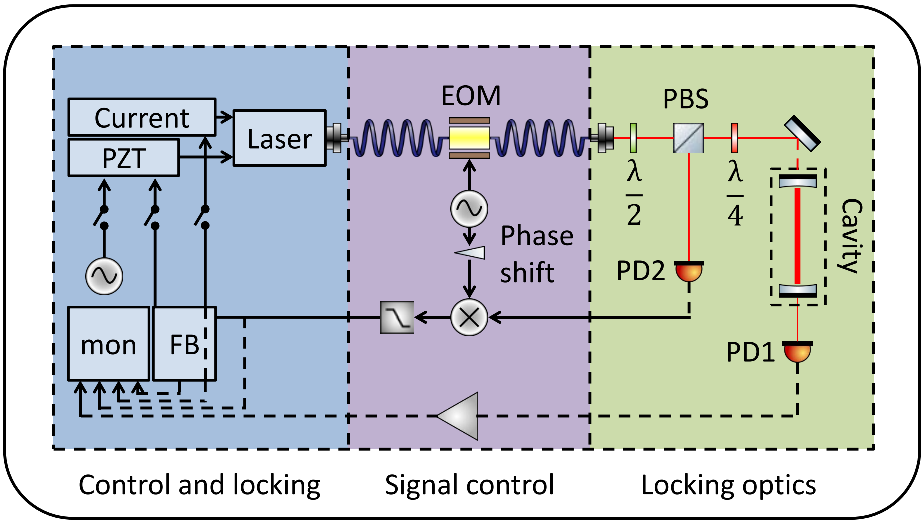

Fig. 4.4 The basic principle of the Pound-Drever-Hall method of laser stabilisation. Where PZT is the piezo-electric transducer which is placed behind the diffraction grating of an external cavity diode laser (ECDL) to tune the laser frequency, FB is the feedback electronics, and mon refers to the oscilloscope used to monitor the locking signals.

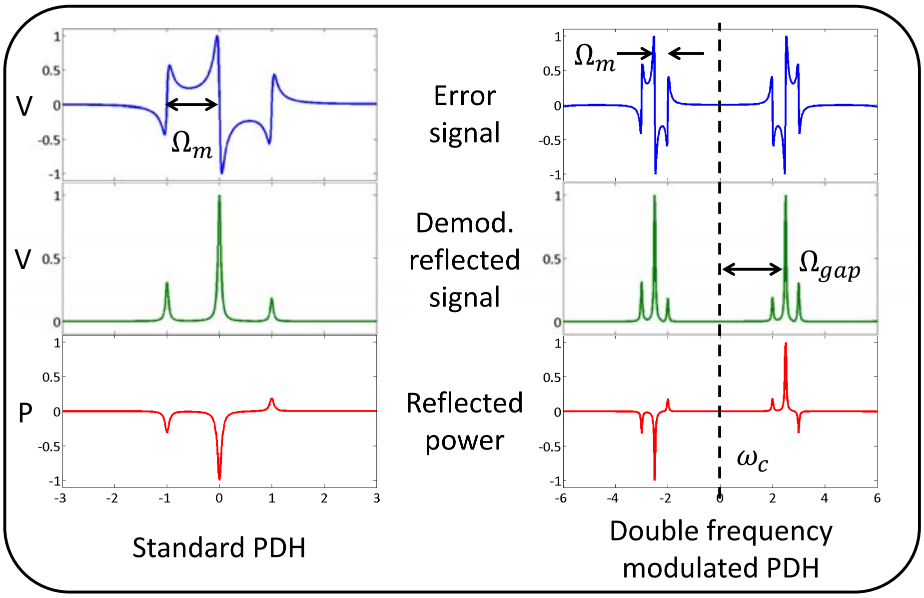

Fig. 4.5 The double frequency modulation sideband locking scheme. Left: Standard PDH signals. Right: Double frequency modulated PDH signals. Top: The error signal. Middle: The signal reflected from the locking cavity after demodulation. Bottom: The power of the reflected signal.

A pound-Drever-Hall (PDH) lock is shown in figure 4.4. The basic idea is that a certain portion of the laser light is sent to a stable reference cavity with a finesse defined by the reflectivity of the cavity mirrors. Whilst observing the light transmitted (reflected) through (from) the cavity on a photodiode (PD), the laser frequency is scanned (as shown in the figure). This produces a transmission (reflection) peak which depends on the laser frequency, the width of which is defined by the finesse of the cavity.

In order to utilise this signal to keep the laser at the frequency which corresponds to the maximum power transmitted through the cavity (the minimum power reflected from the cavity), an electronic feedback loop is used which adjusts the frequency of the laser if it drifts higher or lower in frequency away from the transmission peak (reflection minima). When simply reading the voltage from the PD, it is impossible to determine whether the frequency has increased or decreased to cause the transmission signal through the cavity to decrease as the signal is symmetric about the peak. Passing the laser beam through an EOM introduces frequency components higher and lower ($\pm\Omega_m$) than the carrier frequency (ω_c) determined by the input frequency to the EOM (Ω_m). If the reflected signal from the cavity is then mixed with the input frequency to the EOM (after some phase alterations and some low pass filters to filter out the high frequency components caused by the mixer), this produces the so-called error signal which is asymetric around the lock point. An example of this can be seen in figure 4.4. This signal can be used with a standard PID control loop to ensure that the error signal is always zero, which corresponds to maximum transmission and minimum reflection from the cavity.

For interest, it is worth noting here that the idea of sideband locking is simply the introduction of yet another frequency to the EOM, Ω_{gap}. Provided that this frequency is much larger than the locking modulation Ω_m, then the frequency spectrum that is produced is shown in figure 4.5 along with the corresponding error signal obtained by sending only Ω_m

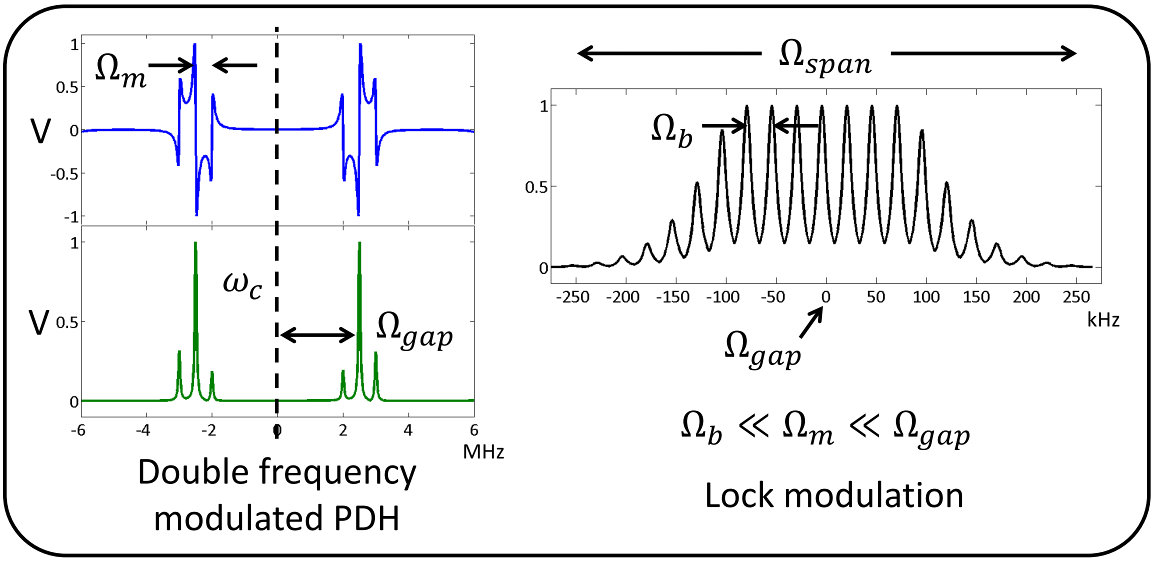

Fig. 4.6 An overview of the lock modulation method for broadening the capture velocity of the ${}^1S_0 \rightarrow {}^3P_1$ magneto-optical trap. Left: the Double frequency modulated PDH signals. Right: The effect of further modulation placed on the lock point. This is an expanded view of the first order sideband in the lower left graph.

to the mixer with the reflected cavity signal. If the DDS (Direct Digital Synthesiser) used to generate this modulation is chosen such that it is half of the FSR (Free Spectral Range) of the cavity to which the laser is locked, then one can lock the laser to any frequency that they require using the same cavity instead of being fixed only to each of the FSR frequencies of the cavity and having to bridge the remaining frequency difference via an AOM.

It is fairly straightforward to then realise that should a further modulation be placed to the EOM, Ω_b, provided that this modulation frequency was not larger than the bandwidth of the locking electronics, then the lock point could be effectively swept through a range of frequencies - which the laser should follow. In the frequency domain this should appear as shown in figure 4.6. We can be sure that this method is a valid way of operating the broadband stage for the red MOT due to the fact that the spectrum produced with this method is the same as that which can be produced by an AOM but without the extra electrical power consumption and optical power loss.

Typical parameters are $\omega_{gap} \approx 100\,\mathrm{MHz}$, $\omega_m \approx 10\,\mathrm{MHz}$ and $\omega_b \approx 50\,\mathrm{kHz}$. The sweep which produces ω_b has a step time of typically 4 ns, a step size of 160 kHz at a width of 4 MHz in order to produce a frequency of 25 kHz. Locking bandwidths can be in the region of 5 MHz at low modulation frequencies of 10 kHz and at high modulation frequencies such as 80 kHz, bandwidths are typically around 1.5 MHz.

Power Broadening Method for Broadband Red MOT

The effective linewidth of a transition is broadened when the intensity of the light driving the transition is increased. This phenomenon can be utilised instead of modulating the red laser for the broadband red MOT stage if the effective linewidth of the ${}^1S_0 \rightarrow {}^3P_1$ transition can be broadened sufficiently to cover the Doppler profile of the atoms cooled in the first stage MOT.

This is something which has not been reported previously in any literature with reference to this cooling stage, however, the benefits have the potential to be very large. For example, provided that sufficient power is available from the second-stage cooling laser to be sent to the MOT beams, this method eliminates the requirement for any modulation for the pre-cooling stage of the red MOT. This greatly simplifies the cooling sequence and removes the requirement for any extra complications which have the potential to introduce noise or instability into the system (for example, the atom number could fluctuate if the modulation applied for the broadband stage is not accurate and precise). This method ensures that the cooling stage can be easily performed adiabatically instead of in separate sections thus ensuring that the optimal temperatures can be reached in a much shorter time.

The fundamental difference about this technique is that the broadening is not introduced upon the laser itself to cover the velocity distribution but upon the effective linewidth of the transition due to the high intensity of the laser beams. The benefit of this technique is that it is very easy to achieve experimentally provided the optical power is available for the MOT laser beams. It is simply the case of adding a stage in the cooling sequence where the intensity of each of the laser beams is large. For example: $7.63\,\mathrm{mWcm}^2$ for red beams of power $3\,\mathrm{mW}$ and diameter $10\,\mathrm{mm}$.

4.3 Trapping Strontium in an Optical Lattice

A vertical 1D optical lattice is sufficient for effectively confining the atoms for use in an optical lattice clock. Early work into lattice trapping with strontium along with investigation into different phenomena occurring in lattice traps can be found in references [75, 76, 77, 78, 79, 80, 81, 82]. The lattice can be orientated horizontally which reduces tunnelling between lattice sites or vertically which reduces the intensity required for trapping against gravity and other gravitational complications [83].

The motion of the atoms can be described as a quantised simple harmonic oscillator with vibrational energy levels described as

$$E_n = h\nu_v \left(n + \frac{1}{2} \right) \tag{4.1}$$

where ν_v is the axial trapping frequency as shown in equation 3.49. In the case that there is on average one atom per lattice site, the atoms will populate the lowest vibrational levels as seen in figure 4.7.

When the single photon recoil frequency shift of the clock laser (ν_r) is much smaller than the axial trapping frequency, the lattice is said to be operating in the 'Lamb-Dicke regime' [84, 85, 86]. In this regime, the recoil caused by absorption of a clock laser photon is not transferred to the atoms, but to the lattice. This means that the absorption of a clock laser photon does not heat the atomic sample and it is said to be Doppler free.

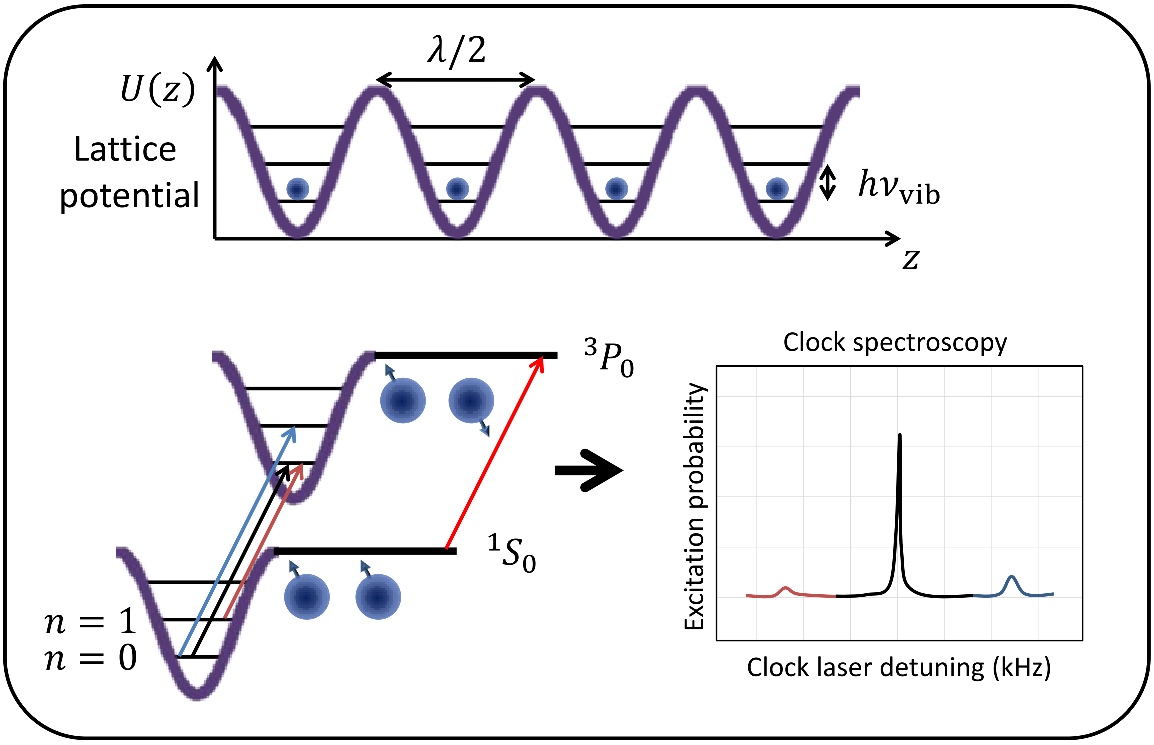

Fig. 4.7 An illustration of the vibrational energy levels found in an optical lattice. Top: Vibrational levels in the optical lattice potential. Bottom left: Atom excitation from different vibrational energy levels in an optical lattice potential, where black denotes $\Delta n = 0$, red is $\Delta n = -1$ and blue is $\Delta n = +1$. Bottom right: An example of the clock spectroscopy signal for each of the cases shown in the bottom left.

Thus far, no consideration has been taken into what exactly the wavelength of the lattice laser should be. The AC Stark shifts upon the energy levels of the atom and this would have an effect upon the clock transition, this can be overcome by operating the lattice at a so-called 'magic wavelength' [76, 87]. This involves using a wavelength which produces an equal AC shift Stark shift upon the ground and excited clock state. There are a number of possible wavelength candidates which could be used as the magic lattice wavelength, and these and an in-depth investigation into in-depth magic wavelength determination can be seen in [87]. The magic wavelength chosen to be used in this clock is 813.427 57 nm [25].

4.4 Magnetic-Induced Spectroscopy of the Clock Transition

The clock transition of strontium is a very narrow transition at 698 nm with a linewidth of $\approx 1\,\mathrm{Hz}$. The clock and ground state are coupled very weakly due to the dipole forbidden dipole transition between these spin states (the transition is doubly forbidden because the it is a $J = 0 \to J' = 0$ transition and the change in spin is $\Delta S = 1$.). Coupling is allowed in fermionic isotopes due to the non-zero nuclear spin and resulting hyperfine mixing on the 3_0^P state. Bosonic isotopes lack this mixing. However, dipole coupling can be induced between the ground and clock state via magnetic-induced spectroscopy first theorised by Taichenachev and Rudin in 2006 [88]. This method uses a laser slightly detuned from the clock transition along with a DC bias magnetic field. The magnetic field induces mixing of the ${}^3P_0$ and ${}^3P_0$ states which the laser probes. The magnetic field or the clock laser intensity can then be carefully increased to increase the effective linewidth of the transition. The resulting second order Zeeman and Stark shifts upon the clock transition from the bias magnetic field and the clock laser intensity respectively must be carefully characterised and controlled. The lifetime of an atom excited to the clock state is around 150 s which makes it a good candidate for a frequency standard. Having such a long lifetime means that electron shelving can take place; when an atom is excited to the clock state, there is a strong probability that it will remain there until detection takes place.

In general, the process by which spectroscopy takes place can be seen in figure 4.8 which first involves illuminating the atoms with a pulse of light which is resonant with the clock transition. In order to ensure that the detection of the atoms in the excited state is not influenced by the atoms which have remained in the ground state, a pulse of light resonant with the strong ${}^1S_0 \to {}^1 P_1$ transition is used to 'blow away' the atoms remaining in the ground state. In order to then detect the atoms in the clock state, the atoms are excited to the ${}^3S_1$

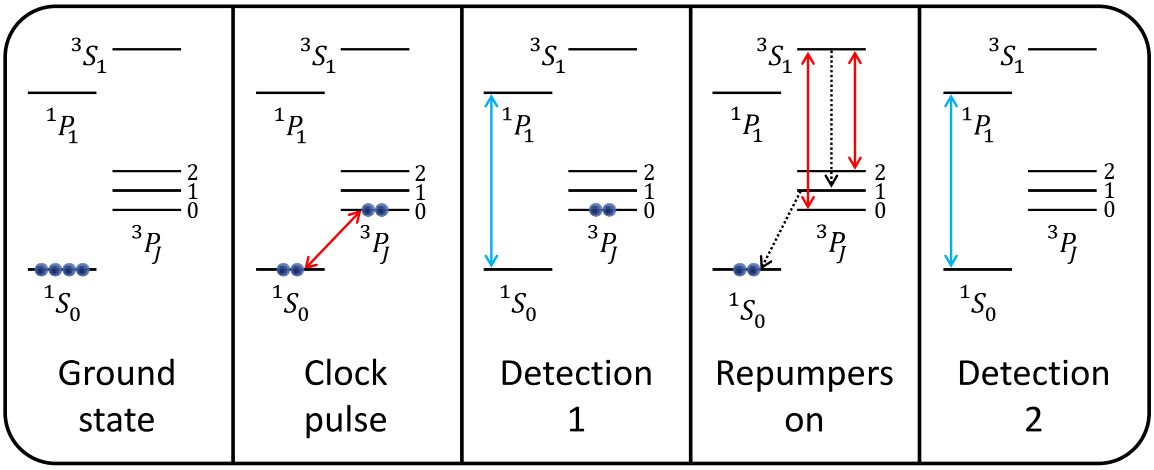

Fig. 4.8 Sequence to perform spectroscopy upon the clock transition showing the atomic population in each energy levels during the clock spectroscopy sequence.

state using the 679 nm repumper laser. With reference to figures 4.1 (and 4.8) it can be seen that the subsequent decay path for the atoms is to either decay to the ground state via the $^3P_1$ or to decay to the $^3P_2$ state. To ensure that all of the atoms are detected, the second repumper is also used to excite the atoms again to the $^3S_1$ state to decay to the ground state. Once the atoms are then in the ground state, another pulse of resonant 461 nm light is used for detection.

As the detection of the atoms that had (and had not) been excited to the clock state have been recorded, a correction can be applied to the fluctuation in atom number by taking the ratio of these two signals and plotting this as excitation probability. If the probability was 1, then this means that no atoms were detected during the first pulse and all atoms were detected in the second pulse etc.

The expected Rabi frequency is given by [36]

$$\Omega_R = \alpha\sqrt{I}|B| \tag{4.2}$$

where $\alpha\,(Sr) = 198\,\mathrm{Hz}\cdot\,\mathrm{cm}\cdot\,\mathrm{T}^{-1}\cdot\mathrm{mW}^{-0.5}$, I is the intensity of the clock laser, and B is the bias field. Therefore, low bias fields and clock laser intensities are required to obtain narrow spectral linewidths.

In order to produce a spectroscopy signal, the frequency of the clock laser must be controlled very precisely over very small intervals. Each measurement is taken with a new ensemble of atoms and logged as a data point. When the spectral line can be resolved, this is when the clock laser can be locked to the transition by use of a feedback loop with a long time constant.

The linewidth of the laser which is used to probe the transition must be smaller than that of the clock transition and the drift rate of the laser must be no more than 1 Hz. To achieve this, the clock laser must be locked to a very stable reference such as a high finesse cavity contained within a temperature controlled, ultra-low vacuum chamber.

4.5 Accuracy and Stability of Strontium Optical Lattice Clocks

As introduced in section 2.1.1, clocks are characterised by two factors; accuracy and stability. The stability of a clock is the fractional measurement of the noise present in the system whereas the accuracy of the clock is determined by the sum of all possible shifts causing the measurement to differ from the true value with the uncertainty on these shifts limiting the quality of the clock. The measurement noise (stability) ultimately limits the uncertainty, so these two factors are linked strongly. The stability of the clock is measured by performing an Allan deviation measurement of the frequency of the clock laser. During this measurement, the clock laser must be locked to the spectral line of the clock transition. Whereas the uncertainty measurement is performed by comparing the measured clock frequency directly with another. This is performed either by comparing the beat note between two independent strontium optical clocks or comparing the beat note between the clock laser and a frequency comb with a caesium clock (either directly or via satellites).

There are a considerable number of noise sources which could affect the stability of the clock and shifts which could alter the measured clock frequency. Examples of shifts which can manifest upon the clock transition and affect uncertainty are outlined below:

4.5.1 frequency Shifts - Uncertainty

Optical Lattice Stark Shifts

- **AC Stark shift:** Neutral atoms become polarised in the presence of an electric field such as that of a laser. This leads to an AC Stark shift of the atomic states; the exact phenomenon which enables atoms to be spatially confined by a laser beam. There are three types of AC Stark shift resulting from the scalar, vector and tensor qualities of the polarisability of an atomic state. The scalar and tensor polarisability are zero for the bosonic isotopes of strontium due to both of the clock states having zero total angular momentum. The scalar quantity is negated by operating the lattice at the magic wavelength to a typical level of below 10^{-18} [89].

- **Hyperpolarisability:** Hyperpolarisability scales with the square of he intensity I^2 of the lattice laser and is not negated by operating at the magic wavelength. It is caused by two photon resonances to which the excited clock state is connected. This effect causes a Stark shift resulting in a shift of 10^{-17} and an uncertainty upon that shift even lower than that.

Zeeman Shifts

- **First-order Zeeman shifts:** Not present when operating a clock with ^{88}Sr due to the lack of nuclear spin.

- **Quadratic Zeeman shifts:** This shift arises from energy levels being separated by the fine structure splitting and is dominated by interaction of the $^3P_0$ and $^3P_1$ states, typically with a magnitude of around $-10^{-6}B^2Hz/\mu T^3$ [90, 91, 92]. The uncertainty on this measurement is typicaly around 10^{-16} [83]. In the case of operating with the bosonic isotope, the majority of the quadratic Zeeman shift comes from the strong magnetic field required for clock spectroscopy. However, as this can be carefully measured and characterised, it can be accurately accounted for.

Blackbody Radiation Induced Stark Shift

- This shift is simply caused from heat sources around the atoms. At room temperature the typical uncertainty due to Blackbody radiation is around 5.5×10^{-15}. The reason for this being so large is that it is difficult to know accurately due to simulation of the system and the large number of sources of BBR which are not constant and uniform. A 1 K uncertainty in temperature causes an uncertainty of 7×10^{-17}. A thermal shield can be used to achieve 1×10^{-18} uncertainty on BBR [93], a uniform temperature can be maintained to achieve an uncertainty of 10^{-17} [89] or cryogenically cool the apparatus [21, 68, 89, 94]

Cold Collision Shift

A large ensemble of atoms is required for a high signal to noise ratio and for measurements with high precision performed rapidly. However, due to the finite trapping volume offered by the lattice, a higher number of atoms results in a higher atom density. This leads to atomic interactions which perturb the clock transition. In fact, the density related frequency shift is the only source of error which effects both the accuracy and the stability of the clock and a good control of collisions is critical to successful operation of a strontium optical lattice clock. In 1D lattice, 2D lattice sites usually have multiple occupancy. As the bosonic isotope allows multiple atoms to with identical wavefunctions to occupy the same quantum state, bosons scatter with s-wave interactions. [89]. The effect of these collisions have been characterised in a bosonic strontium clock as: inelastic collisions, collision broadening of the transition and a collision induced frequency shift [83]. With 10^5 atoms:

- **Inelastic collisions:** Inelastic two-body losses are possible by collisions of $^3P_0$ atoms with $^3P_0$ or $^1S_0$ atoms the typical uncertainty due to inelastic collisions is 2.3×10^{-19}.
- **Density dependent broadening:** Due to elastic collisions with ground state atoms causing dephasing. Typically around 10 Hz
- **Frequency shift:** At low atom density: the shift on the clock transition is linear as a function of atom density. At high atomic density, saturation occurs. Typically this channel of uncertainty is around 10^{-16}

Stark Shift from Clock Laser

- Even though the ground and excited clock states have identical polarisability at the magic wavelength, the polarisabilities of these two states differ at the clock transition frequency [89] and thus, off-resonant coupling to intermediate states induces a dynamic Stark shift. This effect depends on the interogation laser intensity and is typically around 10^{-18}.

Doppler Effects

- **Quantum Tunelling:** Confining the atoms to a lattice removes the doppler and recoil frequency shifts but sensitivity to motion can be introduced by quantum tunnelling between sites along the interrogation axis. Aligning the lattice along the same axis as gravity suppresses tunnelling by gravity-induced non-degeneracy between lattice sites. This uncertainty can be easily kept below 10^{-17} [89].

- **Vibration:** Any vibration between the lattice and clock laser - particularly that which is periodic and therefore does not average away can cause systematic shifts upon the clock. This effect differs from experiment to experiment and can be negated by keeping the experimental area quiet and actively phase stabilising the lasers.
- **Second order Doppler shift:** This phenomenon accounts for relativistic time dilation and is proportional to atomic velocity and laser frequency. It is typically $< 10^{-20}$.

DC Stark shifts

- Caused by static electric fields. Grounding of system causes a Faraday cage which shields the system from any static electric fields in the vicinity og the clock. However, charges can accumulate on insulator surfaces such as viewports (whether or not they have a dielectric coating or not). Typically this causes a shift below 10^{-17} [89, 95].

4.5.2 Noise Sources - Stability

Quantum projection noise (population fluctuations in two level systems) is the fundamental limit to relative stability for strontium optical lattice clocks and at 1 s the instability is typically around 2×10^{-17} for stationary ^{88}Sr clocks [83]. A high stability (low instability) is achieved through a combination of narrow atomic resonances and a high signal to noise ratio.

The largest contributors to systematic instability caused by: a long experimental time between measurements, the requirement for a high signal to noise ratio (this includes the requirement for a high atom number, a high quantum efficiency for detection etc), shot to shot atom number fluctuations and probe laser frequency noise.

The stability of a strontium optical lattice clock is affected by the following:

- **Quantum projection noise:** This is the largest contributor to instability.
- **Photon shot noise:** This contribution is much lower than the quantum projection noise and can be reduced using the electron shelving technique for measuring the clock excites state population by improving the signal to noise ratio.
- **Technical fluctuations in atom number:** This can be a major contribution to instability. However, it can be easily negated by measuring both the ground and excited state populations and calculating the normalised excitation probability.
- **Probe laser frequency noise:** This can be particularly problematic and cause large systematic shifts if the frequency noise on the interrogation laser is periodic with the experiment cycle as then the noise is not averaged. This source of instability is made worse by dead time in experiment and prevents a lower QPN instability.

Typically clocks reach an instability of 10^{-17} at 1000 s.

4.5.3 Typical Uncertainty Budget

A breakdown of a typical uncertainty budget can be seen below in table 4.2. This is the uncertainty budget as reported by the first stage of the Space Optical Clocks project in 2014 performed upon a 8.0 Hz measured clock linewidth. They measured a total fractional uncertainty of 7×10^{-15} and a stability of 4×10^{-15} at 1 s[10].

It is expected that the uncertainty budget of this clock would be lower than that found the first stage of the SOC project. In the future when the experiment utilises ^{87}Sr instead of ^{88}Sr it is hoped that the apparatus could be competitive with the best strontium optical lattice clocks.

Contribution	Shift / Hz	Uncertainty
Second-order Zeeman	-33.5	2.4
Clock laser	-16.6	0.2
Collisions	1.0	0.4
Blackbody radiation	-2.5	0.5
AC Stark (lattice)	-0.7	0.9
TOTAL		2.8

Table 4.2 A typical uncertainty budget as reported by bosonic strontium optical lattice clocks [10].

Chapter 5

SOC2: Fully Transportable Apparatus

Established stationary optical clocks are the most accurate and stable in the world but being stationary, there are a few main technological drawbacks which limit their usability. Firstly, to assess the performance of an optical clock, it must be compared to another with a similar stability and accuracy. An avenue that could be explored is the idea of making a transportable optical clock to fill this requirement.

A transportable piece of apparatus could also in principle become a prototype for a space clock to be fitted on board the international space station. The latter was the goal of the Space Optical Clocks 2 mission as discussed in chapter 2. The realisation of this goal will be discussed in this chapter.

5.1 Vacuum System

In order to isolate the strontium vapour from collisions with background gasses, it is necessary that the entire experiment be performed under vacuum. The vacuum level required for optical clock experiments should be as low as possible, typically in the ultra high vacuum regime (around 1×10^{-10} mbar), to lengthen the background gas limited lifetime of the traps employed.

Vacuum technology is advanced and a vast variety of vacuum compatible parts can be purchased commercially to find exactly what is required for each specific experiment from such companies as Kurt J. Lesker, Gamma Vacuum and Pfeiffer Vacuum among others. For example, the necessary vacuum components for an optical clock can all be purchased commercially and many groups take advantage of this readily available, well tested and reliable equipment. When designing and building transportable apparatus however, some parts must be designed specifically for purpose.

The vacuum system can be seen in figure 5.1 and performs two functions; the preparation of strontium vapour and the cooling and trapping of said vapour. Strontium atoms are evaporated from a hot atomic source (around 400 °C) in the oven and the atoms are cooled and trapped in the science chamber. Between these two regions there exists a differential pumping stage which serves to decouple the pressure in both regions which is important for the cooling and trapping of atoms in the science chamber. This differential pumping stage is a standard CF16 tube which is 30 cm in length. Such a differential pumping stage ensures that the pressure in the MOT chamber is always an order of magnitude lower than at the oven. The ion pumps used in the experiment are both from Gamma Vacuum (25S and 3S) and pump at speeds of $25\,\mathrm{ls^{-1}}$ and $3\,\mathrm{ls^{-1}}$ for the oven and MOT region respectively and are controlled with a Digital Small Pump Controller (SPC). These two regions can be separated by the use of the atomic beam shutter if required (see section 5.1.2 for details). At the same side of the MOT chamber as the small pump, there exists a CF16 4 way cross. The side with direct line of sight to the atoms is fitted with a flange containing a sapphire window which can be heated to a high temperature to remove any strontium deposits from the highly collimated atomic beam effusing from the atomic oven. The other 2 sides of the 4 way cross

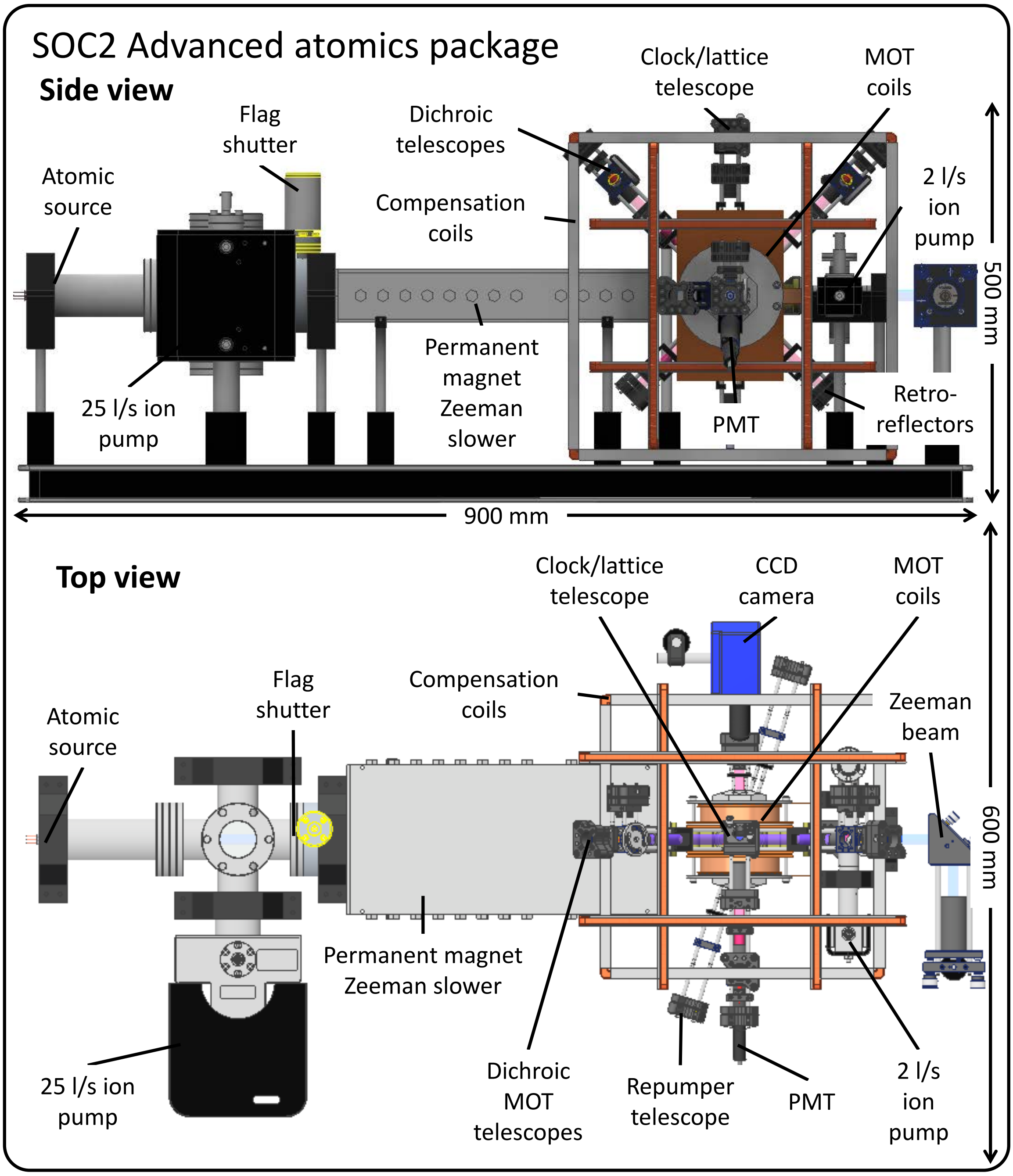

Fig. 5.1 A CAD drawing of the vacuum system used in the SOC2 clock experimental apparatus. Top: A side view of the SOC2 atomics package with each component labelled. Bottom: A top view of the SOC2 atomics package with each component labelled.

are connected to the ion pump and a valve through with rough pumping can take place via a turbo molecular pump using which, pressures down to around 1×10^{-6} mbar are achievable. The reduction of the last few orders of magnitude comes from the addition of pumping speed from the ion pumps and through baking of the system to remove any outgassing materials from the inner surfaces of the vacuum apparatus with the turbo molecular pump still attached to the system.

Due to this being a transportable set up, it is important that no space is wasted on the apparatus. A smaller differential pumping stage could have been used with a much narrower inner diameter to achieve the same level of decoupling. However, this comparably long differential pumping stage also serves as the region over which Zeeman slowing takes place. This involves slowing the thermal atomic beam in vacuum to increase the loading efficiency into the MOT. This is done using a novel permanent magnet Zeeman slower. The Zeeman slower consists of a steel box, inside which a series of neodymium magnets is placed on both sides, over the entire of the 30 cm length. Each set of magnets can be easily adjusted externally to create a specifically shaped magnetic field which compensates for the Doppler shifts as seen by the high velocity atoms from a laser beam blue detuned from an atomic resonance. The optical access for the Zeeman slowing beam is provided through a sapphire window on side of the vacuum system furthest from the atomic oven. The Zeeman slower is described in more detail in sections 5.2 and 4.2.1 and general Zeeman slowing theory is covered in section 3.1.3 along with the original paper for the permanent magnet Zeeman slower in reference [71].

The 3D MOT chamber is made as small as possible to still have present 10 mm diameter slowing beams for efficient trapping with a high capture velocity of $50\,\mathrm{ms}^{-1}$. This small size has other benefits such as a smaller inner volume of 75 ml which means smaller pumps can be used, the MOT coils can be much smaller with a diameter of 46 mm at a distance of only

32 mm which means that the desired magnetic field gradient of 45 G cm^{-1} can be generated with a lower current of 10 A and with a much lower power dissipation as heat from the coils of only 5 W - which would transfer to the atoms in the form of BBR which can be seen on the clock transition and is one of the main limiting factors to innaccuracy and stability of stationary clocks and many stationary clocks around the world are focussing on addressing this limitation [19, 21, 68, 93, 94, 96].

An important design feature to include in the construction of an optical clock apparatus is to either ensure that no viewport is placed directly in the atomic beam path, or to ensure that such a viewport can be heated to a high temperature to remove any strontium deposits. This is important as this is the viewport through which the Zeeman slowing laser beam is passed, if the transmittance of this viewport is comprimised by strontium deposits then this results in an effective reduction in the quality and intensity of the Zeeman slowing beam and therefore the efficiency of the Zeeman cooling. In order to keep the vacuum system simple, the latter solution was employed. The viewport is a standard cf16 flange with a sapphire viewport from Kurt J. lesker Company. Sapphire has a melting point of 2030 °C and thus the viewport can be heated up to at least 1000 °C without compromising the quality of the vacuum. Strontium deposits can be removed with a temperature as low as 100 °C as found in this work. The window was heated with a thermoelectric heating strip from Watlow to a maximum temperature of 150 °C.

5.1.1 Atomic Oven

The point at which strontium atoms will effuse from bulk is around 300 °C in vacuum. Thus, to have a diffuse gas of strontium upon which to experiment, one must first heat the bulk metal to at least this temperature. The oven performs this role.

There are a few important design specifications to take into account when designing an oven for atomic clocks, especially transportable atomic clocks.

- Firstly, **commercial dispenser vs oven**: one could consider the option of purchasing a dispenser instead of designing and using an oven. Whilst dispensers are acceptable for prototype clocks, if one is hoping to operate a piece of apparatus for many years, one must consider the possibility of using something which does not require replenishment for the lifetime of the experiment. Dispensers typically have a capacity of 500 mg of strontium which would typically allow 1 year of continuous operation [97]. This becomes problematic when the dispenser must be changed. This can be a quick process but there is often the requirement to outgass the dispenser by heating it and allowing the vacuum pumps to remove the sealant material - typically indium. There is also the possibility that baking of the dispenser area is required to remove any impurities which became present upon the inner vacuum surface during exchange of the dispenser. Both of these scenarios take time, and in the case of a transportable clock, it is necessary to be making measurements for as much of the time as possible. If the clock is not able to make measurements for a few days then this can become problematic. Another problem with dispensers is that they often consume a lot of power compared with specifically designed ovens and the solid angle over which atoms are ejected from the dispenser is often very large (12.1 sr which corresponds to a cone with a 2θ angle of 100°) meaning that only a very small fraction of around 13 % the strontium emitted could be utilised in the experiment. The latter issue can be easily solved in the design of an atomic oven by placing a tube, or an array of tubes to collimate the atomic beam and only allow atoms with a velocity parallel to the tube direction to pass through into the main vacuum chamber. This ensures a much higher efficiency of atoms effused from the bulk strontium will be used in the experiment.

- Secondly, **size and energy consumption**: it is important to consider the size and energy consumption of the device. As stated previously, ovens often consume less power than dispensers. Materials can be chosen such that the heat is directed only to the chamber in which the strontium is stored and ejected instead of across the entire housing. For a transportable apparatus, these factors are very important. In order to be transportable, the size and weight must be reduced and there is often a limitation upon the amount of power available to run the experiment. Therefore, savings in space, and energy should be made wherever possible. Due to the fact that often, many experiments will use standard CF flanges and tubing, it would also be beneficial for the oven design to be able to be mounted upon a CF standard blank flange, and for the external housing of the oven to fit completely inside the corresponding tube size for that flange to reduce the complexities of the set up. This then allows the oven to be manufactured and assembled faster and cheaper with less wasted space on the apparatus.

- And finally, **blackbody radiation**: the amount of blackbody radiation being emitted from the oven which is in direct line of sight with the cold, trapped atoms in the science chamber must be considered and reduced. Blackbody radiation induces AC Stark shifts upon the energy levels of the clock transition and thus reduces the accuracy of the reference and is the limiting factor of many stationary clocks upon accuracy [19, 91, 93, 96]. There have been many innovative ideas which try to tackle this problem such as placing the atoms in a cryogenic environment [21, 68, 94], mounting the oven with no line of sight to the atoms and directing the atoms with another laser beam via the use of a 2D MOT [98], using a 2D MOT instead of a Zeeman slower to pre-cool the atoms which removes the need for the atomic source to be placed with the atoms effused in the direction of the atomic chamber [99]. With exception of the last approach, all of these ideas are not well suited to a transportable clock. A cryogenic environment would require a constant source of liquid nitrogen/helium, and to add an extra laser beam to push the atoms away from the line of sight of the oven would make the apparatus significantly larger. The last approach would indeed make the apparatus more compact, however, a 2D MOT such as the one described would require large (elliptical with the major axis waist being 3 cm [98]) and high power (total power 220 mW [98]) laser beams to slow atoms as efficiently as a Zeeman slower. If more power were available in the blue laser, this may be an applicable option for the future, however with the present set up, this was simply not possible. Therefore, one needs a different approach.

Inbuilt to the design of the oven is a heat shield. This is polished aluminium on the inside which reflects the BBR instead of allowing it to traverse along the vacuum system. We have also installed an in vacuum shutter which can be controlled digitally if required to completely close off the atomic beam during the clock measurements. These factors allow for a reasonable amount of shielding of the atoms from the BBR whilst not compromising upon size, power consumption and complexity.

Design specifications

The restrictions for the oven design were imposed by the other components of the clock. For example, a pump with a high enough pumping speed which is compact enough to keep the whole apparatus using only CF16 flanges and tubes was not available at the time of designing and building the apparatus and therefore the oven must be mounted onto a CF35 flange instead of a CF16 one.

Such an oven had been recently built and tested which can be found in the appendix of the thesis of Marco Schioppo [61] which was developed as part of the first phase of the SOC project. Thus, using this design as a highly reliable template, I proceeded to design my own oven. The resulting final design did not deviate greatly from the design by Schioppo, with

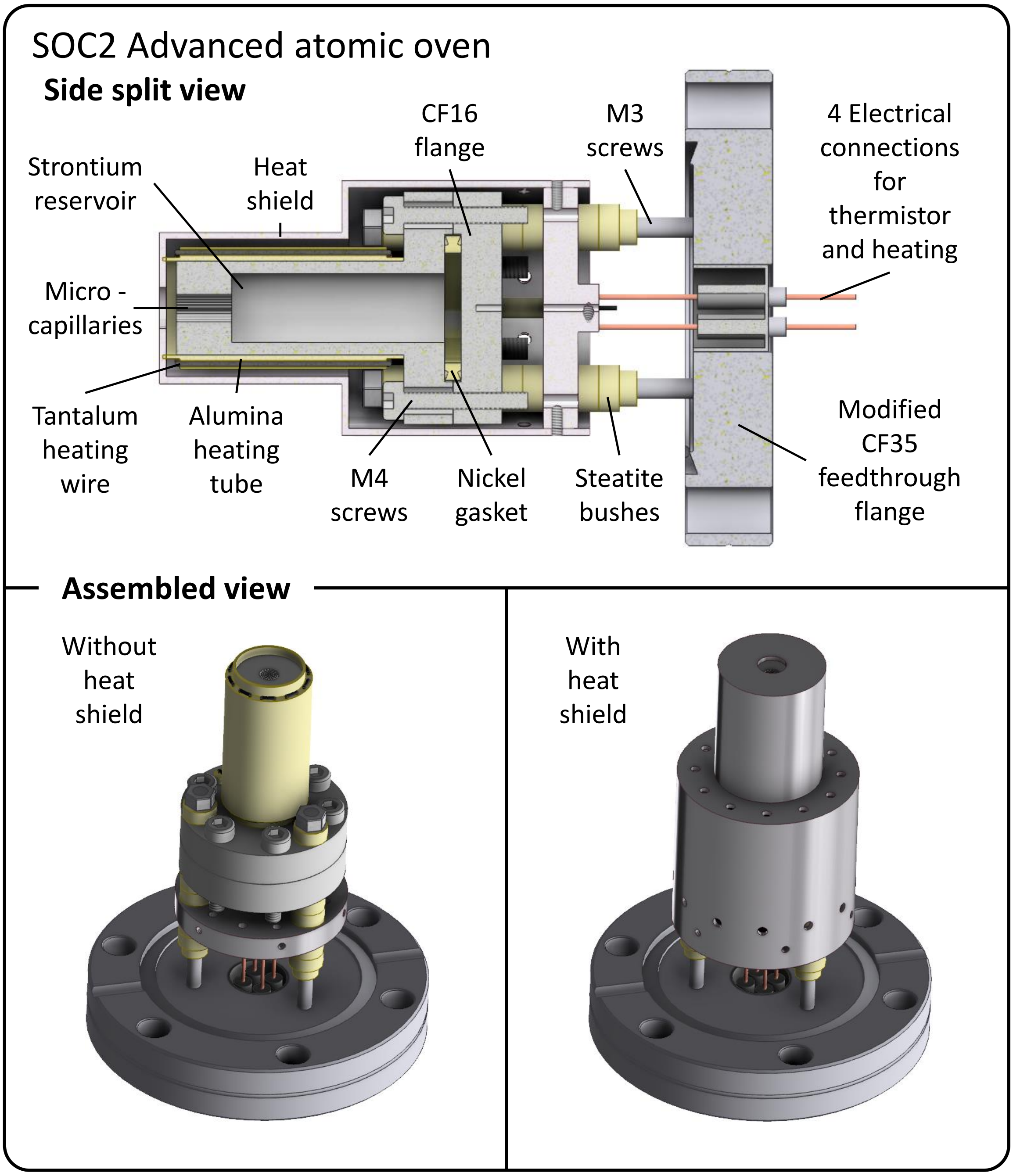

Fig. 5.2 A CAD drawing of the strontium oven design used in the SOC2 clock experimental apparatus. Top: the split side view of the atomic oven with each part labelled. Bottom: The assembled view of the atomic oven with and without the heat shield.

just a few slight changes due to incompatible systems. The oven design used in this work can be seen in figure 5.2.

The general design features of the oven can be read in ref. [61]. But I will describe the design briefly here along with the changes that I made to the design for the SOC2 project. The major features being the reservoir for the strontium metallic pieces, the heating element and insulating materials (for high efficiency), the micro-capillaries which serve to collimate the atomic beam, and the heat shield. The reservoir for the housing of the strontium pieces is sealed with a standard CF16 nickel gasket between a standard blank flange with a custom nipple in which a maximum of 5 g of strontium is placed. Nickel is used as it can be heated to a higher temperature without compromising the seal in comparison to copper. This nipple has a hole in the far end of diameter 8 mm and depth 8 mm. Inside this is placed around 25 micro-capillaries. These were purchased from La Guellec Tubes with an inner diameter of 200 µm and an outer diameter of 600 µm. These capillaries were chosen to be as smooth and uniform as possible to reduce the likelihood of any strontium becoming stuck to the inside during operation and causing a blockage - which as well as reducing the amount of strontium atoms which will arrive into the science chamber, could also cause a build up of pressure inside the oven which could be dangerous. The heating element was chosen to be tantalum wire of diameter 800 µm. Tantalum was chosen due to its favourable malleability, electrical conductivity and melting point but comparable thermal conductivity when compared to copper (for example) this comparison can be seen in table 5.1.

		Tantalum	Copper
Malleability	(Mohs Hardness)	6.5	3
Thermal conductivity	$\mathrm{Wm^{-1}K^{-1}}$	57.5	401
Electrical conductivity	$\mathrm{MSm^{-1}}$	7.63	59.6
Melting Point	K	3290	1358

Table 5.1 A material comparison between tantalum and copper [100].

The diameter was chosen to fit inside the alumina (Al_2O_3) multibore tube which was used to house the tantalum wire for a more uniform distribution of heat to the nipple. Alumina, or aluminium oxide was chosen as the material for this because it is an electrical insulator with a relatively high thermal conductivity and hardness which means that it is unlikely to break during installation or operation and has a melting point much higher than the operating temperature of the oven. The material properties of alumina can be seen in table 5.2.

		Alumina
Hardness	(Mohs Hardness)	9
Thermal conductivity	$\mathrm{Wm^{-1}K^{-1}}$	15
Electrical resistivity	$\mathrm{p\Omega\,m}$	10
Melting Point	K	3245

Table 5.2 Material properties alumina at 650 K [100].

The oven is secured to a standard CF35 flange in which three threaded holes were drilled. The flange was isolated from the rest of the oven by means of a series of steatite bushes as washers. Steatite ceramic has a very low thermal conductivity ($2.5\,\mathrm{Wm^{-1}K^{-1}}$) [101] and can be easily shaped - making it a candidate for this application. The heat shield is a housing which fits exactly over the entire oven. The inner surface of this housing is highly polished aluminium and thus any BBR escaping the oven will become reflected on the inner surface of the heat shield. The heat shield contains a few holes to allow the air inside the oven to pass through the heat shield when the apparatus is being evacuated. It fits exactly onto the base of the oven and is secured using M2 screws.

The design ensures that the capillaries are always kept at the same temperature as the reservoir. This ensures that the capillaries do not become blocked with condensated strontium. The idea of the capillaries is to collimate the atomic beam by not allowing through any atoms whose velocity vector deviates too far from being parallel with the capillaries. However, it is possible that the benefit from this collimation is small as atoms with a large entrance angle would simply collide with the inner surfaces of the capillary and exit with a large angle. Due to lack of vacuum apparatus, the divergence of the beam was not measured close to the exit of the oven but at a position around 5 cm from the exit nozzle and the beam was found to have a significant improvement upon collimation when compared to the commercial dispenser (results and discussion in section 6.3). However, in the similar design employed in ref. [61], the measurement was taken at the exit of the oven and the capillaries were found to have a collimating effect. It can be debated that the collimated effect would be present in the absence of the capillaries with just the large hole serving to collimate the atomic beam; however, it was not possible to make this measurement during this project.

5.1.2 Atomic Beam Shutter

It is conceivable that the highly collimated and high flux laser beam could affect the lifetime of the atomic traps by heating of the atomic sample by the thermal atomic beam. This problem could be eliminated by introducing an in vacuum shutter. Such a shutter can be found at Kurt.J.Lesker Company (CF35 Pneumatic Viewport Shutter). It allows the atomic beam to be completely blocked from entering the science chamber. The added benefits of including an atomic beam shutter is that cold atomic sample can be shielded from the BBR produced by the atomic oven. This has implications for the overall performance of the clock as BBR is found to be the limiting factor of many strontium optical clocks worldwide as previously discussed in section 5.1.

The shutter was manufactured to be controlled pneumatically. Due to the experiment being transportable in nature, it is beneficial to avoid such constraints as the requirement of a pressurised air source for use with the atomic beam shutter. For this reason, the shutter was adapted to be controlled with a stepper motor which can be controlled and triggered by the FPGA control sequence. The digital triggers are handled via an arduino micro-controller.

5.2 Zeeman Slower (NPL)

The Zeeman slower was designed, realised and optimised by NPL and a paper was published about the slower that is used in this project [71] and can be seen in figure 4.2 in section 4.2.1. The slower consists of a series of permanent neodymium magnets configured in such a way as to have the maximum slowing for the geometry of the slower. The slower was designed for atomic speeds from 0 - 1000 $\mathrm{ms^{-1}}$ and the atomic speed upon exiting the Zeeman slower is around 30 $\mathrm{ms^{-1}}$ using a Zeeman slowing beam with power of 70 mW and a diameter of 13 mm which is slightly focussed at the atomic source. The slower was tested for differing beam intensities and detuning from resonance to fully characterise the device. During operation after installation upon SOC2, the Zeeman slower was used with a slowing beam which is slightly focussed upon the exit aperture of the atomic oven, with an initial diameter of only 10 mm, power of around 25 mW and a detuning of 400 MHz. This produced an exit velocity of 30 $\mathrm{ms^{-1}}$ with a beam intensity of 4.52 $\mathrm{mWcm^{-2}}$.

5.3 Atomics Package

The atomics package was designed to be as robust, compact and lightweight with the aim to be a prototype for a mission to the ISS and to be used as a transportable clock between different laboratories. This was the main workpackage within the SOC2 project for which I was responsible (the workpackages are outlined in appendix A).

The first stage was to design and realise a compact atomics package as seen in figure 5.3 and integrate that with the existing apparatus at Birmingham for preliminary testing. The

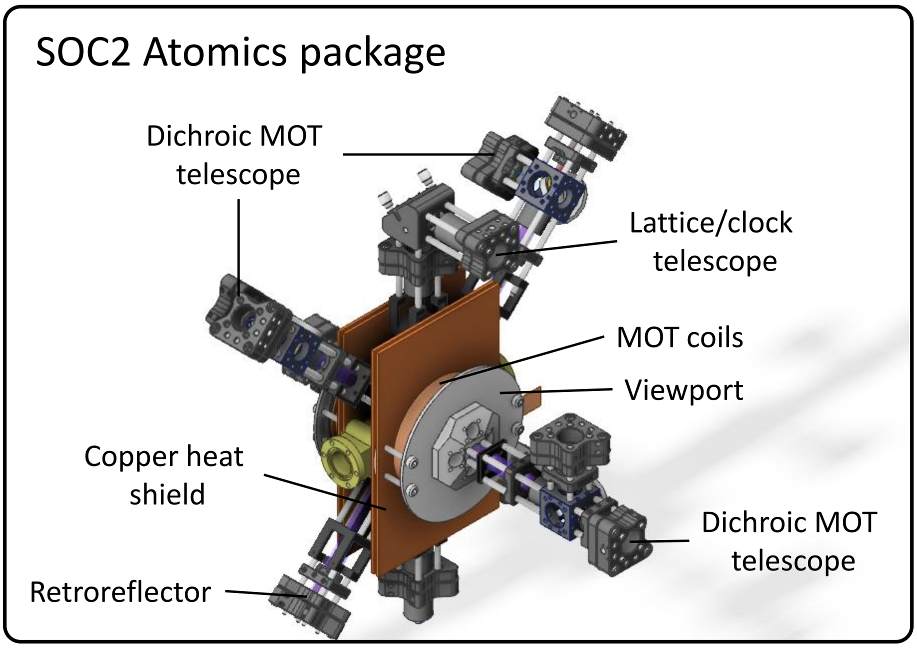

Fig. 5.3 A CAD drawing of the compact and fully transportable atomics package designed and realised for the SOC2 clock project with each of the components labelled.

idea here was to ensure that the new atomics package was functional before integrating it with the SOC2 lasers. Then the SOC2 lasers had been tested with the apparatus at UNIFI and shown to perform to the required level for use in a fully transportable apparatus. Upon delivery of these lasers to Birmingham, they were integrated with the SOC2 atomics package. Once the clock apparatus was at a stage where spectroscopy of the clock transition was ready to take place, the entire clock was transported in a small van to PTB in Germany for final characterisation.

The main components of the atomics package are explained in the following sections.

5.3.1 3D MOT Chamber

With the lower limit to the miniaturisation of the chamber found to be the MOT beam size, the configuration of the chamber is fixed. Due to the requirement of a magnetic field

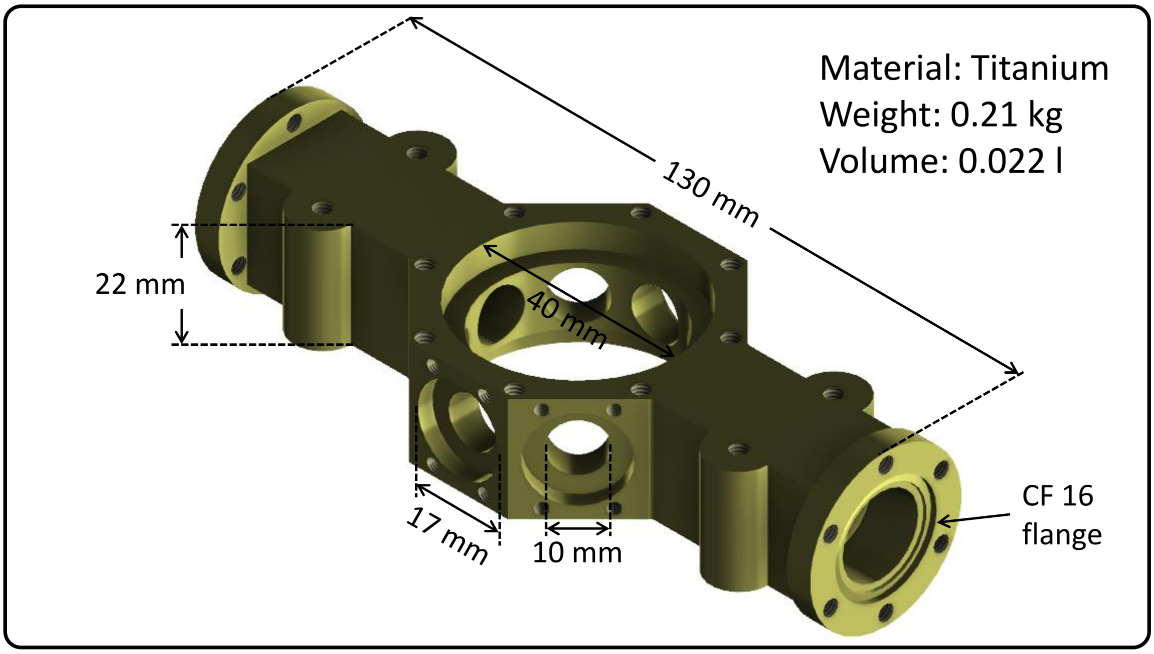

Fig. 5.4 A CAD drawing of the novel science chamber which is currently the smallest strontium optical clock chamber in use. Dimensions of the chamber are shown and some material properties.

gradient for MOT operation, it is beneficial to reduce the width of the chamber along one axis as much as possible. By ensuring this dimension is reduced, the power consumption and heat dissipation of the anti-Helmholtz coils used to generate the magnetic field gradient is reduced. In turn, this factor has the potential to remove the requirement for external cooling of the MOT coils which not only reduces the complexity of the system but also the power consumption and the vibrations experienced on the apparatus.

This leads to a preferable chamber geometry to be based upon an octagonal prism based on the requirement for three orthogonal optical accesses along with access for the atomic beam and Zeeman slowing beam and the 1D vertically orientated optical lattice. With a beam size of 10 mm, the width of the chamber can be reduced to 22 mm and to accommodate each beam and the chamber geometry the height can be reduced to 51 mm. Now all that remains is to ensure that the chamber can be attached to the vacuum components. In order to

Fig. 5.5 Photographs showing the indium sealing technique for securing vacuum chamber windows. Left: The prepared atomic chamber with the indium ring shown in the top right. Middle: The indium seal placed upon the chamber in preparation for sealing the window. Right: The chamber after all windows had been sealed together with the compression flanges.

ensure compatibility, I decided to utilise a standard CF16 flange design in both sides of the remaining axis to connect the components required for Zeeman slowing. This design can be seen in figure 5.4 where the atomic beam / Zeeman slowing beam axis is along the long 130 mm direction, the axis passing through the centre of the 40 mm window is the z axis and the remaining axis is the y axis.

I decided to use BK7 as the material for the windows used on the chamber with a custom anti-reflection coating for all wavelengths (461 nm, 679 - 707 nm - to cover 679, 689, 698 and 707 nm - and 813 nm) and for the chamber material to be titanium. BK7 and titanium have similar coefficient of thermal expansion of $7.1 \times 10^{-6}\,\mathrm{K}^{-1}$ and $8.6 \times 10^{-6}\,\mathrm{K}^{-1}$ which means that a temperature changes are less likely to compromise the quality of the vacuum. Titanium has the added benefits of being durable, lightweight and non-magnetic which are all qualities which are beneficial for use with a transportable strontium optical lattice clock. The windows were secured to the chamber using the indium sealing technique. This is a very simple technique which is well suited to small, circular windows. The technique involves simply placing a ring of indium between the chamber surface and the window and securing a sealing flange with no more torque than 61×10^3 Nm-1 [102]. This can be seen in figure 5.5. In order to ensure a good overlap between the chamber and the windows for the indium sealing, the smaller windows are 16 mm in diameter, and the larger windows are 40 mm which, in both cases, leaves a ring with a width of 3 mm which is sufficient to ensure a seal. If indium sealing is performed correctly, one can achieve a pressure inside the chamber in the ultra-high vacuum regime and as indium has a relatively low melting point of 156 °C, the windows can be easily replaced by heating the indium and removing the window. The low melting point of indium also has obvious disadvantages that the assembled chamber cannot be baked to a very high temperature to remove impurities inside. Therefore, every effort should made to ensure that the chamber is kept as clean as possible during assembly and that the baking temperature does not exceed 120 °C.

5.3.2 MOT Coils

In order to ensure that the coils which produce the magnetic field gradient are as compact as possible, I decided to use copper wire with a rectangular cross-section. The width of which is 14 mm with a thickness of 0.25 mm. This is preferable over using standard wire with a circular cross-section as no space is lost between each winding. With the minimum distance between the coils established to be 22 mm, and the minimum diameter fixed by the requirement for optical access through the larger window. However, A factor which must be taken into account is the fact that the coils should not sit directly upon the chamber. During operation the current flowing through the coils will produce heat which should be shielded from the trapped cold atoms as much as possible to reduce the uncertainty of the clock transition due to the Stark shift induced from Blackbody radiation. In order to isolate the chamber from heat transfer as much as possible, I designed the use of a multi layer heat shield which can be seen in figure 5.6. This heat shield was designed to have the coils mounted upon one copper plate which is extended in the y direction and is mounted upon

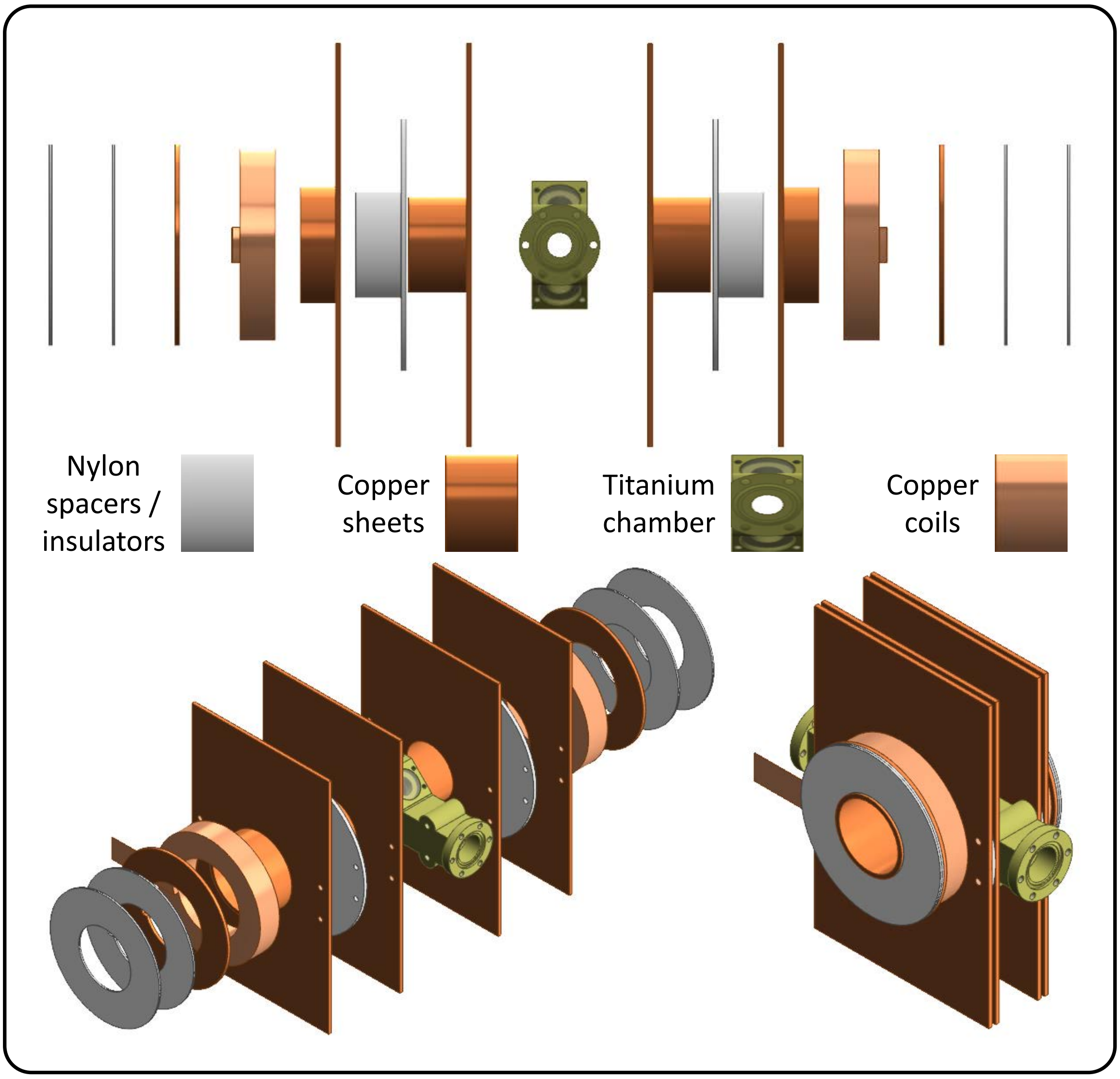

Fig. 5.6 A CAD drawing of the design of the multi layer heat shield employed as the mount for magneto-optical trapping coils which generate the quadrupole magnetic field with each component labelled. Top: extended side view. Bottom left: extended orthographic view. Bottom right: compact orthographic view.

another copper heat shield of the same length and separated by an insulating layer. The idea behind this is to transfer the heat to the edges of the heat shield where it can dissipate into the surroundings and act as a passive temperature control or cooling elements could be attached to the edges of the heat shield as described and shown in section B.3 in appendix B. Thus, the heat should not transfer efficiently to the inner heat shield. Each layer is 2 mm thick, which increases the distance between the coils to be 32 mm. This fixes the inner diameter of the coils to be 46 mm.

Given these parameters, the number of windings required for the desired magnetic field can be calculated by considering the magnetic field produced by a current flowing through a pair of anti-helmholtz coils. If $x = \frac{nT}{2} + r_i$ is the position of the middle winding of the coil, r_i is the inner radius of the coils and T is the thickness of the wire,

$$B_z(z) = \frac{n\mu_0 I x^2}{2[(z-b)^2+x^2]^{\frac{3}{2}}} - \frac{n\mu_0 I x^2}{2[(z+b)^2+x^2]^{\frac{3}{2}}} \tag{5.1}$$

where n is the number of windings in each coil, z is the position where the field is being measured, b is half of the coil separation, μ_0 =$4\pi \times 10^7\,\mathrm{Hm^{-1}}$ is the permeability of free space and I is the current flowing through each coil. Differentiating this with respect to z gives the gradient along the strong axis:

$$\frac{dB_z}{dz} = -\frac{3n\mu_0 I x^2 (z-b)}{2(x^2+(z-b)^2)^{\frac{5}{2}}} + \frac{3n\mu_0 I x^2 (z+b)}{2(x^2+(z+b)^2)^{\frac{5}{2}}} \tag{5.2}$$

if the gradient is being measured at the centre of the chamber, then $z = 0$ and therefore

$$\frac{dB_z}{dz} = \frac{3n\mu_0 I x^2 b}{(x^2+b^2)^{\frac{5}{2}}} \tag{5.3}$$

Which can be rearranged for n to give the number of windings required in each coil.

At a given current, the coils will dissipate power in the form of heat which is undesirable. The amount of power dissipated is calculated simply by using Ohm's Law and the Power Law equations,

$$P = I^2 R \tag{5.4}$$

where $R = \rho L/A$, L is the length of the wire and A is the cross-sectional area and ρ is the resistivity of the material used.

From experience gained building stationary clock components in the lab, it was found that if the power dissipated per coil was more than roughly 10 W then some external cooling would be required. As no external cooling is preferable in this project, the aim was to keep the power dissipated per coil to be minimal.

Using equation 5.3, and a measured maximum value for n as 48, the minimum current that could be used to generate a magnetic field gradient of 45 G cm^{-1} in this system is 10.4 A which produces only 4.96 W of heat. This is using copper wire with a rectangular cross section of 14× 0.25 mm. Therefore, due to the miniaturisation of the system, no external cooling is required but could be introduced at a later date in order to reduce the Blackbody radiation shift upon the clock transition.

5.3.3 Homogeneous Magnetic Field Generation

As previously described in section 4.4, to perform spectroscopy on the clock transition in ^{88}Sr, a strong, homogeneous magnetic field is required to produce admixing of the intercombination ^1P_J lines. This could be done by introducing another set of coils connected to another power supply which can be triggered on and off by the FPGA. However, the most compact solution would be to use the 3D MOT coils in a Helmholtz configuration to generate a homogeneous magnetic field. The benefit of this method is that these coils are already set

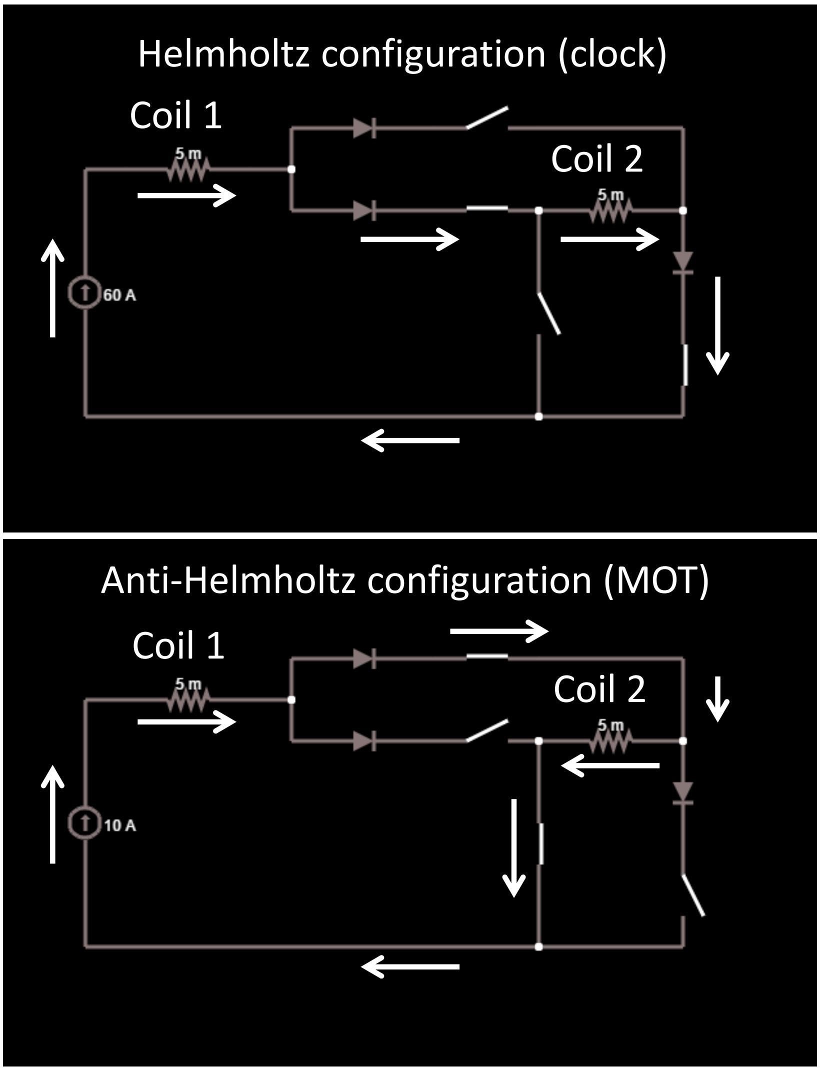

Helmholtz configuration (clock)

Anti-Helmholtz configuration (MOT)

Fig. 5.7 The circuits used for the generation of a homogeneous magnetic field used for spectroscopy of the clock transition by switching the polarity of one of the coils used for magneto-optical trapping

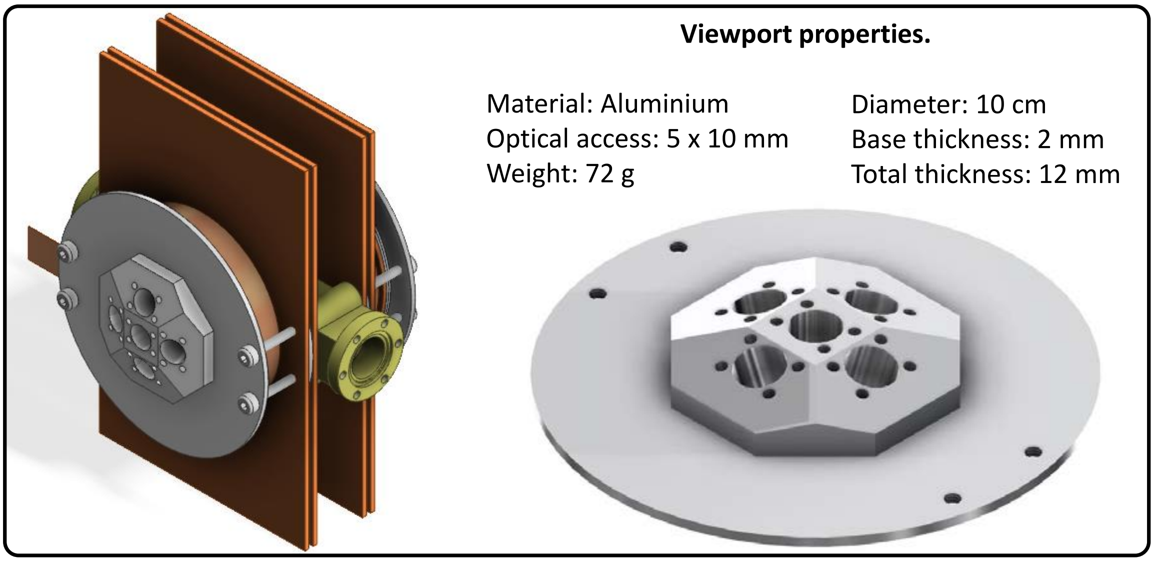

Fig. 5.8 A CAD drawing of the design for the viewports used over the large windows of the main SOC2 atomic chamber with properties listed above.. Left: orthographic view of the position of the viewports on the atomics package. Right: a CAD drawing of the viewport.

up to handle a large current to produce a high magnetic field. In order to use the 3D MOT coils in this way, the polarity of one of the coils needs to be switched. We designed a circuit based on a more complex design which performs this task at PTB. The external circuit is an array of switches to switch the polarity of one of the MOT coils which are triggerable by the FPGA. The magnitude of the current is controlled by an analogue trigger from the FPGA.

5.3.4 Viewports, Dichroic Telescopes and Adapters

On top of the coils lies a viewport upon which there should be five optical accesses, each passing through the centre of the chamber. The central port must be exactly orthogonal to four other ports to house the third MOT beam. The optical access must also be unimpeded by any of the coil apparatus or chamber. This led to a design such as that shown in figure 5.8. Telescopes which house the optics for docking each fibre, collimating, aligning and ensuring the correct polarisation can be attached to this viewport and to the main chamber.

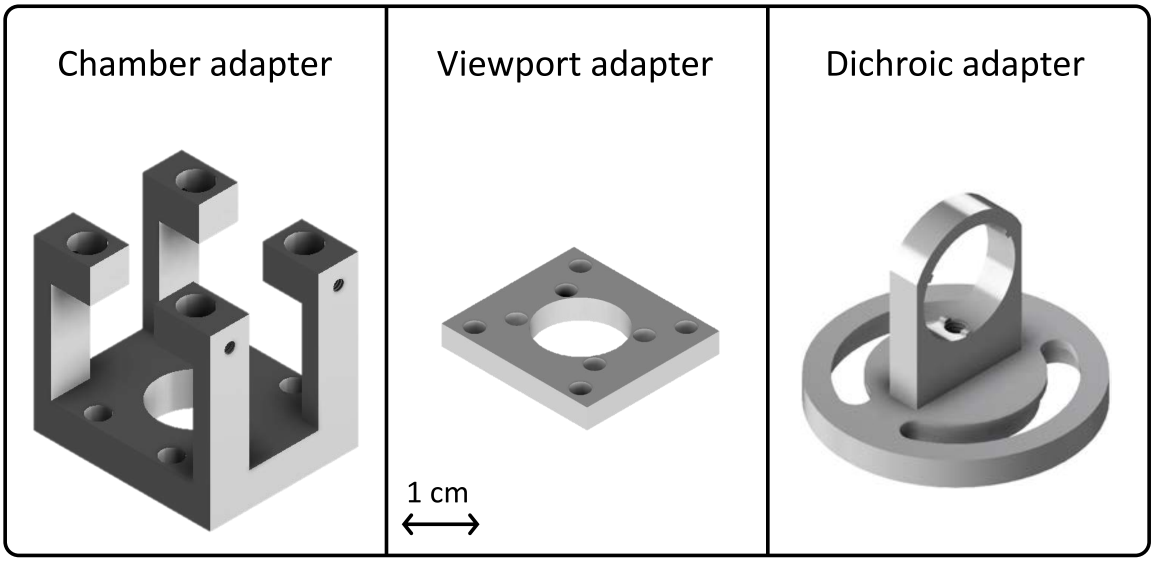

Fig. 5.9 A CAD drawing of the adapters designed and used to attach the optical telescopes to the SOC2 clock atomic chamber. Left: The adapter used to secure the telescopes to the main atomic chamber. Middle: the adapter used to secure the telescopes to the viewport. Right: The adapter used to hold the dichroic mirror for combination of the laser light used in the first and second cooling stages in the MOT telescopes.

To ensure robustness and compatibility to available optical components, I decided to use commercial parts instead of designing an entirely new set of telescopes. The 16 mm cage system from Thorlabs provides such flexibility, compactness and robustness as required for this project. The only issue to overcome with using this solution is the compatibility with the chamber and viewport. For this reason I designed two types of adapter. These adapters provide the possibility to roughly align as well as serving to secure the telescopes to the system. These adapters along with the adapter I designed which holds the dichroic mirror for dichroic coupling can be seen in figure 5.9.

The MOT beam telescopes contain as few optical components as possible to be robust and compact and can be seen in figure 5.10. The beams are expanded from a fibre coupler contained within a kinematic mount after which is a half-waveplate in a rotatable mount. Then the red and blue beams are overlapped upon a dichroic mirror contained within an

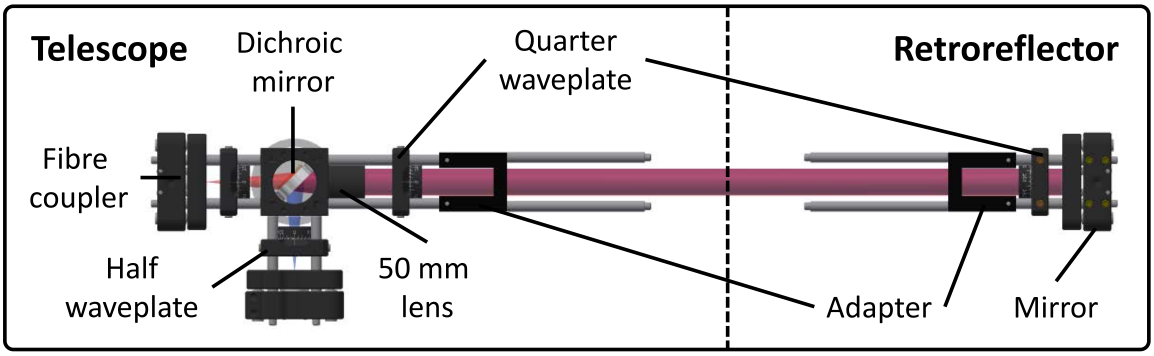

Fig. 5.10 A CAD drawing of the optical telescopes to deliver, combine, collimate and prepare the laser beams for magneto-optical trapping in the SOC2 clock experiment with all of the components labelled.

adjustable custom mount. After overlapping, the two beams then pass through a 50 mm lens for collimating the beams at 10 mm which pass through a quarter-waveplate and the vacuum system. On the opposite side they are reflected from a mirror in a kinematic mount after being passed through a second quarter-waveplate which serves to switch the handedness of the circular polarisation.

The laser light for the 1D lattice is coupled into a fibre (FC1) with a numerical aperture of 0.11. This beam is then collimated using a 6.24 mm lens (L1). This collimated beam then passes through a half-waveplate (HWP1) and is focussed using a 75 mm lens (L2) to a waist of 35 µm situated at the centre of the chamber and collimated again using another 75 mm lens (L3) and is reflected using a hot mirror (HM1) from Edmund optics. The clock laser is coupled into a fibre (FC2) with a numerical aperture of 0.12 and collimated using a 3.1 mm lens (L4). This is then passed through a half-waveplate (HWP2) and reflected from a mirror at 45° and then passed through a polariser (PBS1). The beam then passes through the hot mirror (HM1) on the opposite side as the lattice laser and is focussed at the centre of the trap with a waist of 65 µm by the 75 mm lens (L3). This can be seen in figure 5.11.

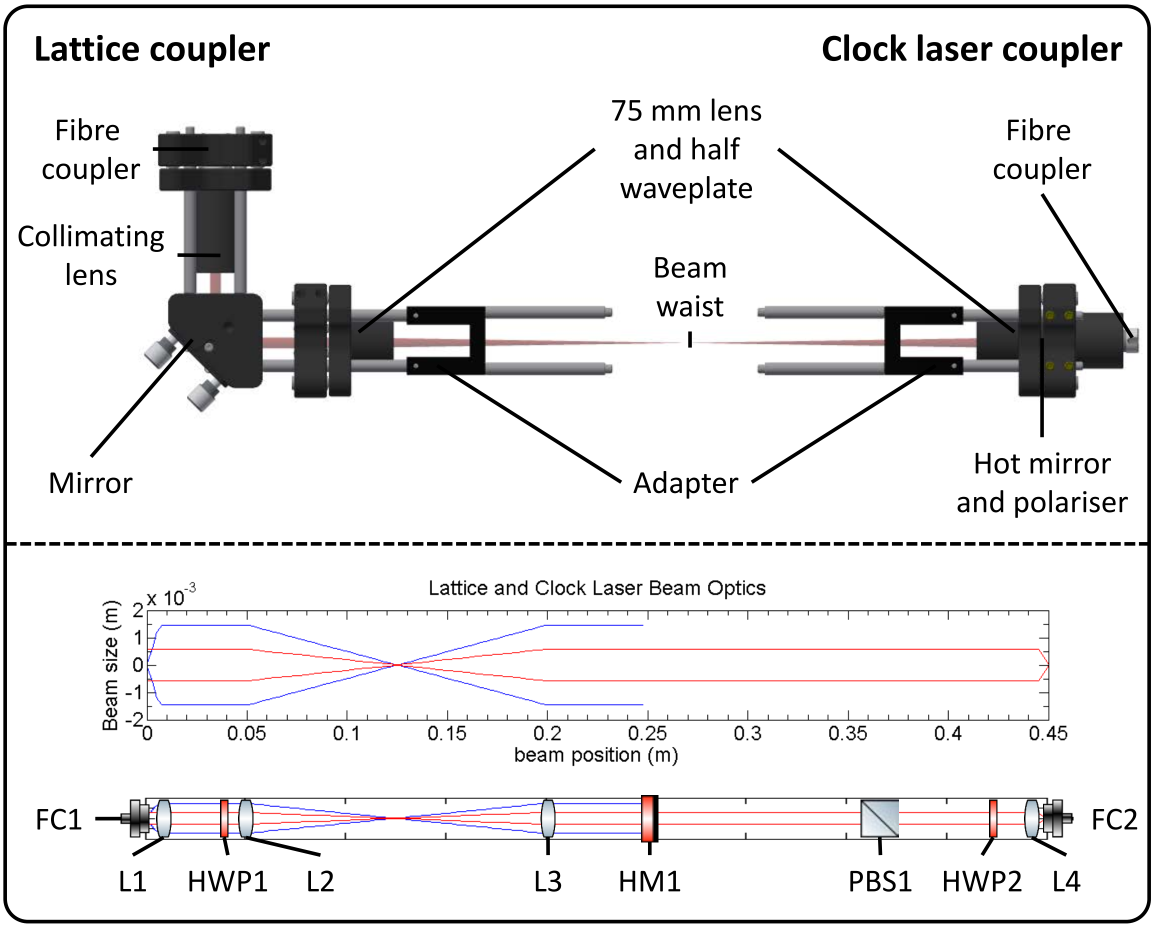

Fig. 5.11 A CAD drawing of the telescope design for the delivery, combination, focussing and preparing of the clock and lattice beams in the SOC2 clock. Top: A CAD drawing with all components labelled. Bottom: The beam sizes along the lattice and clock laser coupler. FC denotes fibre coupler, L denotes a lens, HWP is half waveplate, HM is hot mirror and PBS is polarising beam splitter.

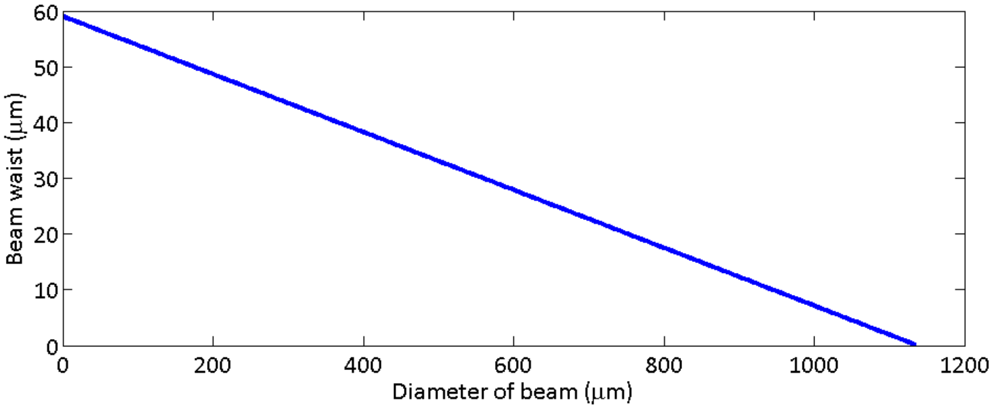

Fig. 5.12 A calculation of how the width of the clock interrogation beam can be altered in the SOC2 clock apparatus design

The width of the clock beam in the centre of the lattice can be easily changed by switching the lens L4. The extent of this change can be seen in figure 5.12. A larger beam diameter results in easier alignment however, a lower intensity of the interrogation beam. The waist of the lattice laser can be altered by switching the lens L1.

5.3.5 Compensation Coils

As has been previously stated, one of the prerequisites for the experiment is that the experiment is as shielded from external influences as possible. External magnetic fields coming from laboratory equipment and the inherent magnetic field of the Earth and successful cancellation of the local magnetic field is imperative for the red MOT, lattice trap and clock operation as the magnetic field shifts the magnetic centre of the MOT and disturbs the cooling and loading of the MOT.

I designed the compensation coils to exactly fit the apparatus and be in a perfect Helmholtz configuration. I also simulated another configuration of coils which would be more compact

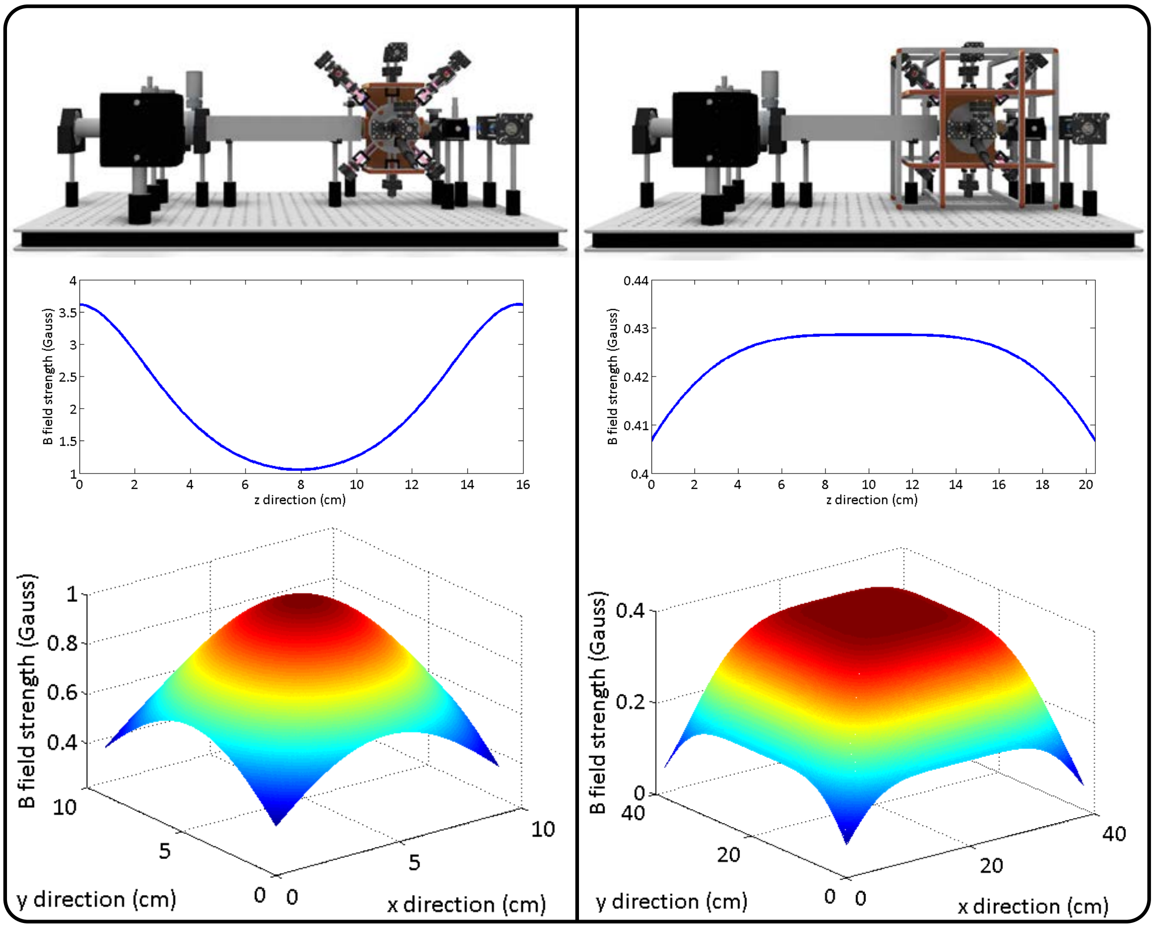

Fig. 5.13 A simulation and CAD drawing of the magnetic field generated by differing compensation coil designs aiming to negate the effects of an external magnetic field upon the atom ensemble. Top: physical compensation coil dimensions. Middle: The magnetic field through the centre of the coils along the z axis. Bottom: the magnetic field through the central x-y plane of the compensation coils.

to compare with the larger but more uniform design. The results of which can be seen in figure 5.13 along with the configuration of each of these designs.

The design of the compensation coils needed to take into account all of the previously mentioned optics mounted upon the apparatus. It is important that the compensation field is as uniform as possible and thus, it is beneficial that the compensation coils are in the Helmholtz configuration. This poses a challenge in terms of where three sets of Helmholtz coils could fit upon the apparatus as they would not fit in a cubic shape as the distance between each pair of coils must equal the radius of the coil. Therefore, I designed three sets of coils which fit inside each other with the limiting factor of the smallest set of coils being the width of the Zeeman slower. The uniformity of these coils can be seen in the simulations shown in figure 5.13. The benefit of having a set of coils which are separated by $2r$ and in the Helmholtz configuration means that the uniformity of the generated magnetic field is less dependent upon the exact geometry of each coil. For example, a slight tilt or shift of the coils with respect to each other or their common axis. Each coil is wound with 1 mm diameter copper wire with 20 windings each. In order to compensate for the local magnetic field each coil should require a maximum of 1 A. The coils are square in shape with dimensions: 25 cm, 27 cm and 29 cm and can be seen in figure 5.13.

5.4 Modular Laser Systems

As part of having a prototype for a space clock, one of the requirements is to have all of the laser systems modular and fibre coupled so that any part can be easily switched if there is a problem. The laser systems used with SOC2 are commercially available and not space ready as the clock apparatus is a prototype for a space mission. The next stage for the SOC project would be to make space ready lasers and to test them on the atomics package.

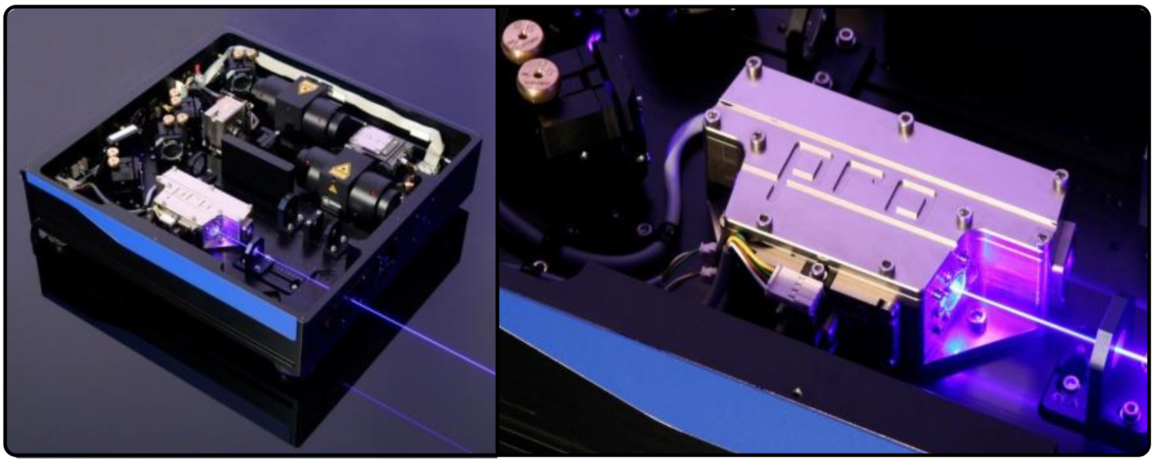

Fig. 5.14 A schematic of the laser used for the generation of 461 nm laser light for the first stage trapping in the SOC2 clock. Left: The whole laser module. Right: the frequency doubling cavity. Images courtesy of TOPTICA.

Part of being a space ready laser means that the electronics and the laser system need to have a specific power consumption and take up a certain amount of space (6.1). They must also be robust against vibrations, high G forces (from launch) and autonomous. They must also be rigorously tested for the long term effect of the lasers and electronics of radiation and the lack of atmosphere. This is something which has been done in parallel with SOC2 by Kayser Italia and Kayser Threde. (For more details see ref. [11] and sections 2.4.1 and A.)

5.4.1 First Stage Cooling Laser: 461 nm TOPTICA Laser using DIGILOCK

The 461 nm laser used in this experiment is a frequency doubled SHG-pro from TOPTICA with a maximum fibre coupled output power of 400 mW and can be seen in 5.14. The master 922 nm laser is locked using the TOPTICA DIGILOCK software to the Frequency Stabilisation System (FSS) [103] which can be seen in figure 5.21 and is explained in more detail in section 5.5. The stability of the cavity to which the 461 nm laser is stabilised has been shown to be 200 Hz over 100 s and after stabilisation the linewidth of the laser is reduced from ≈ 5 MHz to < 1 MHz.

Thus, the 461 nm laser is locked and stabilised to an external cavity, however, for the experimental procedure, a number of similar frequencies around the resonance frequency are required and these frequencies can be bridged using a selection of AOMs. There are three main frequencies required: a probe beam for atom number calculations is required to be exactly on resonance, the MOT beams must be detuned to be around 2Γ below resonance and finally the Zeeman slowing beam must be around 400 MHz detuned from resonance [71]. Due to the modular nature of the experiment, a separate frequency distribution breadboard was designed to generate all of these frequencies from a single fibre coupled input frequency.

5.4.2 461 nm Frequency Distribution Module

The distribution module for the blue laser was designed to be as versatile and compact as possible and the layout can be seen in figure 5.15. The custom made mounts used in the distribution module are compact and robust and fully adjustable. The fibre couplers used are from Schäfter and Kirchoff and the optics are all purchased from Thorlabs. It contains eight fibre coupled outputs with one input for the 461 nm light shown in blue. There are three outputs for the MOT beams (red), one for the Zeeman slower (purple), one for the probe beam (green) and three outputs and one input to be used for the possibility of utilising a 2D MOT as a pre-cooling mechanism (yellow and orange).

The benefit to using a 2D MOT is that in principle it should occupy a smaller volume than the Zeeman slower. However, it also requires a high optical power of around 220 mW and large eliptical beam sizes of 3 cm [98]. This approach was investigated during the first phase of the Space Optical Clocks project [99] and it was decided upon the outcome of these investigations to use the Zeeman slower as the primary method for pre-cooling the atoms.

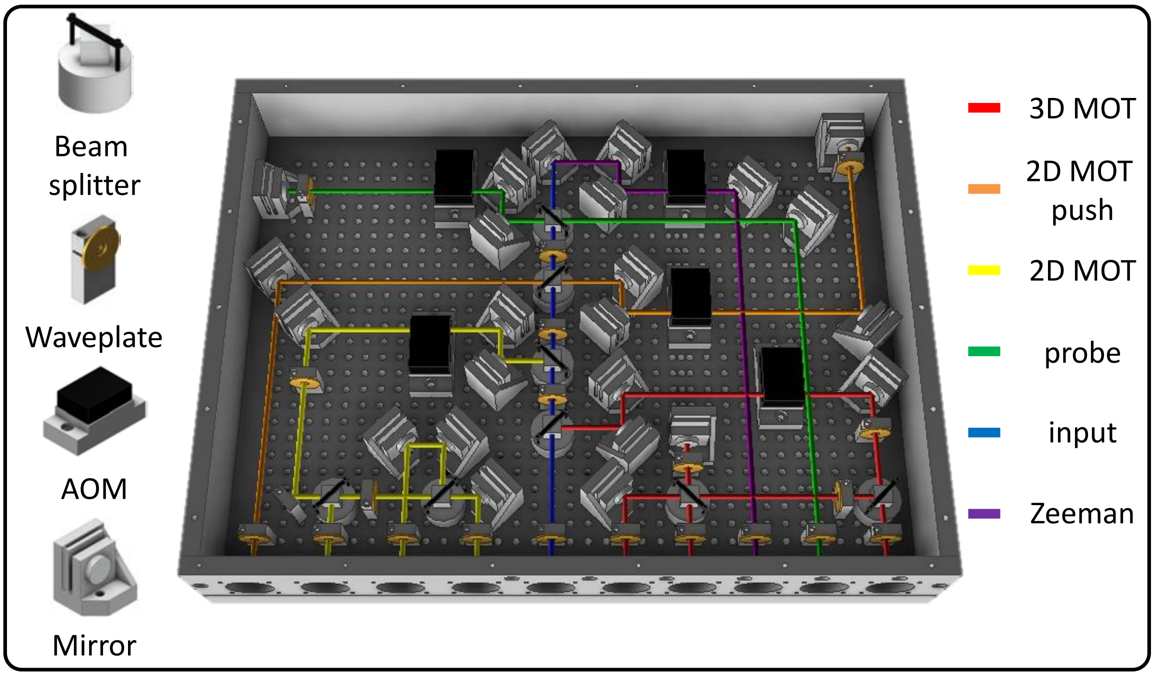

Fig. 5.15 A schematic of the frequency distribution module designed for the dividing of 461 nm laser light for various uses in the trapping and detection processes with each component labelled. The beam paths are described in the text.

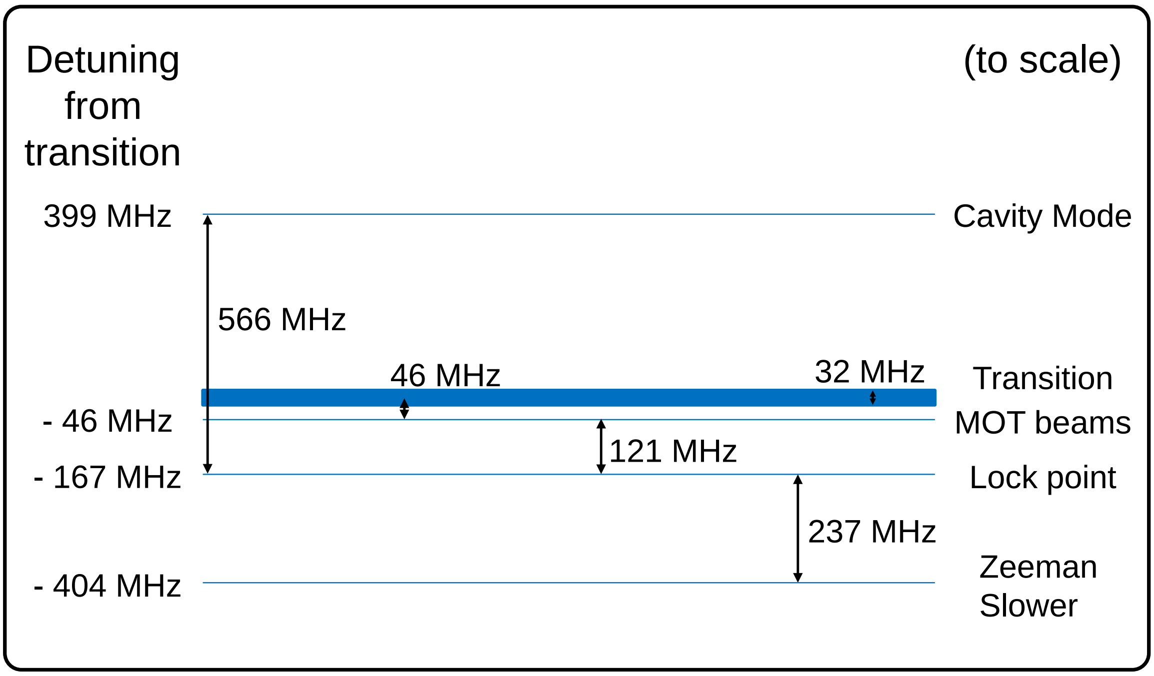

Fig. 5.16 An illustration of the various detunings required for the 461 nm laser during operation of the SOC2 clock.

However, there still remains the possibility to use a 2D MOT instead of the Zeeman slower in the distribution breadboard for the 461 nm laser light. This section consists of one input for repumpers, two outputs for the 2D MOT and one output to be used as a pushing beam (which can be seen in orange and yellow in figure 5.15). The pushing beam is shown in orange and is double passed through an AOM for a larger detuning and to have the ability to alter the detuning without the alignment into the fibre coupler being lost. The 2D MOT beams and repumper input is shown in yellow. The 2D MOT beams are passed once through an AOM and then overlapped with the input repumping beams before being split into two fibre coupled outputs. The idea would then to reflect these beams to create four beams for the 2D MOT.

The remaining five outputs are used in the experiment as MOT beams, a probe beam and the Zeeman slowing beam. As previously mentioned, the frequency requirements for each of

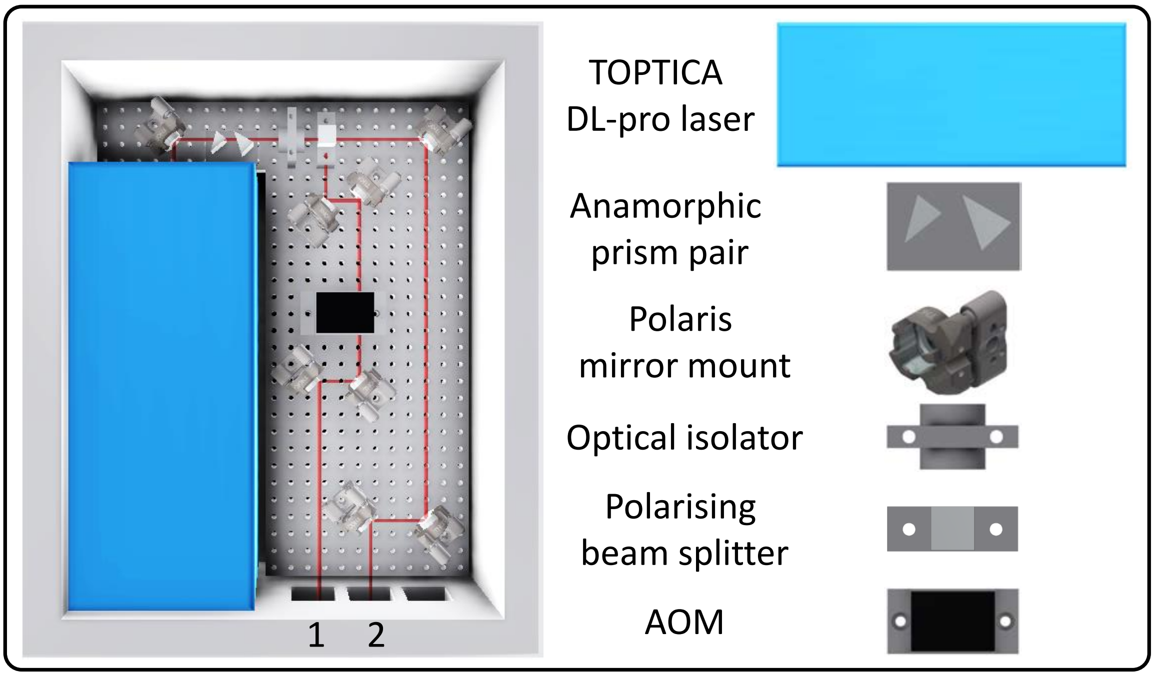

Fig. 5.17 A schematic of the repumper laser breadboards used in the SOC2 clock apparatus with each component labelled. Beam path 1 is sent to the experiment whereas beam path 2 can be used for diagnostics or locking.

these is slightly different and the different frequencies with respect to the atomic resonance frequency can be seen in figure 5.16. The MOT beams are split into three outputs after passing through an AOM which is centred around 120 MHz, the Zeeman slower is coupled after passing through an AOM centred around 220 MHz and the probe beam is coupled after a double pass through an 80 MHz AOM. By optimising the coupling into each AOM for opposing orders of modulation, the frequency detunings required can be bridged as shown in figure 5.16

5.4.3 Repumper Lasers: 707 and 679 nm TOPTICA lasers

The two repumper lasers used in this experiment have wavelengths of 679 nm and 707 nm and can be seen in figure 5.17. These two lasers are DL-PRO TOPTICA lasers which have free running linewidths of around 1 MHz and a maximum optical power output of 11.9 mW and 25.5 mW respectively. Due to the passive stability of these lasers, they are not locked to any external cavity. Should they be required to be locked, this could easily be implemented with the breadboards which were designed at UNIFI as part of the SOC2 project. Each laser is fibre coupled at the output of the breadboard and the beam can be switched on and off using a shutter which is triggered by an external voltage controlled by an FPGA.

5.4.4 Second Stage Cooling Laser: 689 nm Master-Slave Laser (TOPTICA/PTB)

The laser used during the second stage cooling is generated via a master-slave laser configuration. The master laser is a narrow linewidth (800 kHz), low power (14.9 mW) TOPTICA ECDL which was removed from it's original housing and placed in custom housing at PTB. This is the laser which is locked to the FSS and modulated for the lock modulated broadband phase of the red MOT. The beam then is split into four paths, one of which is for diagnostics (< 1 mW), one of which is for offset locking the stirring laser for trapping of ^{87}Sr (3 mW), the third is used for stabilising the laser to the cavity (7 mW), and the fourth is used for injection locking of the slave laser (1 mW). The slave laser has a higher output power of 30 mW but has a larger free-running linewidth of $\approx$ 1 MHz. When the laser is injection locked to the master laser, the slave laser has an inherently low linewidth ultimately determined by the master laser and thus, the finesse of the cavity to which the master laser is locked. The slave laser is split into two paths, one for diagnostics (< 1 mW) and one which is sent through an AOM for intensity and switching control and is then coupled into a 1-3 fibre splitter and sent to the atoms (15 mW).

The final linewidth of the laser is around 1 kHz and a schematic of the laser breadboard can be found in figure 5.18. The output to the MOT from the breadboard is split using a 1-3 fibre splitter from Evanescent optics.

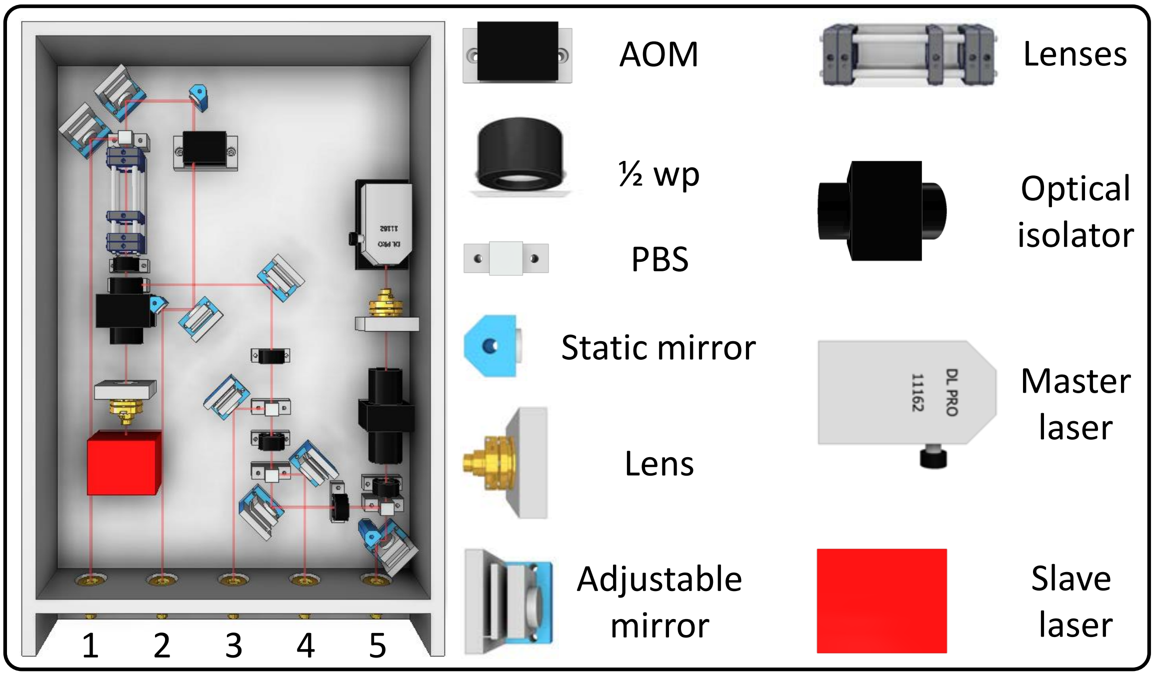

Fig. 5.18 A schematic of the 689 nm laser used for the second stage magneto-optical trap in the SOC2 clock apparatus with each component labelled. Beam paths are as follows: 1 - slave diagnostics, 2 - MOT cooling light, 3 - Master locking beam, 4 - to the stirring laser (Not used for ^{88}Sr) and 5 - Master diagnostics.

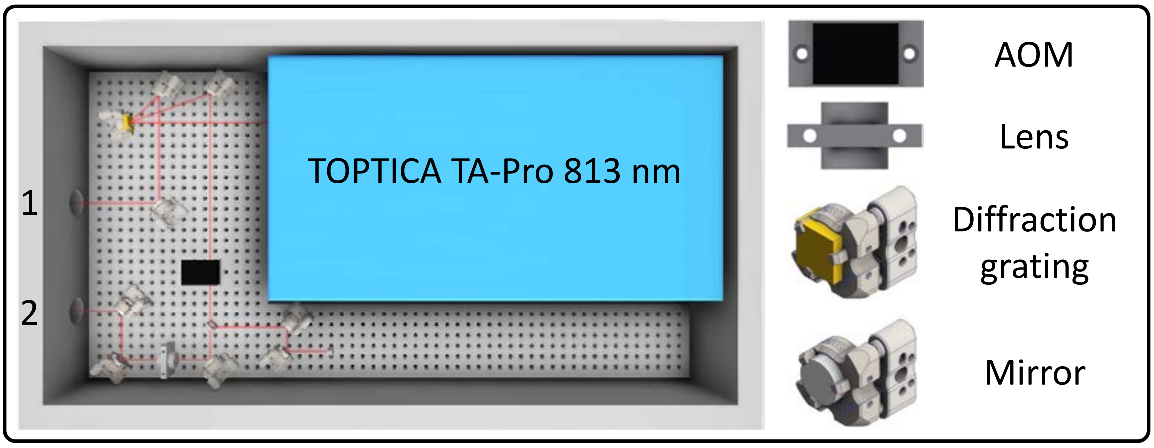

Fig. 5.19 A schematic of the 813 nm lattice laser breadboard used in the SOC2 clock apparatus with each component labelled. Beam path 1 is for diagnostics. Beam path 2 is sent to the experiment.

5.4.5 Lattice Laser: 813 nm TOPTICA Laser and DIGILOCK

The 813 nm laser is a TOPTICA TA-PRO housed in a custom box designed by UNIFI. The laser consists of an ECDL with a power output of typically 2.5 W and a linewidth of $<$ 1 MHz. This is then passed through a tapered amplifier which increases the output power to a maximum of 2 W. This beam is then split into two with around 20 mW being sent to the FSS via an optical polarisation maintaining fibre for PDH stabilisation using the DIGILOCK software with the rest of the power being delivered into a high-power polarisation maintaining fibre to be used on the atoms.

A schematic of the laser can be seen in figure 5.19. The final linewidth of the laser was found to be 1 MHz with a power to the atoms of a maximum of 1.2 W with typical coupling efficiencies.

5.4.6 698 nm Clock Laser and Reference Cavity (LUH/PTB/SYRTE)

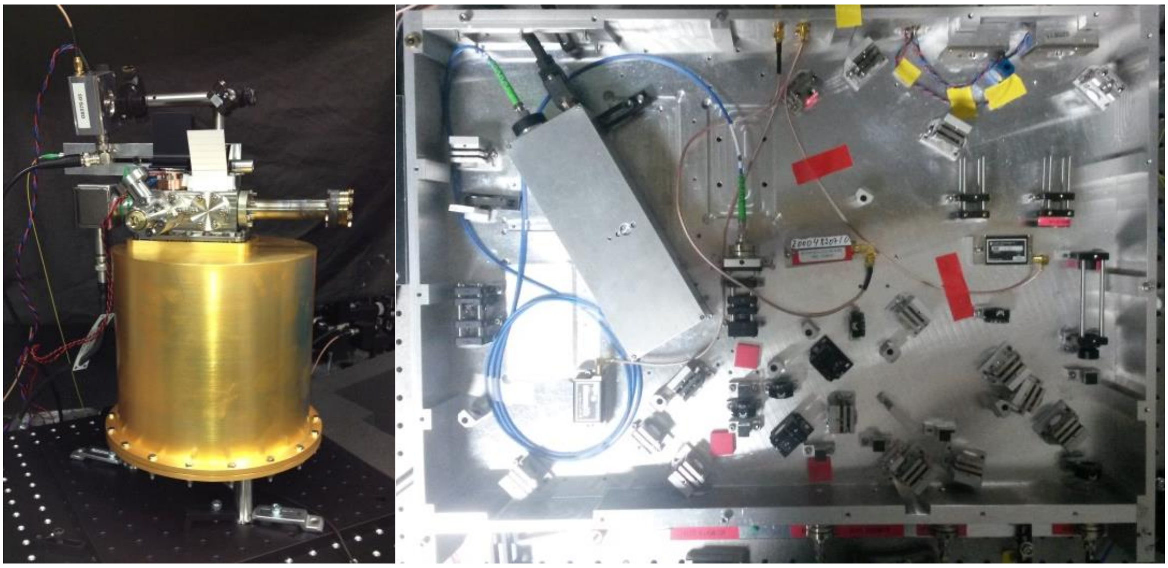

Fig. 5.20 A photograph of the 698 nm clock laser and ultra-stable reference cavity used in the SOC2 clock apparatus.

The clock laser was produced and tested at PTB before being used at UNIFI with their SOC1 apparatus and was stabilised to the first iteration of the highly-stable compact cavity for stabilisation which was built by SYRTE. The laser was then sent back to PTB for extensive modifications and for integration with a new iteration of the cavity which was also designed and tested at SYRTE. A schematic of the clock laser and new generation cavity can be seen in figure 5.20.

The laser head was designed and tested at LUH before being integrated with the breadboard. The design of the clock laser is complex and must be able to perform a large number of roles without introducing any noise onto the clock laser signal. The breadboard contains three outputs which are used for interrogation of the atoms, locking to the ultra-stable cavity, and the final output is used for locking to a frequency comb or to compare with another 698 nm laser.

The typical power from the laser is 15 mW with up to 1 mW being available for use to interrogate the atomic sample, 20 µW sent to the ultra-stable reference cavity and 1 mW available to send to the frequency comb or for a beat note with another laser.

The final linewidth of the laser locked to the SOC2 reference cavity was found to be 500 - 800 Hz which is not at present sufficient for use in accurately probing the clock transition. The drift rate of the cavity was measured to be 0.2 - 0.4 Hzs^{-1} which shows that the cavity was stable, but severely limited by the pressure of the vacuum system which fluctuated between 1×10^{-7} mbar and 1×10^{-9} mbar. This could be due to the two layer temperature stabilisation present in the system. If the time constant between the two temperature stabilisation loops are not chosen and optimised to be significantly different to each other then it is likely that these two stabilisations systems could be working against each other to create a positive feedback loop which causes the temperature of the cavity to vary largely.

5.5 FSS: Frequency Stabilisation System (HHUD)

The FSS is a novel, compact (< 10 l), all-fibre coupled piece of equipment that has been developed at HHUD. Internally there is housed a triple cavity constructed from a single ultra-low expansion glass block (ULE) with vacuum compatible optics inside a small aluminium housing and can be seen in figure 5.21. The vacuum maintained is low 10^{-6} mbar via a model 3S 3 ls^{-1} ion pump purchased from Gamma Vacuum. Three lasers can be stabilised to the FSS using a standard Pound-Drever-Hall (PDH) control loop with the exception that the signal is double frequency modulated and control loop is locked either one of the primary sidebands to the carrier frequency. The three laser frequencies that are stabilised are: the 922 nm, 813 nm and 689 nm.

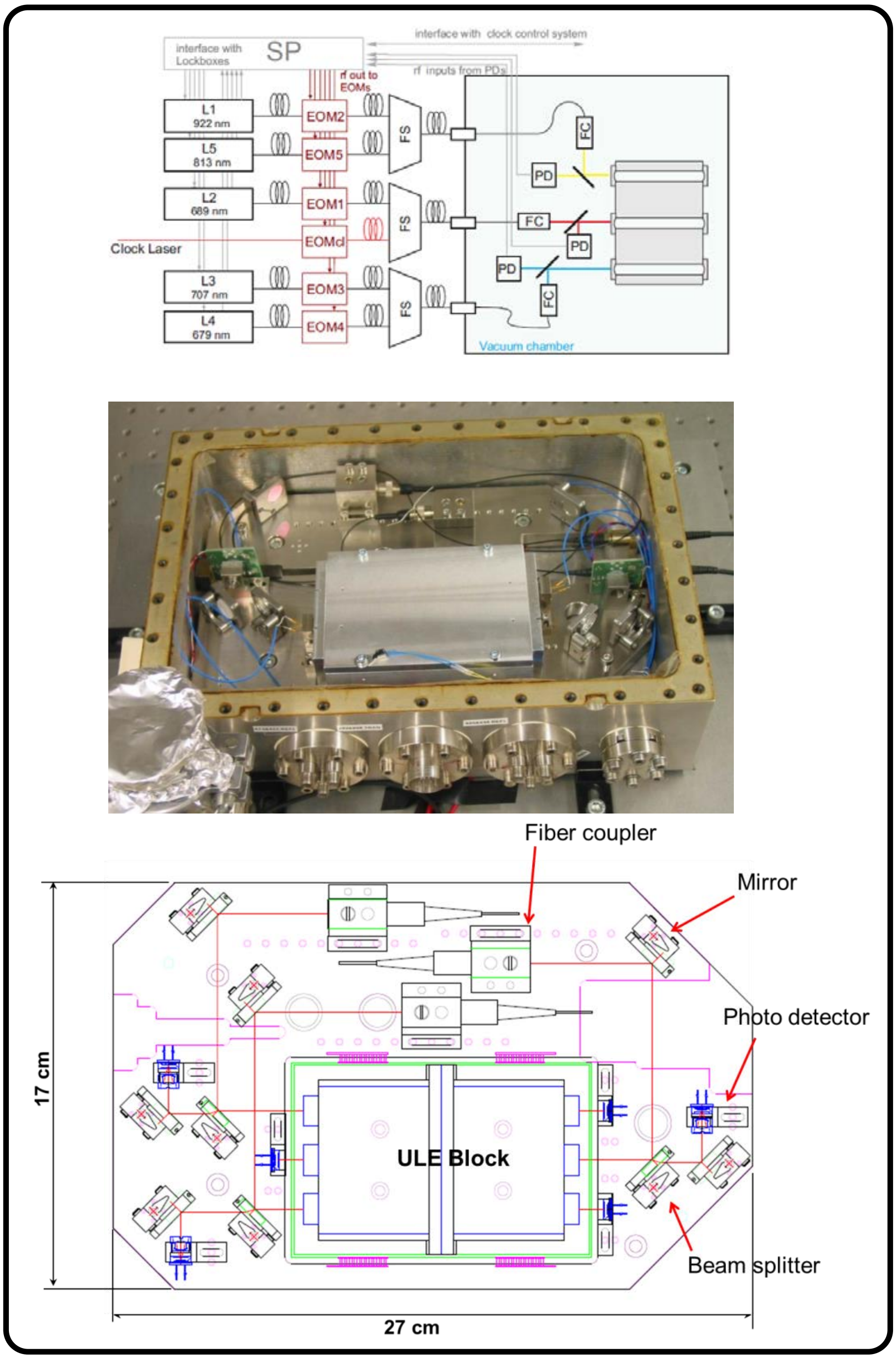

Fig. 5.21 Top: Schematic of the frequency stabilisation system (FSS) breadboard and electronics. Middle: Photograph of the FSS before evacuation. Bottom: Schematic of the optics used in the FSS. [104]

The 698 nm clock laser can be used to compensate for any drift introduced upon the stabilised lasers by small changes in the length of the cavities caused by temperature fluctuations or cavity tilt. This is done by delivering a portion of the clock laser light to the FSS on the same cavity as the 689 nm laser. The electronics which control the offset frequency of each of the lasers is then switched from manual to computer controlled. After calibration, the computer program then finds the offset frequency for which the transmission of the clock laser through the cavity is maximal and alters the other three lasers should the offset frequency for the clock laser drift. Detailed analysis has been performed upon the cavities inside the FSS and the relationship between the drift on the central cavity and the other cavities is known and in-built to the drift compensation routine.

The four laser frequencies are delivered via fibres, pass through electro-optic modulators (EOMs) and delivered to the cavities through vacuum fibre feedthrough ports. Each EOM is driven separately with an FM microwave signal.

The cavity with the highest finesse is placed centrally in the FSS for enhanced stability and is dedicated to the stabilisation of the 689 nm radiation. The light reflected from this cavity is detected on a photodiode, and the error signal produced from this signal is used by the locking electronics. One feedback servo is used to lock each of the three lasers.

This piece of equipment was realised and tested at HHUD and was pre-tested by being integrated into the pre-existing setup at UNIFI using the SOC2 lasers before finally being shipped to Birmingham. There I integrated all of the lasers and FSS into the SOC2 atomics package before moving the entire clock apparatus to PTB in Germany for clock comparisons. The ULE block was produced by AT Films and was realised as a cavity and tested initially by NPL. The mirrors have a radius of curvature of 500 mm and each cavity has a length of 100 mm. The finesse of each cavity is slightly different and this can be seen in table 5.3.

Cavity	Wavelength (nm)	Finesse	Beam waist (mm)	Beam size on mirrors (mm)
1	813	1,500	0.197	0.207
1	922	1,500	0.209	0.221
2	689	10,000	0.181	0.191
2	698	10,000	–	–

Table 5.3 Table listing the finesse of each ULE cavity with the corresponding beam size at both the waist of each beam and at the mirrors [104].

Precise tuning of the lasers with respect to each atomic transition is achieved by sideband locking the lasers to the cavities using the Pound-Drever-Hall method for laser stabilisation. Each cavity is 10 cm in length and thus has a free spectral range (FSR) of 1.5 GHz. Locking the lasers to their modulation sidebands allows for vast tuning range as the maximum offset frequency to which the laser can be locked from the carrier is 800 MHz. Therefore, the entire span between two subsequent FSR peaks of the cavity can be bridged using the sideband locking technique. This means that no accusto-optic modulators (AOMs) are required to offset the cavity frequency to the frequency at which the laser should be operational - which saves in electrical power consumption and also optical power loss and complexity of the optical breadboards.

A typical signal using double frequency modulation can be seen in figure 4.5. Under normal operation, two frequencies are sent to the EOM are the normal ($\approx$ 10 MHz) PDH modulation frequency ω_{PDH} which is kept constant and is used in the PDH control loop and an additional lock offset frequency ω_{lock} which is used to bridge the gap between the desired operating frequency and the reference cavity frequency ω_{ref}. The spectrum of a laser passing through such a phase modulation can also be seen in figure 4.5.

5.6 Transportable Rack

A major design challenge was to incorporate all components of the apparatus together in one mobile unit. The idea was to design and build a rack in which the lasers could be stowed, on top of which the atomics package could be secured. In this way, all of the electronics cables could be neatly and easily transferred from the electronics rack to the apparatus horizontally, and the optical fibres could be mated with the atomics package vertically, thus ensuring that all of the cables and fibres are robustly and neatly packaged.

In order to keep the apparatus as versatile as possible, I decided to include in the design that each laser was mounted upon it's own shelf which can be completely extended to realign beam paths, change components or replace the laser module for example. The design also takes into account the fact that each laser has different dimensions and weight. Effort was made to ensure that the centre of gravity of the apparatus was as low as possible to ensure that the experiment was more stable. As the apparatus is designed to be transportable, a set of collapsible wheels were fitted upon the base of the apparatus for use during transportation as well as more permanent rubber feet which can be pneumatically pumped to isolate the apparatus from vibrations travelling from the ground to the system.

The total dimensions of the transportable rack are 170 x 100 x 60 cm with a weight of roughly 200 kg. The entire set up can be seen in figure 5.22. The shelves are made from 10 mm thick aluminium which is mounted upon drawer runners from SDS London. They are 600 mm full extension, heavy duty drawer runners and can withstand a weight of up to 50 kg. Each shelf is mounted upon a custom designed frame, the parts for which were ordered from KJN aluminium profile. The frame is constructed from the 45 x 45 profile to maintain robustness at the expense of extra weight and also to house the drawer runners which have a width of 45 mm.

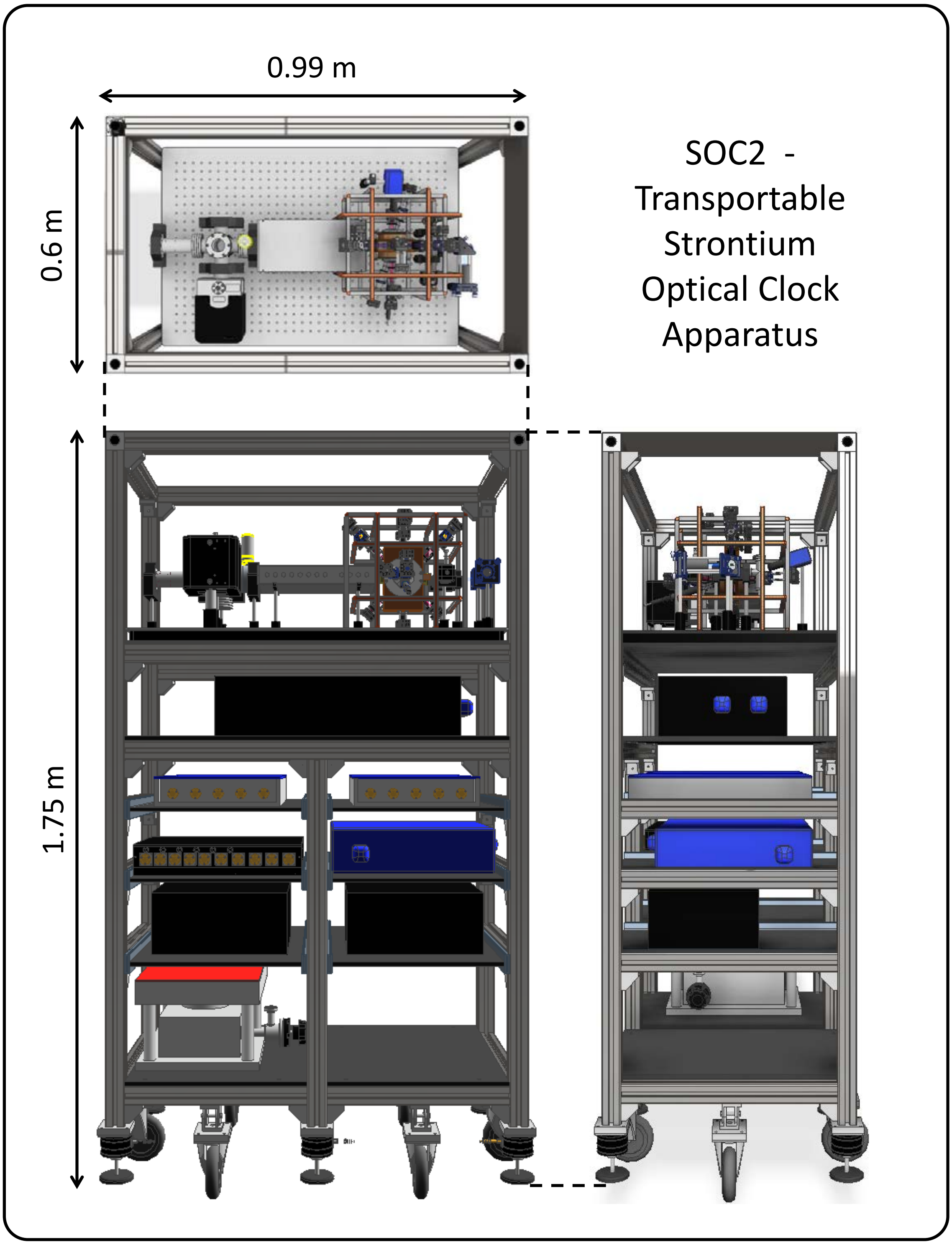

Fig. 5.22 A CAD drawing of the design of the fully transportable rack upon which the atomics breadboard and lasers are housed with dimensions as indicated. Contents of shelves from top to bottom: Atomics package, lattice laser, red cooling laser and stirring laser, blue distribution module and blue laser, repumper lasers, FSS and power supplies.

The atomics package is mounted upon a Thorlabs breadboard of dimensions 900 x 600 mm which is secured to the frame with brackets also purchased from KJN aluminium profile. The total weight of the atomics package without the breadboard and ion pumps is less than 15 kg. This means that a majority of the weight and volume of the total clock apparatus is dominated by the laser breadboards. It is hoped that in the further stages of the project, that the laser modules could be vastly miniaturised and that the apparatus could be housed in a much smaller container such as that achieved by the iSense project [105]. This project was also performed in an EU collaboration like SOC2, with one of the main goals being to miniaturise the electronics and lasers.

Chapter 6

Experimental Method and Results

In this chapter I will present the characterisation of each of the important stages of the development of a transportable optical clock:

- the characterisation of the design of the apparatus compared with that of the proposal [11],
- the characterisation of the new atomic dispenser design,
- the characterisation of the first and second stage MOT using the new compact chamber and miniature telescope designs,
- the characterisation and comparison of the novel second-stage cooling techniques,
- the characterisation of the compact optical lattice trap,
- the results of the spectroscopy of the clock transition,
- the most recent stability measurement of the experiment
- and finally an estimated uncertainty budget for the clock.

This clock is currently the smallest (in both volume and weight) fully functional strontium optical clock and is a vital technological step towards an optical clock in space.

6.1 Volume-Mass-Power budget for SOC2

One of the main aims for this experiment was to demonstrate that optical clocks have the ability to be miniaturised to the extent that they are compact enough to satisfy the payload requirements for a space mission - with an intermediary stage being a transportable clock.

The clock has been realised by the integration of the modular laser systems, the FSS and the atomics package onto a fully adaptable rack. The laser light is delivered to the system via fibres in all cases and the beams are all aligned and shaped using miniature telescopes secured directly to the chamber. The vacuum system is mounted to the optical breadboard and can be fixed into any desired position. The breadboard is then secured to the posts of the rack which can be seen in figure 6.1, underneath which are the shelves for the laser modules. The shelves can be fully opened and each has a layer sorborthane to isolate vibrations from the ground from disturbing the laser stability. The electronics are housed in a single separate electronics rack with the PC and FPGA for computer control of the experiment.

The rack is compact and has dimensions of only 170 x 100 x 60 cm including all of the components with a total weight of 200 kg. The rack components are commercially available and were assembled over the course of a few days. After transportation to PTB, it was found that the vibration isolation of the wheels coupled with the sorborthane sheets was sufficient to isolate all laser systems and the atomics package from vibrations in the lab and the vibrationally isolating pneumatic feet were not required..

The payload budget as outlined in the proposal can be seen in table 6.1 compared with the measured values in 6.2. The final column of the table shows the extent to which the payload was met.

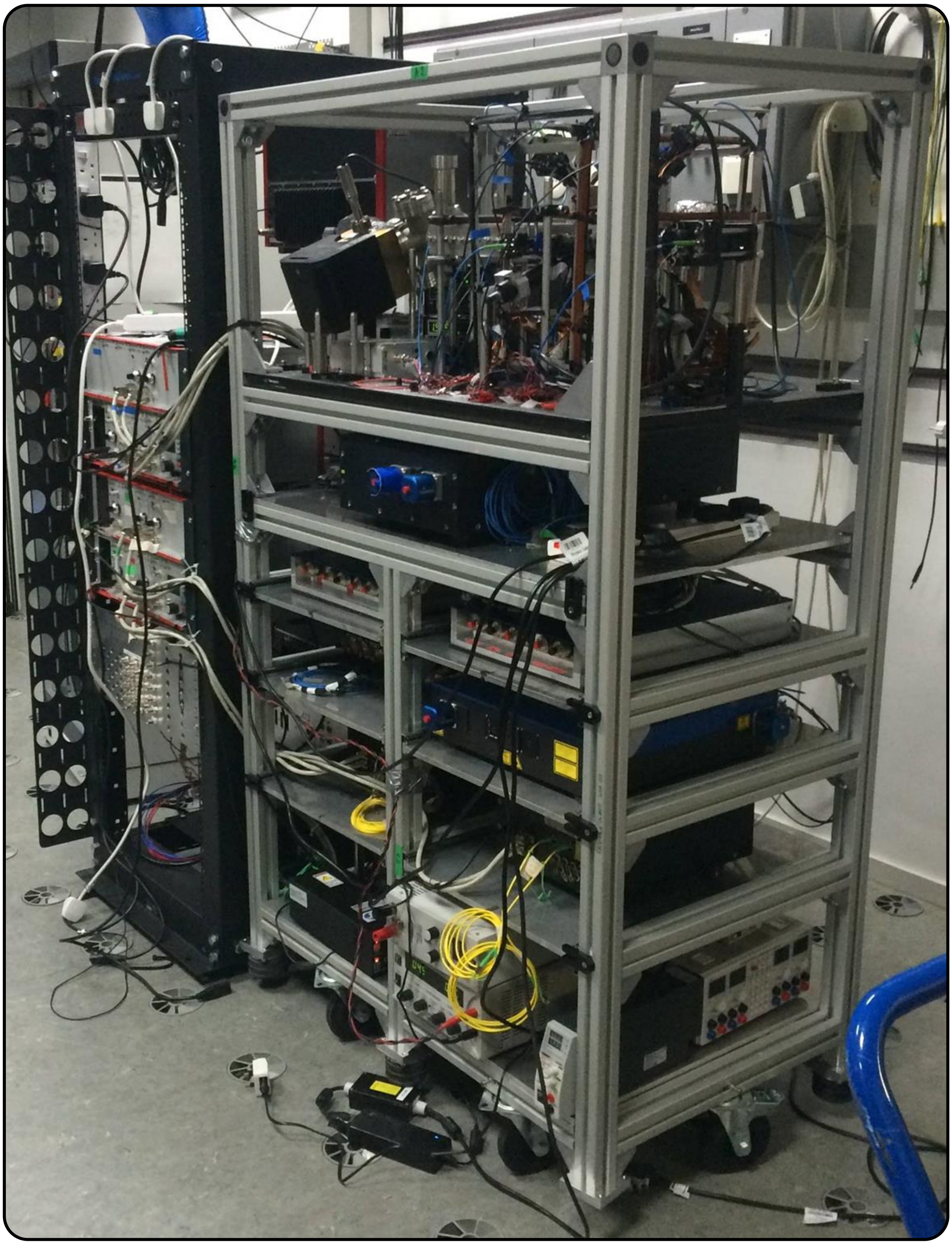

Fig. 6.1 A photograph of the atomics breadboard and SOC2 lasers all housed in the fully transportable rack.

	size (cm)	volume (l)	weight (kg)
461 nm laser	60 x 45 x 10	27	20
FDM	30 x 45 x 10	13.5	12
689 nm laser	60 x 45 x 12	32.4	20
repumpers	30 x 45 x 10	13.5	12
813 nm laser	30 x 45 x 10	13.5	12
698 nm laser	60 x 45 x 12	32.4	20
reference cavity	55 x 55 x 55	166	30
atomics package	80 x 30 x 30	72	30
FSS	-	-	-
electronics	1 x 19 inch rack	-	-

Table 6.1 Proposed volume mass power budget for SOC2.

	size (cm)	volume (l)	weight (kg)	power (W)	met goal?
461 nm laser	40 x 38 x 11	16.72	20	145	yes
FDM	30 x 40 x 8	9.6	5	140	yes
689 nm laser	30 x 45 x 7	9.45	12	62	yes
repumpers	27 x 33 x 15	13.4	15	59	partially
813 nm laser	60 x 32 x 15	28.8	30	93	no
698 nm laser	60 x 45 x 12	32.4	20	unknown.	yes
reference cavity	40 x 40 x 80	int. 5 ext. 128	9	unknown	yes
atomics package	80 x 30 x 30	72	10	32	yes
MOT chamber	13 x 5.1 x 2.2	0.15	0.21	0	n/a
FSS	40 x 40 x 22	35.2	30	153	n/a
electronics	48 x 73 x 175	620	50	unknown	yes

Table 6.2 SOC2 measured volume mass power budget. The atomics package dimensions are measured without the ion pumps, compensation coils and breadboard. With these included, the dimensions increase to 90 x 60 x 40 cm. The reason for not including these is that they can all be easily replaced with smaller versions.

The proposed dimensions of the SOC2 apparatus were estimated from the SOC1 apparatus [61]. The SOC1 apparatus was also branded as transportable but was never housed as such, and the equipment used for this experiment used an entire laboratory. In the proposal nothing was listed for the power consumption of each component and neither was the size of the electronics other than they must fit into one standard 19 inch rack. The next stage for the SOC project will be concerned with reducing the size and power consumption of these electronic components and laser sub-systems.

A majority of the components met with the project proposal goals. The repumpers and lattice lasers both meet the requirements outlined in the proposal without their custom housing. This housing was designed by UNIFI for the inclusion of an AOM and fibre coupling. The housing is robust, but also very large and heavy when compared with the original specifications (See table 6.2). Many of the other components are either exactly to specification or better (in terms of reduction of volume and weight).

6.2 Transportation of SOC2

The apparatus was transported from the University of Birmingham to PTB in Braunschweig, Germany via a standard van (as seen in figure 6.2) with only 15 working days of downtime before the apparatus was achieving the same results as before transportation. The vacuum was maintained during transportation via the use of an uninteruptable power supply (UPS) and a simple DC-DC converter to ensure that the UPS has enough power. The majority of the downtime was caused by realigning fibres which were removed before transportation and fixing technical problems related to the operation of the FPGA.

6.3 Characterisation of the Atomic Oven

I designed a new low-power atomic dispenser based upon the designs by UNIFI and PTB [61] introduced in section 5.1.1. The fully constructed oven can be seen in figure 6.3. The basic SOC2 oven design was found to have a low power consumption of 8.8 W at the highest running parameters of 1.6 A at 5.5 V and would not require any replenishment of strontium for up to a few years of normal operation.

Fig. 6.2 A selection of photographs taken during transportation of the SOC2 clock apparatus through Europe. Left: In the van at Birmingham. Middle: During transportation in the Eurotunnel. Right: After transportation to PTB in Germany.

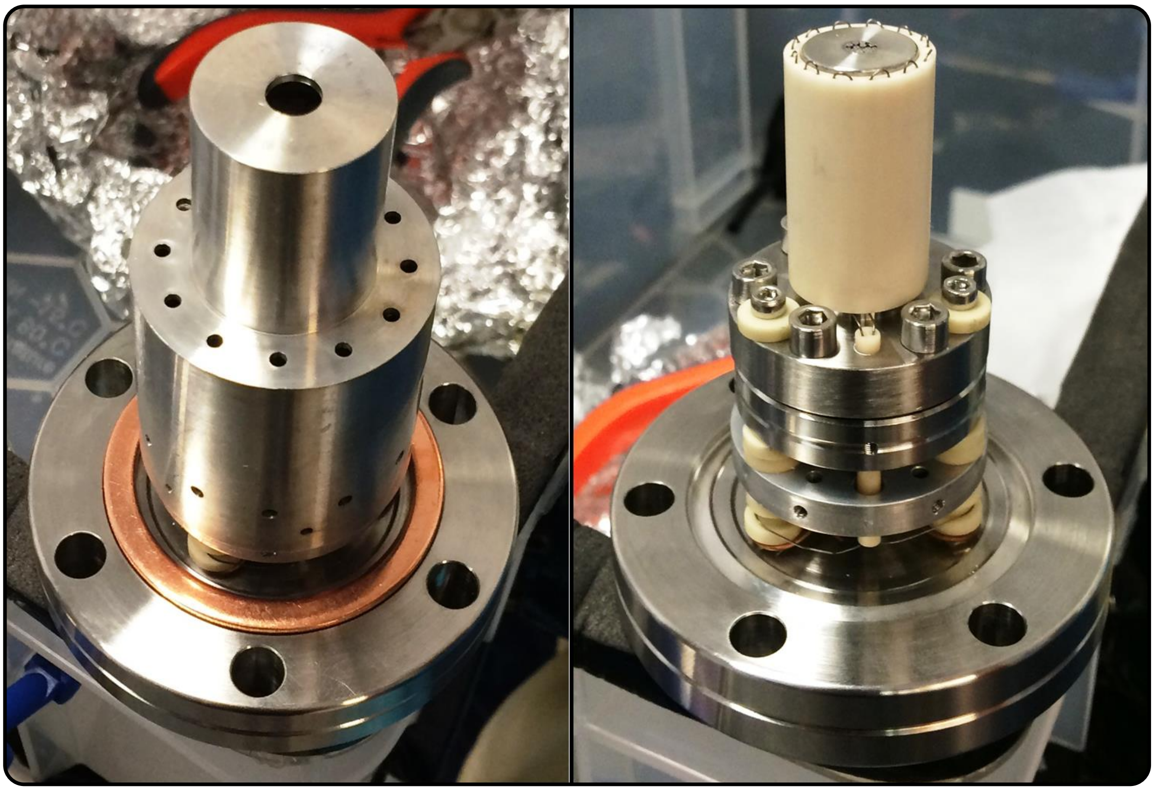

Fig. 6.3 Photographs of the realised low power strontium atomic oven for use in SOC2. Left: with heat shield. Right: without heat shield.

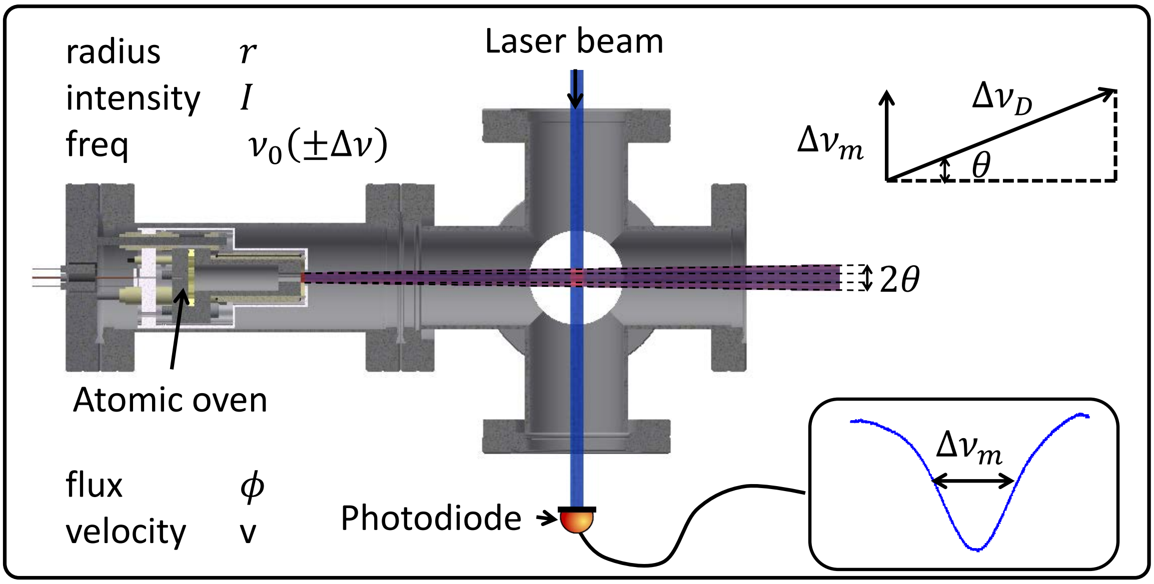

Fig. 6.4 A diagram of the orthogonal crossed beam spectroscopy method used to characterise the atomic beam. Relevant parameters are defined in the diagram.

6.3.1 Theory - Spectroscopy of Strontium

The atomic beam was characterised using a orthogonal crossed beam spectroscopy as seen in figure 6.4. The laser beam is passed perpendicularly through the atomic beam which is exactly on resonance with the transition. The frequency of this laser beam is periodically scanned and the transmission through the atomic beam is recorded on a photodiode. When the photons are on resonance with the atomic transition in the frame of reference of the atoms, one of the atoms in the beam will absorb a photon. This photon is then spontaneously re-emitted in a random direction and a negligible amount of spontaneously emitted photons contribute to the photodiode signal. As the laser is scanning in frequency, different velocity distributions of the atoms in the beam will be excited and therefore the absorption signal as recorded on the photodiode gives an indication of the speed of the atoms in the atomic beam. If the velocity of the atoms is known, this can be used along with the information about the probe laser beam and the atomic transition to estimate the flux of atoms (equation 6.3) and the divergence of the laser beam (equation 6.2).

6.3.2 Atomic beam divergence

It is easy to see with reference to figure 6.4 that the atomic beam divergence can be calculated by measuring the transverse linewidth, $\Delta\nu_m$, of the atomic beam by simple trigonometry if the only contribution to the broadening of the transverse linewidth is due to the transverse velocity components of the atoms. However, the total broadening, $\Delta\nu$, might not be simply due only to Doppler broadening $\Delta\nu_D$ as calculated in equation 3.12, but also the finite measurement time of the interrogation or due to power broadening.

In the specific case of an atom with velocity v being interrogated with a laser beam (with a radius r) perpendicular to its direction of travel there exists another appreciable shift of the energy levels of the atom. This case limits the light-atom interaction time τ which causes a broadening of the observed frequency which is roughly proportional to the inverse of duration of this finite interaction time given by $\Delta\nu_t$.

$$\frac{2r}{v} = \tau \simeq \frac{1}{\Delta\nu_t} \tag{6.1}$$

The extent of the effect of frequency broadening due to the finite interrogation time can be estimated if one considers the most probable velocity of the atoms emitted from the oven which is given by equation 3.9. This value can then be substituted in equation 6.1 to calculate the transit time broadening along with the known size of the interrogation beam to extract the expected value of $\Delta\nu_t$. At a typical oven temperature of 360 °C the mean velocity of the atoms is $420\,\mathrm{ms^{-1}}$ which gives a broadening of 84 kHz which is much smaller than the natural linewidth of the transition, 32 MHz and is therefore negligible.

The beam could also be power broadened $\Delta\nu_p$ if the saturation parameter is much larger than one (see section 3.1). This would manifest in the Lorentzian contribution to the Voigt profile used to describe the spectral line. For a beam power used here of 4 mW with a diameter of 20 mm, the saturation parameter, s is only 0.06, and therefore the power broadening $\Delta nu_p = \Gamma\sqrt{1+s}$ is also negligible.

Doppler broadening is therefore the only broadening mechanism which dominates. Doppler broadening would be evident upon the Gaussian contribution to the Voigt profile used to fit to the spectral line. For an oven temperature of around 360 °C, Doppler broadening is 1.25 GHz which is much larger than the natural linewidth of the transition. As the broadening mechanisms are dominated by Doppler broadening, it can be see that the atomic beam divergence θ can be calculated by,

$$\theta = \arcsin\frac{\Delta\nu_m}{\Delta\nu} \tag{6.2}$$

where $\Delta\nu_m$ is the measured linewidth using the orthogonal interrogation beam (which consists of Doppler broadening due to the transverse components of the atomic beam velocity v) and $\Delta\nu = \Delta\nu_D$ which is the calculated total Doppler broadened linewidth. If there is no atomic beam divergence then $\Delta\nu_m = \Gamma$.

6.3.3 Atomic beam flux

The flux of atoms from the oven can be estimated by considering the amplitude of the signal produced using the same method of orthogonal crossed beam spectroscopy. Atomic flux can be defined as the number of atoms released from the oven per second. The variable being measured during spectroscopy is the number of scattered photons from an incident laser beam upon a detector. In the case of absorption spectroscopy, all scattered photons are detected as a reduction in the power incident upon the detector. Thus, for a given laser beam intensity, one can deduct the number of photons which have been absorbed by the atoms.

If the total measured power of the interrogation laser in the absence of atomic absorption is given by P_{laser} and in the presence of absorption given by P_{abs}, the measured power which is absorbed by the atoms P is given by the difference of these two values. This can be converted into the number of photons present by dividing this by the energy of one photon, $h\nu$.

Because of the finite interrogation time of the laser, this value must then be divided by the transit time τ as defined by equation 6.1, which then gives the number of photons detected per unit time. The number of atoms to which this number of detected photons corresponds can be determined by further dividing this value by the scattering rate of photons for the transition which is being interrogated, Γ_{scat}.

Thus, the amplitude of the signal P is related to the atomic flux ϕ by

$$\phi = \frac{P}{h\nu\Gamma_{scat}\tau} \tag{6.3}$$

This equation is valid under the assumptions that the absorption parameter is low, $s \ll 1$ and the laser beam diameter is large compared with the atomic beam diameter. If little divergence on the atomic beam is assumed then the atomic beam diameter is 8 mm. The diameter of the beam used in the oven characterisation was 20 mm with a power of 4 mW which corresponds to a saturation parameter of 0.06 and an atomic beam of diameter at least 8 mm. This shows that the limits of equation 6.3 are valid in this case.

6.3.4 Oven Evaluation

The main design criterion for the oven was to increase the efficiency of the oven by reducing any losses of energy to the surroundings. Heat transfer by conduction and convection to the atomics package via the vacuum system has been reduced by placing the heating element through thermal insulators and in vacuum. The heat dissipation by radiation has been reduced

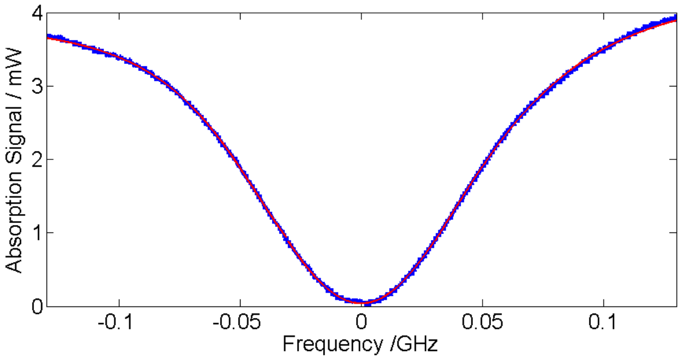

Fig. 6.5 A graph showing the spectroscopy signal obtained using the orthogonal crossed beam spectroscopy method to characterise the atomic beam emitted from the SOC2 strontium oven. Data points are shown in blue with a Voigt fit to the data in red.

by operating the oven inside a heat shield. Under normal conditions in which the oven is operated at 1.2 - 1.4 A the heat dissipation is only 5 - 6.7 W.

The oven was constructed following UHV vacuum cleaning techniques and first tested whilst being connected directly to a turbo molecular pump. The realised oven can be seen in figure 6.3.

The laser beam used to characterise the oven was a collimated 461 nm laser source with no detuning from the atomic transition. The diameter of the beam was 20 mm with a power of 4 mW which corresponds to a saturation parameter of 0.06 and an atomic beam of diameter at least 8 mm. This shows that the limits of equation 6.3 are valid in this case. The characterisation of the oven was performed using absorption spectroscopy whilst scanning the laser frequency. The signal can be seen in figure 6.5. The contribution of the Voigt fit coming from the Gaussian distribution being 30.2± 0.7 MHz and the contribution from the Lorentzian distribution being 35.2± 0.9 MHz - close to the natural linewidth of the transition of 32 MHz. This indicates that the spectral line was broadened by 30 MHz from the divergence of the beam as the Gaussian contribution comes from Doppler broadening in the transverse beam direction. Using equations 6.2 and 6.3 and using the $\Delta\nu_D$ value of

30.2 MHz obtains values of 24± 3 mrad and 7.2± 0.2 × 10^{10} atoms s^{-1} respectively for the atomic beam divergence and flux under normal operating conditions at around 340 °C with a power consumption of 5 W.

The main source of error upon this measurement was the alignment of the probe beam with respect to the atomic beam. For a perfect measurement it must be performed with the laser beam exactly perpendicular to the atomic beam in the same plane. However, it was impossible to ensure this geometrically due to not being able to see the oven once it was placed onto the vacuum system. This could have been improved by ensuring that the measurement was taken with the width of the absorption signal as narrow as possible as this ensures that no additional broadening is occurring from the angle of the interrogation beam. This measurement contributed to a total error of ± 0.7 × 10^{7} atoms s^{-1} to the measurement.

The divergence of the beam was similar to that which was measured in the previous iteration of the design recorded in ref. [61] of 60 mrad. The atomic flux measured here was 7.2± 0.2 × 10^{10} atoms s^{-1}at 340 °C, in ref. [61] the flux at 340 °C was measured to be almost 1 × 10^{11} atoms s^{-1}. The slight difference in both measurements can be attributed to the difference in design. This design uses capillaries with a the same inner diameter but larger outer diameter and a heating sleeve which has a larger number of bores into which the heating element is wound. The results here seem to indicate that having larger outer diameter capillaries (which essentially reduces the area through which the strontium atoms can be emitted) serves to better collimate the beam, which would result in a slightly reduced flux at a similar temperature.

6.4 Experimental Sequence

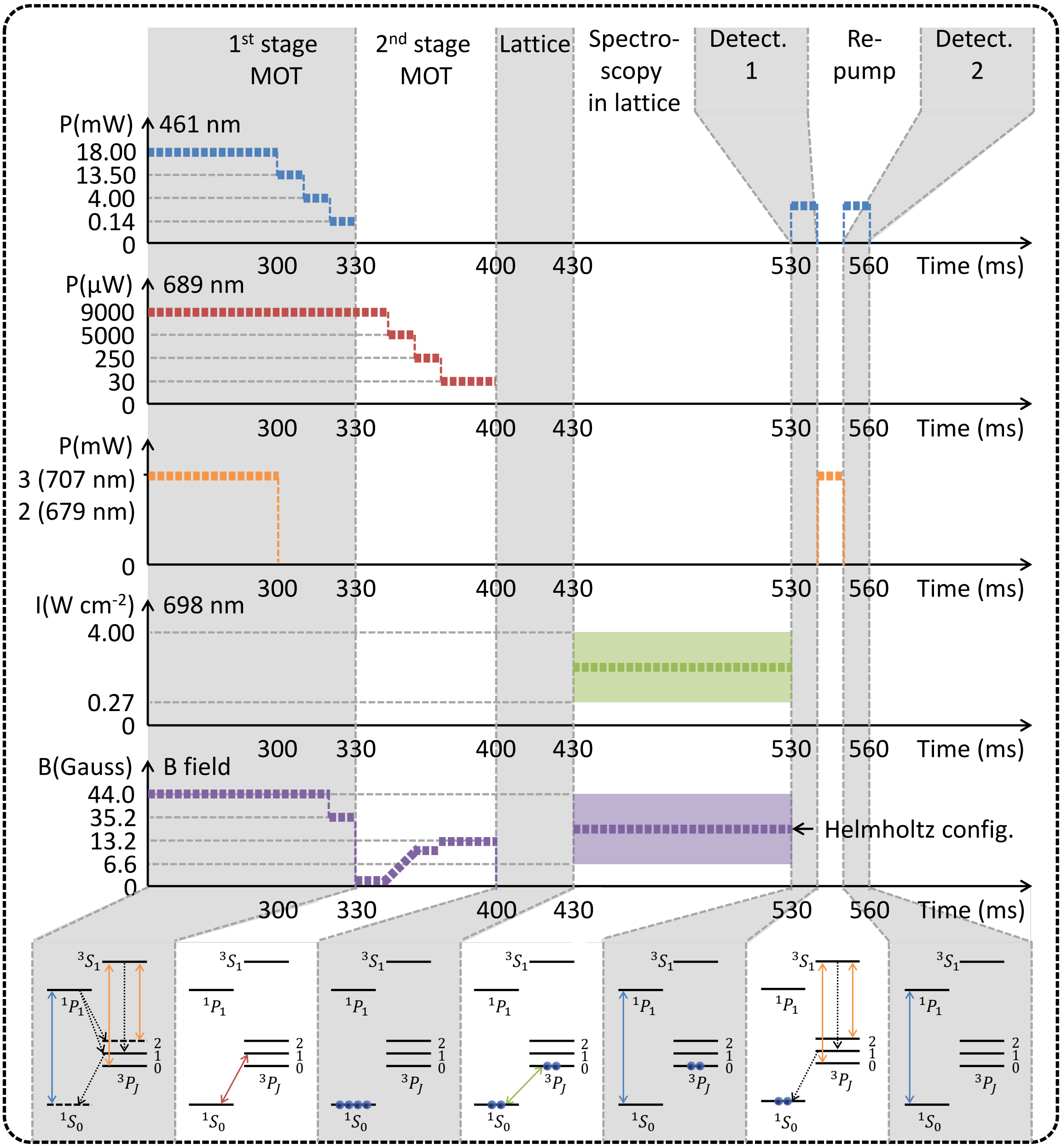

Fig. 6.6 Top: A schematic of the timing sequence for all of the relevant components for the experimental control of the SOC2 clock. Bottom: Diagrams showing the population of each energy level after each stage.

The full sequence for obtaining the spectroscopy signal of the clock transition can be seen in figure 6.6. The sequence was synchronised using the FPGA with digital and analogue triggers which can be placed at any time stamp of the user's preference.

The blue MOT is loaded over 300 ms with the blue MOT beams running a total power of 18 mW at a detuning of -46 MHz, the Zeeman slower at 30 mW at a detuning of -167 MHz, the repumpers at maximum power and the magnetic field gradient at 44 G cm^{-1}. During this stage up to 10^7 atoms are collected in the MOT chamber. The atoms are then cooled over 30 ms by switching off the Zeeman slower, reducing the power in the MOT beams to 0.14 mW and the magnetic field gradient to 35.2 G cm^{-1}. Reducing the power in the MOT beams cools the atomic cloud because the re-absorption of spontaneously emitted photons is reduced. The magnetic field is reduced to increase the trapping volume. This reduces the average temperature by reducing the density of the atoms and thus decreasing the heating caused by reabsorption of spontaneously emitted photons.

The atoms begin to interact with the red beams during the last stage of the blue cooling sequence when the red beams are at a maximum power of 9 mW and a detuning of 800 kHz and the magnetic field is at 35.2 G cm^{-1}. The blue beams are switched off and the magnetic field is switched to 2 G cm^{-1} for 15 ms after 330 ms. The magnetic field gradient is low to ensure that the capture volume for the power broadened red MOT is large. During this stage the red transition in power broadened to cover the velocity distribution of the atoms in the blue MOT. The atoms are then cooled over 55 ms by gradually reducing the power in the red MOT beams to only 30 µW and ramping the magnetic field gradient gradually up to 13.2 G cm. In this case, the reduction of the power in the red MOT beams reduces the effective linewidth of the transition which reduces the average temperature of the atomic cloud and increasing the magnetic field gradient reduced the trapping volume of the MOT and increases the trapping force in order to increase the number of trapped atoms at a low temperature.

From 400 to 430 ms, the magnetic field and trapping beams are turned off and the atoms are trapped into the optical lattice trap. The lattice beam is on for the entire sequence at 300 mW. During this 30 ms, the polarity of the MOT coils is switched to prepare for spectroscopy of the clock transition. The lattice laser is typically run at a power of 170 mW with a waist of 35 µm.

From 430 up to 530 ms the clock laser is on at between 0.27 and 4 Wcm^{-1} and the magnetic field is between 3 and 19.6 mT. Three laser pulses lasting 20 ms are then performed. The first is resonant with the blue MOT transition and removes any atoms from the lattice which are in the ground state. This fluorescence signal is recorded via the PMT. The next laser pulse is the 707 nm repumper to pump the atoms in the clock state to the ground state. The final pulse then records the fluorescence signal of the atoms which were excited to the clock transition.

These signals are recorded by the PMT and analysed via a computer as the experiment is running to show an excitation probability graph.

6.5 First Stage Magneto-Optical Trap Characterisation

The first important stage in the cooling process is the first stage MOT. This is the MOT operating upon the $^1S_0 \rightarrow ^1 P_1$ transition as described in sections 3.1 and 4.2.2. Thermal atoms with an average velocity of 400 ms^{-1} are emitted from an atomic oven. The atomic beam is cooled to an average velocity of 30 ms^{-1} by a counter-propagating laser beam and shaped magnetic field in a process called Zeeman slowing. The atoms are then trapped in the centre of the 3D MOT chamber in a MOT. The first stage MOT uses a magnetic field gradient of 45 G cm^{-1} along the z-axis and three orthogonal, retroreflected, collimated and circularly polarised laser beams with a wavelength of 461 nm are used for trapping (see section 4.2.2 for details).

The Zeeman slowing magnetic field configuration was thoroughly investigated by NPL and the results of which can be seen in reference [71]. However, due to the fact that this Zeeman slower was tested on a different experimental apparatus it was important to characterise and optimise the parameters used for this configuration. For example, NPL found that the maximum increase in atom number using a beam size of 13 mm and an oven temperature of 600 °C was to use a detuning of -540 MHz and a beam power of 70 mW. However, the oven used in this experiment was run at 340 °C and the beam size was 10 mm, therefore, it was not straightforward to analyse and find the optimal parameters for the Zeeman slower. This was particularly important to optimise because the Zeeman slower was found to increase atom number typically by a factor of 30. Therefore, slight deviations from this optimum causes a large variation in trapped atom number and also causes the loss channel Γ_L in equation 6.6 to increase and thus the loading time and lifetime of the MOT to change. This is particularly problematic in terms of the timing of the experimental sequence.

For these reasons, a number of parameters were altered to assess the optimal values for the detuning and power of the Zeeman slowing beam. It is important to note that these values change if the temperature of the oven is altered - therefore it is important to record these values once the oven is at a steady state temperature and also to perform the experiment under those same conditions. The results of this can be seen in figure 6.7. What can be seen here is that the optimal detuning for a typical oven temperature of 340 °C was found to be -404 MHz with a beam power of 30 mW and size of 10 mm. In comparison with the paper from NPL where they measured -540 MHz at 70 mW for an oven temperature of 600 °C and a beam size of 13 mm. The discrepancy here could be easily explained by the lower average velocity of atoms emitted from an atomic oven at 340 °C when compared

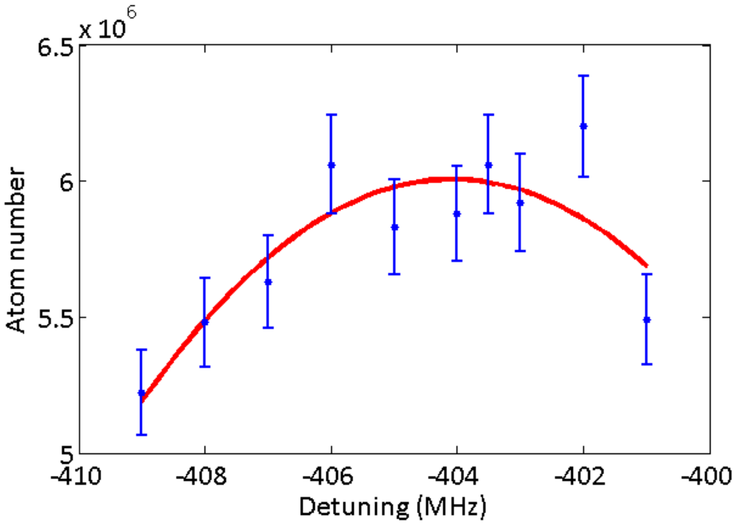

Fig. 6.7 Measurements taken to establish the optimal beam parameters for the Zeeman slowing beam with the magnetic field configuration kept constant. Data points are plotted in blue with a fit to the data in red.

with 600 °C (400 ms^{-1} compared with 500 ms^{-1}). A higher average velocity would require a larger detuning of the slowing beam in order to slow the atoms effectively. Unfortunately, a higher beam power was not available to compare at 70 mW. However, with an 8.5 mm beam, the same beam intensity could be achieved for 30 mW as with 70 mW. It is possible that the focus of the slowing beam that I used was focussed more tightly than the one used at NPL, this would increase the intensity experienced by the atoms and would explain such a discrepancy.

To measure the temperature of the atom cloud, the time-of-flight method was used. This involves switching off the MOT for a set amount of time and then imaging the falling atomic cloud. In this way, one can determine the average velocity of the atoms due to the expansion of the atomic cloud. If the starting radius of the trapped atom cloud is σ_0, the elapsed time is t with the falling cloud radius measured to be σ_t then the average distance moved by the atoms is given by $\sigma_t - \sigma_0 = \mathrm{v}t$ where v is the average velocity of the atoms. The average velocity of the atoms can be found by relating the kinetic energy of the atoms is given by

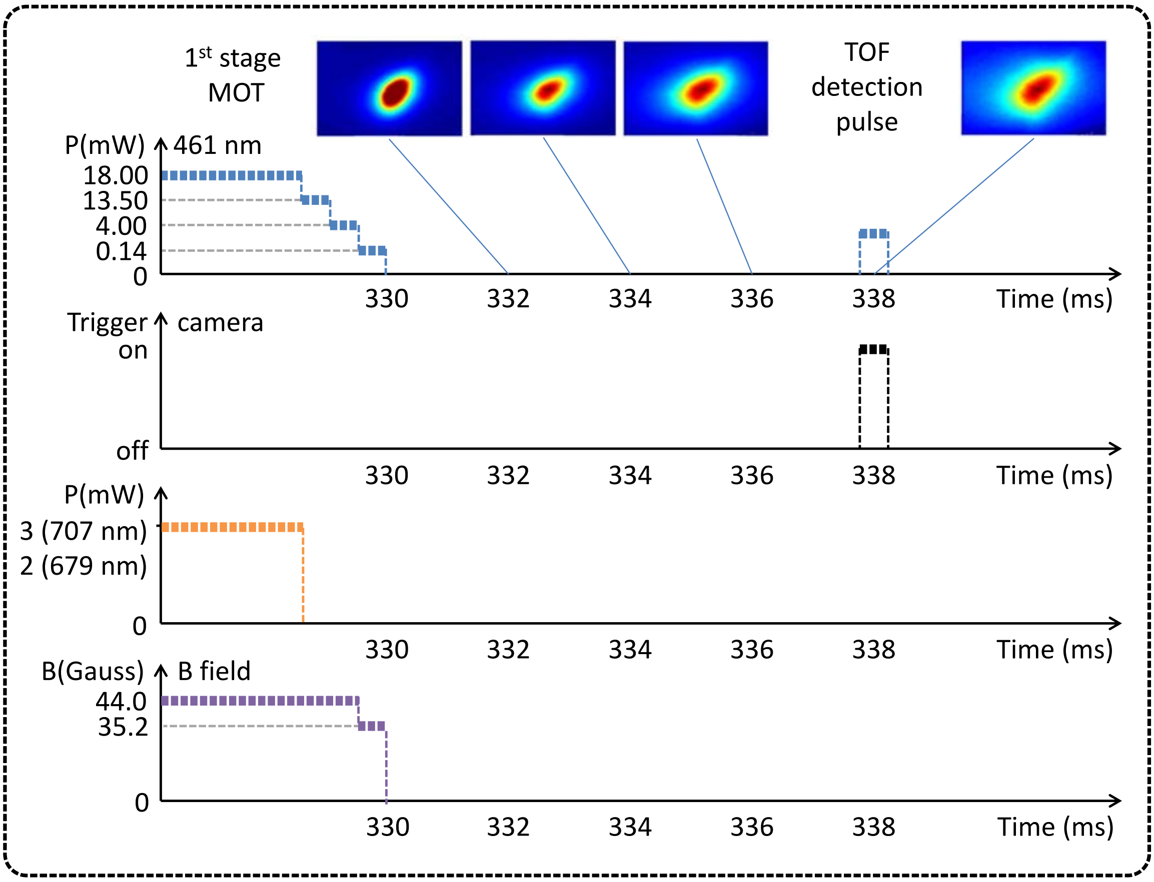

Fig. 6.8 The timing sequence for time-of-flight temperature measurements of the first stage magneto-optical trap with in-situ image of the falling atoms.

$\frac{1}{2}M\mathrm{v}^2$ where M is the mass of each atom to the average thermal energy given by $\frac{3}{2}k_bT$ where k_b is the Boltzmann constant and T is the temperature. This gives $\mathrm{v} = \sqrt{\frac{3k_bT}{M}}$. Therefore, the size of the expanded cloud compared to the initial size is given by

$$\sigma_t = \sigma_0 + \sqrt{\frac{3k_bT}{M}}t \tag{6.4}$$

Using this and varying the time t over which the atomic cloud is allowed to expand gives an estimation of the temperature of the atomic sample. A schematic of the blue loading sequence with in-situ images of the falling atoms can be seen in figure 6.8.

In order to increase the transfer efficiency from blue to red MOT, I decided that I would include a cooling sequence after the MOT had become fully loaded. This involves ramping down the intensity of the MOT beams over 20 ms which serves to decrease the temperature of the atomic sample by reducing the scattering rate within the MOT and thus number of photons which are re-absorbed and can be seen in figure 6.8.

Typically, the blue MOT beams were detuned to -64 MHz and each contains 6 mW of power with a diameter of 10 mm. This corresponds to a capture velocity of 50 ms^{-1} using equation 3.26. Using these parameters, the measured temperature of the blue MOT without the cooling stage was found to be 2.4± 0.2 mK using a time of flight measurement. By carefully choosing the duration of each step change in intensity, a final blue MOT temperature after cooling of 1.2± 0.2 mK has been achieved. The Doppler limited temperature for atoms trapped in a blue MOT with typical beam parameters is 768 µK calculated using equation 3.21. It is worth noting that this temperature relates to the temperature of the blue MOT without the red MOT beams on. The temperature of the composite blue / red MOT is found to be 460± 30 µK in this case and is discussed further in section 6.6.2. The sequence for the blue MOT cooling phase can be seen in figure 6.8 and can be seen on the left of figure 6.14.

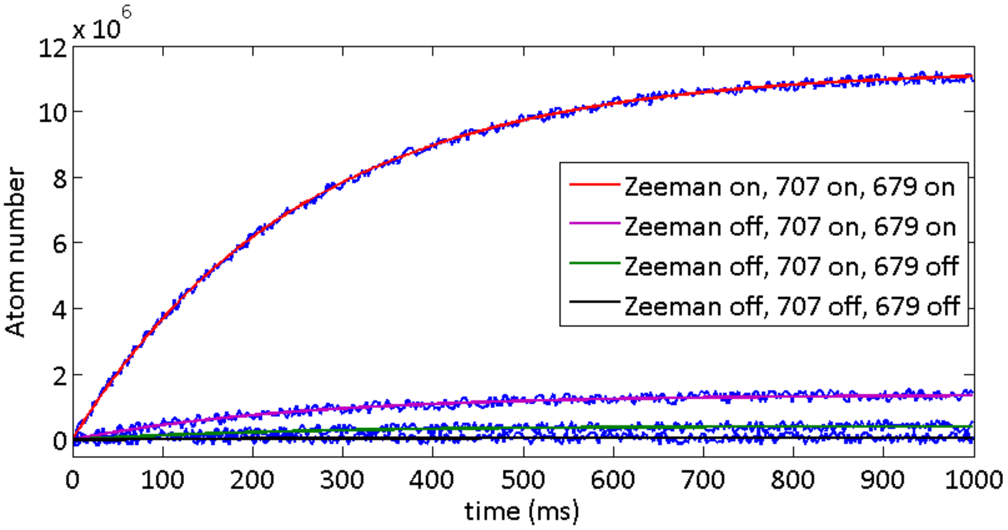

Fig. 6.9 Comparisons between the maximum attainable atom number of the first stage magneto-optical trap under different experimental conditions such as Zeeman slowing on/off and repumper lasers on/off.

This cooling mechanism can be understood by considering the scattering rate for differing intensities of the MOT beams. The scattering rate is proportional to $\frac{s}{1+s}$ where $s = \frac{I}{I_{sat}}$. This means that if the intensity of the MOT beams is decreased then the scattering rate also decreases, it follows then that the number of spontaneously emitted photons is also decreased, and thus the number of re-absorbed spontaneously emitted photons is decreased.

The number of atoms captured in the first stage MOT is dependent upon the successful operation of the Zeeman slower and the repumpers as shown in figure 6.9. The results of which are not unexpected. With reference to figure 4.1 in section 4.1, the $^1S_0 \rightarrow ^1P_1$ transition is only quasi-closed. A majority of the atoms excited to the $^1P_1$ state will not decay to the ground state but to the $^1D_2$ state and then further to either the $^3P_2$ or $^3P_1$ state. The lifetime of the $^3P_1$ state to the $^1S_0$ ground state is 21 µs. Thus these atoms will be excited once more by the 461 nm laser. Those which decayed to the $^3P_2$ state however will not decay to the ground state. This is where the first repumping laser at 707 nm is used. The use of this repumping laser increases the number of trapped atoms by a factor of 6.8 ± 0.7. This excited the atoms in the $^3P_2$ state to the $^3S_1$ state which decays to each of the three ^3P_J states. Those which decay to the $^3P_2$ state are excited once more by the 707 nm laser, the atoms in the $^3S_1$ state decay to the ground state and the atoms decayed to the $^3P_0$ clock state will remain there for the lifetime of the experiment. Without the addition of a second repumping laser, all of the atoms in the MOT would eventually be excited to the clock transition in a method known as electron shelving - the preparation of a sample of atoms in a dark state for later use. Therefore the additional 679 nm ensures that this does not happen. With the addition of both of the repumpers, the number of trapped atoms is increased by a factor of 22 ± 1 compared with the absence of both repumpers, as shown in figure 6.9. With the addition of the Zeeman slower, this number is again typically increased by a factor of 8.2 ± 0.8. This gives a total increase in atom number of 185 ± 20.

It is worth noting that the data was not taken for just the 679 nm laser on. This is because the presence of this repumper laser alone does not increase the atom number. This becomes obvious with reference to figure 4.1. The $^1D_2$ state does not decay to the $^3P_0$ clock state which the 679 nm laser acts upon and therefore without the 707 nm laser, atoms are never found in the clock state.

The blue MOT was typically run to capture $3 \pm 0.2 \times 10^6$ atoms in order to decrease the pressure in the vacuum chamber to increase the lifetime of the lattice trap. However, $4 \pm 0.3 \times 10^7$ can be easily trapped in the blue MOT if a larger atom number is required.

To describe the number of atoms trapped during this cooling stage, one can consider that the number of atoms per unit time (N) would be the captured flux of atoms at the trap position (ϕ_c) minus some losses which occur over time (Γ_L). Written mathematically as:

$$\frac{dN}{dt} = \phi_c - \Gamma_L N \tag{6.5}$$

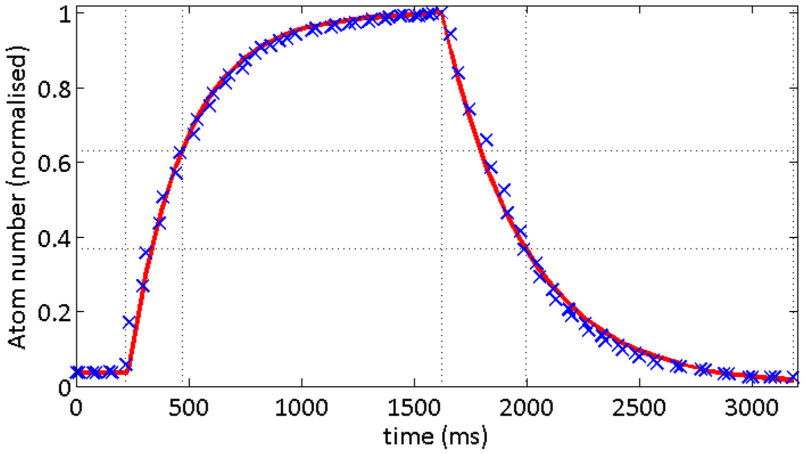

Fig. 6.10 Typical loading and lifetime curves for the first stage magneto-optical trap indicated upon which is the determination of the lifetime of the trap. Data points are shown in blue with a fit to the data in red.

Setting an initial condition of $N(t=0)=0$ gives the solution

$$N(t) = N_{ss}\,(1 - \exp - t/\tau) \tag{6.6}$$

where $N_{ss} = \phi_c/\Gamma_L$ is the steady state number of trapped atoms and $\tau = 1/\Gamma_L$ is the loading or the lifetime of the blue MOT.

The lifetime and loading time of the MOT give values for τ of 250± 5 ms for loading and 374± 5 ms for the lifetime fitting equation 6.6 to the loading curves seen in figure 6.10, the value $N_{ss} = 1 \times 10^7$ was found by detecting the fluorescence of the blue MOT with a camera and verified using a PMT (see section B.1 in appendix B for more details). Using these two values one can obtain a measured value for the captured flux of atoms at the trap position of $\phi_c = N_{ss}/\tau$ which gives $\phi_c = 4 \pm 0.3 \times 10^7$ atoms s^{-1}. As previously measured in section 6.3.3, the atomic flux at the oven was found to be 7.2± 0.2×10^{10} atoms s^{-1} with a divergence of 24± 3 mrad which should correspond to around 0.06 % of atoms being trapped. Most of the atomic flux is therefore untrapped. Even though the divergence of the atomic beam is small, this loss could be due to the small diameter of the MOT beams. It is also possible that the atomic beam does not pass directly through the point at which all of the MOT overlap meaning that these atoms will not interact with the MOT beams and be cooled.

6.6 Second Stage Magneto-Optical Trap Characterisation

The atoms are then further cooled by use of the second stage MOT utilising the ${}^1S_0 \rightarrow {}^3P_1$ transition, the excited state of which is a triplet intercombination line. This transition is well suited to use as a second cooling stage due to the fact that it has a particularly narrow linewidth of 7.6 kHz which corresponds to a Doppler limited temperature of $T_D = 180\,\mathrm{nK}$. The Doppler limited temperature is not, however, the theoretical lower limit of the temperature which can be reached by cooling using this transition; this is limited by half of the photon recoil temperature $T_r/2 = 460\,\mathrm{nK}$ [62] as shown in equation 3.19. The purpose of this work was not to fully investigate the features of cooling upon a narrow transition but relevant theory can be seen in section 4.2.3 and for further reading of the dynamics of narrow line cooling can be found in refs.[60, 63, 64, 72, 106].

Optimal magneto-optical trap parameters for the second cooling stage vary from experiment to experiment. There is some agreement between different cold-atom laboratories and these were used as a starting point for the SOC2 red MOT parameters. A summary of the main parameters from nine strontium optical lattice clocks worldwide is shown in table 6.3.

Two different methods for the first stage red MOT are presented in this thesis which are different to those which have been used historically. These methods are relevant in the consideration of simplifying the trapping processes and minimising the electrical power consumption of the experiment, both of which are of particular importance to transportable clocks.

Group	Frequency Modulation	Detuning	Beam Power	Beam Diameter	B field	BB duration	Frequency Span	Atoms in Blue MOT	Atoms in Red MOT	ref.
UNIFI	25 kHz	−400 kHz	2 mW	5 mm	3 G cm^{-1}	50 ms	800 kHz	10^8	8×10^6	[61]
Torun	-	−540 kHz	2−3.3 mW	-	3−10 G cm^{-1}	-	1 MHz	8×10^8	1.6×10^8	[107]
NPL	50 kHz	-	2.7 mW	-	-	-	4 MHz	10^8	10^7	[108]
Tsinghua	50 kHz	−1.25 MHz	2 mW	10 mm	3−10 G cm^{-1}	60 ms	2.5 MHz	10^8	2×10^7	[74]
Paris	15−40 kHz	−1 MHz	3 mW	-	1−10 G cm^{-1}	-	-	-	40%	[109]
Tokyo	50 kHz	−1.6 MHz	2.2 mW	-	3 G cm^{-1}	20 ms	1.5 MHz	-	20%	[60]
JILA	-	−3 MHz	-	5 mm	3 G cm^{-1}	60 ms	1−5 MHz	10^7	3×10^6	[69]
Innsbruck	20 kHz	−200 kHz – −5 MHz	2.5 mW	3 mm	1−1.15 G cm^{-1}	50 ms	4.8 MHz	-	-	[70]

Table 6.3 Magneto-optical trap parameters from laboratories worldwide used for the second cooling stage in a strontium optical lattice clock.

6.6.1 Lock Modulation Method for Broadening

Three of the lasers used in the cooling and trapping processes for this experiment are stabilised to two cavities housed in the same vacuum chamber. The lattice laser at 813 nm and the master laser for the first cooling stage at 922 nm are stabilised to the same Fabry-Perot cavity using the same output signal. The 689 nm laser is stabilised to the second cavity which can also be used with the 698 nm clock laser to compensate for any drifts in the length of the cavities with a direct feedback to the offset lock frequencies.

The laser is locked to the FSS using double frequency modulation and PDH locking. Applying further modulation to the lock to produce the required spectrum for the broadband red MOT introduces the flexibility that the modulation can be controlled via a computer and easily altered to find optimal parameters. The modulation was applied via a LabVIEW programme which waits for a TTL trigger as sent from the FPGA (used to synchronise the experiment) and sweeps the lock point. The sweep is performed by choosing a step size (Ω_s (Hz)), a step time (t_s (ns)), a start (Ω_-) and an end (Ω_+) frequency (Hz). The latter two frequencies refer to the offset frequency of the lock, Ω_{gap}, and constitute the amplitude, Ω_A, of the sweep $\Omega_A = \Omega_+ - \Omega_-$. All four values form the modulation frequency, $\Omega_b = 1/t_b$, of the sweep, where t_b is the time period of the sweep given by, $t_b = 2\left(\frac{\Omega_A}{\Omega_s}\right) t_s$.

As previously discussed in section 4.2.3, the locking bandwidth was found to be large enough to maintain the laser lock whilst this additional modulation was applied. The lock became unstable if the lock point was modulated at a frequency, Ω_b higher than 80 kHz at an amplitude, Ω_A of 1.5 MHz. It was found manually that the lock was stable if the lock point was manually changed in increments of 2 MHz. Therefore, it can be assumed that the bandwidth of the lock was 80 kHz with reference to the first example of lock instability. This means that the rate of change of the frequency cannot exceed roughly 250 Hzns^{-1}. Due to

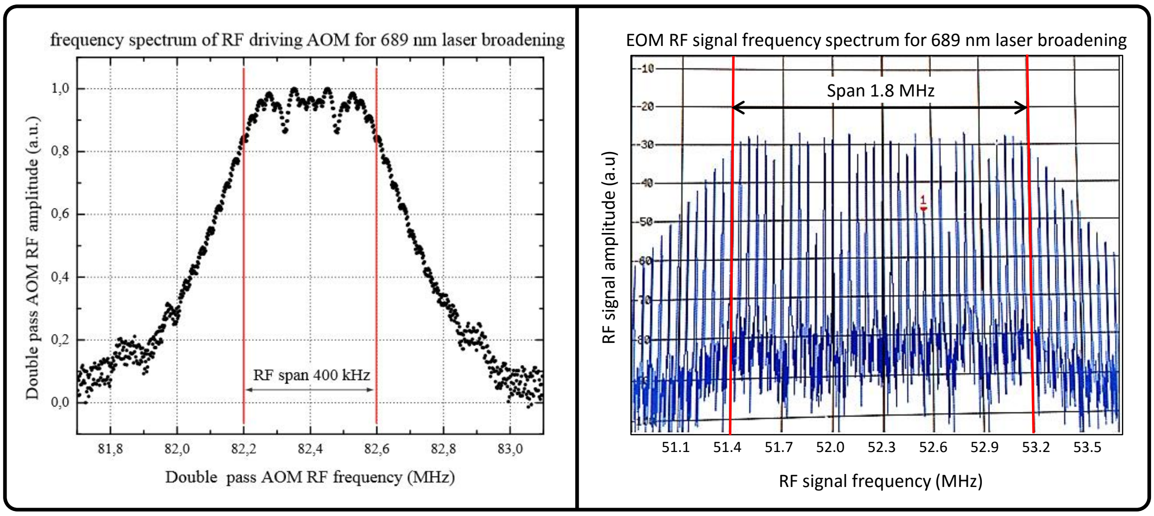

Fig. 6.11 A comparison between the rf modulation signal obtained through the AOM modulation technique (taken from ref. [61]) used for the broadband red MOT and the lock modulation technique introduced in this work.

the fact that the shortest step time t_s in this apparatus was 4 ns, this means that the step size Ω_s cannot be exceed 1 kHz at this step time.

Typically, the modulation amplitude chosen for the broadband stage using the AOM modulation method is between 1 and 5 MHz and the modulation frequency is between 15 and 50 kHz as can be seen in table 6.3. The detuning was typically between -400 and -500 kHz. The intensity for each MOT beam varies but the saturation parameter per sideband is fairly constant at $10I_{sat}$. As the physical system is not dissimilar to all of these experiments, it was expected that the parameters would not differ significantly even when using a different modulation method. To test that the frequency spectrum was also similar to that of the AOM broadening technique and therefore a valid method for the broadband red MOT, I recorded the frequency components which were to be sent to the EOM for locking whilst the modulation was present. In figure 6.11 a comparison can be seen between this data and the rf modulation signal obtained through modulation of an AOM and the mechanisms behind this lineshape for the lock modulation method are shown in figure 4.6 and described in section 4.2.3.

Using this method, I found that the number of atoms which can be cooled is comparable to the AOM modulation method and the temperature is also comparable. With reference to table 6.4 it can be seen that the amount of atoms regularly trapped in the single frequency red MOT in other strontium optical lattice clock experiments is between 10 and 40 % of the atoms in the blue MOT. The transfer efficiency from blue to broadband red MOT is not typically stated in literature, if a conservative estimate of a 50 % transfer efficiency is assumed, this means that using the conventional AOM modulation technique traps 20 to 80% of the trapped atoms from the broadband red MOT to the single frequency red MOT. In the case of using the lock modulation method introduced in this work, the transfer efficiency from blue to broadband red MOT was consistently around 60% with a 90 % transfer efficiency from broadband to single frequency red MOT (discussed later in section 6.6.3). This translates to an overall transfer efficiency of 54% which is a larger transfer efficiency than for the AOM modulation method. A comparison between the broadband modulation method, the power broadening method (the results of which are discussed in section 6.6.2) and the typical values in the AOM modulation method can be seen in table 6.4. This method also provides advantages over the AOM modulation method as no laser power is lost by double passing through an AOM or losing alignment due to the modulation scanning. The modulation can be added with already existing electronics which were used for the locking of the laser and thus no surplus parts are required like a DDS for example. And finally, AOMs require a significant amount of electrical power to operate (normally the single would need to be amplified to around 1 W before the AOM will operate efficiently) and therefore for a space mission, this is not desirable.

Using beams of diameter 10 mm, each with an intensity of 7.6 mWcm^{-2} resonant with the $^3P_1$ transition, the percentage of atoms which could be transferred to the lock modulated broadband red MOT was found to typically be 60 %. A typical loading sequence can be seen in figure 6.12 with various parameters adjusted depending on what would be measured. For

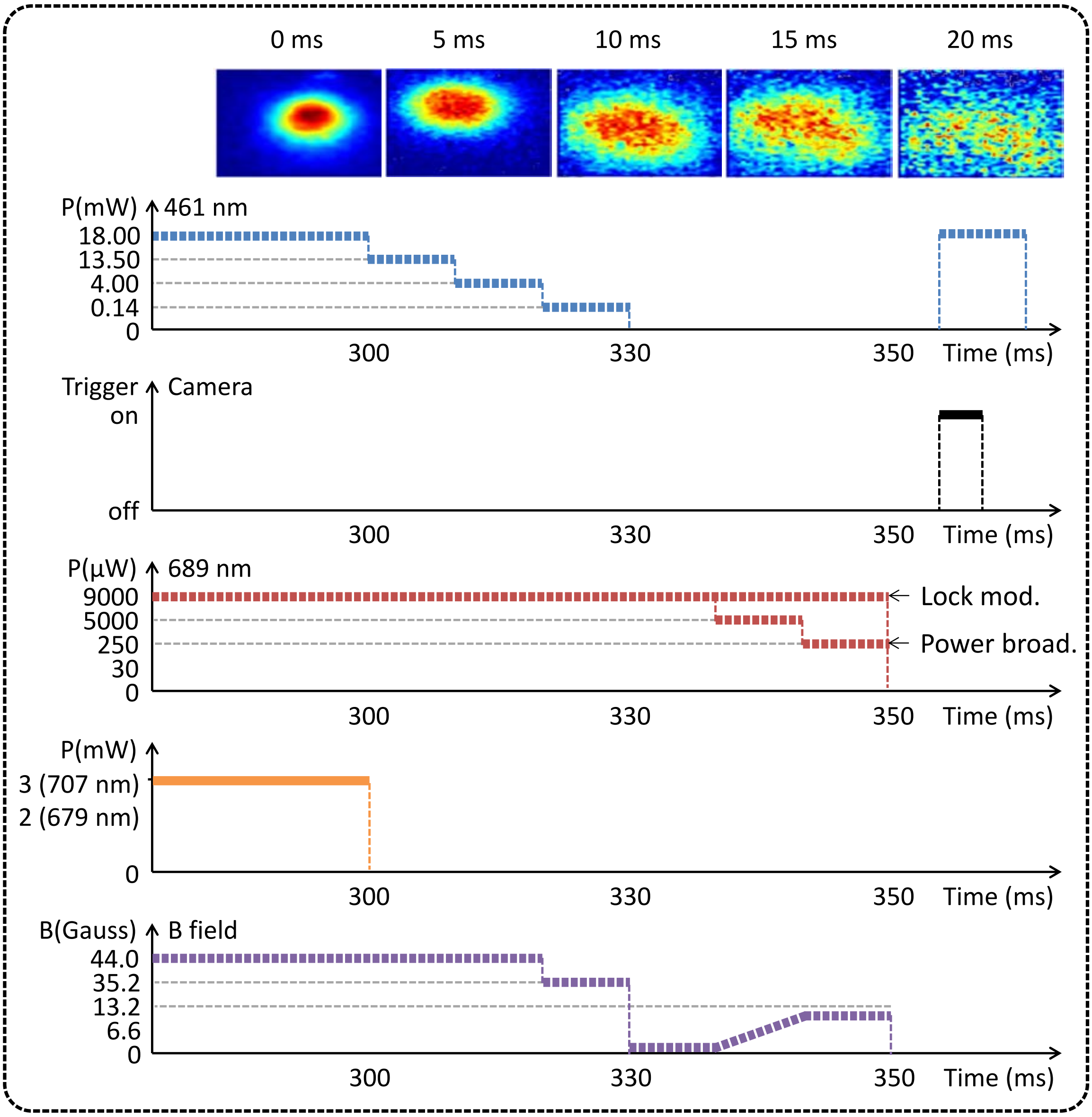

Fig. 6.12 The timing sequence used for the loading and cooling of the broadband red MOT with TOF images of the atomic cloud.

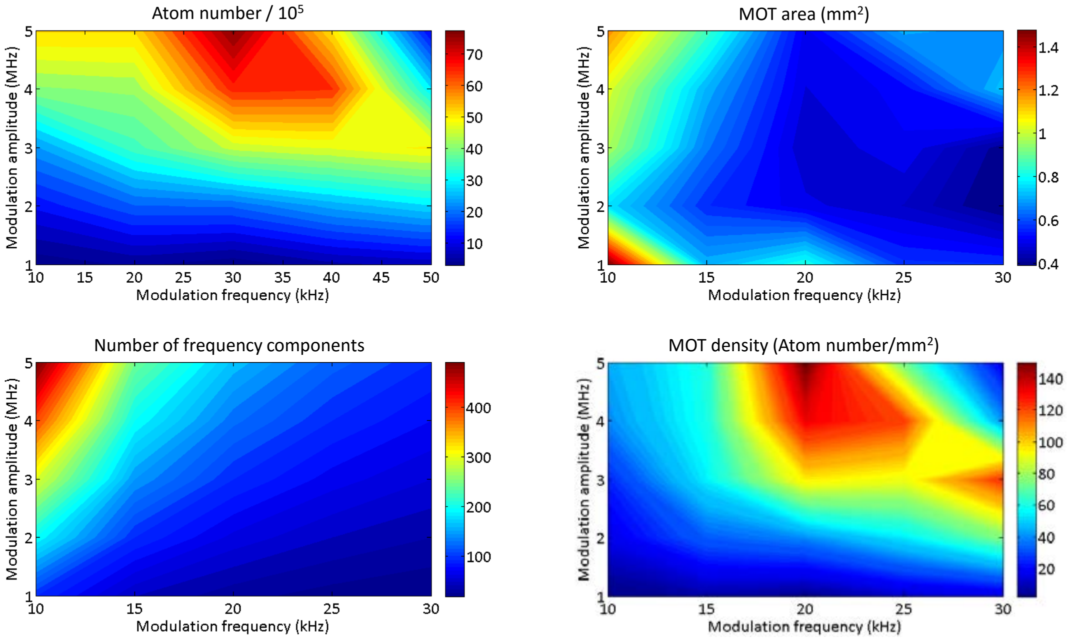

Fig. 6.13 A graph showing the measured optimal modulation parameters for the lock modulation technique. Top left: The atom number in the lock modulated red MOT as a function of the modulation parameters. Bottom left: The number of 'comb' lines produced for as a function of the modulation parameters. Top right: The size of the MOT cloud as a function of the modulation parameters. Bottom right: The density of the MOT cloud as a function of different modulation parameters.

example, to measure the temperature, all beams and magnetic field is switched off for some time t and then the probing beam is switched on for imaging of the cloud using the time of flight method (TOF). The temperature after this stage was found to be $230 \pm 10\,\mu$K and could be minimised to even $150 \pm 10\,\mu$K with loss of atom number. A graph of the optimal parameters can be found in figure 6.13. This shows the effect of changing the modulation amplitude and frequency using this method and the number of atoms which were trapped.

This method was found to be very robust and easy to optimise. The frequency could be swept independently to the experimental control sequence at well defined intervals to find the most optimal parameters as shown in figure 6.13.

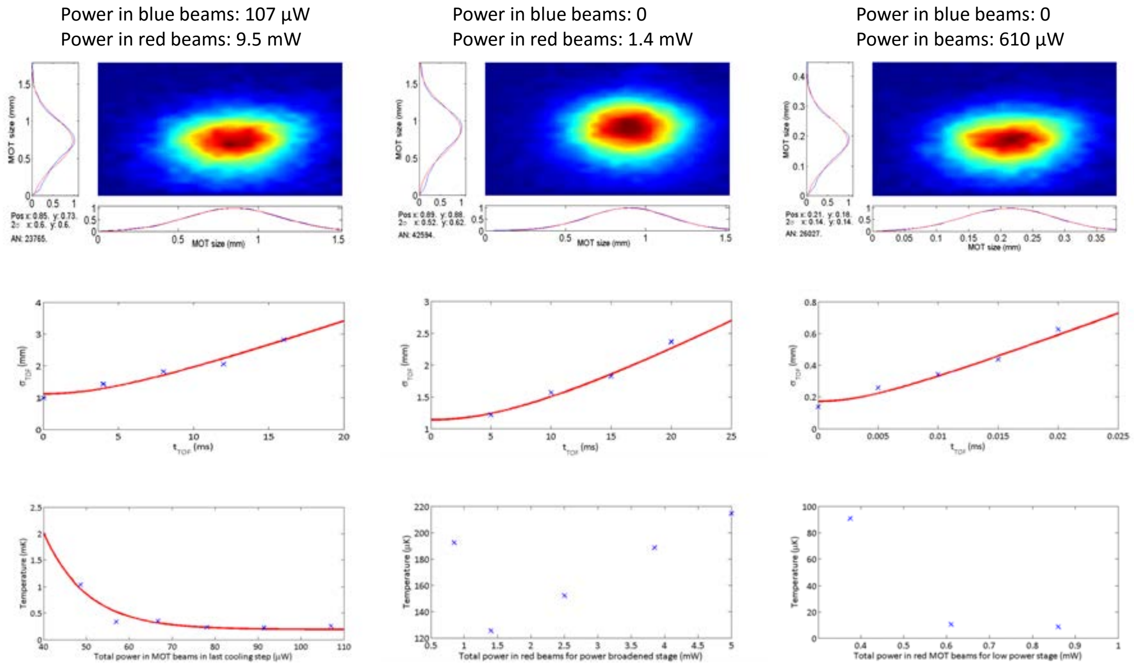
Power in blue beams: 107 µW
Power in red beams: 9.5 mW

Power in blue beams: 0
Power in red beams: 1.4 mW

Power in blue beams: 0
Power in beams: 610 µW

Fig. 6.14 The temperature dependence upon the laser intensity of each stage of the power broadened red MOT sequence. Left: Analysis of the last cooling stage for the blue MOT. Centre: Analysis of the high power stage of the power broadened red MOT. Right: Analysis of the low power stage of the power broadened red MOT. Top: an image of the atom cloud under the conditions stated above. Middle: a graph showing the time-of-flight analysis and fitting for determination of the temperature for the parameters stated above. Bottom: The temperature of the atomic cloud for different beam powers.

6.6.2 Power Broadened Red MOT

In this experiment we have a reasonable maximum power per beam of around 3 mW after optimising the splitting of the laser light in the red laser breadboard outlined in section 5.4.4 which corresponds to a saturation parameter of 1910, where the saturation intensity of the transition is 3 µWcm^{-2}. The power broadened linewidth of the transition with these beam parameters becomes 3.28 MHz.

One of the interesting results of this technique is the lowest temperature achievable at different intensities when compared with the atom number. Of course this follows a trend as one would expect - the higher the intensity, the higher the temperature and the higher the

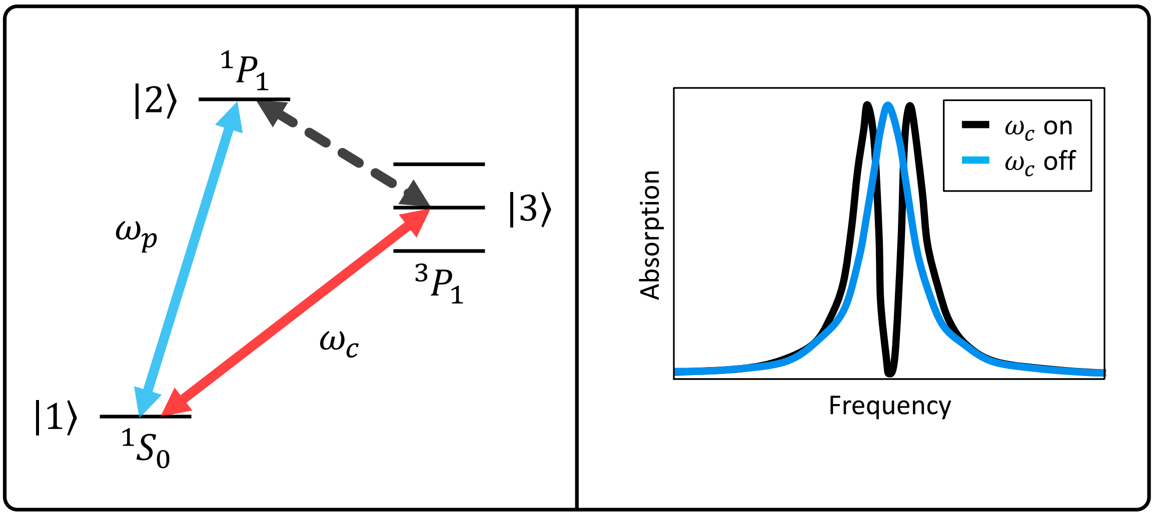

Fig. 6.15 Left: The scheme by which electromagnetically induced spectroscopy is possible using the two cooling stages in strontium. ω_p refers to the probe beam and ω_c is the control beam. The transition in blue is the 461 nm first cooling stage, red is the 689 nm second cooling stage and black is forbidden. Right: a graph of the theoretical absorption as a function of frequency for the probe laser with the coupling laser on and off.

number of atoms captured into the red MOT. This trend can be seen in figure 6.14. However, the atom number in the first stage of the power broadened red MOT also seems to be heavily dependent upon the power of the blue MOT beams and the duration of the last cooling stage of the blue MOT. The atom number in the first cooling stage of the power broadened red MOT fluctuates by 50% when changing the duration of the last cooling stage of the blue MOT by ± 2 ms.

This can be explained as a complication of electromagnetically induced transparency (EIT). An extensive review of EIT can be seen in ref. [110] but can be understood briefly as the phenomenon by which a medium becomes transparent to a particular frequency to which it is normally strongly resonant by introducing resonant light with another transition.

In order for EIT to occur, at 2 of the three transitions must be dipole allowed, and the third must be dipole forbidden.

EIT can be observed when two lasers are tuned to interact with three quantum states, $1, 2, 3$ as shown on the left in figure 6.15. The probe laser must be tuned near resonance and measures the absorption spectrum as shown on the right in figure 6.15. A stronger coupling laser must then be tuned near resonance of another transition. By doing so, the presence of the coupling laser creates a region over which the atoms are transparent to the probe light. This is due to the destructive interference of the transition probability amplitude between the atomic states.

In this case however, the case is not ideal due to the requirement of being in a MOT configuration. Here the presence of the high intensity 689 nm laser light at a saturation parameter of 1910 should cause EIT for the 461 nm light which was observed. With the first stage MOT running, tuning of the red laser light caused the signal for blue MOT fluorescence to fluctuate by up to 10 %. With the frequency of the blue probe light kept fixed, this is the equivalent of switching between the cases where the coupling laser is on and off in the graph in figure 6.15. With the red laser tuned for the correct frequency for the red MOT, the blue MOT signal was reduced by 5 %.

When the atoms are cooled in the blue MOT, the higher velocity atoms will have a higher probability of interacting with the blue MOT beams as they are detuned from the atomic transition. When the red laser light is introduced, this causes the atoms which are on resonance with the blue laser beams to become transparent to the blue light. However, due to the presence of the magnetic field and the high intensity power broadened second stage cooling light, those atoms and the very cool atoms will be cooled further by the second stage cooling light.

When the blue cooling stage is initiated, the intensity of the blue MOT beams are rediced and the heating due to reabsorption of spontaneously emitted photons is reduced. The atoms are then slowly transferred from the blue to the high power red MOT aided by the EIT process. This results in a temperature at the end of the last blue cooling stage of as low as 250 μK due to the interaction of both the weak blue beams and the very high intensity red beams simultaneously.

In general, the transfer efficiency from blue to red MOT is around 80 % using this technique with a lowest temperature at the end of the broadband stage found to be 125± 8 μK with the cooling sequence as shown in figure 6.12. For the first stage of the high intensity red MOT, the intensity of each of the beams is 76 mWcm^{-2} with the magnetic field at 4.4 Gauss cm^{-1}. The magnetic field is ramped to be 12 Gauss cm^{-1} over 15 ms in order to create a tighter trap region which results in an increase in atom number. After this first stage, the beams are switched to a lower intensity of 8 mWcm^{-2}. The second stage lasts for 15 ms before entering into the low intensity (single frequency) regime. In the high intensity regime of the red MOT, the sagging due to the gravitational field is not obvious yet - probably due to the high intensity of the last stage in this regime before transferring into the $s \approx 1$ stage. The diameter of the MOT at the end of the power broadening stage is typically as small as 0.5 mm. An image of the red MOT at this stage, imaged from the side can be seen in figure 6.12 using fluorescence imaging of the 461 nm light.

In conclusion it can be seen that this new method for efficient transfer from a broad line MOT to a narrow line is as valid as the widely used method of broadening by applying modulation to an AOM or to the locking point of a laser stabilised to cavity. A comparison between these methods and the power broadening method can be seen in table 6.4. Where the beam power is the optical power per 10 mm diameter beam, and the atom number is assuming a blue MOT with 10^7 atoms. The advantages of the power broadened method over any other broadening mechanism is that this method uses less electrical power, the laser

	Lock modulation	Power broadening	AOM modulation
Duration	60 ms	20 ms	60 ms
Temperature	230± 10 μK	125± 8 μK	unspec.
Beam power	3 mW	3 mW	2 mW
Atom number	6×10^6	8×10^6	4×10^6
Pros	• No power loss from AOM • Simple	• No power loss from AOM • No additional modulation • Simple • Stable • Quick	• Conventional • Stable
Cons	• Unstable due to electronics • Requires double frequency modulation locking technique • Unconventional	• Requires higher power laser • Unconventional	• Power loss from AOM • High power consumption

Table 6.4 Comparison between the two broadband red MOT techniques investigated in this thesis and the AOM modulation technique.

breadboard is simpler, it is practically simple to optimise and the transfer efficiency from blue to broadband red MOT is larger when operating using the power broadening technique.

6.6.3 Single Frequency red MOT

Using any of the methods employed above, one must then enter the regime of the single frequency red MOT in which the saturation parameter approaches unity. During this stage, the MOT beams are reduced to an intensity of 0.95 mWcm^{-2} with the magnetic field kept at 13.2 Gauss cm^{-1} for a duration of 50 ms. The transfer efficiency from broadband to single frequency MOT is typically around 90 % and the temperature at the end of the red MOT stage is 1.6± 0.2 μK. A fluorescence image taken from above of the final stage red MOT can be seen in figure 6.16 along with the timing sequence for loading. In this image, the effect of gravity cannot be seen as the image was taken from above but the deformity of the shape of the trapped atoms can clearly be seen in figure 6.17 as these images were taken from the side of the vacuum system.

6.6.4 Background Magnetic Field Cancellation

The effect of the external magnetic field during the first stage cooling with the 461 nm laser is negligible due to the strong trapping forces arising from high beam powers, high magnetic field gradients and large linewidth of the trapping transition. During the second stage cooling, the effect of the background magnetic field becomes significant. If the background magnetic field was not compensated for during this stage the efficiency of the trap is severely compromised in terms of the loading time, atom number, lifetime and temperature. This is due to an imbalance of forces arising in the central trapping region. This imbalance of forces results from the background magnetic field shifting the centre of the magnetic field gradient away from the volume over which the MOT beams overlap. Deformities are introduced on the trapping potential from an improperly compensated external magnetic field cause the

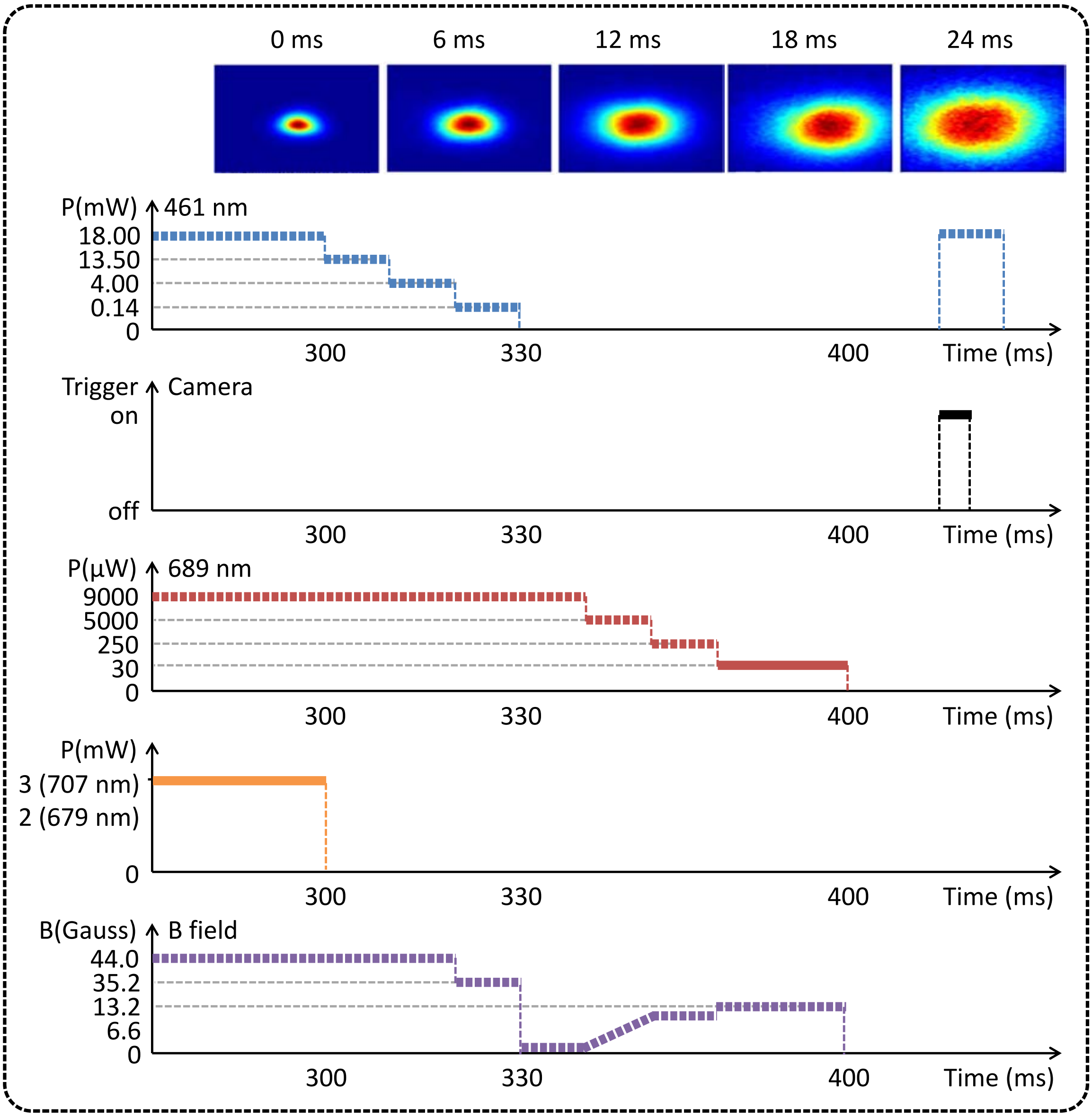

Fig. 6.16 The timing sequence used for the loading and cooling of the single frequency red MOT with TOF images of the atomic cloud.

temperature of the trapped atoms and the lifetime of the trap to be worsened. The background magnetic field is typically compensated for using three sets of Helmholtz coils, one for each axis.

The CCD image of the red MOT was initially used to indicate whether the local magnetic field was compensated. This was done by running the red MOT sequence twice in succession; once with a high magnetic field gradient (13.2 Gauss) and again with a low magnetic field gradient of around 1 Gauss whilst observing the change in MOT position. It is then possible to optimise the signal for a high atom number by changing magnitude of current flowing through each set of compensation coils whilst observing the MOT position and atom number. Once the MOT position does not change from a high magnetic field to a low magnetic field, the shape is generally more spherical and the atom number, temperature and lifetime are improved. This method should be followed by performing a slight realignment of MOT beams to improve the atom number further, and then optimising the current through the compensation coils again until no improvement is found.

During normal operation, the optimal current for each of the coils is 1.3 A in the vertical z direction, 0.5 A in the x direction along the axis of the atomic beam and 0 A in the y direction along the axis of the MOT coils. This corresponds to a background magnetic field of 1.9 gauss with a positive azimuthal angle of 70.4°. As previously stated, the magnetic field of the Earth ranges from only 0.25 G to 0.65 G which means that the dominant background magnetif field was not the Earth but an external background magnetic field source.

6.7 Lattice Trapping

The atoms cooled in the red MOT are then transferred to the optical lattice to ensure a long trapping time with no external magnetic field and one electric field which can be controlled

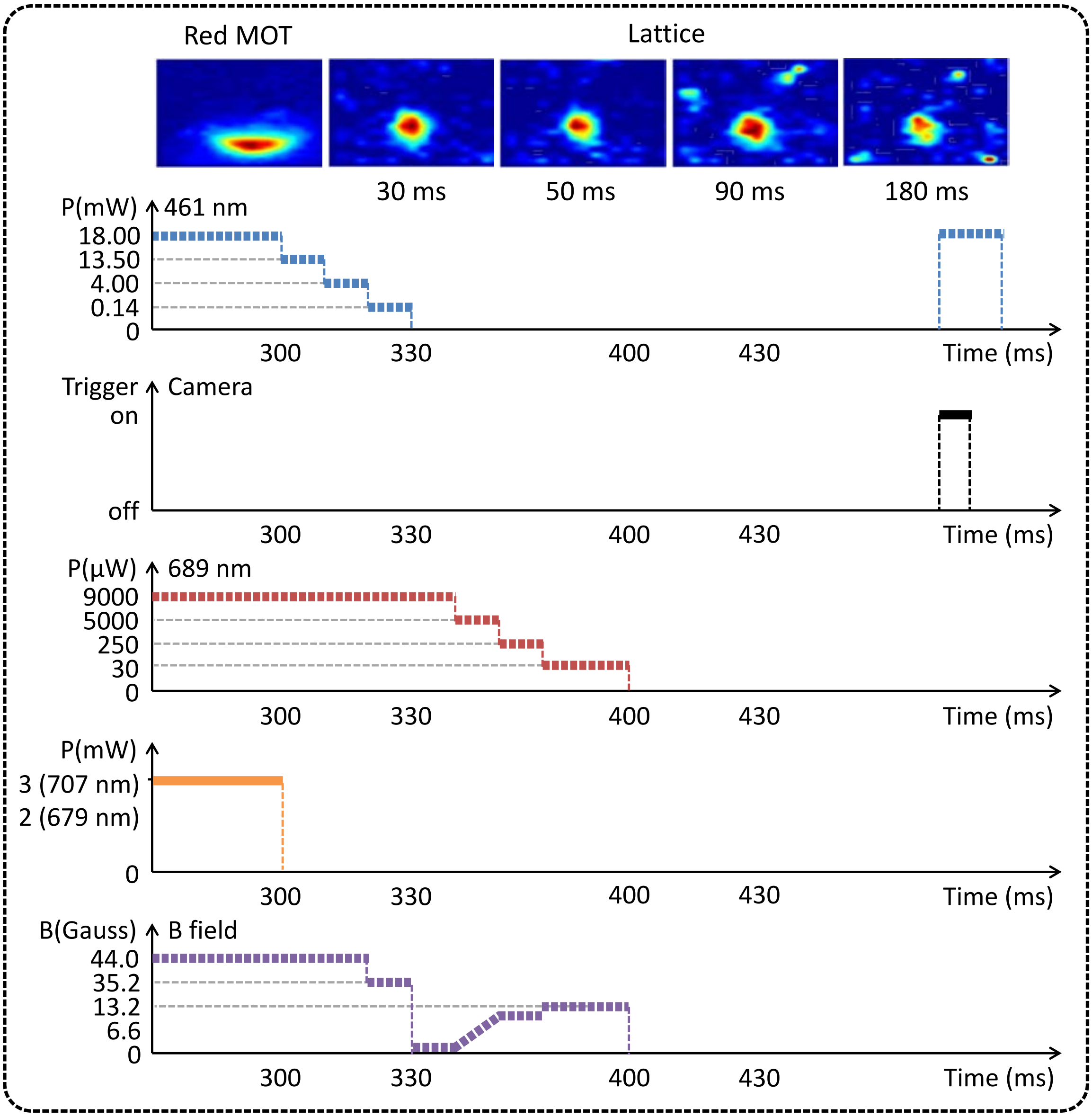

Fig. 6.17 The timing sequence used for the loading and cooling of the 1D lattice trap with an image of the atomic cloud.

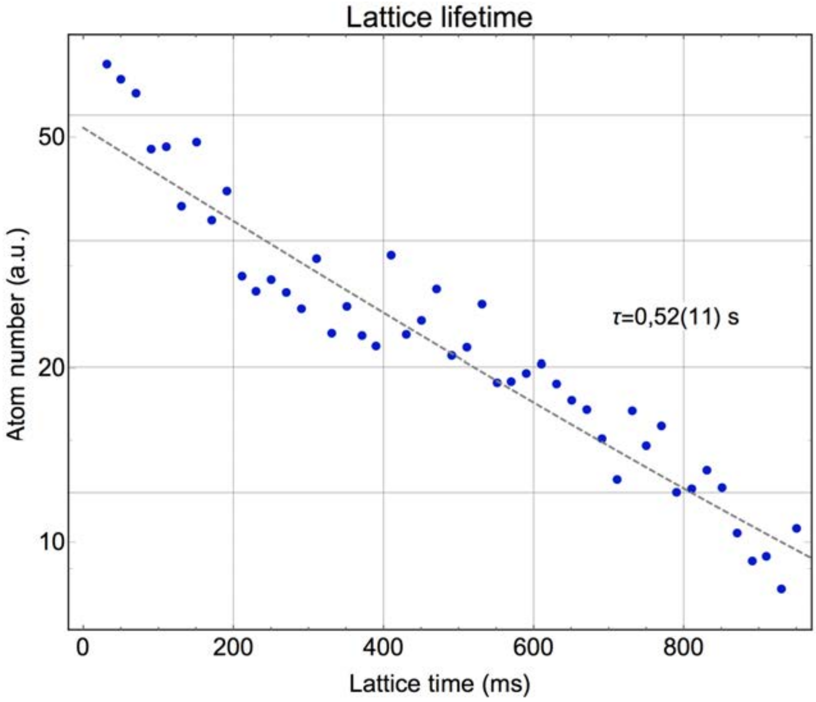

Fig. 6.18 Evaluation of the lifetime of the optical lattice trap in the SOC2 optical clock apparatus.

to ensure that the AC Stark shift upon the clock transition is negated. The optical lattice is operated at 813 nm. The power available in the beam is up to 1.1 W but the experiment is typically performed using 170 mW which is focussed to a waist of 35 µm at the position of the atomic cloud which corresponds to a trap depth of $150E_R$. This beam was then collimated, reflected and refocussed into the same position as the incoming beam to produce a 1D standing wave/optical crystal into the antinodes of which atoms are trapped due to the dipole force arising from the interaction of the electric field with the dipole moment of the atoms.

Using these parameters, the lifetime of the trap was found to be 520 ms which can be seen in figure 6.18. This measurement was performed by recording the trapped atom number at different waiting times using a resonant 461 nm laser beam. The transfer efficiency from red MOT to lattice was typically around 10 % after just 400 ms of loading and cooling. The typical number of atoms trapped in the lattice was more than 1×10^5 and the sequence by

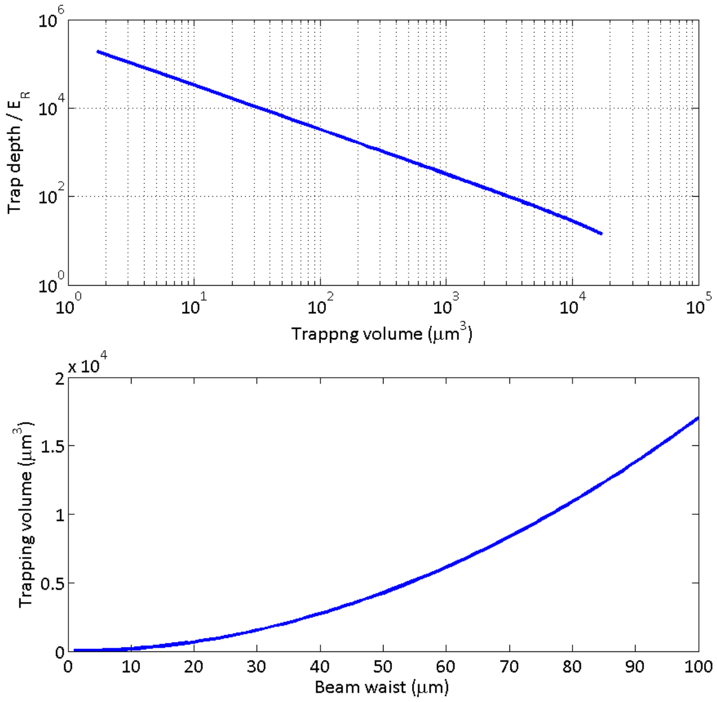

Fig. 6.19 The effect upon the trapping volume upon changing the lattice waist size. Top: The trap depth of the lattice as a function of the trapping volume. Bottom: The trapping volume of the lattice as a function of the beam waist.

which this was achieved can be seen in figure 6.17 with a fluorescence image of the atoms trapped in the lattice. As the lattice beam is always kept on, it is sufficient to load the atoms into the lattice by simply switching off the red MOT beams and the MOT magnetic field.

The trap depth could be easily increased at the expense of a large trapping volume (or vice versa) by reducing the size of the waist of the lattice beam as the trap depth scales as the inverse of the trapping volume. The effect of performing these changes can be seen in figure 6.19 with a power in the lattice beam of 170 mW.

The stability and lifetime of the lattice could be improved via implementation of the atomic beam shutter. However, the method used to control the shutter was a stepper motor controlled via an Arduino and triggered from the FPGA. It was not possible to secure the

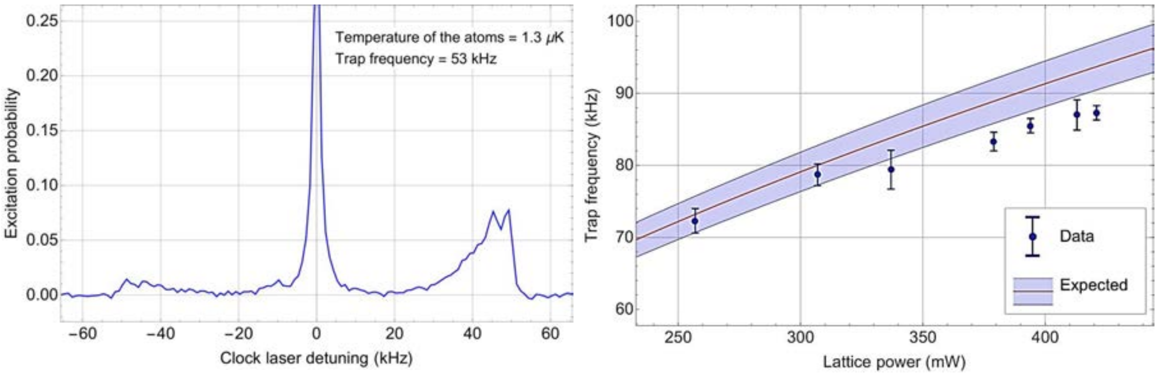

Fig. 6.20 Left: Spectroscopy of the red and blue sidebands to the clock transition. Right: The trap frequency of the optical lattice as a function of the optical power in the lattice beam. The expected values are shown vs the data obtained for different power in the lattice beam.

motor in such a way that the vibrations from opening and closing the atomic beam travelled all along the system. Not only did this cause a larger variation in atom number on average, and cause vibrations upon the alignment of the lattice beam, but also as the vibrational noise was periodic with the experimental sequence, it has the potential to be a large contributor to systematic uncertainty in the system as discussed in section 2.1.1. The improvement in the lifetime of the lattice from shielding the trapped atoms from the atomic beam was roughly negated by the presence of these vibrations. A quieter stepper motor should be used.

The lattice trap frequency was calculated using equation 3.45 and measured as a function of the power in the lattice beam as can be seen in figure 6.20. The trap frequency effects the separation of the blue and red sidebands to the clock spectroscopy peak arising from vibrational levels in the optical lattice (Discussed in section 4.3) and also the value of the polarisability of the clock transition.

6.8 Clock Transition Spectroscopy

The light from the clock laser breadboard is delivered via optical fibre to the atomics package The clock laser light is then overlapped with the lattice laser using the telescope shown in figure 5.11 with a hot mirror which is 99 % reflective at 813 nm and 90 % transmissive at 698 nm. The reflected component is not wasted however, as this can be used for active fibre noise cancellation and as a tool to monitor any vibrations in the system which could induce heating of the atoms during spectroscopy (explained in section 2.1.1). A maximum power of 500 µW of 698 nm light can be delivered to the system from the laser breadboard. The clock laser beam is focussed to 65 µm at the atomic position to give a maximum available laser intensity of 4 Wcm^{-2}.

The laser can be stablised using a number of different external references. The primary reference to which the laser is stablised is the SOC2 compact clock laser cavity with a finesse of 10,000 which is kept under vacuum to a level of around 1×10^{-7} mbar. The stability of the cavity is currently limited by the stability of the vacuum level in the cavity vacuum chamber and thus, other external references have since been explored with the aim to perform preliminary evaluations of the stability of the clock and to perform high resolution spectroscopy of the clock transition whilst the vacuum chamber in which the clock cavity is housed is improved by colleagues at SYRTE. These other references include the use of a large ultra-stable cavity used by PTB called the 'beast'. This locking scheme can be seen in figure 6.21 and the use of this ultra-stable cavity has since enabled the measurement of the clock transition to a 3.6 Hz level.

The sequence followed for performing spectroscopy upon the clock transition is seen in figure 6.6. The atoms are trapped in the lattice for 30 ms before being interrogated with the clock laser. This 30 ms wait ensures that the bias magnetic field for magnetically induced spectroscopy upon the clock transition has completely switched. As discussed in section 4.4,

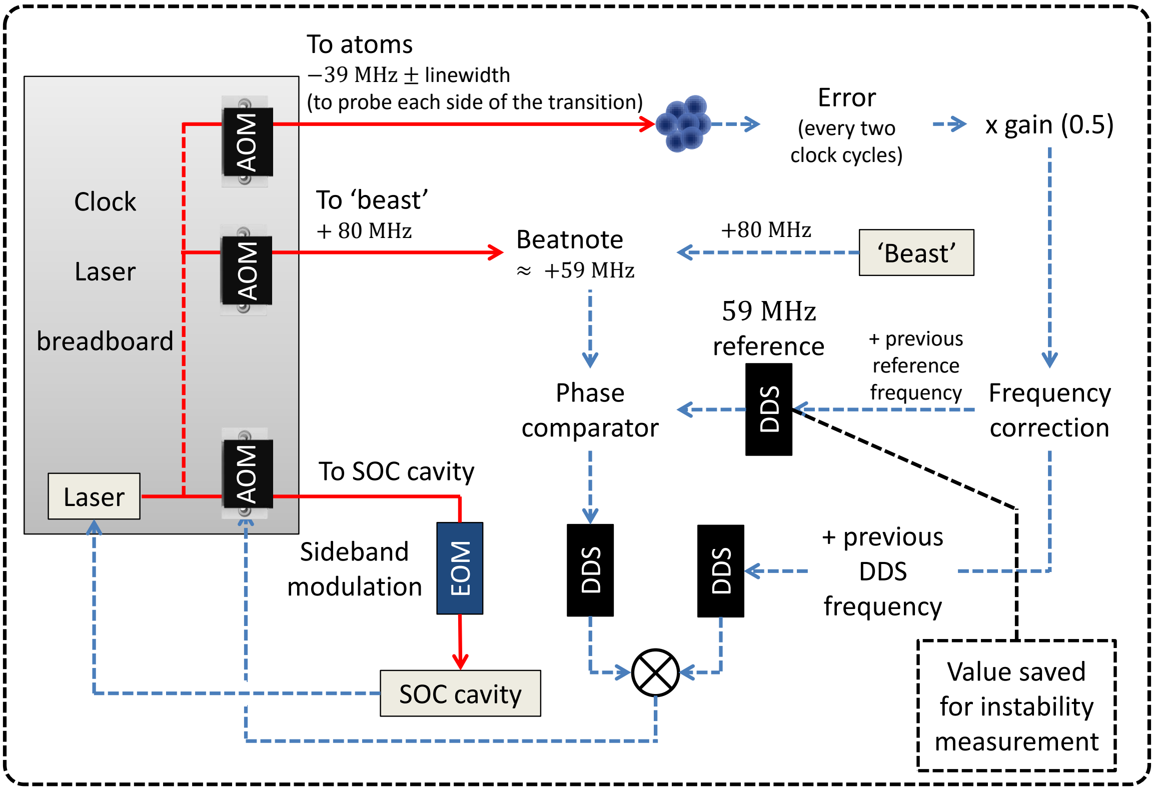

Fig. 6.21 Locking scheme used for external stabilisation of the SOC2 clock laser to the stationary ultra-stable cavity at PTB for preliminary measurements.

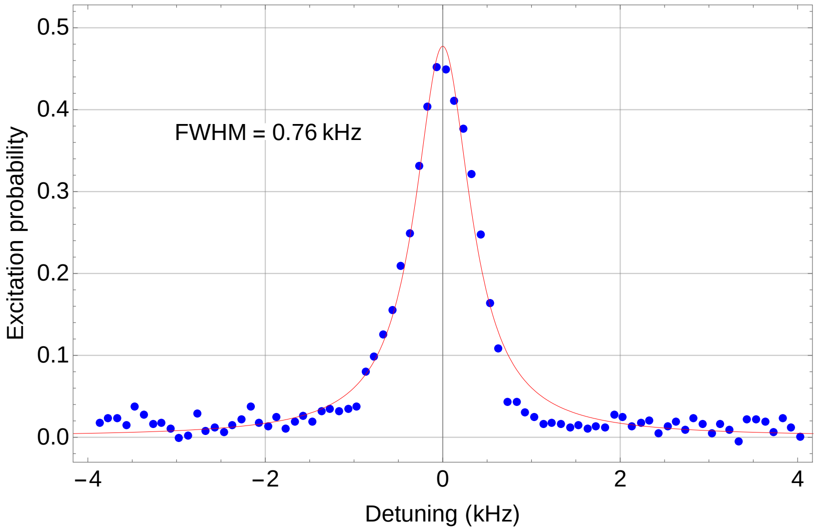

Fig. 6.22 The first clock spectroscopy signal of the SOC2 transportable strontium optical lattice clock. Data is shown in blue with a Lorentzian fit in red.

an external magnetic field is required to perform spectroscopy upon the clock transition in ^{88}Sr. The method used to produce this homogenous magnetic field is discussed in section 5.3.3 and in practice this magnetic field is generated using the same coils which produce the quadrupole field for magneto-optical trapping and can be manipulated via the use of digital and analogue triggers from 2.94 to 19.6 mT. The clock interrogation time used is currently 100 ms with a Rabi frequency of 10 Hz. In order to maximise the excitation probability, the Rabi frequency must be lower and thus the interrogation time longer (see section 4.4 and equation 4.2).

Using a clock laser intensity of 9.98×10^4 mWcm^{-1} and an external homogeneous magnetic field of 20 mT the first spectroscopy signal for the SOC2 transportable strontium optical lattice clock can be seen in figure 6.22. This has a linewidth of 760± 4 Hz with an excitation probability of almost 0.5 and was found to be limited as previously mentioned by the fluctuating vacuum level in SOC2 clock reference cavity chamber. The linewidth of the clock transition has been reduced to 3.6± 0.2 Hz with an excitation probability of almost

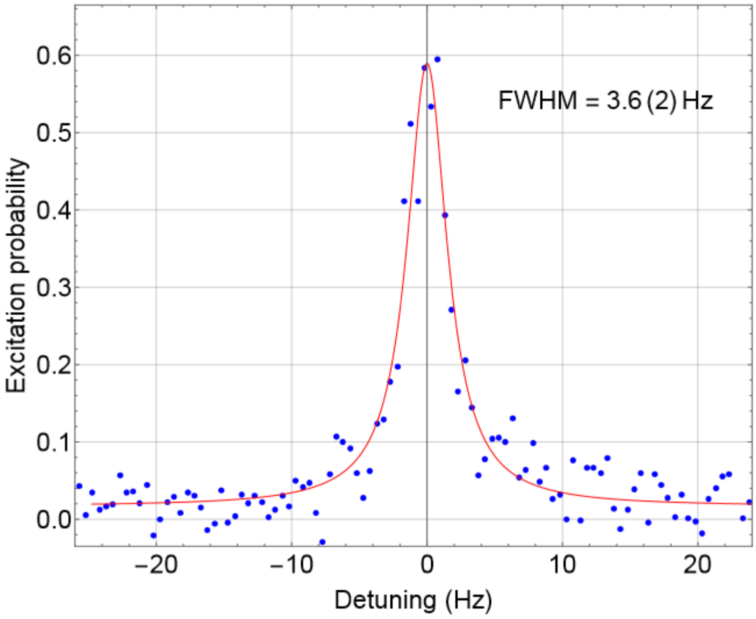

Fig. 6.23 The most recent clock spectroscopy signal of the SOC2 transportable strontium optical lattice clock with a linewidth of 3.6 ± 0.2 Hz. Data is shown in blue with a Lorentzian fit in red. [111]

0.6 with use of the ultra-stable cavity at PTB and can be seen in figure 6.23. This was done using a bias field of 5.9 mT, interrogation time of 230 ms and a probe beam intensity of 249 mWcm^{-2}.

6.9 Stability of the clock

The next step for the optical lattice clock is to lock the clock laser to the clock transition. As the sample rate is around 1 s this requires a very low drift rate of the clock laser with respect to the transition in order to be able to keep the clock laser on resonance with the transition. The stability of the clock is then calculated by performing an Allan deviation calculation (discussed in section 2.1.1) over as long of a time period as possible. The most recent calculation of the instability of the SOC2 clock was found to be 8×10^{-17} at 300 s as can be seen in figure 6.24. This is a remarkable result for a clock using ^{88}Sr and shows great

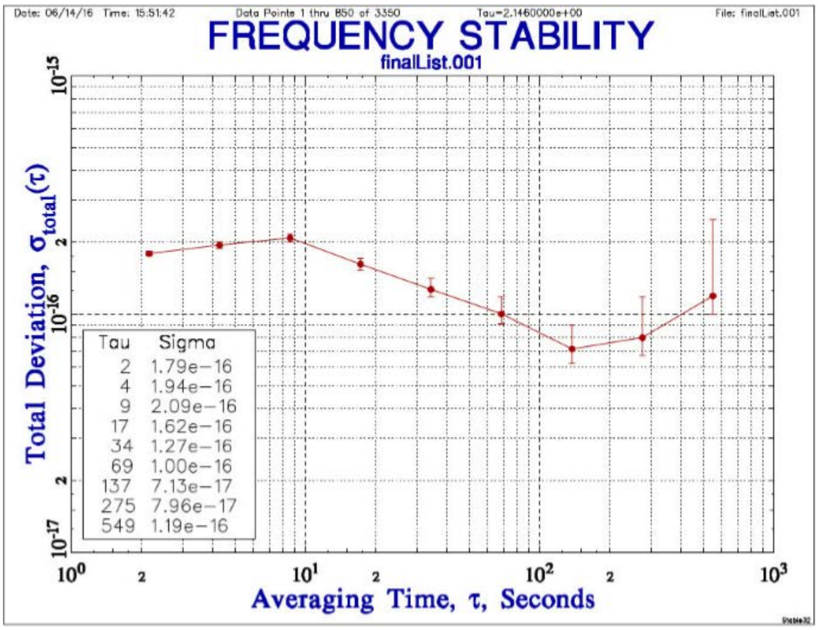

Fig. 6.24 Allan deviation determination of the stability of the SOC2 transportable strontium optical lattice clock. [111]

promise towards the stability goal for the project which was 5.8×10^{-17} within the same averaging time of 300 s.

This result was found through careful consideration of the experimental apparatus as a whole. For example, the reduction in the linewidth of the spectroscopy signal to 3.6 Hz was found by decreasing the magnetic field gradient from 13.5 Gauss cm^{-1} in the single frequency MOT stage to 9 Gauss cm^{-1}. The remarkable stability measurement was found by decreasing the power fluctuations in the clock laser caused by amplitude and polarisation changes and an investigation into the optimal number of atoms in the lattice. The stability was found to be improved with a lower trapped atom number in the optical lattice due to collisional broadening as described in detail in section 4.5. These measurements were performed with less than 10^5 atoms.

Fluctuations in the clock probe beam of just 1 % can cause a shift of 75 mHz upon the clock transition which is the equivalent to a relative shift of 1.3×10^{-16}. Therefore, it is important to keep these fluctuations to a minimum in order to achieve a low instability measurement. A high atom number in the lattice results in a higher signal-to-noise ratio but collisions between atoms cause shifts in the clock transition and broadening [83].

Another important feature for future considerations is the reduction of Blackboady radiation incident upon the atoms. No measurement has been done to try to reduce or evaluate this but it is planned for the coming months. However, all of the results obtained and reported in this thesis have been taken with no active cooling upon the MOT coils. The steady state temperature of the vacuum chamber is stable to 28.2 °C within 0.2 °C after being in operation for a few hours using eight thermistors placed around the chamber. This shows that the design is effective at dissipating the heat generated by the coils to the surroundings without the additional complications of active cooling. This factor is paramount for a transportable clock as ease of use and low complexity along with compact size are key to successfully operating a transportable clock.

6.10 Estimated Clock Uncertainty Budget

A full characterisation of the apparatus has yet to have been performed. However, knowledge has been gained of the performance of all of the components (apart from the atomics package and clock laser with cavity) has been gained through the first iteration of the Space Optical Clocks project [10] which is reported in section 4.5 along with some preliminary measurements of the clock transition and fractional stability of the clock, an estimated clock uncertainty budget can be made as shown in table 6.5.

Contribution	Shift Hz	Uncertainty
Second-order Zeeman	-10	1.0
Clock laser	-10	0.1
Collisions	1.0	0.2
Blackbody radiation	-1.0	0.3
AC Stark (lattice)	-0.5	0.4
TOTAL		2.0

Table 6.5 An estimated uncertainty budget for the strontium SOC2 clock.

Due to the already demonstrated reduction in stability and linewidth compared to the first stage of the Space Optical Clocks project, the estimated uncertainty budget for the second stage clock was based upon a reduced uncertainty budget for that clock with an upper limit being the results shown in table 4.2.

Chapter 7

Conclusions and Outlook

In this chapter I will conclude and summarise the work covered in this thesis by the author and give an overview of future activities which could be pursued for the next round of the project to enable the apparatus to become space-ready and a candidate for operation on board the International Space Station. The realisation of a transportable optical lattice clock is a challenging and vital technological step towards the operation of an optical clock in space which would pave the way for a redefinition of the second and a revolution in technologies dependent on frequency standards such as GNSS and GPS systems.

7.1 Conclusions

The second phase of the Space Optical Clocks project started in 2011, one year before I began my doctoral studies and officially ended at the end of October 2015. The aim of the project was to realise two transportable optical lattice clocks as prototype clocks for a mission on the International Space Station in 2018. One based in ytterbium and one using strontium. The main focus of this work to make a major technological breakthrough in miniaturisation of optical lattice clocks which typically consumed an entire laboratory with complex optics and very large vacuum systems. Even the first stage of the space optical clocks project was classified as transportable [61], however, whilst great strides were made towards miniaturisation during this phase of the project, these clocks would be challenging to physically transport. The clock that I have designed and realised has been transported across Europe in a small van and was unloaded quickly upon arriving at our destination. The realisation of such a system involved departing from the conventional approaches into the unknown in order to firstly meet the objectives within the very strict time frame, and also to make a truly novel system. Despite the project being officially over, the system is still in operation and continues in the so-called 'SOC2+' phase by SOC2 partners.

The result of this Ph.D can be summarised as the design and realisation of the world's most compact transportable optical lattice clock. More specifically: the design, realisation and characterisation of a compact optical clock atomics package; the design, realisation and characterisation of a low-power consumption atomic oven; the integration of all modular laser systems including some modifications to the laser breadboards; the realisation and characterisation of all cooling and trapping stages of the optical lattice clock and some preliminary characterisations of the performance of the apparatus as a clock.

The full atomics package, integrated laser systems and atomic oven have been described in detail in chapter 5 along with important design features and the main features of the laser systems including the compact frequency distribution breadboard for the 461 nm laser light. The atomic oven characterisation is discussed in detail in section 6.3 and was found to have an atomic beam with a divergence of $24 \pm 3\,\mathrm{mrad}$ and a flux of $7.2 \pm 0.2 \times 10^{10}\,\mathrm{atoms\ s^{-1}}$ under normal operating conditions at around 340 °C with a power consumption of 5 W. The low power consumption of the oven is vital for a transportable apparatus and for a space prototype as both scenarios have a limited power source from which to power the experiment. The characterisation of all of the cooling and trapping stages has been shown in sections 6.5, 6.6 and 6.7. The main results of which can be seen in figure 7.1.

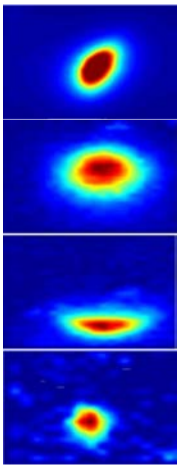

	Atom number	Temperature
Blue MOT	$1 \pm 0.2 \times 10^{7}$	1.2 ± 0.2 mK
BB red MOT (lock mod)	$6 \pm 0.3 \times 10^{6}$	230 ± 10 µK
BB red MOT (p. broad.)	$8 \pm 0.2 \times 10^{6}$	125 ± 8 µK
Single freq. red MOT*	$7 \pm 0.2 \times 10^{6}$	1.6 ± 0.2 µK
Lattice	$1 \pm 0.4 \times 10^{5}$	1.3 ± 0.2 µK

Fig. 7.1 A summary of the main results from the characterisation of the cooling and trapping processes in the clock (images not to scale). BB stands for broadband, lock mod: lock modulation technique, and p. broad: power broadening technique. The asterisk beside the single frequency MTOT means that the data here was taken after the power broadened red MOT stage and not after using the lock modulation method.

The performance of the clock in terms of the characterisation of these cooling and trapping stages is comparable to other stationary optical lattice clocks which are currently leading the race for the most stable and accurate timekeepers showing that the apparatus is well designed and sufficient for purpose. As discussed in sections 6.6 and 4.2.3, the methods employed for the second cooling stage in this work have advantages when compared to conventional cooling methods. The conventional use of the AOM for broadening the first stage of the red MOT has been shown to not be required. This saves electrical and optical power usage from using an extra AOM in the system. Instead, two new methods have been introduced to produce the same broadening effect. The first being the lock modulation method which involves applying a modulation to the lockpoint of the 689 nm laser, and the second being the power broadening method which is much more simple to operate and easy to optimise, the only requirement is that the second stage cooling laser beams have an saturation parameter of almost 2000.

The method, sequence and apparatus involved in performing spectroscopy upon the clock transition has been introduced in sections 4.4 and 6.8 and the first preliminary measurements have been shown, along with the most recent results. The linewidth of the first recorded clock spectral line (with no effort made to reduce the linewidth) was a promising $760 \pm 4\,\mathrm{Hz}$ and the most recent linewidth of $3.6 \pm 0.2\,\mathrm{Hz}$. The lowest preliminary instability measurement has been stated as being 8×10^{-17} which is already close to the aims of the project at 5.8×10^{-17} within an averaging time of only $300\,\mathrm{s}$. The project continues to progress and has aims to perform the first inaccuracy measurement in late 2016. This shows that the design of the apparatus has been more than sufficient for facilitating ultra-precise clock measurements in a compact housing.

The housing for the atomics package and laser systems was introduced in section 5.6 and transportation was described in section 6.2. Whilst this all-in-one rack was not part of the specifications for SOC2, housing the experiment in a neat and compact way would ensure that any future transportation would be hassle free and result in the least amount of downtime of the experiment. Therefore, I designed a sturdy and compact rack with extendible shelves for the housing of the modular laser systems (which can be easily removed and altered if necessary). The rack is mounted upon 6 heavy-duty wheels which can be switched for pneumatic feet once in a stationary position simply by extending down the feet and inflating them with a foot pump. The rack has dimensions of only 170 x 100 x 60 cm including all of the components with the top shelf containing the atomics package with the modular lasers housed beneath.

The improvements in the quality of the clock come from the advanced techniques used for miniaturisation of the apparatus which have removed superfluous complexity. Working, designing and problem solving in such a physically constrained environment facilitates innovative thought for methods and necessary components as space becomes a valuable commodity which is not to be wasted.

7.2 Outlook

Building upon the knowledge gained from the advancements made and outlined in this thesis as well as learning from research made in other research laboratories, there are a number of improvements that could be further made to the system in the short and long term. An overview of the major, long-term improvements can be seen in table 7.2, with the short-term improvements summarised in table 7.1 with explanations for each upgrade listed below each table.

> **Thermal control of the system**: With reference to upgrade number 1, the expected benefits from including a thermal enclosure of the entire system is down to an increase in stability and accuracy of the clock. With the external parts of the clock in a thermal enclosure, the fluctuation in temperature across the system would be minimised. This is beneficial because it means that the temperature at the atomic position can be fixed within a known and controlled margin. Knowledge of the blackbody radiation present at the atomic position can allow for accurate evaluation of systematic uncertainty of the clock frequency. If this blackbody radiation does not fluctuate from shot to shot, this means that the correction would be valid for an entire measurement campaign with a smaller error than if the blackbody radiation was known to fluctuate. The first steps towards this temperature stabilisation have been undertaken and is outlined briefly in section B.3 of the Appendix B.
>
> **Multi-wavelength fibre array**: Using a multi-wavelength fibre array with 3 inputs and 3 outputs, the blue and red trapping light along with the stirring laser light for the trapping of ^{87}Sr could be overlapped and split in the fibres to vastly simplify

Label	Description	Expected benefits	Predicted timescale
1	Thermal control of system	Reduction of black body radiation shifts the clock transition	3 months
2	multi-wavelength fibre array	Reduction in complexity of chamber telescopes and easier alignment	1 month
3	ITO coated chamber windows	Better knowledge and compensation for charge build-up at chamber	3 months
4	In vacuum temperature sensors	Better knowledge of BBR at the atomic position	1 month
5	Pump upgrade	Lighter, more compact system, more efficient pumping	2 months
6	Oven upgrade	After smaller vacuum system upgrade, miniaturise the oven further	2 months
7	Vacuum system upgrade	After smaller pumps are sourced, smaller vacuum system is possible	2 months
8	FPGA upgrade	More efficient and versatile program, user-friendly interface	4 months
9	Autonomous, remote operation	Experiment can be controlled remotely	4 months
10	Rearrangement of rack	Inclusion of clock laser and cavity to transportable setup	1 month
11	Blue distribution board upgrade	More compact efficient laser frequency distribution	1 month
12	FSS upgrade	Inclusion of repumper stabilisation and improved vacuum level	3 months

Table 7.1 Short term improvement suggestions for the outlook of the SOC2 project.

the telescope design with the only requirement being a dichroic collimating lens and dichroic quarter waveplate. The added benefit here from a technical point of view is that the red beams will be aligned by definition after optimisation of the blue MOT. In addition, the inclusion of the stirring laser could be done by using a 3 to 3 fibre splitter.

The next five upgrades involve changes in the vacuum system. Such upgrades can be time consuming and it is often beneficial to perform as many upgrades as possible at the same time to reduce the downtime of the experiment and the exposure of the inner surfaces of the vacuum apparatus to air and contaminants.

ITO coated chamber windows: It is known that the proximity of two dielectric objects will cause them to become charged in a vacuum. This applies to the two large dielectrically coated windows used in many trapping experiments [95]. One way to avoid this is to include an extra indium tin oxide (ITO) coating upon the large windows of the vacuum chamber. ITO is known to dissipate charges which would otherwise cause an electric field across the centre of the chamber.

In vacuum temperature sensors: This upgrade could also be coupled with the temperature control of the entire system. The benefit is that if the temperature in the vicinity of the atoms is known, then more accurate calculations can be made upon the BBR shifts induced upon the clock transition.

Vacuum pump upgrades: New developments in vacuum pump technology mean that pumps with a higher pumping speed than used in this work which fit onto a standard cf16 flange rather than the cf35 flange. An example of such a pump is produced by CapaciTorr with a weight of only 28 g with a pumping speed of up to $200\,\mathrm{ls}^{-1}$. This means that the majority of the weight of the atomics package can be removed, and the pumping rate of the entire atomics package could be improved by a factor of up to 14 if the small $3\,\mathrm{ls}^{-1}$ pump was replaced too. This has the potential to enable a lower typical background pressure in the chamber allowing for a longer vacuum limited lifetime of the various traps employed in the clock which would allow longer clock pulses to be used.

Oven upgrade: The oven could be replaced with one based upon a cf16 flange instead of cf35 to reduce the size of the atomics package further. The disadvantages of this is that the amount of strontium that could be housed in a smaller oven would be reduced by a factor of 8 which would mean that the reservoir would need to be replenished more often.

Vacuum system upgrade: With the oven and large pump no longer requiring a cf35 flange, all tubing can be reduced to have an inner diameter of 16 mm. The benefit is a reduction in inner volume of the atomics package which would further increase the effective pumping rate of the vacuum pumps with the same benefits as described above. Another benefit is that it could be possible to include some in-vacuum components which could reduce the BBR at the atomic position. The idea would be to place two smaller tubes in the path of the atomic beam. The first being a polished, high-quality copper tube with a thickness of 10 mm and an inner diameter of 10 mm to reduce the amount of BBR as seen by the atomic sample by absorbing any radiation emitted by the oven apart from that which passes through with the atomic beam. In addition a tube of graphite of similar dimensions could be included. As graphite is a getter, this would also improve the vacuum quality [112].

I would estimate that the atomics package would look similar to the computer rendered image found in figure 7.2 after performing all of these upgrades. The remaining improvements listed as number 8 to 12 in table 7.1 will now be discussed.

FPGA upgrade: The benefit to upgrading the FPGA is to enable a more user friendly interface and more efficient programming. The apparatus could then be more easily used by scientists who have not worked on this piece of equipment before, and the experiment could be operated autonomously. It could also be possible to program a sequence which optimises different parameters daily such as the frequency detuning of each laser, the oven temperature, the length of each step in the sequence etc. The idea here would be that this would no longer have to be done manually and there is the possibility of finding a more efficient loading sequence.

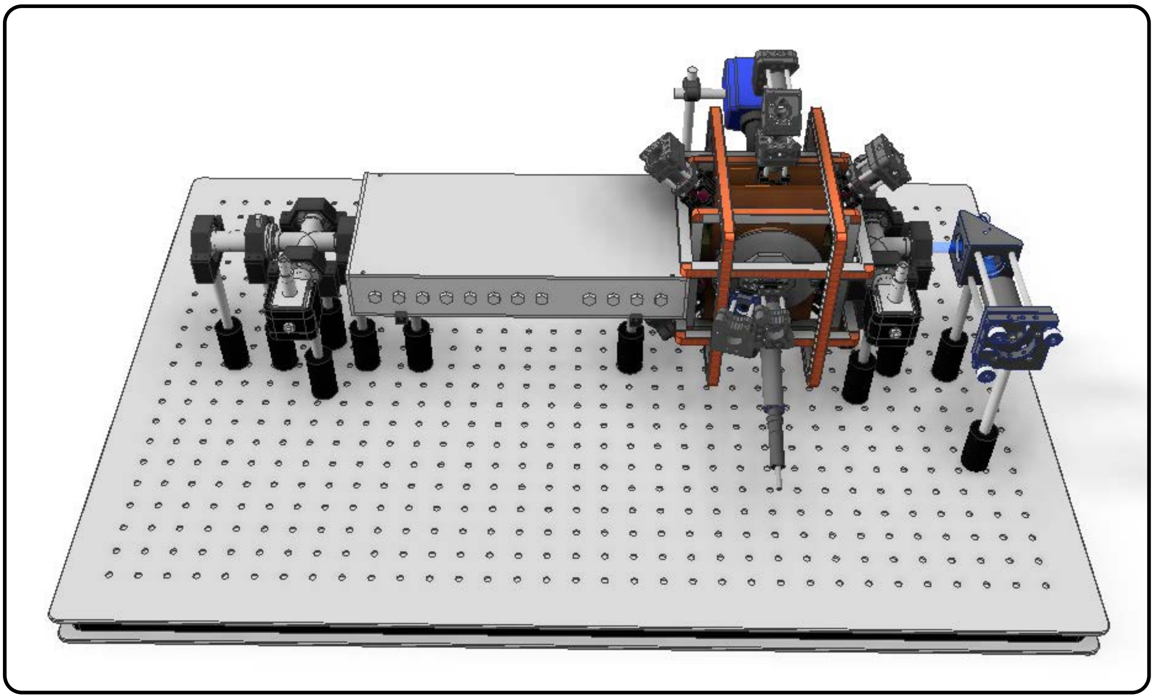

Fig. 7.2 A CAD drawing of the SOC2 atomics package after undergoing the proposed upgrades outlined in this work.

Autonomous remote operation: This would allow the apparatus to be operable in the field, whether that be in a different laboratory or in space. Coupled with the improvements made by the FPGA upgrade, this would allow the experiment to be run without physical supervision.

Rearrangement of transportable rack: A minor change which would ensure the inclusion of the clock laser in the transportability of the clock which can be seen in figure 7.3.

Blue distribution breadboard upgrade: With the upgrade to the fibre splitting array, two more of the outputs to the blue distribution breadboard would be unused, along with the outputs which were reserved in the case of using a 2D MOT instead of a Zeeman slower. Due to the extra redundancies, it would make sense in terms of preserving as much optical power as possible to take out the unnecessary components. The only necessary outputs now would be one for the Zeeman slower, one for the MOT beams, and one for detection. A possible rearrangement of the blue distribution board can be seen in figure 7.4. The volume of the smaller blue frequency distribution breadboard is 60 % of that of the original board. This volume could be reduced further with the inclusion of smaller optics and optic holders.

FSS upgrade: Finally, one of the most important possible upgrades is to the FSS. Inside the FSS there contains a third cavity which is currently unused. This cavity was designed to be used with the two repumper lasers and has been tested to the same extent as the other two cavities for performance. Even though the passive stability of the two rempumper lasers is sufficient for long measurements, it would be beneficial for long-term operation if these lasers could also be stabilised to the FSS. This would involve including one more rack unit of electronics to control these two locks. Because of this, this upgrade also opens up the opportunity for an upgrade to the existing electronics. For example, it was found that during the investigation into the lock

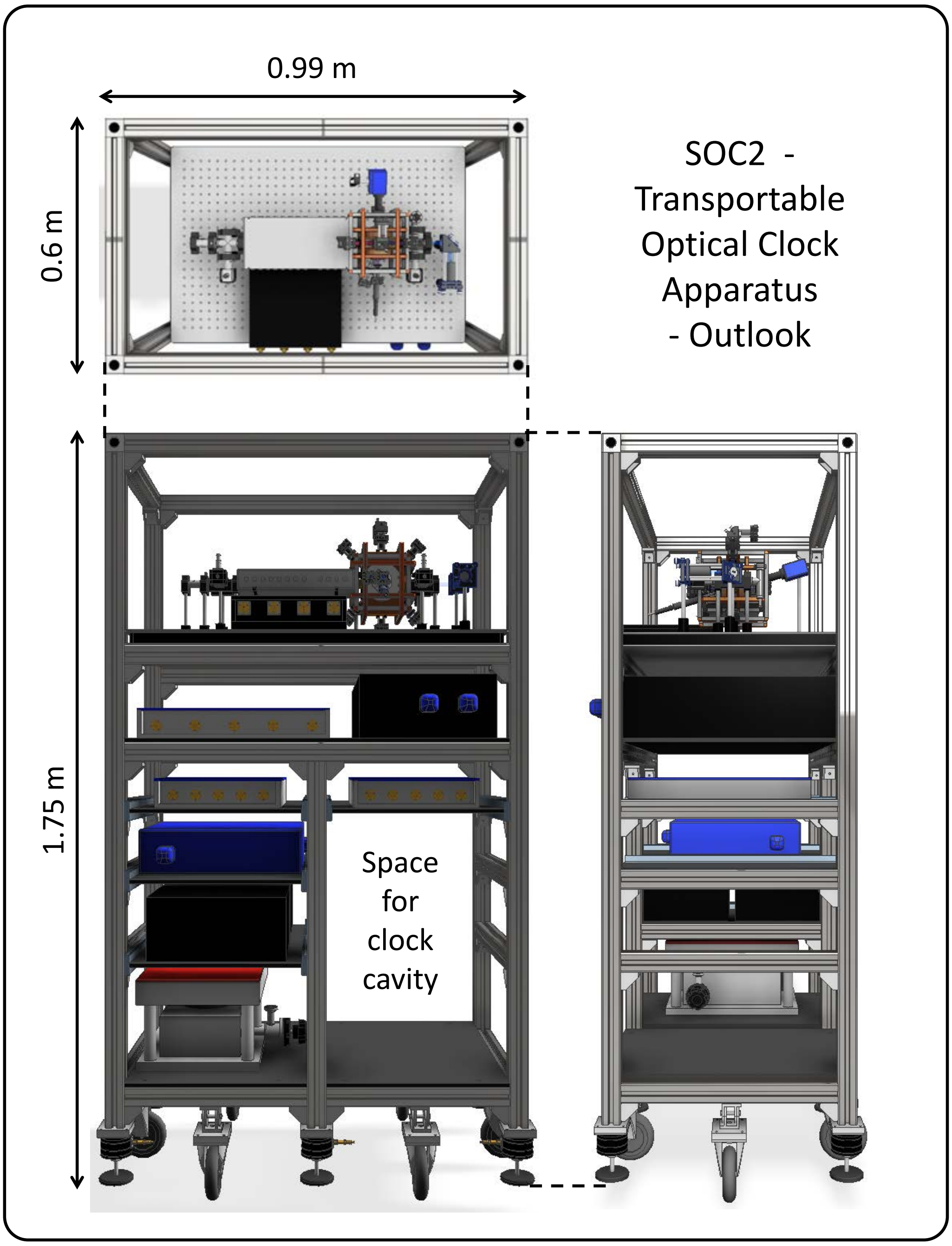

Fig. 7.3 The possible short term placement of the clock laser and ultra stable cavity onto the transportable SOC2 rack after slight adjustments to the positioning of the existing laser breadboards. From top to bottom: Atomics package and blue distribution module, clock laser and lattice laser, red cooling laser and stirring laser, blue laser, repumper lasers and FSS with the lower 2 shelves on the right side removed to place the clock laser cavity.

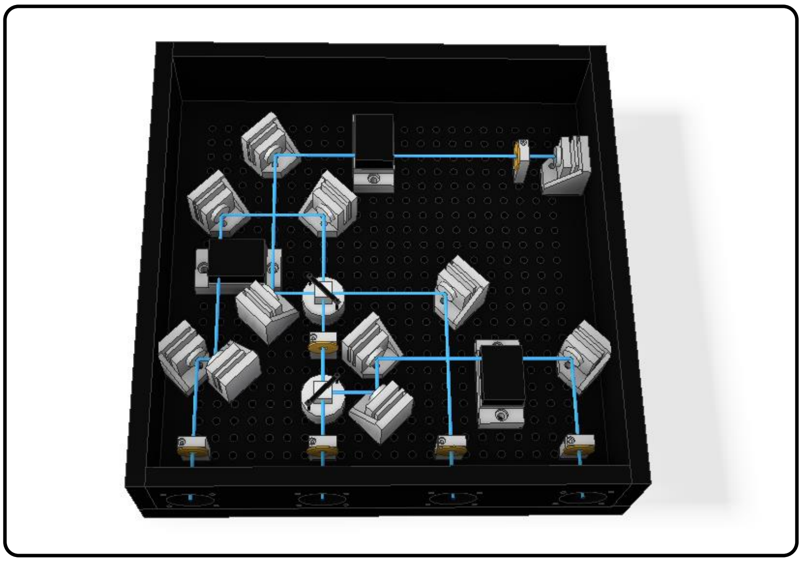

Fig. 7.4 Possible configuration of a new 461 nm laser frequency distribution breadboard.

modulation method for the broadband red MOT that it would have been beneficial if the electronics which controlled the lock could be easily externally triggered by a TTL signal. Another beneficial upgrade to the FSS would be the housing. Currently the housing is quite large and heavy. Some of the wires inside the cavity are also not vacuum compatible and outgass at a rate which means that pressures lower than 5×10^{-7} mbar level cannot be reached. This adds strain to the small $3\,\mathrm{l s^{-1}}$ vacuum pump currently installed. This pump could also be upgraded at the same time. These improvements would allow for the repumpers to be stabilised and more stable cavities due to the improvement in vacuum quality.

A summary of the long term improvements that I could foresee would benefit the project can be seen in table 7.2 with further explanation below.

Switching to ^{87}Sr: The strontium optical lattice clock in this thesis was built using ^{88}Sr, one of the bosonic isotopes of strontium. A strontium optical lattice clock using ^{88}Sr is simpler to realise due to the absence of nuclear spin in bosonic isotopes and

Label	Description	Expected benefits	Predicted timescale
1	Switch to ^{87}Sr	Improved stability and precision	at least 6 months
2	Laser upgrades	More compact, space ready lasers	at least 6 months
3	Electronics upgrade	More compact, efficient electronics - low power	at least 6 months

Table 7.2 Long term improvement suggestions for the outlook of the SOC2 project

thus the electronic structure is simpler and does not experience the 1st order Zeeman shift. The fermionic ^{87}Sr isotope however is particularly sensitive to external magnetic fields and the intercombination line is split in the presence of a magnetic field. Because of this, the loading of the red MOT is more complex. It requires the addition of another laser which serves to randomise the population of the magnetic sub-states. Doing so ensures that the atoms can be cooled by the 689 nm radiation [8, 73, 82, 113]. A stirring laser was realised at PTB and is offset locked to the 689 nm laser at a frequency of 1.46 GHz as part of the SOC2 project. The stirring laser also has a dedicated place in the transportable rack. A schematic of the stirring laser can be seen in figure 7.5. Another complication of working with the fermionic isotope is that with reference to table 4.1, it can be seen that the natural abundance of ^{87}Sr is relatively low when compared to the most abundant bosonic isotope ^{88}Sr with an abundance of only 7% compared to almost 83% respectively. This means that the expected yield of ^{87}Sr atoms should be around 12 times lower than that for the bosonic isotope with the same atomic flux. This problem could be overcome by simply heating the oven to a higher temperature or working with the lower atom number. The collisional shifts associated with the fermionic isotope are also lower than that in the bosonic isotope [83] and the linewidth of the clock transition in ^{87}Sr is narrower.

Laser and electronics upgrade: Secondly, the lasers and electronics could be upgraded to be smaller, more energy efficient and space ready. Such technologies have

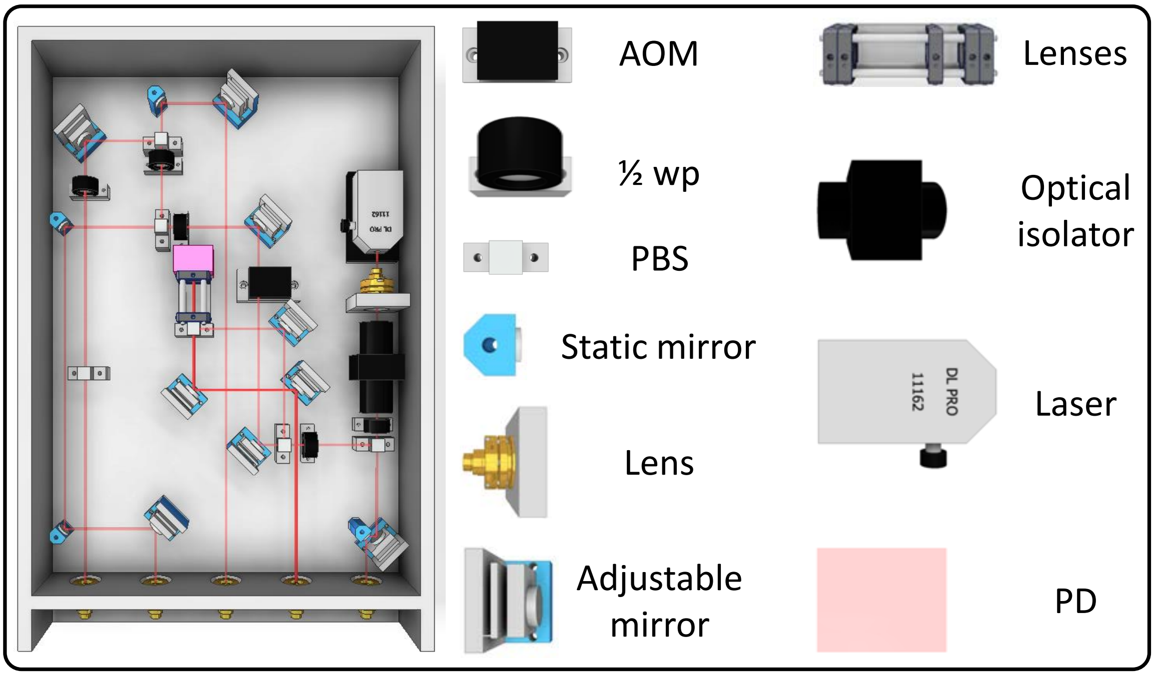

Fig. 7.5 A schematic of the stirring laser breadboard realised for the SOC2 clock apparatus with components labelled.

been used to great success in another European collaborative project called iSense [105] . The lasers and electronics used in iSense were very compact and geared towards a transportable gravity sensor. The benefit to this is not only for the sake of transportability with the aim for a space mission, but also this would mean that the apparatus would produce less heat. The apparatus as a whole would then be much simpler to temperature stabilise without the need for extensive and complex cooling solutions. The frequency of the lasers would also be more stable when free-running. Therefore, should the lasers unlock due to an unexpected external shock, the any autonomous locking electronics (if present) could re-lock the laser at a higher success rate than if the lasers were drifting at a larger rate due to temperature variations. The optics would also be more stable through the reduction in temperature variations.

References

[1] BIPM. *SI Unit of Time (Second)*. 2016.

[2] Thomas P Heavner et al. "First accuracy evaluation of NIST-F2". In: *Metrologia* 51.3 (2014), p. 174. ISSN: 0026-1394. DOI: 10.1088/0026-1394/51/3/174.

[3] Tushna Commissariat. "Atomic clock is smallest on the market". In: *Physics World* (2011).

[4] Philippe Laurent et al. "The ACES/PHARAO space mission". In: *Comptes Rendus Physique* 16.5 (2015), pp. 540–552. ISSN: 16310705. DOI: 10.1016/j.crhy.2015.05.002.

[5] Andrew D. Ludlow and Jun Ye. "Progress on the optical lattice clock". In: *Comptes Rendus Physique* 16.5 (2015), pp. 499–505. ISSN: 16310705. DOI: 10.1016/j.crhy.2015.03.008.

[6] Jérôme Lodewyck, Philip G. Westergaard, and Pierre Lemonde. "Nondestructive measurement of the transition probability in a Sr optical lattice clock". In: *Physical Review A - Atomic, Molecular, and Optical Physics* 79.6 (2009), pp. 1–4. ISSN: 10502947. DOI: 10.1103/PhysRevA.79.061401. arXiv:0902.2905.

[7] E. M. Bridge et al. "Progress towards a strontium optical lattice clock at NPL". In: *EFTF-2010 24th European Frequency and Time Forum* (2010).

[8] St. Falke et al. "The 87-Sr optical frequency standard at PTB". In: 399 (2011), p. 9. ISSN: 0026-1394. DOI: 10.1088/0026-1394/48/5/022. arXiv:1104.4850.

[9] Tomoya Akatsuka, Masao Takamoto, and Hidetoshi Katori. "Three-dimensional optical lattice clock with bosonic Sr88 atoms". In: *Physical Review A - Atomic, Molecular, and Optical Physics* 81.2 (2010), pp. 1–11. ISSN: 10502947. DOI: 10.1103/PhysRevA.81.023402.

[10] N. Poli et al. "A transportable strontium optical lattice clock". In: *Applied Physics B: Lasers and Optics* 117.4 (2014), pp. 1107–1116. DOI: 10.1007/s00340-014-5932-9. arXiv:1409.4572.

[11] S Schiller. "Towards Neutral-atom Space Optical Clocks : Development of high-performance transportable and breadboard optical clocks and advanced subsystems Proposal acronym : SOC2 Type of funding scheme : Collaborative Project Work programme topics addressed : and he". In: *ESA Proposal* (2010).

[12] BIPM. *International Atomic Time*. 2013.

[13] B Guinot. "Is Tai a Coordinate Time or Proper Time?" In: *Kluwer Academic Publishers* (1986).

[14] Willis. J. Milham. *Time and Timekeepers*. New York: Macmillan, 1945, p. 190. ISBN: 0-7808-0008-7.

[15] Martha Baldwin. *Chronometer*. 2004.

[16] D B Sullivan. *Time and frequency measurement at NIST: The first 100 years*. 2001.

[17] H. S. Margolis. “Optical frequency standards and clocks”. In: *Contemporary Physics* 51.1 (2010), pp. 37–58. ISSN: 0010-7514. DOI: 10.1080/00107510903257616.

[18] N Hinkley et al. “An atomic clock with 10(-18) instability.” In: *Science (New York, N.Y.)* 341.6151 (2013), pp. 1215–8. ISSN: 1095-9203. DOI: 10.1126/science.1240420. arXiv:1305.5869.

[19] T L Nicholson et al. “Systematic evaluation of an atomic clock at 2 × 10(-18) total uncertainty.” In: *Nature communications* 6 (2015), p. 6896. ISSN: 2041-1723. DOI: 10.1038/ncomms7896. arXiv:1412.8261.

[20] B J Bloom et al. “An optical lattice clock with accuracy and stability at the 10 2 18 level”. In: *Science (New York, N.Y.)* 341.6151 (2014), pp. 5–11. ISSN: 1095-9203. DOI: 10.1038/nature12941. arXiv:1305.5869.

[21] Ichiro Ushijima et al. “Cryogenic optical lattice clocks with a relative frequency difference of 1x10 -18”. In: *arXiv preprint* (2014), pp. 1–20. arXiv:1405.4071.

[22] C. W. Chou et al. “Frequency comparison of two high-accuracy Al+ optical clocks”. In: *Physical Review Letters* 104.7 (2010), pp. 1–4. ISSN: 00319007. DOI: 10.1103/PhysRevLett.104.070802. arXiv:0911.4527.

[23] N. Huntemann et al. “Single-Ion Atomic Clock with $ 3 times 10^{-18} $ Systematic Uncertainty”. In: 2 (2016), pp. 1–5. ISSN: 10797114. DOI: 10.1103/PhysRevLett.116.063001. arXiv:1602.03908.

[24] William Thomson Baron Kelvin and Peter Guthrie Tait. *Treatise on Natural Philosophy*. Oxford: Clarendon Press Series, 1879.

[25] Andrew D Ludlow et al. “Optical Atomic Clocks”. In: *Preprint at arxiv.org/abs/1407.3493 (to appear on Rev. Mod. Phys.)* (2014), pp. 1–90. arXiv:1407.3493.

[26] L. Essen and J. V. L. Parry. “An Atomic Standard of Frequency and Time Interval: A Cæsium Resonator”. In: *Nature* 176.4476 (1955), pp. 280–282. ISSN: 0028-0836. DOI: 10.1038/176280a0.

[27] Herbert. J. Kramer. *ISS Utilization: ACES (Atomic Clock Ensemble in Space) / PHARAO*. 2016.

[28] T. H Maiman. “Stimulated Optical Radiation in Ruby”. In: *Nature* 187.4736 (1960), pp. 493–494.

[29] Eric Black. “Notes on the Pound-Drever-Hall technique”. In: *Technology* 4.617 (1998), pp. 16–98.

[30] P. A. Franken et al. “Generation of optical harmonics”. In: *Physical Review Letters* 7.4 (1961), pp. 118–119. ISSN: 00319007. DOI: 10.1103/PhysRevLett.7.118.

[31] Nobelprize.org. *The Nobel Prize in Physics 2005*. 2014.

[32] Laura Ost. *A New Era for Atomic Clocks*. 2014.

[33] Masao Takamoto et al. “Frequency ratios of Sr, Yb, and Hg based optical lattice clocks and their applications”. In: *Comptes Rendus Physique* 16.5 (2015), pp. 489–498. ISSN: 16310705. DOI: 10.1016/j.crhy.2015.04.003.

[34] Kai Bongs et al. “Development of a strontium optical lattice clock for the SOC mission on the ISS”. In: *Comptes Rendus Physique* 16.5 (2015), pp. 553–564. ISSN: 16310705. DOI: 10.1016/j.crhy.2015.03.009. arXiv:arXiv:1503.08457v1.

[35] N. Poli et al. “Optical atomic clocks”. In: *Rivista del Nuovo Cimento* (2014), pp. 1–70. arXiv:arXiv:1401.2378v2.

[36] S Origlia et al. “Development of a strontium optical lattice clock for the SOC mission on the ISS”. In: *ArXiv* (2016), pp. 1–21. arXiv:1603.06062.

[37] S. Blatt et al. “New limits on coupling of fundamental constants to gravity using Sr87 optical lattice clocks”. In: *Physical Review Letters* 100.14 (2008), pp. 2–5. ISSN: 00319007. DOI: 10.1103/PhysRevLett.100.140801. arXiv:0801.1874.

[38] Brett Altschul et al. “Quantum tests of the Einstein Equivalence Principle with the STE-QUEST space mission”. In: *Advances in Space Research* 55.1 (2015), pp. 501–524. ISSN: 18791948. DOI: 10.1016/j.asr.2014.07.014. arXiv:1404.4307.

[39] Stephan Schiller et al. “The Space Optical Clocks Project : Development of high-performance transportable and breadboard optical clocks and advanced subsystems”. In: *European Time and Frequency Forum*. Sweden, 2012.

[40] P Gill et al. “Optical Atomic Clocks for Space”. In: *National Physical Laboratory Technical Supporting Document* 1.21641 (2008), pp. 1–145.

[41] Helen Margolis. “Timekeepers of the future”. In: *Nature Physics* 10.2 (2014), pp. 82–83. ISSN: 1745-2473. DOI: 10.1038/nphys2834.

[42] Shimon Kolkowitz et al. “Gravitational wave detection with optical lattice atomic clocks”. In: (2016). arXiv:1606.01859.

[43] B. P. Abbott et al. “Observation of gravitational waves from a binary black hole merger”. In: *Physical Review Letters* 116.6 (2016), pp. 1–16. ISSN: 10797114. DOI: 10.1103/PhysRevLett.116.061102. arXiv:1602.03837.

[44] R Le Targat et al. “Experimental realization of an optical second with strontium lattice clocks.” In: *Nature communications* 4 (2013), p. 2109. ISSN: 2041-1723. DOI: 10.1038/ncomms3109. arXiv:1301.6046.

[45] F. Levi et al. “LIFT-the Italian link for time and frequency”. In: *2013 Joint European Frequency and Time Forum and International Frequency Control Symposium, EFTF/IFC 2013* (2013), pp. 477–480. DOI: 10.1109/EFTF-IFC.2013.6702195.

[46] Anthony Bercy et al. “Ultra-stable optical frequency dissemination on a multi-access fibre network”. In: *Journal of Physics* Conference.1 (2013), pp. 1–11.

[47] Olivier Lopez et al. “Frequency and time transfer for metrology and beyond using telecommunication network fibres”. In: *Comptes Rendus Physique* 16.5 (2015), pp. 531–539. ISSN: 16310705. DOI: 10.1016/j.crhy.2015.04.005.

[48] J. C. Hafele and R. E. Keating. “Around-the-World Atomic Clocks: Predicted Relativistic Time Gains”. In: *Science* 177.4044 (1972), pp. 166–168. DOI: 10.1126/science.177.4044.166.

[49] J. C. Hafele and R. E. Keating. "Around-the-World Atomic Clocks: Observed Relativistic Time Gains". In: *Science* 177.4044 (1972), pp. 168–170. DOI: 10.1126/science.177.4044.168.

[50] M. P. Heß et al. "The ACES mission: System development and test status". In: *Acta Astronautica* 69.11-12 (2011), pp. 929–938. ISSN: 00945765. DOI: 10.1016/j.actaastro.2011.07.002.

[51] S Schiller. *SOC2-Towards Neutral-atom Space Optical Clocks*. 2011.

[52] D. J. Wineland, R. E. Drullinger, and F. L. Walls. "Radiation-pressure cooling of bound resonant absorbers". In: *Physical Review Letters* 40.25 (1978), pp. 1639–1642. ISSN: 00319007. DOI: 10.1103/PhysRevLett.40.1639. arXiv:arXiv:1011.1669v3.

[53] W M Itano and D J Wineland. "Laser Cooling and Double Resonance Spectroscopy of Stored Ions". In: *Laser Spectroscopy V, Proceedings of the Fifth International Conference* (1981), p. 360. DOI: 10.1007/978-3-540-38804-3_65.

[54] T. W. H\"{a}nsch and A. L. Schawlow. "Cooling of gases by laser radiation". In: *Optics Communications* 13.1 (1975), pp. 68–69. ISSN: 00304018. DOI: 10.1016/0030-4018(75)90159-5.

[55] E. L. Raab et al. "Trapping of Neutral Sodium Atoms with Radiation Pressure". In: *Physical Review Letters* 59.23 (1987).

[56] H. J. Metcalf and P. van der Straten. "Laser cooling and trapping of atoms". In: *Journal of Optical Society of America* 20.5 (2003), pp. 887–908. ISSN: 0098-907X. DOI: 10.1364/ON.12.12.000018.

[57] Christopher.J Foot. *Atomic Physics*. Oxford University Press, 2005.

[58] N. V. Vitanov et al. "Power broadening revisited: Theory and experiment". In: *Optics Communications* 199.1-4 (2001), pp. 117–126. ISSN: 00304018. DOI: 10.1016/S0030-4018(01)01495-X.

[59] Jonathan Levine. "A simplified calculation of power-broadened linewidths, with application to resonance ionization mass spectrometry". In: *Spectrochimica Acta Part B: Atomic Spectroscopy* 69 (2012), pp. 61–66. ISSN: 05848547. DOI: 10.1016/j.sab.2012.02.001.

[60] Hidetoshi Katori et al. "Magneto-Optical Trapping and Cooling of Strontium Atoms down to the Photon Recoil Temperature". In: *Physical review letters* 82.6 (1999), pp. 1116–1119.

[61] M. Schioppo. "Development of a Transportable Strontium Optical Clock". PhD thesis. Universit\"{a} Degli Studi di Firenze, 2012, pp. 1–159.

[62] Thomas H. Loftus et al. "Narrow line cooling and momentum-space crystals". In: *Physical Review A - Atomic, Molecular, and Optical Physics* 70.6 (2004), pp. 1–14. ISSN: 10502947. DOI: 10.1103/PhysRevA.70.063413. arXiv:0407021 `[physics]`.

[63] Thomas H. Loftus et al. "Narrow line cooling: Finite photon recoil dynamics". In: *Physical Review A - Atomic, Molecular, and Optical Physics* 70.6 (2004), pp. 11–14. ISSN: 10502947. DOI: 10.1103/PhysRevA.70.063413. arXiv:0407021 `[physics]`.

[64] T. Chanelière et al. "Three dimensional cooling and trapping with a narrow line". In: *European Physical Journal D* 46.3 (2008), pp. 507–515. ISSN: 14346060. DOI: 10.1140/epjd/e2007-00329-8. arXiv:0704.0855.

[65] Rudolf Grimm and Yurii B Ovchinnikov. “Optical dipole traps for neutral atoms”. Gaithersburg, 1987.

[66] R.L. Kurucz and B. Bell. *Atomic line data*. Kurucz CD–. Cambridge: Smithsonia, 1995.

[67] NIST. *Basic Atomic Spectroscopic Data for Strontium*. 2016.

[68] Thomas Middelmann et al. “Tackling the blackbody shift in a strontium optical lattice clock”. In: *IEEE Transactions on Instrumentation and Measurement* 60.7 (2011), pp. 2550–2557. ISSN: 00189456. DOI: 10.1109/TIM.2010.2088470. arXiv:1009.2017.

[69] Mm Boyd. “High Precision Spectroscopy of Strontium in an Optical Lattice: Towards a New Standard for Frequency and Time”. In: (2007), p. 245.

[70] Simon Stellmer. “Degenerate quantum gases of strontium”. Thesis. University of Innsbruck, 2013, pp. 1–256.

[71] Ian R Hill et al. “Zeeman Slowers for Strontium based on Permanent Magnets”. Teddington, 2014.

[72] Kurt R. Vogel et al. “Narrow-line Doppler cooling of strontium to the recoil limit”. In: *IEEE Transactions on Instrumentation and Measurement* 48.2 (1999), pp. 618–621. ISSN: 00189456. DOI: 10.1109/19.769671.

[73] Gretchen K. Campbell et al. “The absolute frequency of the 87Sr optical clock transition”. In: 45 (2008), pp. 539–548. ISSN: 0026-1394. DOI: 10.1088/0026-1394/45/5/008. arXiv:0804.4509.

[74] Qiang Wang et al. “Sr atoms with 689 nm Laser”. In: *Chinese Physics Letters* 28.3 (2011), p. 033201. ISSN: 0256-307X. DOI: 10.1088/0256-307X/28/3/033201.

[75] Pierre Lemonde and Peter Wolf. “Minimizing the Required Trap Depth in Optical Lattice Clocks”. In: *IEEE* (2005), pp. 947–955.

[76] V D Ovsiannikov and V G Pal’chikov. “Magic Wavelengths for Frequency Standards of Deeply Cooled Alkaline-Earth Atoms in a Stark-Free Optical Lattice”. In: *Laser Physics* 15.7 (2005), pp. 1040–1045.

[77] Immanuel Bloch. “Quantum gases in optical lattices”. In: *Physics World* 17.4 (2004), pp. 25–29. ISSN: 09538585.

[78] Immanuel Bloch. “Ultracold quantum gases in optical lattices”. In: *Nature Physics* 1.1 (2005), pp. 23–30. ISSN: 1745-2473. DOI: 10.1038/nphys138. arXiv:0912.3646.

[79] Thomas Legero et al. “Ultracold Sr atoms for an optical lattice clock”. Braunschweig, 2007.

[80] Anders Brusch et al. “Hyperpolarizability effects in a Sr optical lattice clock”. In: *Physical Review Letters* 96.10 (2006), pp. 17–20. ISSN: 00319007. DOI: 10.1103/PhysRevLett.96.103003. arXiv:0512201 `[physics]`.

[81] K. Beloy. “Lattice-induced nonadiabatic frequency shifts in optical lattice clocks”. In: *Physical Review A - Atomic, Molecular, and Optical Physics* 82.3 (2010), pp. 1–4. ISSN: 10502947. DOI: 10.1103/PhysRevA.82.031402. arXiv:1008.5005.

[82] Takashi Mukaiyama et al. “Recoil-limited laser cooling of 87Sr atoms near the Fermi temperature.” In: *Physical review letters* 90.11 (2003), p. 113002. ISSN: 0031-9007. DOI: 10.1103/PhysRevLett.90.113002.

[83] Ch Lisdat et al. “Collisional losses, Decoherence, and frequency shifts in optical lattice clocks with bosons”. In: *Physical Review Letters* 103.9 (2009), pp. 1–4. ISSN: 00319007. DOI: 10.1103/PhysRevLett.103.090801. arXiv:0904.2515.

[84] Shoichi Okaba et al. “Lamb-Dicke spectroscopy of atoms in a hollow-core photonic crystal fibre.” In: *Nature communications* 5.May (2014), p. 4096. ISSN: 2041-1723. DOI: 10.1038/ncomms5096. arXiv:1408.0659.

[85] Tetsuya Ido and Hidetoshi Katori. “Recoil-free spectroscopy of neutral Sr atoms in the Lamb-Dicke regime.” In: *Physical review letters* 91.5 (2003), p. 053001. ISSN: 0031-9007. DOI: 10.1103/PhysRevLett.91.053001. arXiv:0303032 `[physics]`.

[86] Masao Takamoto, Tetsushi Takano, and Hidetoshi Katori. “Frequency comparison of optical lattice clocks beyond the Dick limit”. In: *Nature Photonics* 5.5 (2011), pp. 288–292. ISSN: 1749-4885. DOI: 10.1038/nphoton.2011.34.

[87] Hidetoshi Katori. “Optical lattice clocks and quantum metrology”. In: *Nature Photonics* 5.4 (2011), pp. 203–210. ISSN: 1749-4885. DOI: 10.1038/nphoton.2011.45.

[88] A V Taichenachev and V I Yudin. “Magnetic Field-Induced Spectroscopy of Forbidden Optical Transitions with Application to Lattice-Based Optical Atomic Clocks”. In: *Physical review letters* 96.083001 (2006), pp. 3–6. DOI: 10.1103/PhysRevLett.96.083001.

[89] Andrew D Ludlow et al. “Optical Atomic Clocks”. In: *arXiv preprint* June (2015), pp. 1–86. ISSN: 0393697X. DOI: 10.1393/ncr/i2013-10095-x. arXiv:1407.3493.

[90] N. Poli et al. “Frequency evaluation of the doubly forbidden S0 1 ??? P0 3 transition in bosonic Yb174”. In: *Physical Review A - Atomic, Molecular, and Optical Physics* 77.5 (2008), pp. 7–10. ISSN: 10502947. DOI: 10.1103/PhysRevA.77.050501.

[91] a D Ludlow et al. “Sr lattice clock at 1x10 -16 fractional uncertainty by remote optical evaluation with a Ca clock”. In: *Science (New York, N.Y.)* 319.5871 (2008), pp. 1805–1808. ISSN: 0036-8075. DOI: 10.1126/science.1153341. arXiv:0801.4344.

[92] Martin M. Boyd et al. “Nuclear spin effects in optical lattice clocks”. In: *Physical Review A - Atomic, Molecular, and Optical Physics* 76.2 (2007). ISSN: 10502947. DOI: 10.1103/PhysRevA.76.022510. arXiv:0704.0912.

[93] K Beloy et al. “An atomic clock with $1 times 10^{-18}$ room-temperature blackbody Stark uncertainty”. In: *ArXiv* (2014), pp. 1–5. arXiv:1412.1029.

[94] Masao Takamoto et al. “Frequency ratios of Sr, Yb, and Hg based optical lattice clocks and their applications”. In: *Comptes Rendus Physique* 16.5 (2015), pp. 489–498. ISSN: 16310705. DOI: 10.1016/j.crhy.2015.04.003. arXiv:1505.03207.

[95] Jérôme Lodewyck et al. “Observation and cancellation of a perturbing dc stark shift in strontium optical lattice clocks”. In: *IEEE Transactions on Ultrasonics, Ferroelectrics, and Frequency Control* 59.3 (2012), pp. 411–415. ISSN: 08853010. DOI: 10.1109/TUFFC.2012.2209. arXiv:1108.4320.

[96] Thomas Middelmann et al. “High accuracy correction of blackbody radiation shift in an optical lattice clock”. In: *Physical review letters* 109.26 (2012), pp. 1–5. ISSN: 00319007. DOI: 10.1103/PhysRevLett.109.263004. arXiv:1208.2848.

[97] Alvatec. *Alvatec Alvasources datasheet*. 2016. DOI: 10.1007/s13398-014-0173-7.2. arXiv:arXiv:1011.1669v3.

[98] Tao Yang et al. “A high flux source of cold strontium atoms”. In: *European Physical Journal D* 69.10 (2015). ISSN: 14346079. DOI: 10.1140/epjd/e2015-60288-y. arXiv:1505.04507.

[99] Bjoern Ole Kock. “Magneto-Optical Trapping of Strontium for use as a Mobile Frequency Reference”. PhD thesis. 2013.

[100] P Patnaik. *Handbook of Inorganic Chemicals*. McGraw-Hill, 2002. ISBN: 0-07-049439-8.

[101] *Steatite Material Properties*. 2016.

[102] Parker. *Metal Seal Design Guide - High performance Engineered Seals and Sealing Systems*. 2016.

[103] a Nevsky et al. “Robust frequency stabilization of multiple spectroscopy lasers with large and tunable offset frequencies.” In: *Optics letters* 38.22 (2013), pp. 4903–6. ISSN: 1539-4794. DOI: 10.1364/ol.38.004903. arXiv:1309.3879.

[104] Soroosh Alighanbari. “Development of laser frequency stabilization systems for high-resolution spectroscopy”. PhD thesis. HHUD, 2013.

[105] Jonathan Ian Malcolm. “Construction of a Portable Platform for Cold Atom Interferometry”. PhD thesis. University of Birmingham, 2016.

[106] M. Chalony et al. “Doppler cooling to the quantum limit”. In: *Physical Review Letters* 107.24 (2011), pp. 1–5. ISSN: 00319007. DOI: 10.1103/PhysRevLett.107.243002. arXiv:1107.2313.

[107] Dariusz Swierad. *Private Communication*. 2014.

[108] Joshua Hughes. *Private Communication*. 2014.

[109] I Courtillot et al. “Efficient cooling and trapping of strontium atoms.” In: *Optics letters* 28.6 (2003), pp. 468–470. ISSN: 0146-9592. DOI: 10.1364/OL.28.000468.

[110] Michael Fleischhauer and Jonathan P Marangos. “Electromagnetically induced transparency: Optics in coherent media”. In: *Rev Mod Phys* 77.2 (2005), pp. 633–673. ISSN: 0034-6861. DOI: 10.1103/RevModPhys.77.633. arXiv:0001094 `[quant-ph]`.

[111] S Origlia et al. “Development of a strontium optical lattice clock for the SOC mission in the ISS - WORKING PAPER”. 2016.

[112] T P Heavner et al. “NIST-F1: recent improvements and accuracy evaluations”. In: *Metrologia* 42.5 (2005), pp. 411–422. ISSN: 0026-1394. DOI: 10.1088/0026-1394/42/5/012.

[113] Xinye Xu et al. “Single-stage sub-Doppler cooling of alkaline earth atoms.” In: *Physical review letters* 90.19 (2003), p. 193002. ISSN: 0031-9007. DOI: 10.1103/PhysRevLett.90.193002.

[114] Mathis Baumert. “Dipole Traps and Optical Lattices for Quantum Simulations”. In: December (2013), p. 128.

Appendix A

SOC2 Participants

The second stage of the Space Optical Clocks project was started in 2011 as a collaboration between 16 universities and institutions (shown in table A.1 and in figure A.1) and is coordinated at Heinrich-Heine-Universität Düsseldorf (HHUD) by Professor Stephan Schiller. Of these 16 participants, half were directly involved with the strontium optical lattice clock.

Participant	Participant organisation name	Acronym	Country
1	Heinrich-Heine-Universität Düsseldorf	HHUD	DE
2	Physikalisch-Technische Bundesanstalt	PTB	DE
3	Leibniz Universität Hannover	LUH	DE
4	Observatoire de Paris	OP	FR
5	Università delgi Studi di Firenze	UNIFI	IT
6	Instituto Nazionale di Ricerca Metrologica	INRIM	IT
7	The University of Birmingham	UOB	UK
8	The National Physical Laboratory	NPL	UK
9	TOPTICA Photonics AG	TOPTICA	DE
10	Kayser-Threde GmbH	KT	DE
11	EADS Astrium Friedrichschafen	ASD	DE
12	Menlo Systems GmbH	Menlo	DE
13	Kayser Italia Srl	KI	IT
14	Université de Neuchâtel	UNEU	CH
15	Centre Suisse d'Electronique et de Microtechnique	CSEM	CH
16	Ecoles Polytechniques Fédérales Lausanne	EPFL	CH

Table A.1 SOC2 participant members [11].

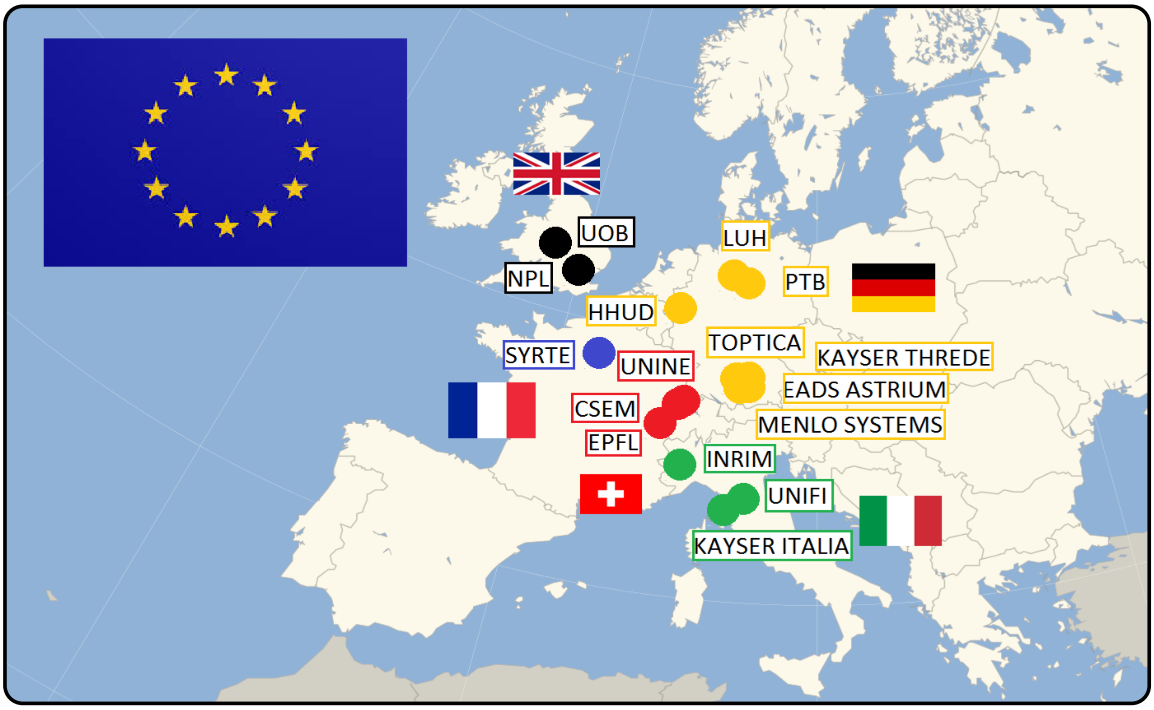

Fig. A.1 A map of SOC2 participant members

The project proposal was divided into seven workpackages. These workpackages as related to the strontium clock can be briefly summarised as follows [11]:

WP1 - Baseline laser systems This workpackage was completed through work by TOPTICA, UNIFI, PTB, LUH and UOB. Broadly it consists of the development of all laser sources and their integration onto compact breadboards, ensuring the uniformity of the electronics, development of an optimised fibre distribution system for all lasers. The work done by us at UOB was the design and realisation of the frequency distribution module for the 1st stage 461 nm cooling light (section 5.4.2) and the investigation into using different 461 nm laser sources [99].

WP2 - Advanced laser systems The advanced laser systems work was performed by NPL, HHUD, OP, PTB, UOB, Menlo and EPFL. The work here was focussed upon the development of the FSS (Frequency Stabilisation System) [103], a space compatible reference cavity for the clock laser [34, 36], tests into the improvement of existing laser systems and research into compact and transportable frequency combs. The tasks for which UOB were responsible in this workpackage were to evaluate the use of different types of periodically poled nonlinear crystals for use in fibre pigtailed waveguides for the generation of 461 nm radiation [99].

WP3 - Advanced atomic package This workpackage and the following WP4 were the areas over which I was most responsible and the bulk of the work for SOC2 was performed. This section of work was made possible through some collaboration with NPL and PTB. It consisted of the design of the atomics package including the Zeeman slower [71], with evaluation of the bonding techniques which could be used in its construction. This atomics package should include a blackbody optimised optical clock chamber with the design of a thermal enclosure for the entire atomics package which allows temperature stabilisation to a precision of 0.1 K. The design and work towards this workpackage can be seen in sections 5.3 and B.3 with input from [99]. The other main part of this workpackage was the development of advanced techniques for atom flux generation which can be seen in section 5.1.1.

WP4 - Integration and characterisation Workpackage four was centred around the integration of all constituent clock parts and the characterisation of them as a whole. Involved in this workpackage were UNIFI, UOB and PTB. UNIFI were responsible for the characterisation of the first generation clock with the second generation lasers [10, 61] before these lasers were sent to UOB for integration onto the second generation breadboard. Due to the complex nature and sheer number of lasers and electronics to be used, I was also part of the team at UNIFI for a short amount of time to assist with these characterisations. Once the laser breadboards (except the clock laser) and FSS were sent to UOB, I was tasked with the integration and characterisation of the entire system. There were some details which were omitted for which I had to find solutions and once the clock had been characterised up to the point of clock spectroscopy, I was charged to then transport the clock to PTB and perform a full characterisation with comparisons to the PTB stationary optical clock.

WP5 - Qualification tests of critical components This workpackage was performed solely by UNEU, CSEM, KT and LTF. These institutes were required to perform tests upon laser modules including those for space requirements (e.g. radiation exposure).

WP6 - Preliminary design of 3rd generation optical clock for space use This workpackage was performed by KT, KI and ASD in order to perform an assessment of space application criticality of proposed components of the transportable system, definition of requirements and preliminary assessment for power distribution and electronics for the 3rd generation clock, an analysis of SOC breadboards and generation of input to optimised space clock designs including the definition of major interfaces and main clock budgets, and the generation of a roadmap towards space optical clock developments.

WP7 - Coordination, dissemination and exploitation activities And finally WP7 which was performed solely by HHUD. This workpackage was mostly managerial in order to keep the project running smoothly from an administrative point of view.

Appendix B

Detection and Control System

B.1 Detection systems

It was decided to use two methods for imaging and detection simultaneously. Firstly we are using a PCO PixelFly USB ultra-compact 14 bit CCD camera in order to image the atoms which can be seen in figure B.1. This camera features state of the art CCD and electronics technology, has dimensions of only 72 x 39 x 47 mm, a low readout noise of typically 6 e^- rms, a high resolution 1392 x 1040 pixel with exposure times from 1 µs to 60 s and a very high quantum efficiency of 60 % at 461 nm. The camera is digitally triggered via the FPGA and the images are analysed by a LabVIEW programme pioneered at the University of Birmingham [99] which has been used as a basis and adapted for the specific needs of the SOC2 experiment. This programme allows images to be saved when a trigger is received and also allows for a round estimation of atom number and temperature. The atom number is estimated using the camera by the following equation,

$$N_A = \frac{4\pi r^2 I_D}{\varepsilon_Q A \Gamma_{scat}} \tag{B.1}$$

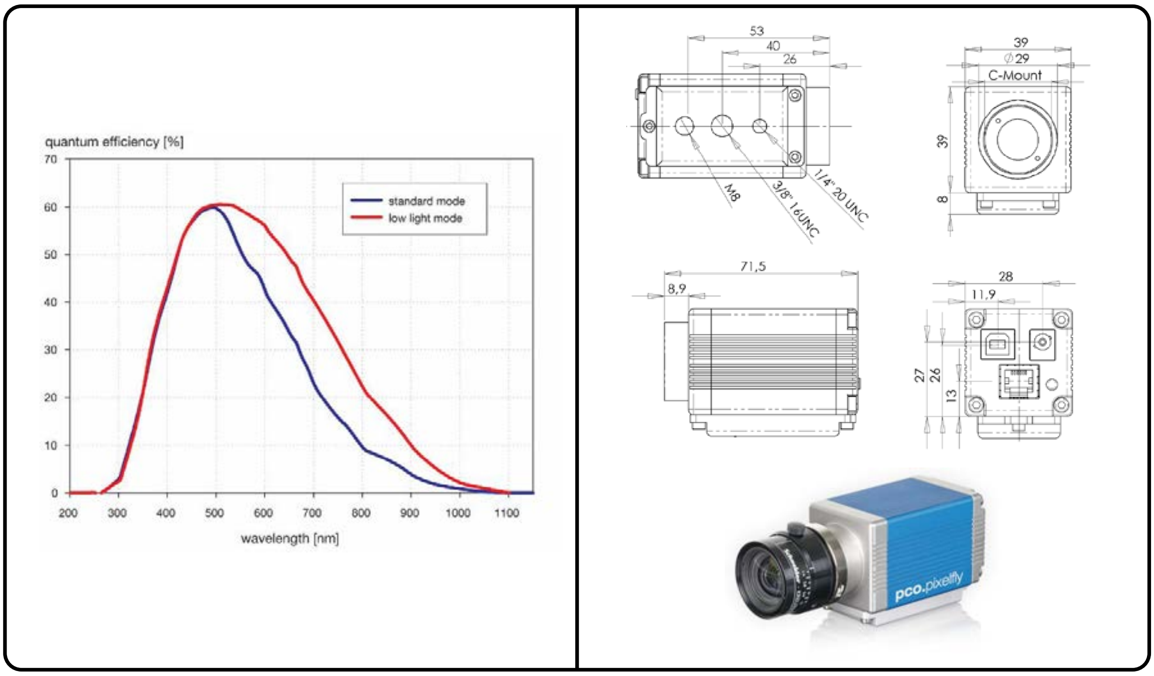

Fig. B.1 Specifications for the PCO PixelFly USB CCD camera. Left: the quantum efficiency of the camera from 200 to 1150 nm. Standard mode shown in blue and low light mode shown in red. Standard mode was used in this work. Right top: technical drawings of the camera. Right bottom: a photograph of the camera. Graphs, image and technical drawings from the PCO PixelFly USB datasheet.

where N_A is the atom number, r is the distance of the camera from the MOT, I_D is the intensity detected by the camera, ε_Q is the quantum efficiency of the camera at the correct wavelength and Γ_{scat} is the scattering rate for the transition which is being probed. The temperature of the MOT is calculated in the programme from the size of the MOT recorded from two images taken with a set amount of time between them. The programme can also be used to capture data of the loading time of the MOT by recording the atom number every 2 ms which is used to establish the lifetime of the MOT. This technique is sufficient for the blue MOT stage and for rough indications, however, we required a more sophisticated way to determine the atom number that was more sensitive and less dependent upon the background being uniform throughout a measurement campaign.

For this reason a photomultiplier tube (PMT) from Hamamatsu was purchased and a custom housing was made to mount this upon the apparatus, both the PMT and housing can be seen in figure B.2. The model R1463 has a spectral response from 185 - 850 nm with the wavelength of maximum response at 420 nm, the photocathode effective area is 10 mm in diameter, the supply voltage maximum is 1250 V, it has a gain of 1×10^6 and a time response of 24 ns. From calibration we established that the lowest number of atoms which we could confidently measure above the background noise was around 5×10^4. Calibration was performed by recording the voltage response of the PMT from a light source of known intensity and factoring this response by the solid angle of the PMT compared with the sphere of emitted radiation from the MOT. The background noise recorded by the PMT arose mainly from scattered light within the vacuum chamber and as much effort as possible was made to attempt to reduce this to a minimum. Another benefit to using the PMT is that this signal can be shown continually in real time, whereas the image from the camera can only be shown once the camera is triggered. This means that during measurement we have an image which we can reference to the PMT signal at any point.

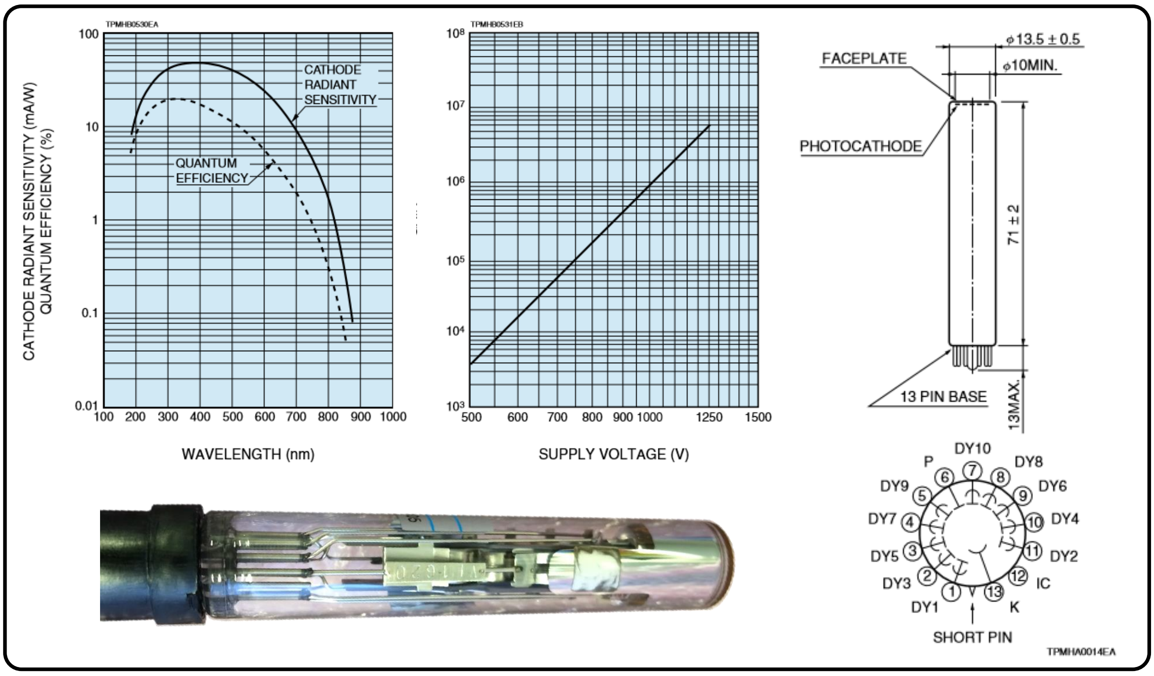

Fig. B.2 Specifications for the Hamamatsu model R1463 photomultiplier tube (PMT) used in detection of the trapped atoms. Top left: Quantum efficiency and cathode ray sensitivity of the PMT from 200 to 900 nm. Top middle: The gain of the PMT as a function of the supply voltage to the PMT. Bottom left: An photograph of the R1463 model PMT. Right: technical drawings of the PMT. Graphs and technical drawings taken from the Hamamatsu PMT model R1463 datasheet.

One of the ways in which the PMT was shielded from scattered background light was to place a flter in front of the PMT and to focus the MOT upon the active area of the PMT. This meant that the PMT was only sensitive to a narrow band around 461 nm where the quantum efficiency of the device was the highest. The PMT was used in conjunction with the camera in order to calculate the number of atoms in the cloud at any point but could not be used for the temperature measurements as this requires one to know the size of the cloud precisely.

The signal from the PMT can be viewed in real time on an oscilloscope or it can be viewed and the data logged on the computer. In order to do this I designed a simple circuit which served to invert the PMT signal and scale it down to be between ±5 V. This circuit was also triggerable so that the signal could be always recorded by the computer program or it could log just the detection signal of interest. The signal was sent through an analogue to digital converter found as part of a piece of data logging hardware from national instruments and the computer program was written in Python. The circuit can be seen in figure B.3.

B.1.1 Detection Method for Lattice and Second Stage MOT

A typical signal of an atom number measurement from the PMT can be seen in figure B.4. This shape is indicative of the atoms trapped in the second stage or lattice traps being illuminated with 461 nm radiation. The background can be seen in comparison on the right side of the figure. The height of the signal is proportional to the number of atoms which were trapped. Due to the fact that the atoms are imaged using the 461 nm radiation, the florescence observed by the PMT is from the atoms which were in the ground state. Once the atom absorbs and re-emits a blue photon, the atom is no longer trapped as the momentum kick caused by absorption and re-emission of the blue photon causes the atom to gain velocity. Therefore we can assume that all atoms in the ground state at the moment of absorption of the 461 nm radiation are no longer trapped. In the case of imaging the atoms trapped in the second stage MOT, these atoms have a very small probability of being re-trapped. The lifetime of the $^1P_1$ excited state is 21 µs, so it can be assumed that any atoms in the excited state when the ground state atoms are blown away will de-excite down to the ground state within this time, and therefore these atoms will then also absorb the 461 nm photons, and then spontaneously emit 461 nm photons and be detected by the PMT. The duration of the blue detection pulse is typically 20 ms and so around 1/40th of the duration of this signal is indicative of the atoms which were trapped. The slow decay down to the background can be explained by assuming that the atoms which have interacted with the 461 nm laser could still remain in the region where the blue laser beams overlap and they could interact again with the radiation due to the large linewidth of the blue transition and the emitted photons being reabsorbed by the surrounding atoms.

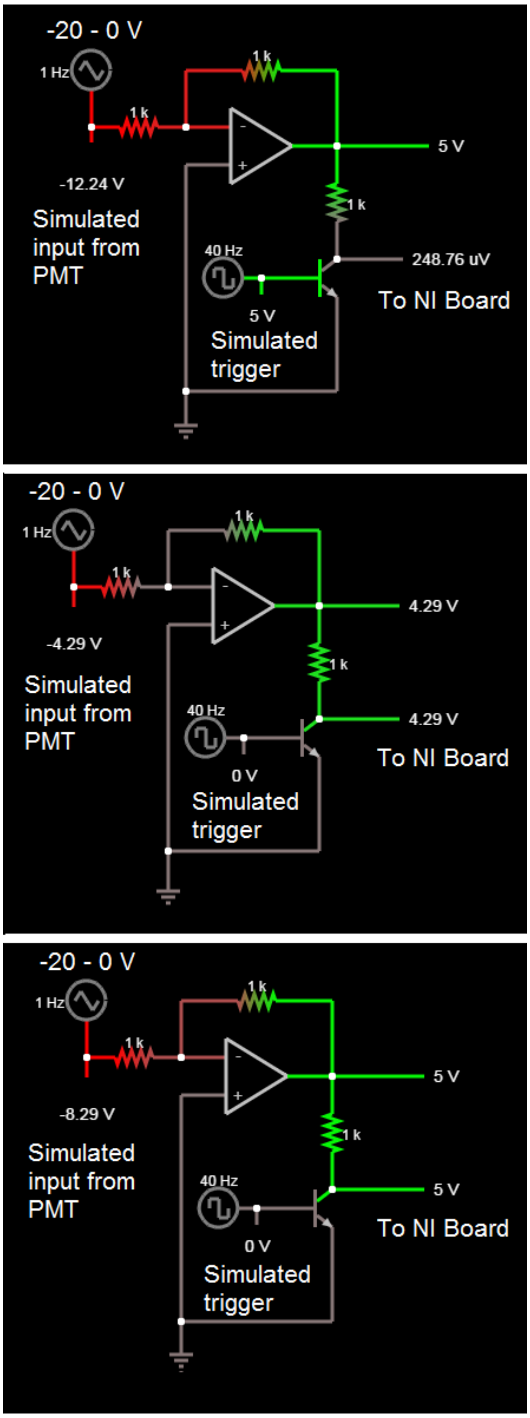

Fig. B.3 An electronic circuit designed for the digitalisation and sampling control of the analogue output from the photomultiplier tube. Image generated using falstad.com/circuit

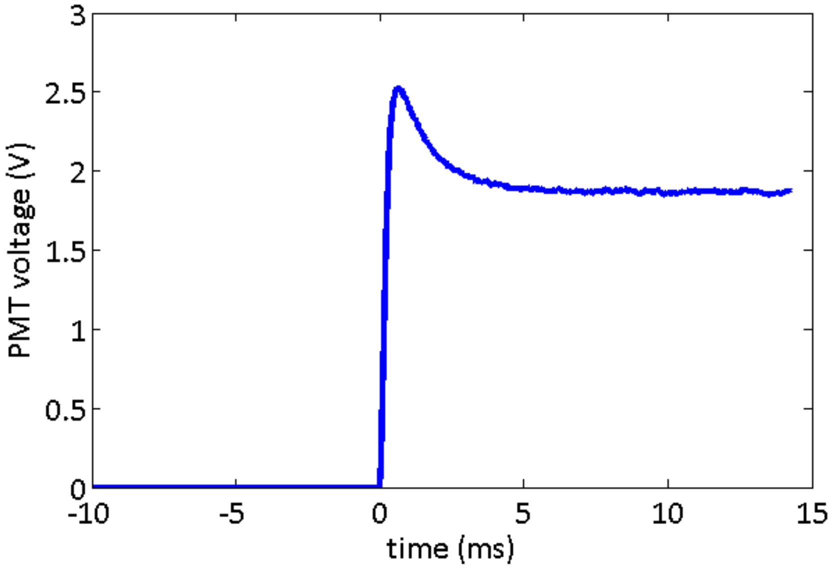

Fig. B.4 A typical florescence signal as recorded by the photomultiplier tube used as a method to determine atom number

B.2 FPGA Computer Control

One of the main goals for the SOC2 project is to realise a clock which could be controlled autonomously and remotely. An important step in the realisation of fully autonomous control has been made via the use of an FPGA. The FPGA is commercially available from National Instruments and is programmed in LabVIEW. The base programming was made by colleagues at The University of Birmingham [114] and was tailored to the needs of the SOC2 project. The FPGA contains analogue and digital outputs which can be configured within the base programming. In the case that the FPGA is connected to an internet network, it can be controlled remotely by a computer which is also on the same network. This could be extended to any computer via the use of VPN connections to the FPGA network. The next steps towards having full autonomous control of the experiment would be to have automatic digital locks for all of the laser systems. The DIGILOCK software offers this capability.

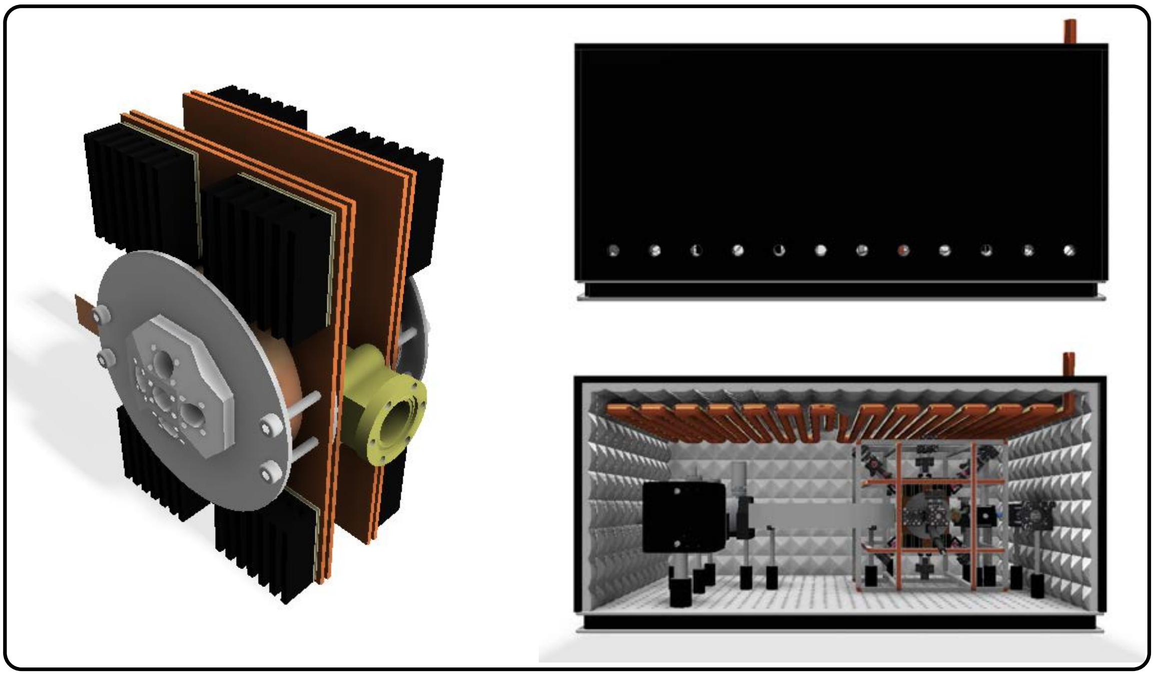

Fig. B.5 A CAD drawing of the temperature control design for the SOC2 apparatus. Left: Temperature control of the main atomics chamber. Right: proposed temperature stabilised and water cooled thermal enclosure for the atomics package.

DIGILOCK was used for the lock of the 922 nm laser and the 813 nm laser but the automatic locking functionality was not utilised at this stage.

B.3 Temperature Control

Due to the fact that the clock has been designed to be transportable, it is important to have as much control over the immediate environment of the optical clock as possible as the external environment of the clock will often change. To do so, a preliminary temperature control housing for the apparatus has been designed. It can be seen on the left in figure B.5. The temperature control has been based on the use of Peltier cells and an ardiuno microcontroller control loop. The temperature sensors used were a mixture of PT100 temperature sensors. Eight of these sensors were high performance sensors with a precision of 0.01 °C and a stated accuracy of 0.01 °C, the remaining sensors were of a moderate performance with a precision of 0.1 °C and a stated accuracy of 0.3 °C and were calibrated by the high-performance sensors. The final goal for the temperature stabilisation system was to ensure that the temperature across the entire experimental chamber is kept within a temperature fluctuation of 0.1 K. The most significant source of heat at the chamber comes from the heating of the 3D MOT coils. When in constant operation, the cooling plates can reach temperatures up to 40 °C. Whilst this is not a significant increase in temperature above room temperature, an increase of 1 °C causes as shift on the clock transition at the level of 10^{-16}. So it can therefore be seen that increasing the external temperature by 20 °C would cause the lowest available uncertainty of the clock to be in the order of 10^{-15} – 10^{-16} which is not acceptable for the final performance target of the clock. The right of figure B.5 shows a preliminary design for the temperature stabilised and water cooled thermal enclosure for the atomics package which has not yet been implemented and is discussed as a future goal in section 7.2.